A quantitative study of diffusion in quasi-periodic fibre networks and complex porous media

A THESIS SUBMITTED TO

THE SCIENCE AND ENGINEERING FACULTY

OF QUEENSLAND UNIVERSITY OF TECHNOLOGY

IN FULFILMENT OF THE REQUIREMENTS FOR THE DEGREE OF

DOCTOR OF PHILOSOPHY

Queensland University of Technology
Brisbane Australia

Sean K. Powell

Principal Supervisor: Konstantin I. Momot

Associate Supervisor: Christian M. Langton

School of Chemistry, Physics and Mechanical Engineering

Science and Engineering Faculty

Queensland University of Technology

2016

Keywords

Restricted diffusion, molecular dynamics, computer simulation, Monte-Carlo, Langevin dynamics, random walks, lattice, percolation modelling, diffusion tensor imaging, tissue engineering, scaffolds, interpretive models, microstructure, articular cartilage, collagen, tissue fibres, heart muscle, neural tractography.

Abstract

Diffusion is the fundamental process behind many important phenomena such as the mixing of substances and the transport of water, oxygen, and nutrients into and around living cells. The physical basis for diffusion is the spontaneous and random motion of molecules and atoms in a fluid and some solids. In complex porous media such as biological tissue, diffusion is restricted by interactions with internal structures. Through these interactions, the local geometry of the structures is, to some extent, 'encoded' in the diffusive behaviour of the molecules. This provides an opportunity to use observations of restricted diffusion to obtain detailed information about the morphology of porous media, via quantitative interpretive models. The development of such models is the central goal of this thesis.

In this work, we present theoretical and experimental studies of restricted diffusion with the aim of efficiently producing quantitative models for interpreting diffusion tensor imaging experiments. The first approach involved the development of equations of motion and associated computer software to simulate water diffusion in model fibre networks. We based the motion of the water molecules on Langevin dynamics to provide physically realistic modelling of water/barrier interactions. This approach is optimal for modelling diffusion within periodic structures and where water displacements are greater than the typical correlation length of the structure. Using Langevin dynamics, we simulated diffusion in volumes surrounding several configurations of collagen fibres of articular cartilage. Specifically, we investigated the

quantitative relationship between the diffusion tensor and the partial alignment and volume fraction of various collagen fibre networks. The results formed the basis for a model to interpret diffusion tensor images of articular cartilage in terms of its tissue microstructure. The model suggests that the diffusion ellipsoid transitions from prolate in the radial zone of articular cartilage to oblate in the superficial zone, with its degree of anisotropy throughout proportional to fibre volume fraction. We also found that the minimum anisotropy of the diffusion tensor occurs when the collagen fibres are oriented at $\sim 54.7^{\circ}$ (the magic angle) with respect to parallel alignment. This angle has significance in magnetic resonance experiments and is a root of the second order Legendre polynomial. The results of the simulations also indicate that the diffusion tensor is invariant to positional and radial disorder in aligned fibre networks. A simplified analytic model was developed to approximate the diffusion tensor in partially aligned fibre networks and used to further investigate the Langevin dynamics simulation results. This research led to the publication of two peer-reviewed papers.

The second theoretical approach aimed to produce highly accurate maps of particle displacement probabilities for complex restricted diffusion problems. Our method, the Lattice-Path Count (LPC) algorithm, considers space as a discrete lattice and enumerates all possible particle trajectories. It accounts for absorbing, reflecting and semi-permeable barriers by computing their effect on path availability. The algorithm can be considered a discretised method for evaluating Weiner path integrals for Brownian motion. We developed computer software to efficiently and exactly enumerate lattice paths using unlimited length integers. This software was further optimised to run on desktop computers and a multi-processor supercomputer. LPC propagators were produced and validated against selected one and three dimensional systems with exact analytic solutions. We also computed LPC and Monte-Carlo propagators for single particle restricted diffusion in a 3D volume containing impermeable aligned cylinders. The LPC propagator was superior in that it contained no statistical noise. Additionally,

we derived an expression for estimating the statistical error of diffusion propagators from stochastic computer simulations. We also computed LPC propagators for multi-particle diffusion in various percolation networks and compared these with respective finite element method (FEM) solutions. In addition to efficiently solving restricted diffusion problems, the LPC approach provides valuable insight into the physical meaning of the restricted diffusion propagator as the relative number of paths of a given length connecting two locations. In its essence, the LPC method exactly counts random walks and therefore has applications beyond diffusion modelling such as in finance and economics, astrophysics, and biological population systems. The LPC algorithm and analysis is presented as a journal paper, and a corresponding applications paper is presented in Appendix D.

The experimental component of this thesis complemented the theoretical work through a diffusion tensor imaging (DTI) study of the fibre networks of tissue engineering scaffolds. The scaffolds were produced using direct-write melt-electrospinning and comprised layers of 90 degree cross-hatch fibres with $\sim 10-50\,\mu m$ fibre diameters and $150\,\mu m$ fibre spacings. Time-dependent diffusion tensor imaging and micro-computed tomography (micro-CT) measurements of the scaffolds were performed. Diffusion anisotropy was found to be consistent with the scaffold geometry, with diffusion least restricted in the direction perpendicular to the fibre layers. We also found that the magnitude of this anisotropy was larger for longer diffusion measurement times. The μ-CT results indicated greater structural disorder in the direction through the fibre layers than across the layers, suggesting the diffusion tensor is invariant to positional disorder of the fibres. In addition to supporting the overall goals of this thesis, the experimental work has important application in tissue engineering for the non-invasive real-time monitoring of the maturation and metabolite transport pathways in tissue engineering scaffolds. This experimental study led to the publication of a peer-reviewed journal article.

In summary, the results of this thesis have particular application for producing quantitative interpretive models to improve the utility of diffusion tensor imaging for investigating the structure and molecular transport within tissues and tissue engineering structures. Each approach was optimised to model diffusion over a given spatial and temporal scale to allow the results of this study to encompass a wide range of the restricted diffusion problem space. The experimental study provided complementary results thought the quantitative analysis of the microstructure of custom-made fibre networks. In addition to the interpretive models, the findings of this thesis provide further insight into the physics underlying restricted diffusion.

List of publications and manuscripts

Refereed papers

Chapter 3

1. **Powell, Sean K.**, and Konstantin I. Momot. "Langevin dynamics modeling of the water diffusion tensor in partially aligned collagen networks." *Physical Review E* 86(3) (2012): 031917

2. **Powell, Sean K.**, and Konstantin I. Momot. "Computer modeling of diffusion in biological tissues." *Procedia Information Technology and Computer Science* 3(1) (2013): 1227-1233

Chapter 4

3. **Powell, Sean K**, Oberman, Glen J and Momot, Konstantin I, Efficient calculation of restricted diffusion propagators using lattice path counts, *Physical Review E* (2015) (submitted).

Chapter 5

4. **Powell, Sean K**, Ristovski, Nikola, Liao, Sam, Blackwood, Keith A., Woodruff, Maria A. and Momot, Konstantin I., Characterisation of the micro-architecture of direct writing melt electrospun tissue engineering scaffolds using diffusion tensor and computed tomography microimaging, *3D Printing and Additive Manufacturing* (2014) ,1(2),95-103

Appendix D

5. Momot, Konstantin I, **Powell, Sean K**, Tourell, Monique C., Further development of discrete computational techniques for calculation of restricted diffusion propagators in porous media, *Microporous and Mesoporous Materials*, (2014), 205(1), 24-30

Conference presentations

1. **Powell, Sean K**, Ristovski, Nikola, Liao, Sam, Blackwood, Keith A., Momot, Woodruff, Maria A. and Konstantin I., Diffusion tensor and computed tomography microimaging study of scaffolds for tissue engineering, Oral presentation, *Australian Society for Biomaterials and Tissue Engineering Conference*, Sydney, Australia, 2015

2. **Powell, Sean K.**, Monique Tourell, Sabrina Barheine, Alf Pawlik, Jean-Philippe Ravasio, Samuel Guesne, Chris Bell, Gary Cowin, James M. Pope, R. Mark Wellard, Konstantin I. Momot, MR microimaging of articular cartilage, Poster Presentation, *Australia and New Zealand Society for Magnetic Resonance Conference*, Torquay, Victoria, 27(2011)

3. Jean-Philippe Ravasio, Sabrina Barheine, Alf Pawlik, **Powell, Sean K.** , Samuel Guesne, Chris Bell, Gary Cowin, James M. Pope, R. Mark Wellard, Konstantin I. Momot, MR microimaging of articular cartilage, Poster Presentation, *European Congress on Magnetic Resonance (EUROMAR)*, Frankfurt am Main, Germany, (2011)

4. **Powell, Sean K.** and Momot, Konstantin I, Langevin dynamics modelling of water diffusion in anisotropic biophysical structures, Poster Presentation, *BioPhysChem 2011*, Wollongong, NSW, (2011).

5. **Powell, Sean K.** and Momot, Konstantin I, A study of water diffusion in partially aligned fibre networks, Poster Presentation, *20th Australian Institute of Physics Congress*, Sydney, (2012).

Table of contents

List of Figures

List of Tables

List of abbreviations

Abbreviations

1D	One Dimensional
2D	Two Dimensional
3D	Three Dimensional
AC	Articular Cartilage
ADC	Apparent Diffusion Coefficient
AM	Additive Manufacturing
BC	Boundary Condition
C	Concentration
C++	Object Oriented C
CPU	Central Processing Unit
CT	X-ray Computed Tomography
$\overline{\mathbf{D}}$	Diffusion Tensor
D_O	Bulk Diffusion Coefficient
D(t)	Time dependent Diffusion Coefficient
DT	Diffusion Tensor
DTI	Diffusion Tensor Imaging

F_C	Interaction Force
FA	Fractional Anisotropy of the Diffusion Tensor
FD	Finite Difference
FDM	Fused Deposition Modelling
FEM	Finite Element Modelling
GMP	GNU Multiple Precision Arithmetic Library
HPC	High Performance Computer
J	Flux
LD	Langevin Dynamics
LJ	Lennard-Jones Interaction Potential
LPC	Lattice Path Count
LSF	Least Squares Fit
MA	Magic Angle
MC	Monte Carlo
MIL	Mean Intercept Length Tensor
MRI	Magnetic Resonance Imaging
MSME	Multiple-slice Multiple-echo
MTM	Markov Transition Matrix
N_i^t	Node at Location i in Time t
N_P	Number of Tracer Particles
N_T	Number of Time Steps
P	Probability
$P(\mathbf{r}_o, \mathbf{r}, t)$	Diffusion Propagator

PCL	Polycapralactone
PDF	Probability Density Function
PG	Proteoglycans
PGA	Proteoglycan Aggregate
PGSE	Pulsed Field-Gradient Spin Echo
R_1	Longitudinal Relaxation Rate
R_2	Transverse Relaxation (Spin-Lattice)
RF	Radiofrequency
RMS	Root Mean Squared
ROI	Region of Interest
S/V	Surface to Volume Ratio
SEM	Scanning Electron Microscope
SGI	Silicon Graphics Incorporated
S_P	Positional Disorder Parameter
S_R	Radial Disorder Parameter
t	Time
T_1	Longitudinal Relaxation Time (Spin-Lattice)
T_2	Transverse Relaxation Time (Spin-Spin)
TE	Tissue Engineering
T_E	Echo Time
T_R	Repetition Time
VACT	Velocity Autocorrelation Time
Δr	Displacement Magnitude

Δ	Diffusion Interval
Δt	Integration Time Step
μCT	X-ray Micro-Computed Tomography
μMRI	Magnetic Resonance Micro-imaging
τ	Tortuousity

Statement of original authorship

The work contained in this thesis has not been previously submitted to meet requirements for an award at this or any other higher education institution. To the best of my knowledge and belief, the thesis contains no material previously published or written by another person except where due reference is made.

Signature:

Date: 19-01-2016

Acknowledgments

My Family,

Tammy, Elijah, Daniel, Timothy, Mum, Dad, Tony, Ben, Maddy.

My Friends,

Monique, Matt, Glen, Nora, the QUT physics group, MRI research group, the Biomaterials and Tissue Morphology Group and other friends :)

Supervisors and Support Team

Konstantin Momot, Mia Woodruff, Christian Langton, Esa Jaatinen, Mark Wellard, John Bell, Stephen Hughes, the QUT physics academics and the many others who have supported me throughout my PhD journey.

Panel members

Matthew Simpson and Andrew Fielding.

Research Support

School of Chemistry Physics and Mechanical Engineering, the Institute of Health and Biomedical Innovation, the Australian Research Council, High Performance Computing Centre and Research Support Group at QUT.

Chapter 1

Introduction

1.1 The problem

Diffusion is the spontaneous and random motion of atoms and molecules that, in fluids, leads to a redistribution of their positions. This process is fundamental to many phenomena such as the mixing of substances and the transport of water, oxygen, and nutrients into and around cells in living systems. In porous media, diffusion is often restricted by the presence of internal structures and by the confining geometry of the pore space. This is the case for biological tissue which is intrinsically heterogeneous, comprising complex arrangements of macromolecules, cell membranes, organelles and larger tissue structures.

The attenuating effect of diffusion on the nuclear magnetic resonance signal was first recognised in 1950 by E Hahn [1]. This was further characterised by Carr and Purcell in 1954 [2], and nine years later Stejskal and Tanner proposed a novel method to indirectly observe translational diffusion through the application pulsed magnetic field gradients during spin-echo magnetic resonance experiments [3]. In 1994, Basser,

Mattiello and LeBihan introduced diffusion tensor imaging [4]. This magnetic resonance modality applies several non-colinear magnetic field gradients to measure diffusion along different directions. These measurements are then combined to produce a diffusion tensor; a mathematical object that represents diffusion anisotropy. An ongoing challenge, and one central to this thesis, is the development of theoretical models of restricted diffusion for the interpretation of diffusion magnetic resonance imaging of porous media.

In this thesis, we present two algorithms for modelling restricted diffusion, each optimised for a given spatial and temporal scale. The purpose of these algorithms is for the production of models to quantitatively interpret tissue structure from diffusion measurements. These theoretical studies are complemented through a series of diffusion sensitive magnetic resonance imaging experiments of specially made 3D micro-fibre networks.

The first algorithm, detailed in Chapter 3, is based on custom Langevin dynamics software to simulate restricted diffusion in the interstitial volume surrounding quasi-periodic partially aligned fibre networks. The software allows the networks to be configured to mimic various fibre structures within biological tissue. One such tissue is articular cartilage (the soft white tissue covering the articulating surfaces of movable joints) which comprises closely packed collagen fibres with various degrees of fibre alignment. The organisation of the collagen fibres is important for the structural and biomechanical performance of the joints. Consequently, knowledge of their arrangement is of significance in research and clinical studies. Using our Langevin dynamics software, we modelled various partially aligned collagen fibre networks. We simulated restricted diffusion in each network and derived a set of corresponding theoretical diffusion tensors. These tensors were then used to produce a model for the quantitative interpretation of articular cartilage microstructure from diffusion magnetic resonance images.

The second algorithm, detailed in Chapter 4, was developed to produce highly accurate diffusion propagators for complex and highly tortuous diffusion problems. Diffusion propagators are maps of displacement probabilities for diffusing particles. Simulation techniques such as Langevin Dynamics produce 'noisy' propagators because they only model an extremely small fraction of the total number of possible particle trajectories. Our approach, the Lattice Path Count algorithm (LPC), represents space as an array of discrete locations (a lattice), and then exactly counts all possible diffusing particle trajectories connecting pairs of locations. We model restricted diffusion by computing the effect of barriers on path counts. In addition to efficiently computing restricted diffusion propagators, the LPC approach provides an intuitive physical insight into the restricted diffusion propagator as the relative number of paths of a given length connecting a pair of points. Using LPC, we produced propagators for selected 1D and 3D restricted diffusion problems with known analytic solutions, compare LPC and Monte-Carlo propagators for diffusion in the volume surrounding an array of aligned cylinders, and compare LPC and finite element method (FEM) propagators for various percolation systems. The use of exact path counting to model restricted diffusion was shown to be intrinsically stable, accurate for single particles random walks, and has application to other random-walk problems such as in lattice percolation modelling [5], finance and economics [6], biology [7], astrophysics [8].

Theoretical models of restricted diffusion problems use idealised representations of barriers and confining structures. For example, the computer models in this thesis used very simple geometries like cylinders and spheres as barriers. In real-world experiments, barriers are almost never smooth and regular. To investigate this further and complement the theoretical work of this thesis, we undertook a series of diffusion tensor imaging experiments of specially made polymer fibre networks (see Chapter 5). The use of these networks enabled us to obtain experimental diffusion measurements

for objects with known architectures. This was distinct from typical diffusion experiments of biological tissue where the tissue architecture is not known a priori. This research also constitutes the initial step in the application of diffusion tensor imaging for the quantification of the internal structures of tissue engineering scaffolds. This is particularly important as the internal structure of these scaffolds are altered by tissue growth which can block vital oxygen and nutrient transport pathways.

In summary, the aim of this thesis is to develop theoretical methods for producing quantitative models for interpreting diffusion tensor images. Using these methods, we produced quantitative interpretive models for DTI measurements of articular cartilage. Diffusion tensor imaging measurements were also performed on the micron-scale fibre networks of tissue engineering scaffolds for experimental validation and to characterise the micro-architecture. The approach taken for the theoretical component of this thesis involved developing Langevin dynamics simulation software (Chapter 3 and Appendix A and B), and deriving a numerical approach for solving Weiner path integrals for restricted Brownian motion (Chapter 4 and Appendix D). The experimental component of this thesis involved a series of diffusion tensor imaging measurements of specially made fibre networks to further investigate the relationship between diffusion and structural anisotropy (Chapter 5).

1.2 Key aims

The aim of this work is to improve the quantitative understanding of restricted diffusion in partially aligned fibre networks and complex pore spaces. This has applications for the development of quantitative models for interpreting diffusion tensor images of anisotropic tissue and tissue engineering scaffolds.

1.3 Key objectives

1. Develop numerical modelling software to simulate molecular translational dynamics in model tissue structures. Optimise the technique for the study of diffusion in periodic structures; particularly diffusion scenarios where the root mean squared displacements of diffusing molecules is greater than characteristic separation between periodic elements. Derive equations of motion using Langevin dynamics to compute physically realistic water/tissue interactions without the need to process all particle interactions.

2. Use the numerical method to produce models for interpreting diffusion tensor imaging experiments of articular cartilage in terms of the morphology of the collagen fibres. Also investigate the effects of statistical noise and fibre positional and radial disorder of the diffusion tensor through further simulations and a simplified analytical model.

3. Develop an algorithm to efficiently compute highly accurate time-dependent restricted diffusion propagators. Optimise the method to investigate complex and highly tortuous restricted diffusion problems, including those where the root mean squared displacement of the of the diffusing molecules is shorter than the typical correlation length of the pore structures. Compare various propagators of this method with those of existing analytical and numerical approaches. Discuss the physical insight of restricted diffusion from a molecular trajectory perspective and the application of this method to producing interpretive models of diffusion tensor imaging experiments. Also discuss the application of LPC for solving general lattice random walk problems.

4. Produce polymer fibre networks with well-defined internal microarchitectures for use in diffusion tensor imaging experiments. Use a combination of magnetic resonance imaging and x-ray computed tomography to provide structural

characterisation of the network architectures.

5. Undertake a series of diffusion tensor imaging experiments of electrospun fibre networks to investigate the relationships between network microstructure and the diffusion tensor. Investigate the time-dependency of the measured diffusion tensor with respect to scaffold architecture. Also investigate the utility of diffusion tensor imaging for the non-invasive study of microstructure and molecular transport in tissue engineering scaffolds.

1.4 Thesis structure and overview.

The development of theoretical models for interpreting DTI measurements of fibre networks is key to enabling a quantitative experimental study of fibrous biological tissue and tissue engineering scaffolds. These models have applications for the diffusion tensor imaging of tissue fibre structures such as that found in the nervous system, muscles, eye lens, and articular cartilage, as well as for studies of the structure and molecular transport pathways in tissue engineering scaffolds. The thesis is organised into the following structure, with each of the research components presented as expanded versions of published papers:

- Chapter 1 introduces the research problem of this thesis, outlines the aims, and discusses how the individual research problems link to address the overall goal of this work. This chapter also outlines the organisation of the thesis.

- Chapter 2 gives a background literature review of the physics and mathematical descriptions of restricted diffusion. It then discusses the principles of diffusion sensitive magnetic resonance imaging and its methods and applications. It concludes by discussing relevant applications for diffusion imaging such as biological tissue comprising fibre structures such as nerves, muscle fibres, and

collagen fibres of articular cartilage, and the fibre networks of tissue engineering scaffolds.

- Chapter 3 presents two published papers detailing the first of the theoretical diffusion modelling methods, the Langevin dynamics simulations (LD). This method is applied to the production of quantitative interpretive models of diffusion tensor measurements of partially aligned collagen fibre networks [9, 10]. The results of the first manuscript include a series of models relating experimental diffusion tensor measurements of articular cartilage to specific characteristics of its microstructure; specifically fibre volume fraction and degree of fibre alignment. The applications and limits of the interpretive models are discussed in the context of diffusion measurements, and the results compared with other studies. A related simplified analytic model was also derived based on the Rayleigh multipole method. The second manuscript presents a study investigating the effects of time-step size on the sampling accuracy of the deterministic potential in LD simulations. It also presents the results of diffusion simulations in volumes containing aligned cylinders with different degrees of positional and radial disorder.

- Chapter 4 extends the research of the previous chapter to the problem of producing diffusion propagators for restricted diffusion in highly complex and tortuous systems. This research was motivated by shortcomings of the Langevin dynamics simulations of the previous chapter, and resulted in the development of the Lattice Path Count algorithm for the efficient calculation of restricted diffusion propagators. The chapter is presented in the form of a publication, with a related extended study presented in Appendix D. The first paper introduces the LPC algorithm and applies it to produce various propagators for select 1D and 3D problems with known analytic solutions, and propagators for highly tortuous percolation problems. The LPC percolation propagators were

also compared with those from finite element solutions to the diffusion equation. This enabled investigations into the limits and stability issues of these numerical approaches. Propagators were also produced for restricted diffusion surrounding aligned cylinders and compared with those produced using Langevin dynamics. This enabled the development of an expression for quantifying the statistical uncertainty of statistical methods such as LD [11]. The second related publication in Appendix D, presents the LPC method alongside another approach, the Markov Transition Matrix method, and explores their application in the context of producing models for interpretation of diffusion magnetic resonance experiments. This publication also further discusses comparisons of the LPC method with stochastic simulations techniques [12].

- Chapter 5 presents the experimental component of this thesis as a published paper [13]. This study involved a series of diffusion tensor imaging studies of customised micron-scale fibre networks of electrospun tissue engineering scaffolds. The use of electrospinning enabled the fabrication of scaffolds with 90 degree cross-hatched fibre networks with fibre diameters of $\approx 10 - 50\,\mu m$ and fibre spacings of $\approx 150\,\mu m$. Diffusion tensor imaging experiments were performed on the scaffolds over a various diffusion measurement times; 50 ms, 200 ms and 250 ms. Given the scale of the scaffolds, this placed the measurements in the intermediate-Δ diffusion regime. We also carried out μCT analysis to quantify the scaffold microstructure. The experimental diffusion tensors were analysed in the context of the aims of this thesis and the time dependent experimental diffusion tensors found to be consistent with an interpretive model described in Chapter 3. The publication also aimed to introduce diffusion tensor imaging as a non-invasive technique for the quantitative study of the microstructure and mapping of molecular transport pathways within tissue engineering scaffolds.

- Chapter 6 concludes the thesis with a summary of the research outcomes and

identifies key issues for further research.

Chapter 2

Theory and background

Diffusion is the thermally driven random motion of particles in a fluid, some solids, or ”soft” materials leading to the mixing of substances [14–16]. This net transport process results in the random redistribution of particle positions and is distinct from bulk transport processes such as advection or convection [17]. Consequently, diffusion is a significant fundamental process in many physical systems, particularly for the transport of metabolites and waste in biological tissue. In addition to its transport function, observations of diffusion that is restricted by the structures of the tissue can yield quantitative information about the structure of the tissue, via the appropriate theoretical interpretive models.

In this chapter we discuss the physics of restricted diffusion and relevant mathematical modelling techniques, followed by the theory and application of diffusion sensitive magnetic resonance as an experimental technique for observing diffusion. In the final two sections, we discuss anisotropic biological tissue and fibre networks of melt-electrospun tissue engineering constructs, respectively, in the context of diffusion experiments and quantitative interpretation of network microstructure.

2.1 Physics of diffusion

The classic picture of diffusion is based on the idea of 'flows' operating under the influence of 'forces'. These flows describe the mixing of fluids and the transfer of electricity and heat across a space. In this picture, the 'forces' are attributed to concentration gradients for chemical mass transport, electric potentials for electric current and temperature gradients for heat [18]. As early as the 1780's, similarities were noted between the diffusion of mixed species and the flow of heat by Claude-Louis Berthollet [19]. This idea was further developed by Joseph Fourier, who formulated a linear relationship between the gradient of the temperature and the flow of heat [20]. A short time later, a similar relationship was identified by Georg Ohm in the context of electric current and the potential difference across a conductor. It wasn't until the 1800's that Adolf Fick combined Berthollet's ideas with Fouriers observations to express his first law of diffusion [21]. The linear relationships driving the flows of these phenomenon can be easily seen by comparing their equations;

Fourier's law:

$$J_q = -k \left(\frac{dT}{dx} \right) \hat{\mathbf{r}} \tag{2.1}$$

Fick's law:

$$J_i = -D \left(\frac{dC_i}{dx} \right) \hat{\mathbf{r}} \tag{2.2}$$

Ohm's law:

$$I = -\kappa A \left(\frac{dQ}{dx} \right) \hat{\mathbf{r}} \tag{2.3}$$

where J_q is the heat flow, J_i is the flow of i across a reference plane, I is the electric current, T is the temperature, C_i is the concentration of i, and Q is the charge, k and κ are the coefficients of thermal and electrical conductivity, respectively, A is the cross-sectional area and D is the diffusion coefficient, and $\hat{\mathbf{r}}$ is a unit vector. Due to their

functional similarity, solutions to these equations are often useful across the various problem domains [18, 22–25]. For example, the basis for the analytic model of diffusion developed in Chapter 3 (see Eq. (3.6)) is an adaptation of the multipole method developed by Lord Rayleigh for investigating the limits of the Lorentz-Lorenz equation that expressed the relation between the refractive index and density of cylinders in an array [26].

Diffusion describes the net transport of particles in a fluid and some solids as due to their thermally driven random motion [22]. In fluids, this process occurs in addition to other bulk transport processes such as convection and advection [27, 28]. As a results of this random motion, a given particle in a bulk fluid will trace out a tortuous trajectory. In the absence of confinements, the corresponding displacement probability density (PDF) is spherically symmetric and Gaussian and the width of the Gaussian PDF spreads out with time [29–33]. This phenomenon is often called Brownian motion, named after Robert Brown who first described the random motion of the organelles from ruptured pollen grains suspended in a liquid in his microscope observations. He also observed the motion of ground glass and other ”dead” materials. In his analysis, he ascribed this motion to the properties of the fluid and not to the observed particles themselves [34].

In many cases diffusion occurs in volumes containing barriers or within the confining geometry of pore spaces. The diffusing particles interact with the barriers and experience a corresponding change in their trajectories leading to a different translation probability distribution than in the unobstructed case. Observations of changes in the distributions of diffusing particles can therefore be a useful indicator of the structure of the confining geometry. The principle behind solving this type of inverse problem was succinctly posed by Mark Kac in his 1966 paper ”can you hear the shape of the drum”, where he set out to investigate how much of the drum’s shape can be inferred using knowledge of all of the eigenvalues of the relevant eigenvalue problem [36]. In the

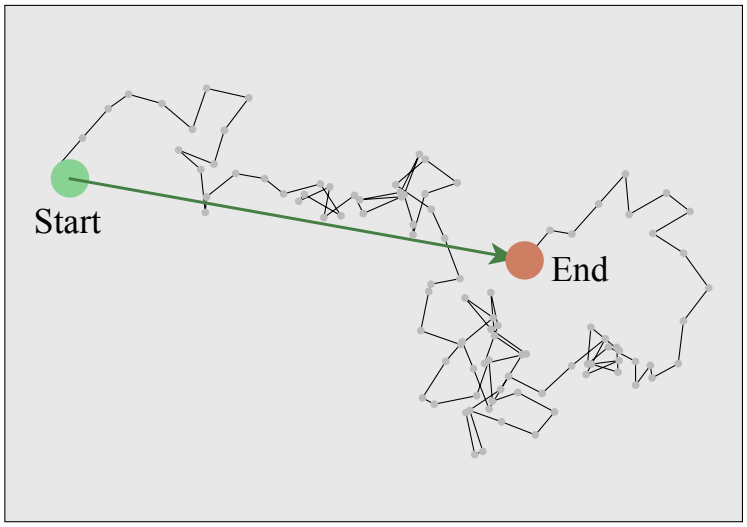

Figure 2.1: Sample trajectory of 100 steps of a Brownian particle generated using a Monte-Carlo simulation co-written by the author and used by Tourell, Powell, and Momot 2013, in the study of diffusion in fibre networks with a distribution of alignments [35]- 2D projection of displacements of 3D simulation. Each step has a fixed displacement and a random direction. The green arrow indicates the displacement of the particle.

context of molecular diffusion, rather than 'hearing' the sounds of a drum, the average net displacements of diffusing particles can be observed along different directions. Various mathematical techniques can then be employed to extract information from these displacements about the microstructure of the diffusion environment. Solving these problems essentially involves finding a diffusion equation solution backwards in time, i.e. finding the initial distribution f from a later distribution g [37]. One example of the inverse diffusion problem is the classic backward heat conduction problem which involves determining the original heat distribution from the distribution at a later time [38]. Mathematically, inverse diffusion problems are considered ill-posed meaning that the "smooth" nature inherent in diffusion processes results in an irreversible loss in the detail of the original distribution. General approaches for solving these problems involves replacing the original inverse problem (with no unique solution) with a problem that has a well defined solution [37]. Much of the work of the present thesis is aimed toward solving relevant inverse diffusion problems to determine from time varying molecular distributions particular aspects of the "shape"

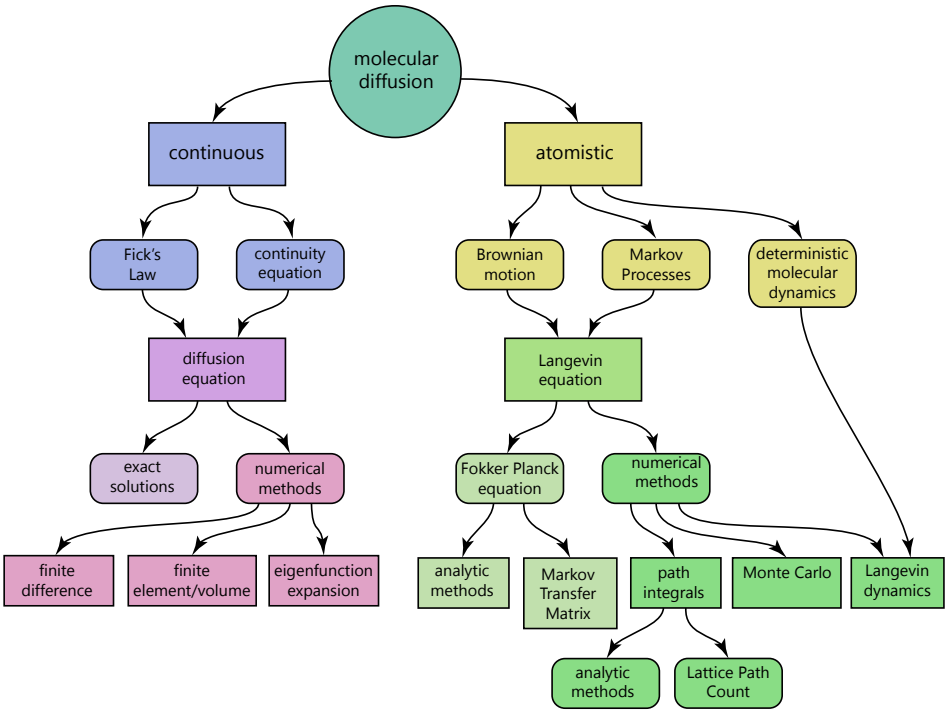

Figure 2.2: Illustration of various diffusion modelling techniques indicating their conceptual roots; continuous or atomistic

of the confining geometries.

The preceding discussion implies two fundamental conceptual models of diffusion; continuum and atomistic. Figure 2.2 is an attempt to summarise various diffusion modelling approaches and their conceptual starting points. The left branch of Fig. 2.2 indicates modelling approaches which derive from Adolf Fick's observations of fluid mixing within a continuum. The right branch illustrates methods which follow from the perspective of particle random walks. The random walks form Markov chains which are either be sampled using molecular simulations, or explicitly modelled using path integrals or path counts. It should be noted that this illustration is not exhaustive, and through application of the central limit theorem [39], the methods can be shown to model the same physical phenomenon [7]. In the following sections, we discuss the origin and mathematics of some of these fundamental diffusion modelling techniques and their applications to the principle work of this thesis.

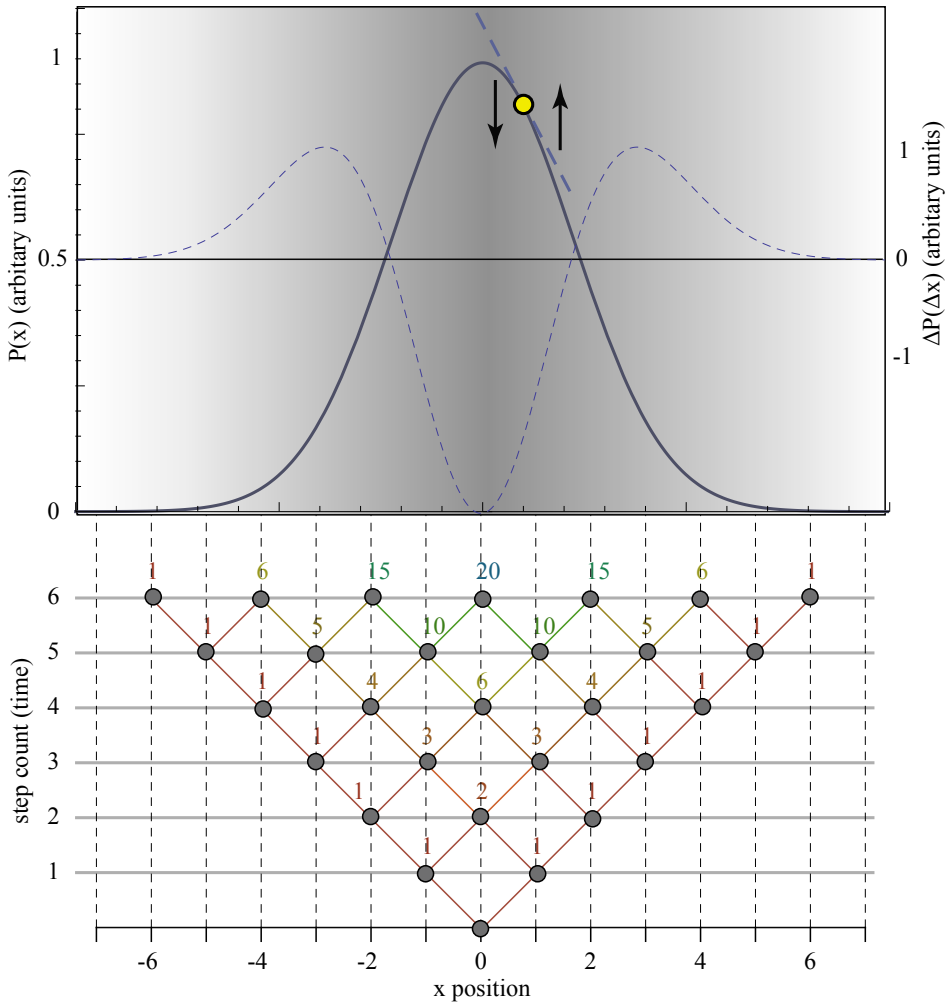

Figure 2.3: Illustration showing a comparison between continuum and atomistic modelling of unrestricted molecular diffusion in one dimension. The top section of the figure shows a plot of particle concentrations (thick grey line). The blue dashed line is the second derivative of the concentration. The bottom section shows diffusion from the perspective of a particle that starts at $x = 0$ and steps either left or right for a total of 6 time steps

2.1.1 The diffusion equation

The earliest mathematical treatments of diffusion were developed by Adolf Fick in the late 1800's. He considered the fluid as a continuum and noted that particles in the fluid tend to move from regions of high concentration to regions of lower concentration on average [17]. In one dimension, the particle flux (or particle current) $J(x,t)$ describes the number of particles that pass point x per unit time. From experiments, it is known that this flux is proportional to the concentration gradient,

$$J(x,t) \propto \frac{\partial C(x,t)}{\partial x} \tag{2.4}$$

This expression is equivalent to Fick's first law of diffusion in equation Eq. (2.2), but without the coefficient of proportionality. Assuming that the number of particles is conserved (particles are neither created nor destroyed), then the continuity equation means that the change in concentration at a given location depends on the flux into and out of this location,

$$\frac{\partial C(x,t)}{\partial t} = -\frac{\partial J(x,t)}{\partial x} \tag{2.5}$$

which results in the well-known diffusion equation,

$$\frac{\partial C(x,t)}{\partial t} = D\frac{\partial^2 C(x,t)}{\partial x^2} \tag{2.6}$$

where the proportionality constant, D, is called the diffusion coefficient. This constant characterises the intrinsic diffusive properties of the fluid; its value is dependent on the particle size, microscopic viscosity and macroscopic obstructions in the local environment [17].

2.1.2 Diffusion propagator

The diffusion propagator is a solution of the diffusion equation. It can be interpreted as either the concentration distribution of an ensemble of particles or as the transition probability for a given diffusing particle. For unrestricted diffusion in one dimension, the propagator is,

$$P(x,t) = \frac{1}{\sqrt{4\pi D_o t}} e^{-\frac{x^2}{4D_o t}} \tag{2.7}$$

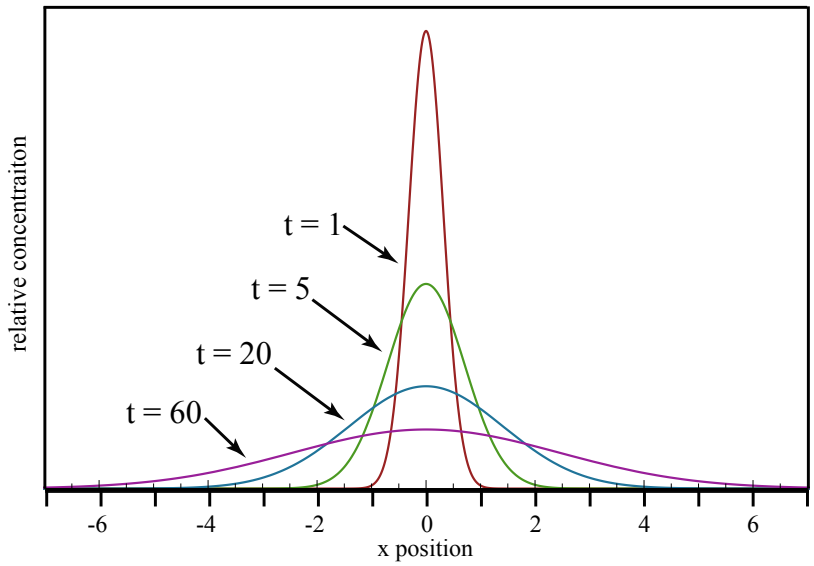

Figure 2.4: Unrestricted 1D diffusion propagators for times $t = 1, 5, 20,$ and 60 units. The concentration spreads out and flattens with increasing time.

where x is the displacement, t is the time, D_o is the bulk diffusion coefficient.

Figure 2.4 shows how Eq. (2.7) describes a Gaussian function which smoothly spreads out over time. Given the independence of diffusion in the spatial dimensions, it is easy to see that the corresponding propagator is spherically symmetric and Gaussian in any given direction.

2.1.3 Brownian motion

The atomistic treatment of diffusion originated with Robert Brown's 1827 microscopy observations where he noted the seemingly random motion of the organelles from ruptured pollen grains suspended in water. He suggested that this motion was spontaneous and intrinsic to the fluid and not a property of the pollen [34]. The mathematical connection between Brown's observations and Fick's diffusion equation was made by Albert Einstein in his 1905 paper, "On the theory of Brownian motion" [14]. His insight went beyond diffusion modelling and lead to evidence of the atomic description of matter experimentally confirmed by Jean Batiste Perrin [40].

The mathematical framework describing Browns observations derived by Einstein was based on the molecular-kinetic theory of heat [14]. He combined Stokes law for drag in fluid and van Hoff's laws of osmotic pressure to derive an expression to calculate the mean square displacement of a Brownian particle [41]. The thermal and dynamic equilibria of these laws allowed the viscosity of particles in a liquid η to be related to a diffusion constant D,

$$D = \frac{kT}{6\pi\eta r} \tag{2.8}$$

where k is Boltzmann's constant, T is the temperature, and r is the hydrodynamic radius of the particle. He then made the Brownian motion subject to Fick's second law (see Eq. (2.6), which in one dimension has the solution,

$$C(x,t) = \frac{1}{\sqrt{2\pi Dt}} e^{\frac{-x^2}{4Dt}} \tag{2.9}$$

resulting in a mean square displacement $\langle x^2 \rangle$ of,

$$\left\langle x^2 \right\rangle = \int x^2 N(x,t) dx = 2Dt \tag{2.10}$$

which, when combined with Eq. (2.8) gives,

$$\left\langle x^2 \right\rangle = \frac{tkT}{3\pi\eta r} \tag{2.11}$$

An important physical insight of this relation is that the mean square displacement of a diffusing particle is directly related to the hydrothermodynamic properties of the fluid. Another physical insight is that diffusive motion occurs independently of any concentration gradients or external potentials.

The diffusion propagator from random walks

The diffusion propagator in Eq. (2.7) is a fundamental solution of the diffusion equation (Eq. (2.6)) (for derivation, see Ref. [42] chapter 2.4). This propagator can also be derived from the perspective of a randomly walking particle. Consider an unbiased particle undergoing a displacement along a straight line by way of equally spaced steps, with a randomly chosen direction in each step. As the direction of each step is independent of all previous steps, all possible sequences of N steps can be assigned the same probability, namely $(1/2)^N$. Consequently, the probability $P(m, N)$ is $(1/2)^N$ times the number of sequences that lead to m in N steps. To arrive at m in N steps, some of the $(N + m)/2$ steps can be taken in the positive direction along the line and the remaining $(N - m)/2$ steps in the negative direction. This leads to the expression,

$$P(m, N) = \frac{N!}{\left(\frac{1}{2}(N+m)\right)! \cdot \left(\frac{1}{2}(N-m)\right)!} \cdot \left(\frac{1}{2}\right)^N \tag{2.12}$$

Using binomial coefficients C_r^n's, Eq. (2.12) can be written as;

$$P(m, N) = C^N_{(N+m)/2} \cdot \left(\frac{1}{2}\right)^N \tag{2.13}$$

which is a Bernoullian distribution [43].

When N is very large and $m \ll N$, Eq. (2.13) can be simplified using Stirling's formula,

$$\log n! = \left(n + \frac{1}{2}\right) \log n - n + \frac{1}{2} \log 2\pi + O(n^{-1})(n \to \infty) \tag{2.14}$$

Which therefore gives,

$$\begin{aligned}\log P(m,N) \approx & \left(N+\frac{1}{2}\right)\log N \\ & -\frac{1}{2}\left(N+m+1\right)\log\left[\frac{N}{2}\left(1+\frac{m}{N}\right)\right] \\ & -\frac{1}{2}\left(N-m+1\right)\log\left[\frac{N}{2}\left(1-\frac{m}{N}\right)\right] \\ & -\frac{1}{2}\log 2\pi - N\log 2 \end{aligned} \tag{2.15}$$

Because $m \ll N$, the series expansion can be used,

$$\log\left(1\pm\frac{m}{N}\right) = \pm\frac{m}{N} - \frac{m^2}{2N^2} + O\left(\frac{m^3}{N^3}\right) \tag{2.16}$$

which when applied to Eq. (2.15) gives,

$$\begin{aligned}\log P(m,N) \approx & \left(N+\frac{1}{2}\right)\log N\frac{1}{2} - N\log 2 \\ & -\frac{1}{2}\left(N+m+1\right)\log\left(\log N - \log 2 + \frac{m}{N} - \frac{m^2}{2N^2}\right) \\ & -\frac{1}{2}\left(N-m+1\right)\log\left(\log N - \log 2 - \frac{m}{N} - \frac{m^2}{2N^2}\right) \end{aligned} \tag{2.17}$$

which can be further simplified to give,

$$\log P(m,N) \approx -\frac{1}{2}\log N + \log 2 - \frac{1}{2}\log 2\pi - \frac{m^2}{2N} \tag{2.18}$$

giving the asymptotic formula for very large N as,

$$P(m,N) = \sqrt{\frac{2}{\pi N}} e^{\frac{-m^2}{2N}} \tag{2.19}$$

In the case of large N it is the net displacement, $x = ml$, that results from m steps of length l that is of interest. After N steps, the probability $P(x)\Delta x$ that a particle is found between x and $x + \Delta x$ can be written as,

$$P(x,N)\Delta x = P(m,N)\left(\frac{\Delta x}{2l}\right) \tag{2.20}$$

which when combined with Eq. (2.19) gives,

$$P(x,N) = \frac{1}{\sqrt{2\pi N l^2}} e^{\frac{-x^2}{2Nl^2}} \tag{2.21}$$

and considering that the particle will undergo n displacements per unit time t, gives the 1D diffusion propagator,

$$P(m,t) = \frac{1}{\sqrt{4\pi D t}} e^{\frac{-x^2}{4Dt}} \tag{2.22}$$

where $D = \frac{1}{2}Nl^2$.

Given the functional similarity of the governing equations for current, heat, and diffusion shown in Eqs. (2.1), (2.2), and (2.3), the random walk process described above is also linked to these phenomenon. More specifically, the above derivation is analogous to estimating the multiplicities of N particle two state systems as in thermodynamics and statistical physics [44].

2.1.4 The Wiener path integral

Another treatment of continuous Brownian motion comes from an analysis of the paths traced out by their random motion. Although these paths are inherently non-deterministic, certain observations can be made about their nature [45]. Path integrals are one of the earliest mathematical attempts to model solutions to diffusion problems, with the concept of a path integral introduced by Robert Wiener between 1921 and 1924 [46]. Its basis is the development of a Wiener measure and Wiener integral to calculate and assign a probability density that a diffusing particle will follow a given trajectory, and then calculate the probability of displacement by integrating over all available trajectories.

For example, consider a randomly diffusing particle in one dimension. From the solutions to the diffusion equation, the probability that this particle will find itself somewhere in the interval $A < x < B$ in time t is,

$$P(x(t) \in [AB]) = \int_A^B C(x,t)dx \tag{2.23}$$

Where $C(x,t)$ describes the probability distribution of the diffusing particle (e.g. Eq. (2.4) for 1D unrestricted diffusion). The diffusion process is a compound event, where the future location of the particle depends on its previous location. For example, the probability that a randomly walking particle will successively pass through a sequence of gates defined as $A_1 \leq x(t_1)B_1, A_2 \leq x(t_2)B_2, ...A_n \leq x(t_n)B_n$ (see Fig. 2.5) is,

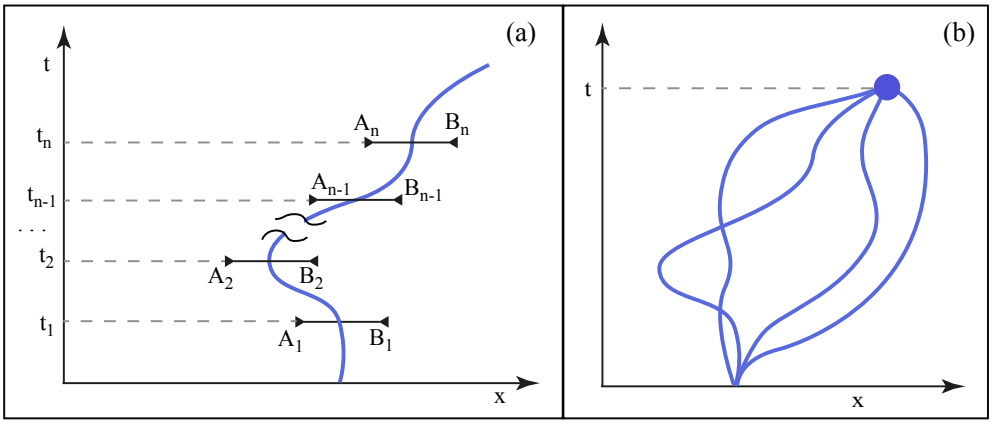

Figure 2.5: (a) a randomly walking particle confined to the x-axis passing through gates A_n, B_n at times t_n (b) sample of some particle trajectories

$$P(x(t_1) \in [A_1, B_1], x(t_2) \in [A_2, B_2], ..., x(t_n) \in [A_n, B_n])$$
$$= \int_{A_1}^{B_1} \frac{1}{\sqrt{4\pi D t_1}} e^{-\frac{x_1^2}{4Dt_1}} dx_1 \times \int_{A_2}^{B_2} \frac{1}{\sqrt{4\pi D t_2}} e^{-\frac{x_2^2}{4Dt_2}} dx_2$$
$$\times \ldots \times \int_{A_n}^{B_n} \frac{1}{\sqrt{4\pi D t_n}} e^{-\frac{x_n^2}{4Dt_n}} dx_n \tag{2.24}$$

(2.25)

The statistical independence of the random walk illustrates the Markov property of diffusion; given the present information about a system, the distribution of future states can be determined without knowing about its past states - i.e. the present state contains all required information for the future.

By decreasing the size of the gates from Eq. (2.24) and increasing the number of gates, the location of the particle becomes continuous. This is termed a "stochastic process", of which a Markov process is a subset [47]. If we consider Eq. (2.24) in the limit of the particle passing through an infinite number of infinitesimal gates along a given trajectory,

$$\lim_{\Delta t\to 0, n\to\infty} \exp\left(-\sum_{i=1}^{n}\frac{(x_i - x_{i-1})^2}{4D(t_i - t_{i-1})}\right)\prod_{i=1}^{n}\frac{dx_i}{\sqrt{4\pi D(t_i - t_{i-1})}}$$
$$\equiv \exp\left(-\frac{1}{4D}\int_0^t \dot{x}^2(\tau)d\tau\right)\prod_{\tau=0}^{t}\frac{1}{\sqrt{4\pi D d\tau}}dx(\tau) \qquad (2.26)$$

This equation (Eq. (2.26)) describes the probability of the particle following a given trajectory $x(\tau)$. In order to determine the probability that a given particle on the x-axis will end up at some gate $[AB]$ in time t, we have to integrate over all of the possible paths leading to this gate,

$$P(x(t) \in [AB]) = \int_{\zeta(0,0;[AB],t)}\prod_{\tau=0}^{t}\frac{1}{\sqrt{4\pi D d\tau}}dx(\tau)\exp\left(-\frac{1}{4D}\int_0^t \dot{x}^2(\tau)d\tau\right) \qquad (2.27)$$

where the symbol $\int_{\zeta(0,0;[AB],t)}$ is the summation over all trajectories and is called a Wiener path integral. This description provides a physically intuitive model that states that the probability that a Brownian particle will displace to a given location is proportional to the total number of ways that it can get there.

2.1.5 Restricted diffusion

Diffusion often occurs in complex environments, where the diffusing molecules interact with various structures on the micro and macroscopic scale. This is particularly the case for biological tissue containing macromolecules with various degrees of organisation. Interactions between the diffusing particles and obstructions leads to restricted diffusion [48–50]. The form of the corresponding restricted diffusion propagators is directly in response to these interactions. Because of this, knowledge of the inverse relationship between certain features of the structure within the diffusion environment

and the corresponding propagator is a valuable tool for investigating characteristics of the environment. This principle is the basis for the interpretation of diffusion tensor imaging and other forms of experimental measurements of diffusion [22, 29, 51–55]. A consequence of these interactions with barriers is that the diffusion propagator is no longer Gaussian, and the diffusion coefficient changes from a time independent unrestricted value D_0, to a time-dependent entity. The time dependence of the diffusion propagator can reveal geometrical characteristics of the confining geometry such as the surface area to volume ratio of confining pore spaces as described by Mitra et al. 1993 [56]. If the obstructions have no particular ordering, their effect is to restrict diffusion isotropically and can be characterised using the time dependent restricted diffusion coefficient $D(t)$. In the majority of porous media, however, the pore shapes are complex and are often interconnected via tortuous passages with features of many different length scales [29, 51, 57]. In these cases, a single coefficient is no longer sufficient to characterise the diffusion and more sophisticated measures are required, including the diffusion tensor [58, 59], spherical harmonics decomposition measures [50, 60] and diffusion propagator representations [61]. In many cases, particularly biological tissue, diffusion is restricted by permeable barriers. A given diffusing particle encountering a permeable barrier has a probability of being either reflected by the barrier or transiting across the barrier. Knowledge of the rate of particle exchange across a permeable barrier is vital for understanding many complex biological processes [62] and is useful for inferring structural characteristics of heterogeneous tissue such as cell-suspensions from nuclear magnetic resonance experiments [63].

Observation time

In the case of unrestricted diffusion, the mean square displacements grow linearly with observation time and can be characterised via a time independent diffusion coefficient

D_o. Restricted diffusion observations, on the other hand, depend on both the observation time, Δ, and the confining geometry [30, 33, 51, 64–66]. Generally, restricted diffusion observations can be grouped into three regimes; short-Δ limit, intermediate-Δ, and the asymptotic long-Δ diffusion regime. This time dependence of the restricted diffusion can be illustrated by considering an ensemble of particles diffusing within a spherical pore space of length a. It is convenient to introduce the dimensionless variable ζ such that,

$$\zeta = \frac{D\Delta}{a^2} \tag{2.28}$$

In this isotropic but restricted scenario, diffusion can be characterised via a time dependent restricted diffusion coefficient $D(\Delta)$. In the very short-Δ limit ($\zeta \ll 1$), only a very small fraction of the particles have sufficient time to encounter the pore walls and experience restricted diffusion. Consequently, diffusion simply reduces to the free diffusion propagator (see Fig. 2.7(a),

$$D(\zeta \ll 1) \approx D_o \tag{2.29}$$

In the intermediate Δ, or crossover regime ($\zeta \approx 1$), a fraction of the particles have time to diffuse sufficiently to encounter the walls of the sphere and have their motion restricted [51, 67]. In this intermediate-Δ regime, Sen 2004 [51] showed that the fraction of the particles encountering the barriers in a given Δ depends is a function of the surface area to volume ratio S/V of the pore space. This is illustrated in Fig. 2.6 where only particles that are within $\sqrt{2Dt}$ of the walls can interact with the walls in time t.

The expression relating the time dependent restricted diffusion coefficient $D(\Delta)$ to the surface area to volume ratio S/V of confining geometry with non-fractal walls is,

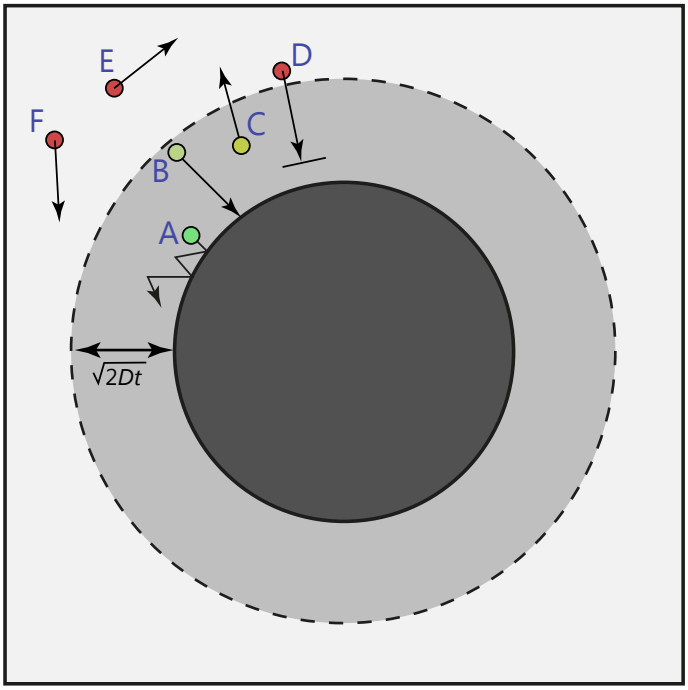

Figure 2.6: 2D illustration of the intermediate restricted diffusion regime. In this regime, particles can be considered to belong in one of four groups, e.g. particle **A** illustrates particles that are within $\sqrt{2Dt}$ of the walls and interact once in time t (see Fig. 2.6 particle **A**), particle **B** represents particles that are within $\sqrt{2Dt}$ of the walls and interact many times in t, particle **C** represents particles that are within $\sqrt{2Dt}$ of the walls but do not interact in time t, the remaining particles represent those that outside the distance $\sqrt{2Dt}$ of the walls at $t = 0$ therefore will not travel far enough in time t to interact.

$$\frac{D(\Delta)}{D_o} = 1 - \frac{4}{9\sqrt{\pi}}\frac{S}{V}\sqrt{D_o t} - \frac{S}{12V}\left\langle \frac{1}{R_1} + \frac{1}{R_2} \right\rangle (D_o t) + \frac{1}{6}\frac{\rho S}{V} D_o t + O\left((D_o t)^{3/2}\right) \tag{2.30}$$

where S and V are the surface area and pore volume, respectively, R_1 and R_2 are the principal radii of pore wall curvature with the angled brackets indicating averages over the barrier walls, and ρ is the relaxivity of the barrier walls. This expression was derived by Mitra et al. 1992 [29] and is based on the observation that in the short-Δ time regime, only diffusing particles that are within $\sqrt{2D_o t}$ of the walls, of area S, interact with the walls. It follows, therefore, that only the fraction $S\sqrt{D_o t}/V$ of the total number of particles are no longer free and potentially undergo restricted diffusion

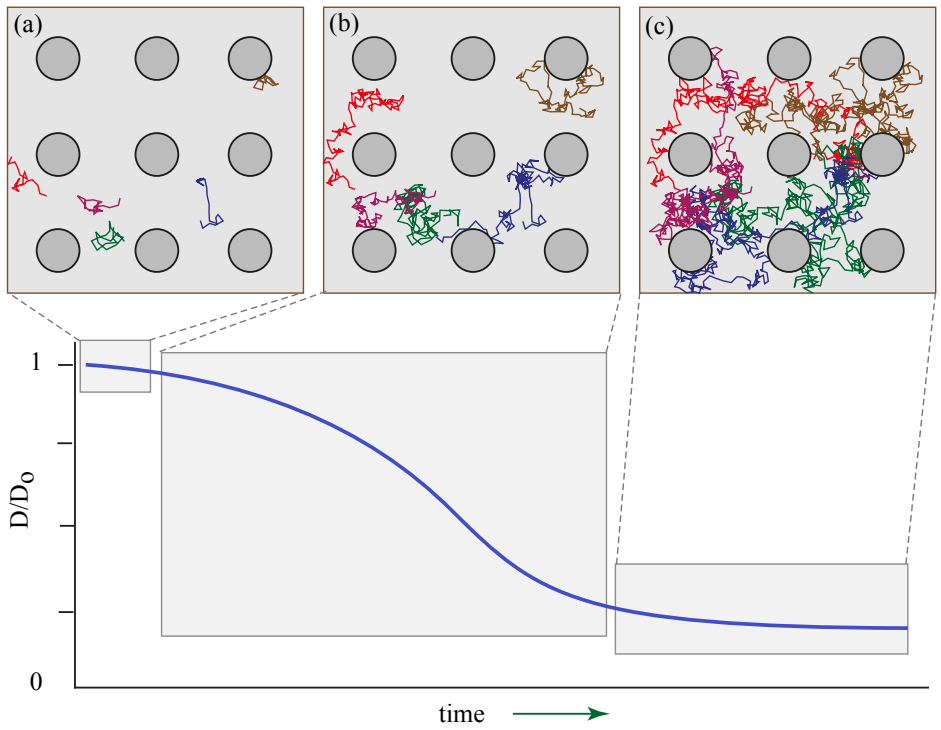

Figure 2.7: Illustration showing key properties of the three diffusion regimes; (a) the short Δ regime, the particles have diffused a small distance and have not had sufficient time to interact with the obstructions. In this regime the diffusivity is approximately the same as in the unrestricted case. (b) The intermediate-Δ regime. The diffusion is becoming restricted as the particles begin interacting with the walls and have their diffusion restricted. The diffusivity is reducing with increasing Δ. (c) The long-Δ regime. The particles have interacted with the walls sufficient time such that further observation time will not appreciable reduce the diffusivity.

(see ref [29] for derivation).

Figure 2.7(b) illustrates the effect of observation time on the reduction of the apparent diffusion coefficient. The short-Δ diffusion coefficient (or tensor for anisotropic environments) for inferring the S/V ratio of a sample also applies in the case of confining geometries with features of many scales as shown by Sen, 2004 [51] and Keating, 2014 [68].Other surface dynamical properties within macro-porous media can also be experimentally obtained in this regime such as the surface activation energies, time of residence, and coefficient of surface affinity as shown by Godefroy et al., 2001 [66].

The asymptotic-long Δ regime ($\zeta \gg 1$) describes the case where the diffusion

reaches an asymptotic value and further increases in observation time do not yield any further information about the geometry. This is illustrated in Fig. 2.7(c). In this regime, the final positions of the diffusing particles will be completely uncorrelated with their initial positions and distributed uniformly in the pore, therefore,

$$D(t \longrightarrow \infty) \propto \frac{a^2}{6t} \tag{2.31}$$

and in the case of completely confined geometries, the term in Eq. (2.31) goes to zero. In connected systems, the time dependent diffusion coefficient approaches a finite, non-zero value below the bulk diffusion coefficient and is inversely proportional to a factor known as the tortuosity τ [51],

$$D(t \longrightarrow \infty) \longrightarrow \frac{D_o}{\tau} \tag{2.32}$$

where the meaning of tortuosity is the ratio of the actual translated distance by a diffusing particle Δl per unit length Δx,

$$\tau = \frac{\Delta l}{\Delta x} \tag{2.33}$$

Boudreau,1996 [69] describes two general requirements for τ; (1) $\tau \geq 1$, meaning that the actual path caused by restrictions needs to be larger than the unrestricted path, and (2) that there is no restriction to diffusion caused by anything other than the barriers.

2.1.6 Anisotropic diffusion

In many systems, particularly in biological structures such as muscle fibres [70–73], the collagen fibres of articular cartilage [74–77], and the nervous system [78–81],

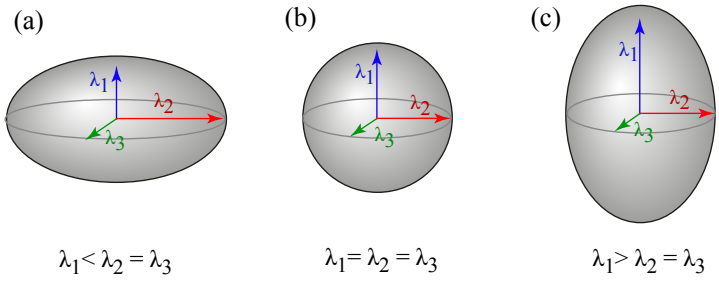

Figure 2.8: Diffusion ellipsoids for three tensors; (a) Oblate, where diffusion is least restricted in a transverse plane, (b) Spherical for isotropic restriction of diffusion, and (c) Prolate where diffusion is most restricted in the transverse plane

diffusion is restricted in some directions more than others. Consequently, diffusion cannot be characterised as Gaussian and spherical but takes on anisotropic form. In these scenarios, the scalar diffusion coefficient can be replaced by a second-order symmetric diffusion tensor $\bar{\mathbf{D}}$ [82]. For three dimensional anisotropic diffusion, this is a 3x3 tensor,

$$\bar{\mathbf{D}} = \begin{pmatrix} D_{xx} & D_{xy} & D_{xz} \\ D_{yx} & D_{yy} & D_{yz} \\ D_{zx} & D_{zy} & D_{zz} \end{pmatrix} \tag{2.34}$$

In diffusion tensor imaging applications, this tensor can be constructed from diffusion measurements obtained along at least six different non-collinear and non-coplanar directions [59]. Diagonalisation of this tensor gives the eigenvalues, λ_1, λ_2 and λ_3, and the eigenvectors, $\mu_\mathbf{1}$, $\mu_\mathbf{2}$, and $\mu_\mathbf{3}$, which corresponds to the magnitude and direction of principle diffusivity, respectively. Conceptually, this tensor describes the diffusion ellipsoid as illustrated in Fig. 2.8. The relationship between diffusion MRI experiments and the diffusion tensor is discussed in more detail in section 2.3.

2.2 Mathematical modelling of restricted diffusion

Mathematical solutions to restricted diffusion problems can be broadly grouped into two approaches based on their conceptual origin; continuum based methods that seek solutions to the diffusion equation, and atomistic based methods that explicitly calculate molecular trajectories. Solutions to the diffusion equation are generally found through analytic methods in the case of simple restricted diffusion problems [21, 22] and discrete numerical methods for more complex problems [45, 83]. Atomistic based diffusion modelling approaches include path integral methods and associated solutions, [84, 85], analytic solutions to restricted random walks for simple geometries [7, 86], path enumeration approaches for complex geometries and percolation clusters [5, 8, 12, 87, 88], and simulations of molecular translations based on the Langevin equation (see Section 2.2.2) [9, 10, 35, 89, 90]. Another approach which explicitly models individual molecular trajectories is the lattice path count method (LPC) introduced and detailed in chapter 4 of this thesis [11, 12]. The LPC approach exactly computes a discrete restricted diffusion propagator by counting all paths available to a diffusing particle on a lattice and can be considered a numerical method for solving restricted diffusion path integrals (see Section 2.1.4).

2.2.1 Analytic solutions to diffusion equation

Analytic solutions to the diffusion equation for simple geometries usually take one of two forms; those that comprise a series of integrals, and those involving related error functions [22]. Solutions in the long-Δ regime often take the form of a trigonometrical series. The most simple analytic solution is the unrestricted diffusion propagator in 1D (Eq. (2.4) which describes the diffusive spreading of particles with a symmetric

Gaussian probability distribution. For restricted diffusion problems, boundary conditions can include reflecting walls, $\partial C/\partial x = 0$, absorbing walls, $C(x) = 0$, and semi-permeable walls, where $\partial C/\partial x$ is a function of the permeability at the boundary. The most simple example of an analytic restricted diffusion solution is confined diffusion along a line x with $x(0) = 0$ and reflecting barriers at $-L/2$ and $L/2$ [91],

$$C(x,t) = \frac{1}{L} + \frac{2}{L}\sum_{n=1}^{\infty} \cos\left(\frac{2\pi n x}{L}\right) \exp\left(-\frac{4\pi^2 n^2 D t}{L^2}\right) \tag{2.35}$$

Mathematical techniques for solving the diffusion equation include the method of reflection and superposition, separation of variables, or through the use of Laplacian transformations [22]. Despite the range of available approaches, exact solutions only exist for relatively simple geometries.

Finite difference methods

For problems where analytic solutions are unavailable, numerical methods such as finite difference and finite element are commonly employed. These involve numerically integrating the diffusion equation by approximating the solution one time step to the next [92]. The integration method can be explicit, where solutions are found for a later time based on the current state, or implicit, where the solution is found for a later time from both the current and later states of the system.

Mathematically, the explicit solution is expressed as,

$$C(t + \Delta t) = f(C(t)) \tag{2.36}$$

where $C(t)$ is the current species concentration and $C(t + \Delta t)$ is the concentration of the system after interval Δt. Implicit methods involve solving the equation,

$$f(C(t), C(t + \Delta t)) = 0 \tag{2.37}$$

to find $C(t + \Delta t)$.

The explicit approximation for solving the 1D diffusion equation for concentration, C, at position x can be derived by considering the Taylor expansions for the function at $x + x_i$,

$$C(x + x_i) = C(x) + x_i \frac{\partial C}{\partial x} + \frac{x_i^2}{2} \frac{\partial^2 C}{\partial x^2} + \frac{x_i^3}{6} \frac{\partial^3 C}{\partial x^3} + ... \tag{2.38}$$

and for $x - i$,

$$C(x - x_i) = C(x) - x_i \frac{\partial C}{\partial x} + \frac{x_i^2}{2} \frac{\partial^2 C}{\partial x^2} - \frac{x_i^3}{6} \frac{\partial^3 C}{\partial x^3} + ... \tag{2.39}$$

and combining Eq. (2.38) and Eq. (2.39) gives,

$$C(x + x_i) + C(x - x_i) = 2C(x) + x_i^2 \frac{\partial^2 C}{\partial x^2} + O(x_i^4) \tag{2.40}$$

which, assuming $O(x_i^4)$ is negligible, can be rearranged to solve for $\frac{\partial^2 C}{\partial x^2}$,

$$\frac{\partial^2 C}{\partial x^2}(x_i, t + 1) = \frac{1}{x_i^2}(C(x + x_i) - 2C(x) + C(x - x_i)) \tag{2.41}$$

Although explicit methods appear more computationally efficient than their implicit counterparts, in that they require few calculations, the maximum size of Δt is restricted by stability considerations [93]. Determining the stability criterion is often carried out using Von Neumann stability analysis. [94]. For problems involving many time steps, this stability requirement can increase the number of calculations.

Implicit methods, on the other hand, are numerically stable for large Δt. For example, an implicit solution to the one dimensional diffusion equation is achieved by first computing the discretised space derivative at step $t+1$ as,

$$\frac{\partial^2 C_i^{t+1}}{\partial x^2} = \frac{C_{i-1}^{t+1} - 2C_i^{t+1} + C_{i+1}^{t+1}}{\Delta x^2} + O(\Delta x^2) \tag{2.42}$$

and computing the time derivative,

$$\frac{\partial C_i^{t+1}}{\partial t} = \frac{C_i^{t+1} - C_i^t}{\Delta t} + O(\Delta t) \tag{2.43}$$

and introducing these to the diffusion equation to give the simple implicit FD approximation as,

$$\frac{C_i^{t+1} - C_i^t}{\Delta t} = D\frac{C_{i-1}^{t+1} - 2C_i^{t+1} + C_{i+1}^{t+1}}{\Delta x^2} \tag{2.44}$$

with accuracy to $O(\Delta x^2, \Delta t)$ and is unconditionally stable [93, 95].

2.2.2 Computer simulations of restricted diffusion

Computer simulations are a method to solve complex restricted diffusion problems by calculating the dynamics of each particle independently. The computed equations of motion are either stochastic (Monte-Carlo simulations) or deterministically computed using pair-wise summation of the relevant interaction potentials [96]. The choice of simulation method depends on the complexity and spatio-temporal scale of the problem [97, 98].

Computer simulations typically involve separating the problem into three phases; (1) model construction, (2) computation of molecular trajectories, and (3) trajectory analysis to determine the required properties [99]. Because simulations only compute

the trajectories of a finite number of particles, they suffer from statistical errors proportional to the square of the number of particles times the value of the propagator [9];

$$\Delta P(\mathbf{r},t) \propto \sqrt{N_P} \cdot \sqrt{P(\mathbf{r},t)} \tag{2.45}$$

This uncertainty is demonstrated in Powell and Momot 2012 [9] (see chapter 4) where Langevin dynamics simulations of unrestricted diffusion of 5000 particles computed a fractional anisotropy of 0.061 ± 0.005 whereas this was reduced to 0.033 ± 0.003 for 20000 particles. This is in contrast to the expected fractional isotropy of zero for an infinite number of particles undergoing isotropic diffusion [100].

Stochastic dynamics computer simulations

The Langevin equation is a stochastic differential equation which describes the motion of a Brownian particle as the sum of a randomly directed force to represent collision with the fluid molecules, $\eta(t)$, a velocity dependent viscous force, $-\lambda\frac{d\mathbf{x}}{dt}$, and a deterministic interaction potential, $-\nabla(\mathbf{U})$,

$$m\frac{d^2\mathbf{x}}{dt^2} = -\lambda\frac{d\mathbf{x}}{dt} + \eta(t) - \nabla(\mathbf{U}) \tag{2.46}$$

Stochastic dynamics computer simulations integrate this equation to determine the molecular displacements of a set of tracer molecules. Monte-Carlo simulations simplify this equation by combining the random and drag forces via Einstein's Brownian equations and computing barrier interactions as simple elastic collisions. This simulation approach is popular for diffusion modelling due to its relatively low computational overhead [35, 52, 54, 90, 101–103]. Other methods such as Langevin dynamics simulations involve more complex equations of motion and compute barrier

interactions deterministically via an interaction potential function (e.g. the Lennard Jones and Morse potentials) [9]. Consequently, Langevin Dynamics (LD) computes more physically realistic barrier interactions than Monte-Carlo (MC) making it applicable to problems where these interactions are significant. Such problems can involve computing the liquid-vapour interface of water [104] and diffusion problems involving rotational correlations of resident molecules [105].

In its most general form, Monte-Carlo methods use sample means to estimate the populations means [99, 106, 107]. Applied to the problem of simulating restricted diffusion, MC is an efficient way to compute the displacement of molecules and their interactions with barriers. After running a simulation for the required number of time-steps, the net displacements of the molecules are computed along various directions. This mimics the scenarios of diffusion tensor imaging experiments, allowing MC results to be used to build quantitative interpretive models [35, 54, 90, 103].

Typically, Monte-Carlo simulations are initialised by randomly distributing the particles throughout the volume. The positions of each particle is then updated by selecting a random and uncorrelated direction vector which is distributed uniformly on a sphere centred on the molecule [90]. The magnitude of this vector is computed via Einstein's equation of Brownian motion,

$$\Delta \mathbf{r} = \sqrt{2dD\Delta} \tag{2.47}$$

where d is the number of dimensions, D is the diffusion coefficient and Δ is the time step interval. Due to the fractal nature of the diffusing molecular trajectories, the only restriction on the value of Δ is that is small enough so each step length enables sufficient sampling of the walls of the confining geometry.

Barrier interactions in Monte-Carlo simulations can be computed as either elastic or inelastic collisions. For example, inelastic collisions can be modelled by choosing

a randomly directed vector leading away from the barrier upon interaction [108].

In many cases, it is of interest to simulate restricted diffusion in the long-Δ regime within periodic pore spaces, or pore spaces containing periodic obstructions. For example, Monte-Carlo simulations have been performed in volumes containing partially aligned fibre networks by Tourell, Powell and Momot in 2014 [35] . In these simulations, a volume was defined as a parallelepiped and molecules that stepped beyond a given boundary of the volume were immediately translated to the opposite boundary, with this translation not contributing toward net displacement calculations. Due to its computational efficiency, the Monte-Carlo simulation method has been widely used to solve restricted diffusion problems in complex biological structures in the long-Δ diffusion regime [52, 54, 101, 102].

Langevin dynamics is similar to MC in that it contains a random component, however each displacement vector is computed as a combination of a randomly directed force and a deterministic force due to interactions with the barriers. Detailed discussion of the application of Langevin dynamics to restricted diffusion problems can be found in chapter 3.

2.3 Diffusion tensor imaging

Magnetic Resonance Imaging is a commonly used tool for the non-invasive imaging of soft tissue with important applications in medical research and clinical diagnosis of disease [109–112]. Diffusion tensor imaging is an imaging modality of MRI which sensitises the imaging sequence to molecular diffusion. This technique is used to probe tissue structures beyond the normal imaging resolution [59, 113, 114] and also can provide valuable information about molecular transport pathways in tissue and tissue engineering constructs [13, 115, 116].

2.3.1 Magnetic resonance imaging

Nuclear Magnetic Resonance (NMR) forms the basis of diffusion tensor imaging. With this technique, the precession of the nuclear spins of certain atoms (e.g. proton ^1H) within a magnetic field ($\mathbf{B}_o$) is measured. The frequency of this precession is described by the Larmor equation,

$$\omega_0 = \gamma B_0 \tag{2.48}$$

where γ_0 is known as the gyromagnetic ratio.

Information about the local molecular environment of an ensemble of these nuclei can be obtained by perturbing their equilibrium magnetisation through the application of a radio frequency (RF) pulse and measuring the time for the nuclei to relax to their equilibrium. The perturbed spins produce a radio frequency signal which decays as they relax at different rates in both the longitudinal (T_1 or spin-lattice) and transverse (T_2 or spin-spin) directions to B_0. Magnetic Resonance Imaging (MRI) produces spatially resolved information by superimposing time-varying magnetic field gradients on the static magnetic field B_0. These gradients are typically applied along each of the three orthogonal directions (x, y, and z). The application of the magnetic field gradient g,

$$g = \left(\frac{\partial B_z}{\partial x}, \frac{\partial B_z}{\partial y}, \frac{\partial B_z}{\partial z} \right) \tag{2.49}$$

means that the magnetic field experienced by the nuclear spins is position dependent, with the consequent variation in their precession frequency. Each spin at position $\mathbf{r}$, therefore, experiences a magnetic field of,

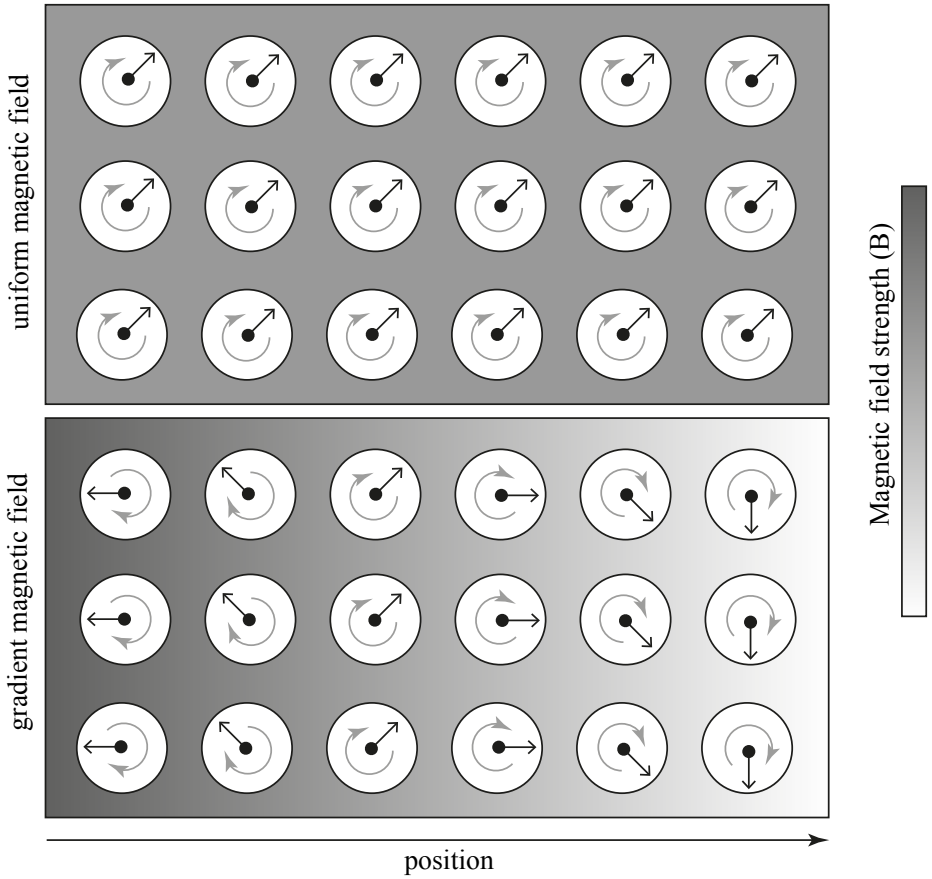

Figure 2.9: Phase of nuclear spins in a magnetic field. Top figure shows a uniform field with all spins in phase. Bottom figure shows a magnetic field gradient which produces a gradient of precession frequencies. If the gradient is applied momentarily, the phases are shifted.

$$B = B_0 + \mathbf{g} \cdot \mathbf{r} \tag{2.50}$$

with the consequent effect on its precession frequency of,

$$\omega(\mathbf{r}) = \frac{\partial \phi(\mathbf{r})}{\partial t} = \gamma(B_0 + \mathbf{g} \cdot \mathbf{r}) \tag{2.51}$$

where ϕ is phase, or transverse precession angle of a spin. This is illustrated in Fig. 2.9.

MRI spatially encodes the spins by periodically applying gradients along different

directions, giving the phase of the spin as,

$$\phi(\mathbf{r},t) = \int_0^t \omega(\mathbf{r},t')dt' = \gamma B_0 t + \gamma \int_0^t \mathbf{g}(t') \cdot \mathbf{r} dt \tag{2.52}$$

For example, additional phase variation along a direction $\mathbf{r}$, $\phi'(\mathbf{r},t)$ can be created through the application of a rectangular gradient pulse of a given amplitude g_x for the duration δ,

$$\phi'(\mathbf{r},t) = \gamma \int_0^\delta g_x(t')x dt' = \gamma \delta g_x x = 2\pi k_x x \tag{2.53}$$

where $k_x = \gamma \delta g_x / 2\pi$ is the spacial frequency, or "k value".

Imaging is performed by selecting a "slice" through the activation of a range of selected spins, and then performing spatial encoding within this slice through the sequential application of the gradients (along x and y axes) as described above. The image can be reconstructed from the 2D data set, $S(k_x, k_y)$ by Fourier transformation,

$$S(x,y) = \int\int S(k_x,k_y) e^{-2\pi i(k_x x + k_y y)} dk_x dk_y \tag{2.54}$$

2.3.2 Diffusion magnetic resonance imaging

A common method for sensitising the NMR signal to diffusion is to apply the Pulsed Field Gradient Spin Echo (PFGSE) imaging sequence [3]. This method capitalises on the attenuation of the basic spin echo NMR signal due to the diffusion of the spins.

Diffusion MRI requires, in addition to the spatial encoding gradients, another "diffusion" magnetic field gradient of duration δ applied along the desired direction. After a short period Δ, the spins moving with velocity v undergo diffusion following which another gradient opposite to the original "diffusion" gradient is applied. During the

period between the application of the gradients, the diffusing spins acquire a net phase shift,

$$\phi(\mathbf{v}) = -\gamma \mathbf{g} \cdot \mathbf{v} \delta \Delta \tag{2.55}$$

An equation describing the attenuation of the NMR signal due to both spin relaxation and diffusion was derived by Stejskal and Tanner [3] and has the form,

$$S(\Delta, g) = S_0 e^{-\frac{TE}{T_2}} e^{-D\gamma^2 g^2 \delta^2 (\Delta - \delta/3)} \tag{2.56}$$

In this equation, the first term describes the signal attenuation due to T_2, or transverse relaxation. This component of the signal can be easily determined using signal measurements over incremental echo times and fitting the results to the exponential function. By repeating measurements over a range of magnetic field gradient amplitudes with a fixed echo time the apparent self-diffusion co-efficient, D, can be measured,

$$S(\Delta, g) = S_0' e^{-bD} = S_0 e^{-\frac{TE}{T_2}} e^{-bD} \tag{2.57}$$

where

$$b = \gamma^2 g^2 \delta^2 \left(\Delta - \frac{\delta}{3} \right) \tag{2.58}$$

for the pulse sequence shown in Fig. 2.10(c). The apparent diffusion coefficient can be determined by fitting the attenuated signals for the range of gradient strengths to the function,

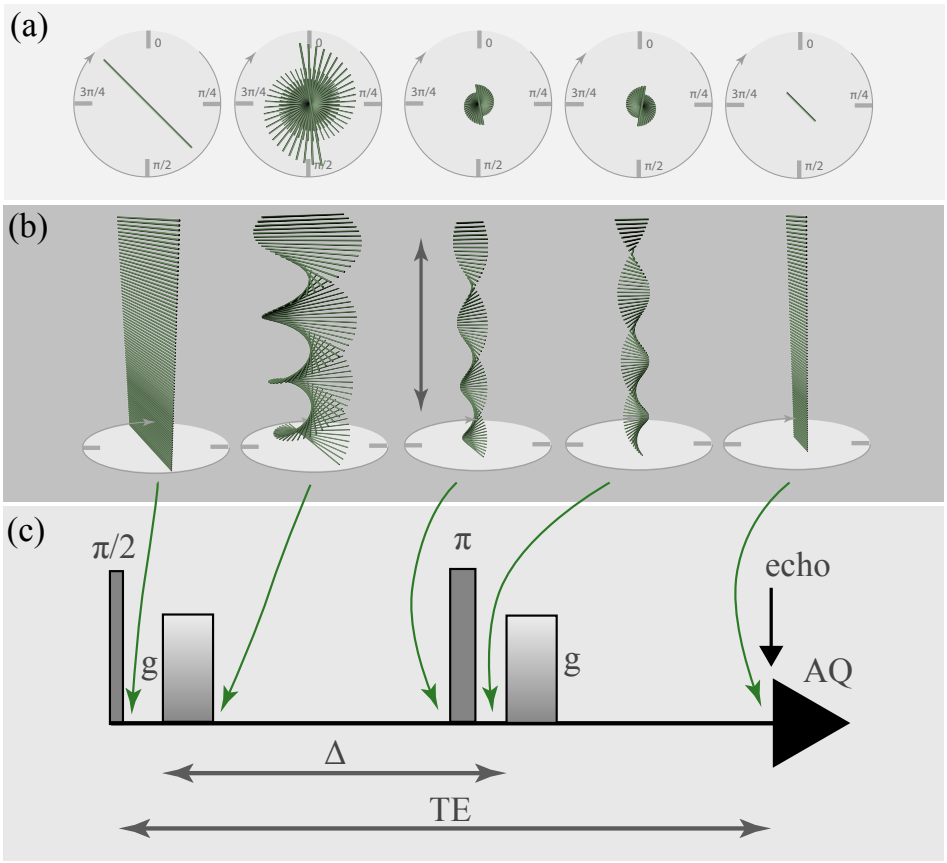

Figure 2.10: Illustration of the PFGSE sequence. The application of the gradient g along a given direction causes the phase of the spins to wind into a helix. After a time Δ, diffusion causes the helix to disorganise with the change in spin locations causing spins of difference phase to occupy similar locations resulting in amplitude cancellation. The application of the π pulse inverts the attenuated helix and the application of the diffusion gradient unwinds the helix revealing the diffusion attenuated signal. (a) shows views of the spins from the perspective along the direction of the diffusion gradient. (b) shows the spins from a perspective transverse to the direction of the gradient. (c) shows the corresponding NMR pulse sequence.

$$ADC = \frac{-1}{b} ln \left(\frac{S}{S'_0} \right) \tag{2.59}$$

Through the application of diffusion gradients along various directions, anisotropic diffusion can be sampled. In this case, a diffusion tensor, $\mathbf{D}$ is used in place of the diffusion coefficient in the equation,

$$S(\Delta, g) = S'_0 e^{-\gamma^2 \mathbf{g} \cdot \mathbf{D} \cdot \mathbf{g} \delta^2 (\Delta - \delta/3)} \tag{2.60}$$

In order to fully determine the diffusion tensor, at least $6+A_o$ (i.e. 6 distinct non-0 g values and $\mathbf{g} = 0$)) diffusion measurements are required [59]. For example, if diffusion gradients are applied along the x, y, and z directions, the off-diagonal elements of the tensor can be sampled by applying gradients in the oblique directions.

The type of pulse sequences and number of gradient directions depends on the requirements of the application and is the subject of ongoing research [100, 117–119]. This is particularly important in clinical applications where limited time exists for diffusion measurements [120]. Various strategies to maximise the available measurement data and minimise noise have been developed and include signal averaging, the use of more gradient directions, and producing optimised imaging parameters such as the set of b values [121–124]. In many cases, anisotropic diffusion measurements benefit from the application of a greater number of diffusion gradient directions that the minimum. Although some authors suggest that the minimum number is sufficient [59], analysis suggests that mean diffusivity, fractional anisotropy and diffusion tensor measurements benefit from approximately 20-30 gradient directions or more with evenly distributed orientations [125–127].

The choice of observation-time, Δ, is also important in DT imaging. This value depends largely on the length-scale of the microstructure under investigation and limited by the relation time of the diffusing spins. The information available from the diffusion tensor depends on the diffusion regime as discussed in previously in section 2.1.5.

2.3.3 Interpretation of DTI data

Typical DTI acquisition data is in the form of a series of diffusion weighted images, with each image corresponding to the measured diffusivity along a given direction. From these images, information about diffusion in the given direction can be determined for volume elements of the sample. Combining voxel information from the

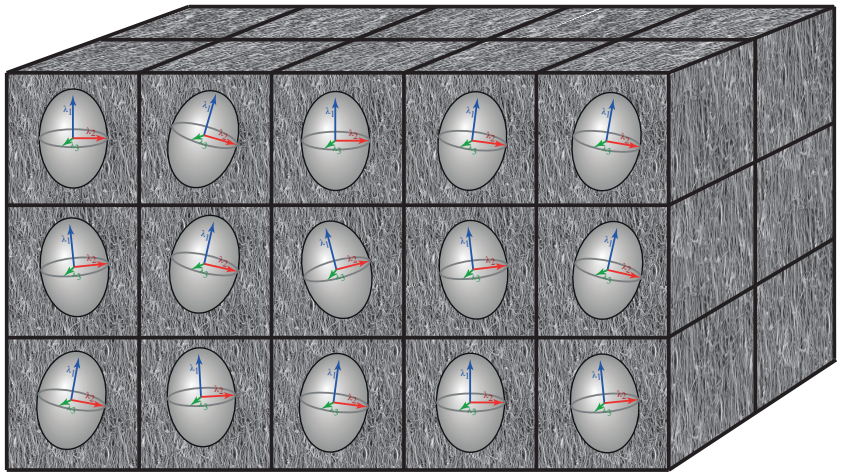

Figure 2.11: Illustration of diffusion tensor voxels for the study of diffusion in articular cartilage. Each voxel is approximately $50\,\mu m$ across. Also shown are examples of oblate diffusion ellipsoids indicating preferred diffusivity along the vertical axis.

acquired gradient directions, ”laboratory-frame” diffusion tensors can be constructed where the coordinate axes correspond to the physical directions of the DTI hardware gradient coils (the ”laboratory-frame”). From these diffusion tensors, the principal diffusivities (eigenvalues of the DT) and their orientations with respect to the laboratory frame (eigenvectors of the DT) can be computed.

The diagonalised voxel map of DT’s can be further analysed to determine the principle eigenvector direction (indicating the predominant direction where diffusion is least restricted), the maximum diffusivity (corresponding to the maximum eigenvalue of the diagonalised DT), the mean diffusivity (the average of the diagonal elements in the diagonalised diffusion tensor), and the fractional anisotropy (the degree of deviation of the diffusion tensor from the isotropic case) [114].

Further processing using inter-voxel considerations are used to reveal larger structural information such as the nerve pathways as in neural tractography [128, 129] or fibre network orientation and ordering of articular cartilage [74, 77, 130–134] (see Fig. 2.11).

2.3.4 Calculating the DT from diffusion weighted images

To simplify processing of the diffusion weighted images and construct the laboratory frame diffusion tensor, it is common to base processing on the "B matrix" [114]. In this case, the signal attenuation diffusion expression (Eq. (2.56)) can be written as,

$$log_2\left(\frac{S(\mathbf{g})}{S_0}\right) = -\sum_{i=1}^{3}\sum_{J=1}^{3} b_{ij}D_{ij} \equiv -\mathbf{b} : \mathbf{D}, \tag{2.61}$$

where indices i and j correspond to the values x, y, and z for construction of the matrix. The values of $\mathbf{b}$ (a real 3×3 matrix) in a spin-echo experiment are given by,

$$b_{ij} = \gamma^2 g_i g_j \delta^2 \left(\Delta - \frac{\delta}{3}\right) \tag{2.62}$$

where g_i and g_j and the matrix components of $\mathbf{g}$.

Solving the diffusion tensor in DTI measurements requires solving the inverse problem associated with Eq. (2.61), where only the signal attenuation and b-matrix values are known. In the simple case where the diffusion gradients correspond to the directions of the "laboratory frame" diffusion tensor, the diffusivities along the applied gradient directions are simply,

$$D_{ii} = -\frac{1}{b} ln\left(\frac{S_{ii}}{S_0}\right) \tag{2.63}$$

for $i = x, y, z$. The off-diagonal elements are,

$$D_{xy} = -\frac{1}{2b}\left[ln\left(\frac{S_{xx}}{S_0}\right) + ln\left(\frac{S_{yy}}{S_0}\right)\right] + \frac{1}{b} ln\left(\frac{S_{ii}}{S_0}\right), etc \tag{2.64}$$

In many diffusion experiments, a greater number of gradient directions than the

minimum six are acquired. In this case, the diffusion tensor components are reconstructed from least squares fitting of all attenuated signal values for all gradient directions simultaneously with Eq. (2.61).

Interpretation of the laboratory frame DT in the context of diffusivities along given directions is difficult because there is no straightforward meaning to its off-diagonal elements. In practice, these values can often be negative, and therefore do not directly correspond to any diffusivities. Consequently, the laboratory frame diffusion tensor is usually diagonalised to determine its eigenvalues and eigenvectors. The diagonalisation process can be viewed (in the first approximation) as a 3D rigid-body rotation to ensure the alignment of the laboratory frame co-ordinate axes with the diagonalised diffusion tensor principle axes. The magnitude and direction of the diagonalised diffusion tensor describes what is commonly called the diffusion ellipsoid, indicating the principle diffusivities and their directions with respect to the laboratory frame. In this way, the diffusion ellipsoids are a means of visualising the direction and degree of restriction to diffusion caused by the alignment order, or microstructure, of the diffusion environment. Generally, diagonalisation is performed through unitary transformations of the laboratory frame DT,

$$\mathbf{D}' = \mathbf{U}(\alpha, \beta, \gamma)\mathbf{D}\mathbf{U}^{+}(\alpha, \beta, \gamma) \tag{2.65}$$

where α, β, and γ describe the Euler angles relating the orientations of the principal axes of the diffusion tensor to the laboratory axes. $\mathbf{U}$ is a unitary matrix, which in this application is the rotation transformations. Unitary transformations conserve the trace of the matrix. This implies that the mean diffusivity is the same in both the laboratory and transformed frames,

$$D_{av} = \frac{1}{3}(D_1 + D_2 + D_3) = \frac{1}{3}(D_{xx} + D_{yy} + D_{zz}) \tag{2.66}$$

2.3.5 Fractional anisotropy

The fractional anisotropy can be considered as a scalar measure of the degree of deviation of the diffusion tensor from the isotropic case [135]. Its values range between 0 and 1 corresponding to completely isotropic diffusion and completely anisotropic diffusion, respectively.

In the case of a prolate diffusion tensor ($D_1 > D_2 \approx D_3$), FA can be calculated as,

$$FA = \frac{3}{\sqrt{2}} \frac{\sqrt{(D_1 - D_{av})^2 + (D_2 - D_{av})^2 + (D_3 - D_{av})^2}}{\sqrt{D_1^2 + D_2^2 + D_3^2}} \tag{2.67}$$

and in the case of an oblate diffusion tensor ($D_1 \approx D_2 > D_3$),

$$FA = \frac{2}{\sqrt{3}} \frac{\sqrt{(D_1 - D_{av})^2 + (D_2 - D_{av})^2 + (D_3 - D_{av})^2}}{\sqrt{D_1^2 + D_2^2 + D_3^2}} \tag{2.68}$$

where $D_{av} = 1/3(D_1 + D_2 + D_3)$ is the average diffusivity.

The theoretical FA from isotropic diffusion is 0. In practice, this is never achievable due to noise in the NMR signal and the finite number of spins undergoing diffusion [114]. In the case of computer simulations of diffusion, this is due to the finite number of molecular trajectories being sampled [9, 90]. This is discussed further in section 3.

2.4 Diffusion in avascular anisotropic biological tissue

Biological tissue is intrinsically heterogeneous containing cell membranes, macromolecules and many structures on a larger scale. Consequently, molecular diffusion in tissue is restricted and, in many cases is anisotropic [114]. The quantitative study of diffusion in biological tissue has important applications for the improved understanding and diagnosis of disease, trauma and genetic disorders [9, 51, 72, 74, 89, 100, 131,

136–139]. As water molecules probe the tissue microstructure on the atomic scale, far below typical imaging resolutions, important nano and microstructural characteristics can be inferred from observations of their diffusive behaviour [100].

The complex organisational structure of tissue exists at many length-scales from cellular to macroscopic and has varying degrees of ordering. In tissue with no preferred ordering diffusion is restricted isotropically. Measurements of the diffusion coefficient within these tissues can indicate the degree of restriction and in conjunction with other techniques, can be used to infer tissue characteristics [140]. In other fibrous tissue such as the neural networks of the nervous system [139], muscle fibres [72, 141], and the collagen fibre networks of articular cartilage [142, 143], cells are organised into structures that restrict diffusion anisotropically. Additionally, many tissue and cells possess semi-permeable barriers with a characteristic membrane transport rates for the diffusing particles [62, 144]. Given the appropriate interpretive models, observations of restricted diffusion along different directions can be used to infer characteristics of the confining geometry of these tissue, often providing structural detail beyond the capabilities of other techniques [30, 51, 67, 143]. For example, neural tractography is a imaging clinical diagnostic technique where diffusion tensor measurements of the brain are used to interpret the neural pathways for diagnosis of brain disorder and damage [78]. Similar techniques are applied in DTI-based muscle fibre tracking to infer skeletal and cardiac muscle architectures [73, 145]. The highly-ordered structures within muscle cells restrict diffusion anisotropically, with diffusion least restricted in the direction of the muscle fibre [136]. Another important application of diffusion magnetic resonance imaging is in the study of articular cartilage, a tissue consisting of fibres with diameters in the nano-scale and varying degrees of structural ordering [131]. In addition to biological tissue *in situ*, the study of diffusion has applications in tissue engineering from measuring microstructure and nutrient pathways and tissue growth and infiltration within the tissue engineering constructs [13].

2.4.1 Neural structures

Neurons are cell that process and transmit electrical signals in the nervous system [79]. These cells include sensory and motor neurons, and white matter in the brain and spinal cord. Neurons consist of the soma, or cell body, the tree-like dendrites, and the axon which transports electrical signals between the soma and dendrites of surrounding neurons (see Fig. 2.12). The diameters of the axons range between $1\,\mu m$ and $25\,\mu m$ and they can reach lengths many times the diameter of the soma. Surrounding the axons is an electrically insulative membrane sheath, the myelin sheath, which in turn is surrounded by a cellular layer, the neurilemma, which together is called the medullary sheath. These cells are organised into complex interconnected networks and form the basis of the nervous system [146].

Water molecules diffuse within and between the neurons, the volume bounded by the medullary sheath, and the surrounding tissue [147]. The observed diffusion measurements correspond to the complex combination of restricted diffusion within, and between, each of these regions. Fiber tractography samples the diffusivity along given directions in a 3D array of voxels throughout the neural structure. By considering the connectivity inferred by the diffusion tensors of corresponding voxels, fibre orientation mapping resolves fibre tracks are computed and represent the neural connectivity [148]. As the diffusion tensor can only resolve a single predominant direction of diffusivity, other techniques such as Q-ball imaging [81, 149] and spherical deconvolution techniques [80] are often employed to resolve issues where two or more fibres cross within a given voxel [150–152].

2.4.2 Articular cartilage

Articular cartilage is a low friction, load bearing and wear resistant soft tissue found on the ends of the long bones and synovial joints [153]. It consists of chondrocytic

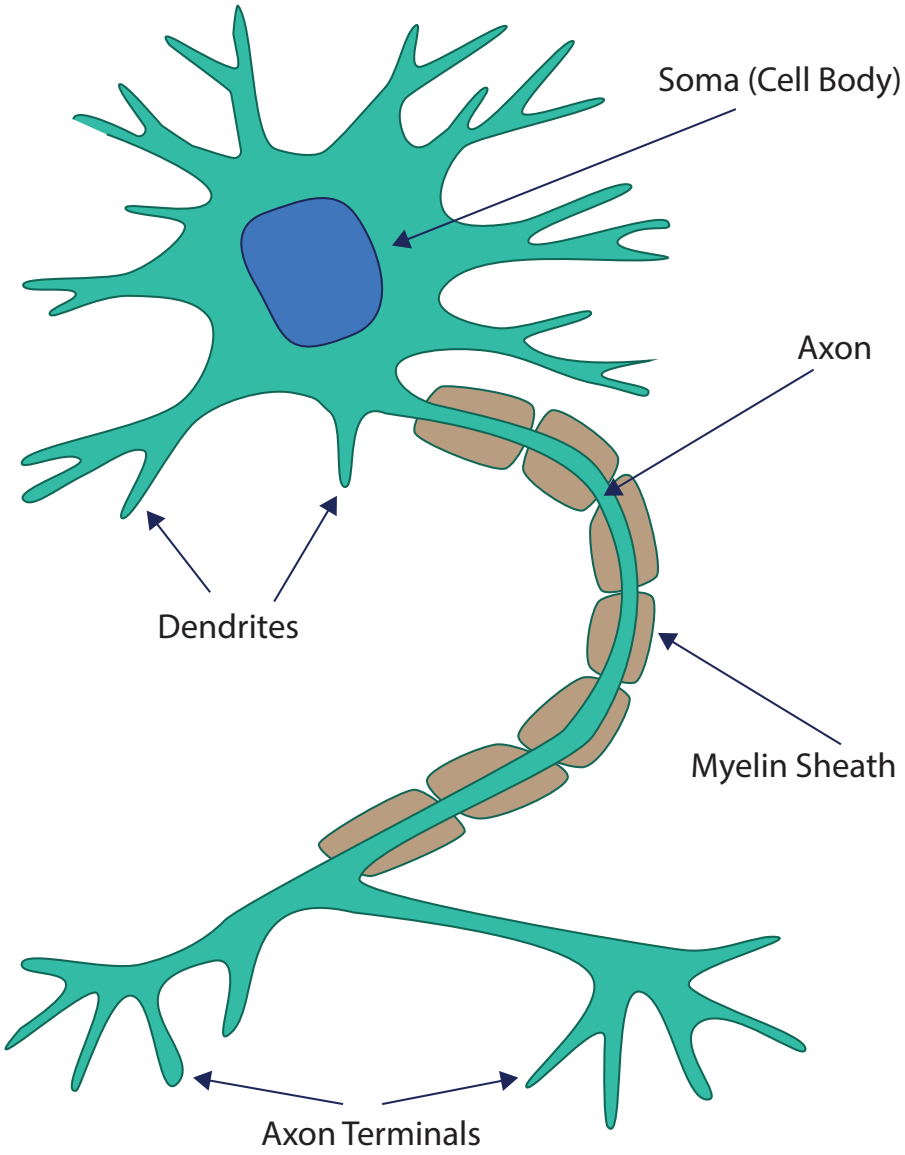

Figure 2.12: Schematic showing the of a typical neuron indicating the cell body, axon, dendrites, myelin sheath and axon terminals.

cells in a three dimensional extracellular matrix containing proteoglycans ($5-10\%$), collagen fibres ($15\%\, w/w$) and water ($65-80\,\%w/w$) [154, 155]. The biomechanical properties of articular cartilage are due to the macro-structure of the collagen fibre matrix and the osmotic properties of the proteoglycans, with the water diffusing in the interstitial volume between the fibres [90].

As much of the biomechanical properties of articular cartilage are due to the collagen fibre networks, knowledge of their organisation is of great importance for research into AC biomechanics [75] and clinical diagnosis of disease [156]. The range of methods for investigating AC microstructure include histology [157], microscopy [158], diffraction enhanced X-ray [159] and magnetic resonance imaging. Various MRI imaging techniques have been used to study AC structure such as spin relaxation imaging [160–163], magic angle imaging [77, 155, 164], and diffusion tensor imaging [74, 130, 132–134, 156].

Collagen fibre networks

The collagen matrix within articular cartilage consists of a highly organised network of collagen fibres with diameters of between 20 nm to 200 nm [165, 166]. The fibres consist of triple helix of polypeptide chains which are assembled into fibrils. These fibrils are further woven into larger fibres [167]. The exact nature of the collagen/proteoglycan interaction is still unknown, however, the compressive stiffness of AC has been found to be due to the electrostatic charge repulsion of the glycosaminoglycan groups. This charge effect generates a swelling pressure which subsequently affects water binding [168] and must be balanced by the arrangement of the collagen fibres [155].

As described in Minns and Steven, 1977, the collagen fibres in articular cartilage exhibit a lamellar organisation throughout the cartilage, and can be grouped into three zones based on their ordering; the radial zone where the fibres are aligned and perpendicular to the articular surface, the transitional zone where the fibres cross-over and have no preferential alignment, and the superficial zone where the fibres are aligned parallel to the articular surface [142, 169]. This is illustrated in Fig. 2.13 which shows a scanning electron microscope image of a cross section of bovine patella articular cartilage with the zones indicated. This image shows the calcified bone toward the

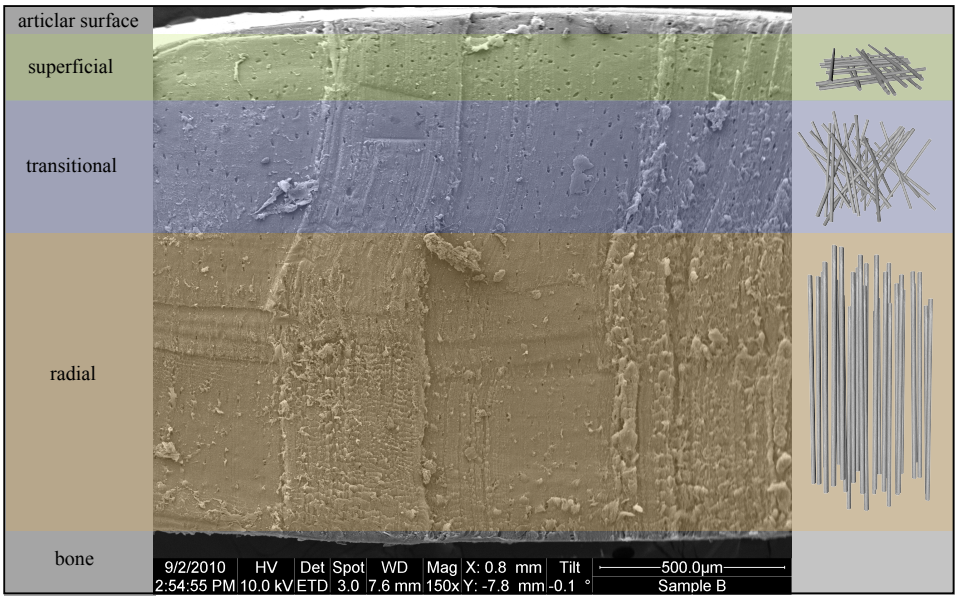

Figure 2.13: Scanning electron micrograph of bovine patella cartilage taken by the author. The fibre organisational zones are superimposed over the image with an illustration of the fibre ordering on the left.

bottom of the image and the articular surface at the top. The small dark hollows are the locations of the condrocytes which are the cellular components of articular cartilage. Figure 2.14 shows four higher magnification SEM micrographs of bovine articular cartilage and shows fibres in the aligned (Fig. 2.14a), transitional (Fig. 2.14b) , and superficial zones (Fig. 2.14c).

A magic angle MRI study by Xia Yang, 2000 [155] found that the typical volume fraction of collagen fibres in AC varies throughout and is approximately 0.2 at the radial and superficial zones and 0.15 in the transitional zone. The corresponding water concentration was also seen to vary throughout the cartilage from $0.65\, w/w$ at the radial zone through to 0.75 at the superficial zone.

Proteoglycans

Proteoglycans are protein-polysaccharide molecules contained within the cartilage via hydrogen bonding with the collagen fibres and have a hierarchical organisation. This enables the efficient placement of anionic charges which then bind with water molecules

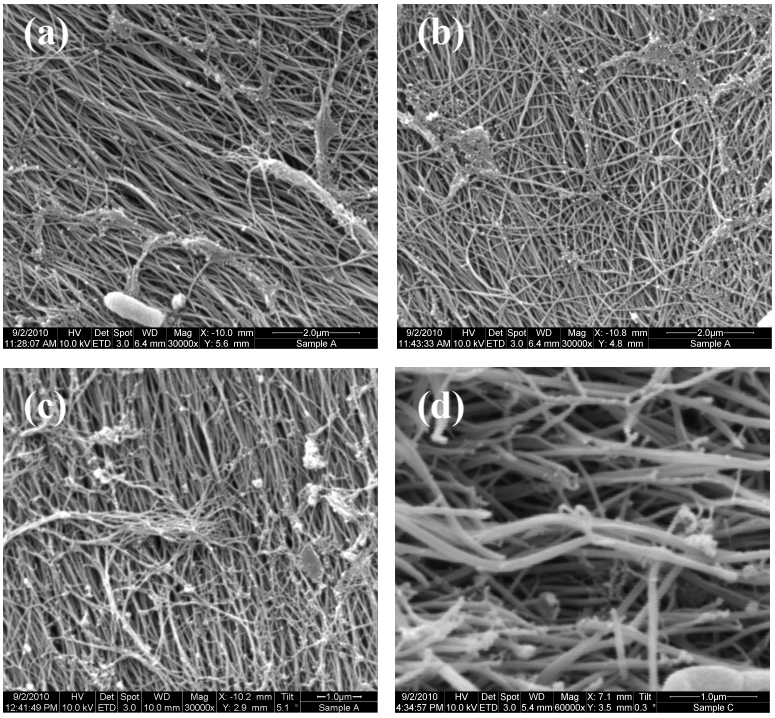

Figure 2.14: Various scanning electron micrographs of bovine articular cartilage taken by the author showing the fibre networks with various degrees of ordering.

and provide the hydrodynamic properties of AC [170]. It is the combination of both the hydrodynamic friction and the osmotic interactions between the proteoglycans and the water that results in the mechanical and load distribution properties of articular cartilage [171, 172]. Throughout articular cartilage, the proteoglycan concentration varies between approximately $0.04\,w/w$ at the articular surface to 0.07 at the radial zone [155].

Diffusion in articular cartilage

Diffusion tensor imaging has great potential as an indicator of early stage osteoarthritis [134, 143, 173] and for research into AC microstructure and biomechanics [74, 130, 132, 174–176]. For example, Deng et. al. found an increase in the apparent diffusion coefficient within samples of human articular cartilage following depletion of the proteoglycan content, indicating that DTI is sensitive to pathophysiological changes

in AC. Micro-structural changes in AC were observed in DTI experiments carried out by de Visser et. al. 2008 [130]. More recently, Ukai et. al. 2015 demonstrated that a combination of DTI and spin-relaxation MRI measurements can detect moderate to severe AC damage and changes in the apparent diffusion coefficient can be used to detect early stage AC damage [177]. This same study also found that fractional anisotropy measurements can be used to identify damaged cartilage.

Because the collagen fibres are partially ordered in AC, the corresponding diffusion tensor is anisotropic. It is the collagen fibres alone that contribute to this anisotropy, with many studies demonstrating that the other major component in AC, the proteoglycans, have no preferred ordering [74, 76, 134, 172]. The effect of the proteoglycans is to isotropically reduce the apparent diffusion coefficient by approximately $10-15\%$ [166]. Comper and Williams, 1987 [171] also demonstrated a corresponding reduction in the ADC with the increase in a proteoglycan aggregate concentration. Because diffusion measurements of AC are restricted by a complex combination of the effect of the collagen network and the proteoglycans, knowledge of their relative concentrations is important for improved quantitative interpretation of fibre microstructure from DTI measurements [9]

2.4.3 Scaffolds for tissue engineering

Tissue engineering involves the fabrication of tissue constructs for the purposes of replacing missing, defected or damaged tissue and restore function [178]. Biofabrication is the application of 3D printing principles to tissue engineering, employing a layer-by-layer controlled deposition of material to build up 3D objects [179–182]. In hybrid scaffold/cell approaches, a 3D biodegradable polymer scaffold is fabricated and cells and growth factors inserted, often by way of hydrogel printing [183, 184]. The scaffold serves as a temporary structure for initial tissue growth providing mechanical support and a organised matrix environment to optimise growth [185]. Following seeding,

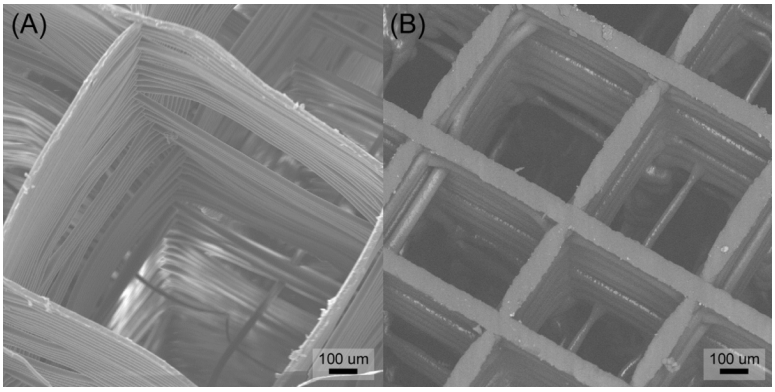

Figure 2.15: Scanning electron micrographs of melt-electrospun scaffolds with 90 degree cross-hatch architecture [181]

cells proliferate within the scaffold until it is ready for transplantation into the patient [186–189].

The internal microarchitecture of the scaffold directly affects seeding efficiency, tissue proliferation, and cell differentiation [190–194]. Futhermore, the pore size, distribution and interconnectivity within the scaffolds are critical for the supply of vital metabolites are the removal of metabolic waste products. Diffusion tensor imaging has potential as a tool for the non-invasive characterisation of the evolution of molecular transport pathways within 3D tissue engineering scaffolds as tissue grows. The use of MRI to monitor tissue regeneration in tissue engineering is outlined in a review article by Xu et al. 2008 which described the applications of various MRI techniques to study regenerated AC, adipose tissue and fat [138]. More recently, Othman et al. 2015 used a proprietary MRI compatible incubator to perform a longitudinal study of bone tissue growth in cross-linked gelatin scaffolds over a four week period. They observed changes in the T_1, T_2 and ADC as the tissue infiltrated the scaffold. The DTI study of melt-electrospun TE scaffolds by Powell 2014 went beyond measuring the ADC to characterising diffusion anisotropy as a non-invasive technique for mapping molecular transport pathways (see Chapter 5) [13].

Scaffold based tissue engineering studies typically use specialised 3D printing

techniques to fabricate a porous polymer scaffold layer-by layer into the desired external shape [195–197]. This process also produces the porous internal structures with the scale of structures within these internal networks shown to affect cell infiltration and proliferation [198]. The scale of the internal features has been shown to effect scaffold performance, with micron-scale fibre networks desirable for cell attachment having larger surface area to volume ratios and surface topology comparable to the dimensions of the cells [199]. Three dimensional printing techniques such fused deposition modelling and stereo-lithography are capable of producing features as small as approximately $100\,\mu m$ but typically $400\,\mu m$ [200]. Higher resolution fabrication technologies such as direct-writing melt electrospinning are capable of producing organised fibre networks with fibre diameters in the order of 10's of microns [201]. However, rapid proliferation of tissue in these scaffolds often results in the restriction of vital fluid pathways leading to cell death [202, 203]. Therefore, one of the challenges in melt-electrospinning based tissue engineering (and other comparable technologies) is to develop scaffold designs for optimal tissue growth and maintain the vital fluid pathways.

Following cell seeding, the scaffolds are placed in cell culture plates or bioreactors to support cell growth. In the case of perfusion bioreactors, the microfluidic environment needs to have very low levels of flow to prevent the cells from detaching from the scaffold [204–206]. Within the scaffold, diffusion is the dominant molecular transport mechanism [207–210]. For this reason, the study of diffusion is critical for successful tissue engineering scaffold design. Most studies of microfluidics within TE scaffolds to date involve perfusion measurements to infer information such as pore connectivity and tortuousity [211]. As advances in micron scale fabrication are relatively recent, there are few studies that use diffusion MRI for the longitudinal study of tissue growth and its effect on diffusion [115, 138, 212]. In addition to characterising the molecular transport within tissue engineering scaffolds, diffusion tensor imaging can be used

to infer geometrical features in much the same way as with tissue such as articular cartilage. Given the much thicker fibres of melt-electrospun scaffolds compared to the collagen fibres of articular cartilage, diffusion measurements are in the intermediate diffusion regime. This enables DTI to probe the changes in surface to volume ratio as tissue growth within the scaffolds [29, 67]. In addition, 3D maps of tissue growth and molecular transport pathways can be obtained by spatially encoding the diffusion measurements [35, 114].

Chapter 3

Computer simulations of restricted diffusion

In this chapter, we detail a simulation technique for producing diffusion tensors corresponding to asymptotic long-Δ diffusion measurements of periodic fibre networks. This method models the trajectories of diffusing water molecules and computes their interactions with fibre structures to produce theoretical diffusion tensors [54]. The simulation software is based on the Langevin equation which computes physically realistic modelling of water/fibre interactions without requiring explicit calculation of the many-body interactions between all diffusing particles [213]. In the following sections of this chapter, we detail the development of the Langevin dynamics simulation software and its application to the problem of diffusion in the interstitial volume surrounding an array of partially aligned model collagen fibres. We also investigate the effect of positional and radial disorder of completely aligned collagen fibres on the diffusion tensor. The chapter is presented as expanded versions of two published peer-reviewed journal papers [9, 10].

The authors listed below have certified* that:

1. they meet the criteria for authorship in that they have participated in the conception, execution, or interpretation, of at least that part of the publication in their field of expertise;

2. they take public responsibility for their part of the publication, except for the responsible author who accepts overall responsibility for the publication;

3. there are no other authors of the publication according to these criteria;

4. potential conflicts of interest have been disclosed to (a) granting bodies, (b) the editor or publisher of journals or other publications, and (c) the head of the responsible academic unit, and

5. they agree to the use of the publication in the students thesis and its publication on the QUT ePrints database consistent with any limitations set by publisher requirements.

In the case of this chapter:

Langevin dynamics modelling of the water diffusion tensor in partially aligned collagen networks

Sean K. Powell and Konstantin I. Momot, Physical Review E 86, 031917 (2012)

Contributor	**Statement of contribution***
Sean K. Powell QUT Verified Signature Signature 10-9-15 Date	Co-designed the research program, wrote the Langevin dynamics simulation software, generated the collagen fibre force field parameters, and ran all simulations on supercomputer, processed and analysed data, co-wrote the paper and discussion and co-developed the simplified analytic model.
Konstantin I. Momot*	Co-designed the research program, co-wrote the paper, co-developed the simplified analytic model, and derived the of equations of motion. Supervised the research.

Principal Supervisor Confirmation

I have sighted email or other correspondence from all Co-authors confirming their certifying authorship.

Konstantin Momot	Konstantin Momot Digitally signed by Konstantin Momot Date: 2015.09.13 00:54:32 +10'00'	13 September 2015
Name	Signature	Date

3.1 Langevin dynamics modelling of the water diffusion tensor in partially aligned collagen networks (expanded)

Sean K. Powell and Konstantin I. Momot

School of Chemistry Physics and Mechanical Engineering, Queensland University of Technology, GPO Box 2434, Brisbane, Queensland 4001, Australia.

Published in: Physical Review E 86 (3), 2012

DOI: 10.1103/PhysRevE.86.031917

3.1.1 Abstract

In this work, a Langevin dynamics model of the diffusion of water in articular cartilage was developed. Numerical simulations of the translational dynamics of water molecules and their interaction with collagen fibres were used to study the quantitative relationship between the organisation of the collagen fibre network and the diffusion tensor of water in model cartilage. Langevin dynamics was used to simulate water diffusion in both ordered and partially disordered cartilage models. In addition, an analytical approach was developed to estimate the diffusion tensor for a network comprising a given distribution of fibre orientations. The key findings are: (1) an approximately linear relationship between collagen volume fraction and the fractional anisotropy of the diffusion tensor in fibre networks of a given degree of alignment, (2) for any given fibre volume fraction, fractional anisotropy follows a fibre alignment dependency similar to the square of the second Legendre polynomial of $\cos(\theta)$, with the minimum anisotropy occurring at approximately the magic angle (MA), (3) a decrease in principal eigenvalue and an increase in the transverse eigenvalues as the fibre orientation angle, θ, progresses from 0° to 90°. The corresponding diffusion ellipsoids are prolate for $\theta < MA$, spherical for $\theta \approx MA$, and oblate for $\theta >$

MA. Expansion of the model to include discrimination between the combined effects of alignment disorder and collagen fibre volume fraction on the diffusion tensor is discussed.

3.1.2 Introduction

Diffusion tensor imaging (DTI) enjoys success as a non-invasive imaging technique for both medical research and clinical diagnostics by enabling in vivo investigations of biological tissue organisation and microstructure [74, 76, 139, 147, 214]. DTI measurements are performed by applying magnetic field gradients in several independent directions to acquire a series of diffusion weighted images, with each image providing information about the diffusivity along the respective direction. The resulting images are combined and processed to produce maps of diffusion tensors. The eigenvalues and eigenvectors of diffusion tensors describe the magnitude and principal directions of diffusivity and the tensor can be visualised as a diffusion ellipsoid [58]. Interpretation of DTI measurements is based on the assumption that the characteristics of the diffusion ellipsoid reflect the macromolecular or cellular environment of the diffusing water molecules [102].

DTI is ideally suited to investigating the collagen fibre organisation of articular cartilage (AC). AC is the load-bearing, low-friction and wear-resistant tissue covering the ends of the long bones inside synovial joints in mammals [215]. The main extracellular components of articular cartilage are water ($65\% - 80\%$), type II collagen ($15 - 20\%$) and proteoglycans ($5-10\%$) [155]. The collagen fibres of AC are based on a triple helix of polypeptide chains. These are assembled into long fibrils, which are further wound into larger fibres [216]. These fibres are cross-linked into a matrix network, with different amounts of ordering throughout the tissue. The organisation of these networks is often described in terms of different zones based on their predominant alignment as shown in Fig. 3.1 [130]. In the superficial zone the fibres are predominantly aligned parallel to the articular surface; in the radial zone the fibres are predominantly aligned perpendicular to the bone surface; and in the transitional zone the fibres have no preferred alignment.

Present knowledge about the relationship between the diffusion tensor and tissue morphology has been developed through the use of DTI experiments on independently characterised models and tissues [74][58][217][31], theoretical analysis of diffusion in anisotropic structures [102][218][48], and computer models that simulate the translational diffusion of tracer molecules in model structures [54][52][101][219][220]. In practice, interpretation of the diffusion tensor with respect to AC microstructure is currently limited to determining the predominant direction of the fibres and qualitative indicators of the degree of alignment [221]. Quantitative determination of the degree of alignment and fibre volume fraction is difficult because of the interplay between these two factors in determining the diffusion tensor.

In this study, we investigated water diffusion in partially aligned model collagen fibre networks. This was done using Langevin dynamics (LD) simulations of molecular diffusion of water restricted by collagen fibres Langevin dynamics was chosen instead of the less computationally expensive Monte Carlo approach because the long-term aim of this work was the development of coarse-grained simulations of the anisotropy of ^{1}H transverse spin relaxation rate ($1/T_2$) [77]. The latter phenomenon is controlled by slow rotational dynamics of water molecules and therefore requires simulations involving both long time scales and molecular detail. In the present work, LD simulations were used to obtain the water diffusion tensors for a range of fibre alignment angles and fibre volume fractions. The simulation results were used to produce quantitative relationships between the diffusion tensor, the degree of structural disorder, and the collagen volume fraction. Additionally, a simplified analytical model was developed to allow efficient estimation of the diffusion tensor for a given distribution of fibre alignments. We discuss the feasibility of using DTI measurements on their own and in conjunction with T_1 mapping for determination of fibre alignment and collagen volume fraction in articular cartilage.

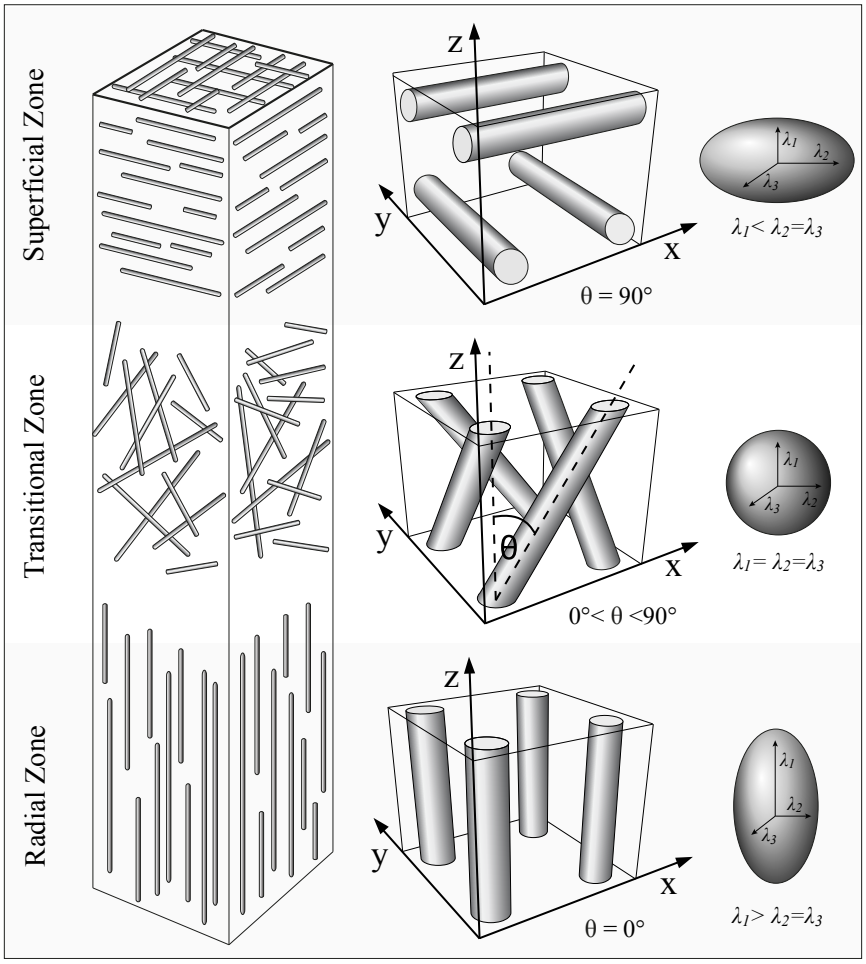

Figure 3.1: (left) Schematic illustration of the typical distribution of collagen fibre orientations in the superficial, transitional and radial zones of articular cartilage. The articular surface is indicated by the bold square at the top of the superficial zone. (centre) Schematic illustration of the fibre orientations of the model collagen networks developed in the present study for $\theta = 90°$, $0° < \theta < 90°$, and $\theta = 0°$. (right) Diagrams of the diffusion ellipsoids for each of the three AC zones: an oblate ellipsoid for the superficial zone, spherical for the transitional zone, and a prolate ellipsoid for the radial zone.

3.1.3 Methods

A Langevin dynamics model of hydrated collagen fibres was used to compute the translational dynamics of water molecules. The software was written in-house; the details of LD simulations are provided in Appendix A. The force applied to each water molecule was calculated in each time step as the sum of a stochastic force (representing

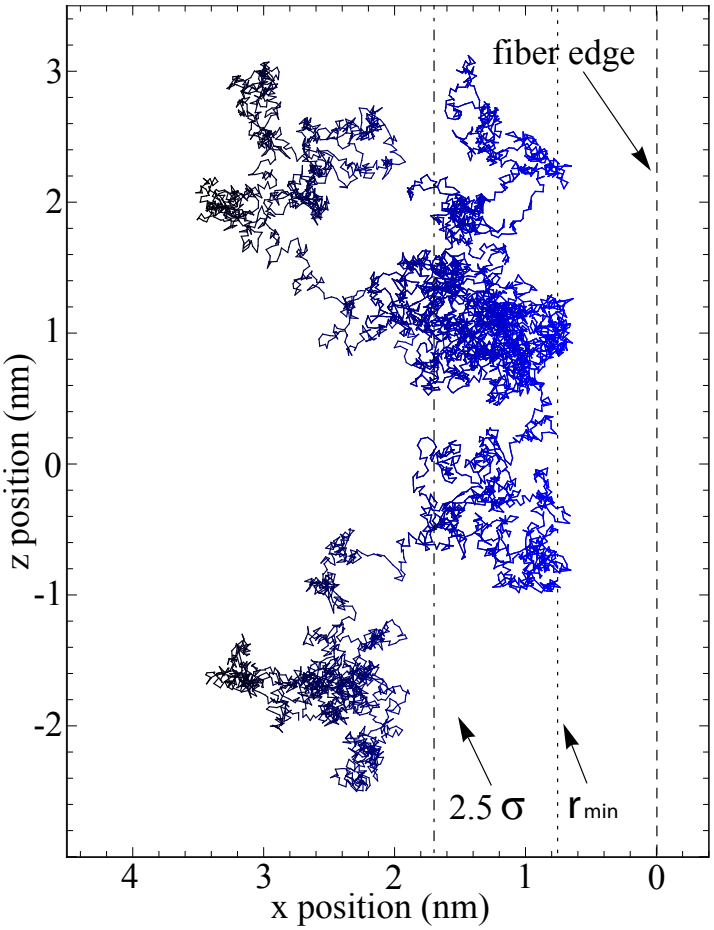

Figure 3.2: The sample trajectory of a single water molecule undergoing an interaction event with a model collagen fibre. The motion of the water molecule was calculated using the Langevin equation, Eq. (A.1). The outer edge of the fibre is located at $x = 0$ and runs parallel to the z-axis. The water/ fibre potential took the form of a Lennard-Jones-like potential; r_{min} is the location of the potential minimum. The water/fibre interaction force is applied to the water molecule in a direction normal to the fibre axis.

water-water interactions), a conservative force (water-fibre interactions) and a hydrodynamic friction force. This approach provides a physically realistic picture of water-fibre interactions and is sufficiently computationally efficient to enable simulations in the long diffusion time (Δ).

The model collagen fibres were represented as smooth walled cylinders. Each cylinder was defined by a vector representing its central axis and a value defining its radius. The interaction force ($\mathbf{F}_c$) between a given water molecule and any nearby fibre was directed normal to the fibre axis. To optimise processing time, a cut-off distance

of 2.5σ was used between the water molecule and the fibre wall (see Fig. 3.2). At this distance, the residual value of $\mathbf{F}_c \approx 4 \times 10^{-13}\, N$, leading to a displacement of $\Delta r_c(r) \approx 3 \times 10^{-14}\, m$ at $\Delta t = 0.2\, ps$.

Model collagen networks

The simulation volume was defined as a rectangular parallelepiped encompassing the model collagen fibres with tracer water molecules diffusing in the interstitial volume. The direction of preferred fibre alignment was taken as the z axis and referred to as the longitudinal direction. The transverse plane was defined as the x,y plane.

In each simulation volume, 64 model collagen fibres were aligned parallel to the z-axis and arranged into a square array across the x-y plane with a spacing of $180\, nm$. For the partially aligned networks, the fibres were rotated by the desired angle. In order to maintain axial symmetry, the fibres were treated in groups of 4, with the fibres in each group rotated about the $+x$, $+y$, $-x$ and $-y$ axis respectively (see Fig. 3.1). The rotation centre of each fibre was also shifted along the z-axis by a randomly chosen integer multiple of $180\, nm$ in order to prevent the fibres rotated at 90° from occupying only one plane.

In total, 46 different fibre networks were constructed. Ten different identically aligned networks were generated using fibre radii of $30\, nm$, $35\, nm$, $40\, nm$, $45\, nm$, $50\, nm$, $55\, nm$, $70\, nm$, $65\, nm$, $70\, nm$, and $80\, nm$. For each of the partially aligned fibre networks, the radii were $40\, nm$, $50\, nm$, $55\, nm$, $60\, nm$, $70\, nm$, and $80\, nm$. The fibre rotation angles, θ, chosen for the partially aligned networks were 22.5°, 45°, magic angle ($\cos^{-1}(1/\sqrt{3}) \approx 54.7^\circ$), 67.5°, and 90°.

The actual fibre volume fractions corresponding to each simulation structure are shown in Fig. 3.3. These were calculated by sampling a 3D array of points throughout each simulation volume and determining the ratio of the number of points within the

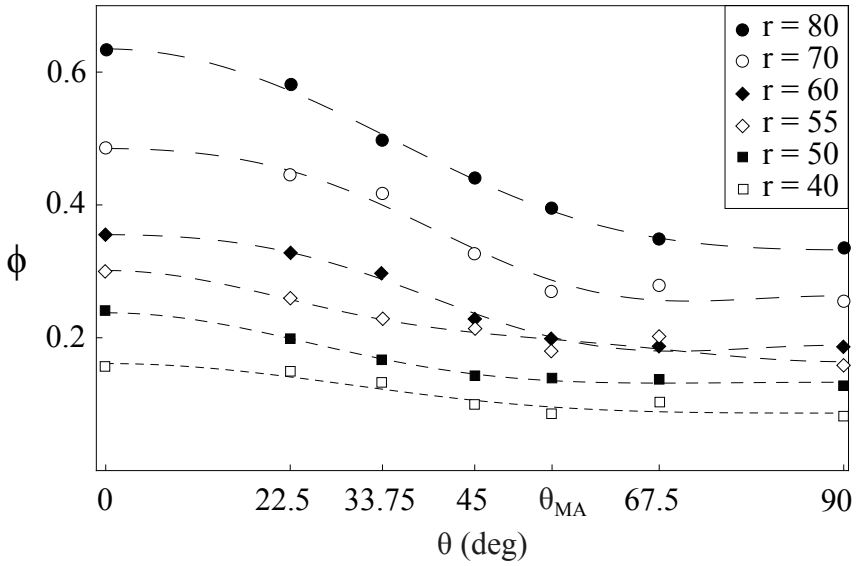

Figure 3.3: The effect of alignment disorder on fibre volume fraction for a given fibre radius. The decrease in fibre volume fraction with increasing θ is an artefact of fibre network construction.

fibres to the total number of points. These plots show that for a given fibre radius, the fibre volume fraction, ϕ, decreases as the fibre rotation angle is increased. Additionally, the fibre volume fraction for the $\theta = 90^\circ$ structures is $52.7 \pm 0.2\%$ of the volume fraction for the aligned case for all fibre radii. This can be explained as an artefact of the network construction method.

Simulation parameters

At the initialisation of each simulation run, the required number of water molecules were randomly placed in the interstitial volume. An implementation of periodic boundary conditions was used whereby water molecules stepping outside the volume boundary were translated to a random location within the interstitial volume. The displacements effected by such boundary crossings were subtracted from the final simulation displacements in order to correctly calculate the net displacement for each water molecule.

The optimal integration time step, Δt, was chosen to be larger than the velocity

autocorrelation time (VACT) of water (to satisfy Eq. (A.2)), yet small enough to enable the diffusing water molecules to sufficiently sample the water/fibre interaction potential. It was found that $\Delta t > 0.2\,ps$ produced unrealistic translational behaviour of the water molecule during interactions with the coarse-grained model fibres. Consequently, $\Delta t = 0.2\,ps$ was chosen as the integration step time.

The total simulation duration, $\Delta = 0.1\,ms$, was chosen for all aligned networks and partially aligned networks with fibres of radius $50\,nm$. $\Delta = 0.05\,ms$ was chosen for the remaining networks. This resulted in RMS displacements of between $480\,nm$ and $680\,nm$, which were larger than the average fibre spacing of $180\,nm$ (see section 3.1.5). This ensures the simulated diffusion tensors are solidly within the long-Δ regime as discussed in Section 3.1.5.

Diffusion tensor

The net displacements of the tracer water molecules at the end of each simulation were used to compute the diffusion tensor according to the established methodology [54][59]:

$$D_{ij} = \frac{1}{2N_s\Delta t N}\sum_{n=1}^{N_p}\left(r^i_{N_s,n} - r^i_{o,n}\right)\left(r^j_{N_s,n} - r^j_{o,n}\right) \tag{3.1}$$

where the indices i and j refer to the axes x, y and z; $N_s\Delta t$ is the duration of the simulation; $r_{o,n}$ is the initial position of molecule n; and $r_{N_s,n}$ is the final position of molecule n after the boundary condition displacements have been subtracted.

The resulting diffusion tensors were diagonalised to determine the eigenvalues and eigenvectors. As axially symmetric rotations were used to construct the partially aligned fibre networks, the eigenvalue sorting problem was solved by defining the unique eigenvalue (longitudinal diffusivity, D_l) as the eigenvalue corresponding to the

eigenvector closest aligned with the z-axis of the simulation volume.

In addition to the diffusion tensor, diffusion in fibrous tissue is often described using a scalar measure, fractional anisotropy (λ_{FA}) [222]. This scalar measure can be considered as the degree of deviation of the diffusion tensor from the isotropic case. It is normalised to the modulus of the diffusion tensor, and is given by:

$$\lambda_{FA} = \sqrt{\frac{3}{2}} \cdot \sqrt{\frac{(\lambda_1 - \lambda_{av})^2 + (\lambda_2 - \lambda_{av})^2 + (\lambda_3 - \lambda_{av})^2}{\lambda_1^2 + \lambda_2^2 + \lambda_3^2}} \tag{3.2}$$

where λ_1, λ_2, and λ_3 are the eigenvalues of the diffusion tensor (DT) and $\lambda_{av} = 1/3(\lambda_1 + \lambda_2 + \lambda_3)$ is the average diffusivity.

3.1.4 Results

DT eigenvalues

Isotropic diffusion simulations were run in the absence of collagen fibres to observe the effect of ensemble size on the diffusion tensor. A simulation of 5000 molecules undergoing isotropic diffusion for 1×10^6 steps resulted in a diffusivity of $\langle D \rangle = (2.30 \pm 0.01) \times 10^{-9}\, m^2 s^{-1}$, and $\lambda_{FA} = 0.061 \pm 0.005$. Increasing the ensemble size to 20000 molecules reduced the fractional anisotropy to $\lambda_{FA} = 0.033 \pm 0.003$.

The diffusion tensor corresponding to each of the model cartilage simulations was calculated using the net molecular displacements in accordance with Eq. (3.1). As discussed previously, the unique eigenvalue was chosen as the eigenvalue corresponding to the eigenvector closest aligned to the z-axis and represented the longitudinal diffusivity, D_l. The average of the remaining two eigenvalues was taken as the diffusivity in the transverse plane, D_t. The normalised longitudinal diffusivity for each of the simulations is shown in Fig. 3.4(a) as a function of both the fibre volume fraction, ϕ, and fibre rotation angle, θ. The isotropic diffusion coefficient of water

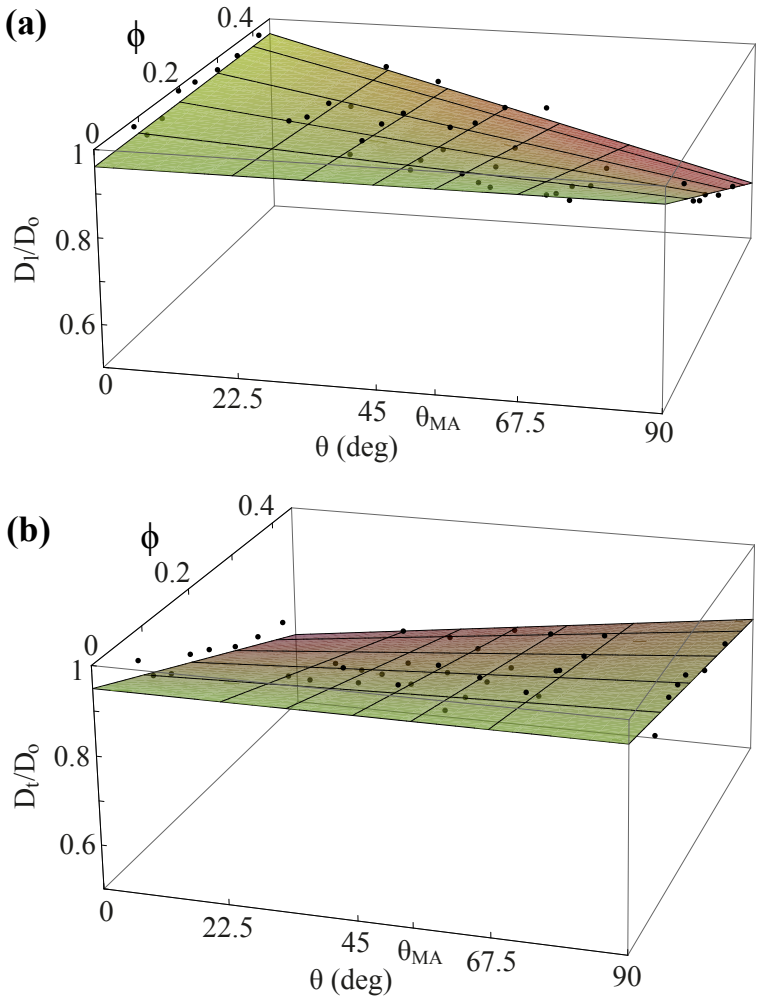

Figure 3.4: (a) Normalised longitudinal diffusivity, D_l/D_o, for LD simulations of water diffusion in model collagen networks, as a function of both the fibre volume fraction, ϕ, and fibre orientation angle, θ. The surface represents the values of the least-squares fit shown in Eq. (3.3). In the present study, $D_o = 2.3 \times 10^{-9}\, m^2 s^{-1}$ was used. (b) Normalised transverse diffusivity, D_t/D_o, obtained from the LD simulations as a function of both the fibre volume fraction, ϕ, and fibre rotation angle, θ. The surface represents the values of the least-squares fit shown in Eq. (3.4).

of $D_o = 2.3 \times 10^{-9}\, m^2 s^{-1}$ was used. A least squares fit (LSF) was performed on this data resulting in the equation:

$$D_l/D_o(\phi, \theta) = -0.46\ \phi\ \theta + 0.962 \tag{3.3}$$

Fig. 3.4(b) shows the normalised transverse diffusivity, D_t/D_o, as a function of both fibre volume fraction, ϕ, and fibre rotation angle, θ. As with the longitudinal

diffusivity, a LSF was performed on the simulation results producing the following equation:

$$D_t/D_o(\phi,\theta) = 0.20\ \phi\ \theta - 0.61\ \phi + 0.950 \tag{3.4}$$

Fig. 3.5(a) shows the simulated values of D_l/D_o and D_t/D_o for the aligned fibre networks ($\theta = 0$). The lines shown are the corresponding cross-sections of the LSF surfaces (Eq. (3.3) and Eq. (3.4)). This plot shows that for aligned fibres, D_l/D_o is invariant to the fibre volume fraction, ϕ. Also, at all values of ϕ the simulated D_l/D_o was greater than D_t/D_o, describing a prolate diffusion ellipsoid. The lines in Fig 3.5 represent the cross-sections of the 3D plot shown in Fig 3.4(a) and (b), and are not simply one dimensional linear fits.

The results shown in Fig. 3.5(b) are for the networks with fibres oriented at the magic angle. Here, the values of the LSF functions that correspond to both D_l/D_o and D_t/D_o appear approximately the same for all fibre volume fractions, ϕ, indicating an approximately spherical diffusion ellipsoid.

Fig. 3.5(c) shows the diffusion tensor eigenvalues for the fibre networks with the fibres oriented at $90°$. This plot shows both D_l/D_o and D_t/D_o are affected by fibre volume fraction unlike the identically aligned case. Also, $D_l/D_o < D_t/D_o$ for this set of networks, indicating an oblate diffusion ellipsoid.

The interpolated values of D_l/D_o and D_t/D_o for networks with fibre volume fractions of 0.1, 0.2, and 0.3 are shown in Fig. 3.6. The average diffusivity ($\langle D \rangle = \frac{1}{3}(D_l + 2D_t)$) is also shown, and is approximately independent of θ for a given ϕ.

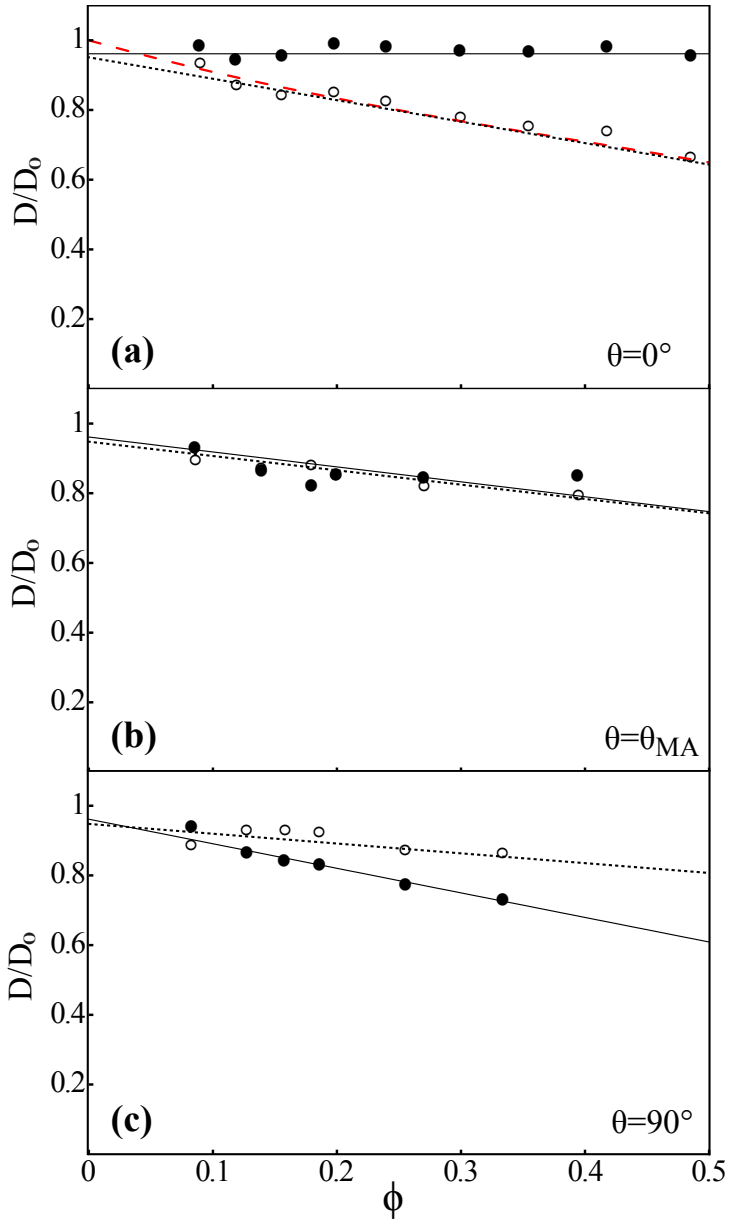

Figure 3.5: Eigenvalues of the simulated water diffusion tensor as a function of fibre volume fraction, ϕ: the solid circles are the LD simulation results for normalised longitudinal diffusivity, D_l/D_o, and the solid lines are the corresponding cross sections of the 3D plot shown in Fig. 3.4(a); the open circles represent normalised transverse diffusivity, D_t/D_o, calculated as the average of the two secondary eigenvalues. The small-dash lines are the corresponding cross sections of the 3D plot shown in Fig. 3.4(b). The size of the symbols is approximately the typical 95% confidence interval. (a) Results for networks of identically aligned fibres. The red (large-dash) line is the transverse diffusivity modelled by the Rayleigh multiple method (Eq. (3.6)). (b) Results for axially symmetric networks of fibres aligned at the magic angle ($\cos^{-1}(1/\sqrt{3}) \approx 54.7°$). (c) Results for networks with fibres oriented at $90°$ with respect to the z axis.

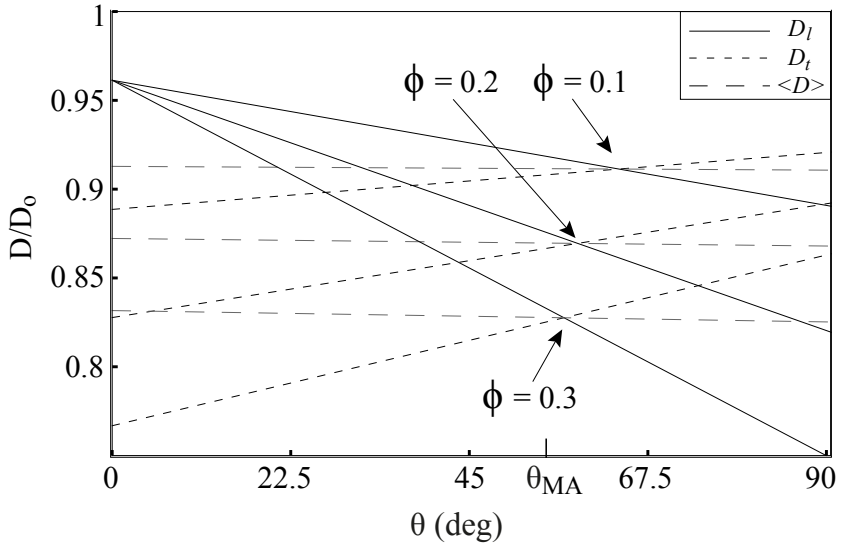

Figure 3.6: Longitudinal and transverse diffusivity as a function of fibre orientation for networks with fibre volume fractions $\phi = 0.1$, $\phi = 0.2$, and $\phi = 0.3$. The values correspond to Eqs. (3.3) and (3.4). The solid lines are the values of D_l/D_o and the small-dashed lines are the values of D_t/D_o. Also shown is the average diffusivities ($\langle D \rangle = \frac{1}{3}(D_l + 2D_t)$) which remain at the same value at all orientations for a given fibre volume fraction.

Fractional anisotropy

The diffusion tensor eigenvalues reported in section 3.1.4 were used to compute the fractional anisotropy of the DT using Eq. (3.2). A plot of λ_{FA} as a function of both fibre volume fraction and fibre rotation angle is shown in Fig. 3.7. Also shown is the LSF surface resulting from the expansion of $\lambda_{FA}(\theta, \phi)$ by the real spherical harmonics up to $Re(Y_2^2)$ [223]. The coefficients of the expansion are shown in Table 3.1.

Fig. 3.8(a) shows the values of λ_{FA} for both the identically aligned fibre networks (solid points) and the networks with fibres aligned at 90° (hollow points), as a function of fibre volume fraction. The lines shown are the corresponding cross-sections of the least-squares fit shown in Fig 3.7. Here, the fractional anisotropy approximately linearly increases with increasing fibre volume fraction for both networks, however, the values of λ_{FA} for the aligned case increase at a greater rate. Additionally, a one dimensional linear LSF was performed on the values of λ_{FA} for the identically aligned

$Re(Y_l^m)$	Coefficient
Y_0^0	0.034
$Y_0^0\phi$	-7.578
$Y_1^0\phi$	9.696
$Y_1^1\phi$	9.627
$Y_2^0\phi$	-3.429
$Y_2^1\phi$	-3.982
$Y_2^2\phi$	-6.187

Table 3.1: Coefficients of the spherical-harmonics expansion of the simulated fractional anisotropy, $\lambda_{FA}(\theta, \phi)$ (Fig. 3.7).

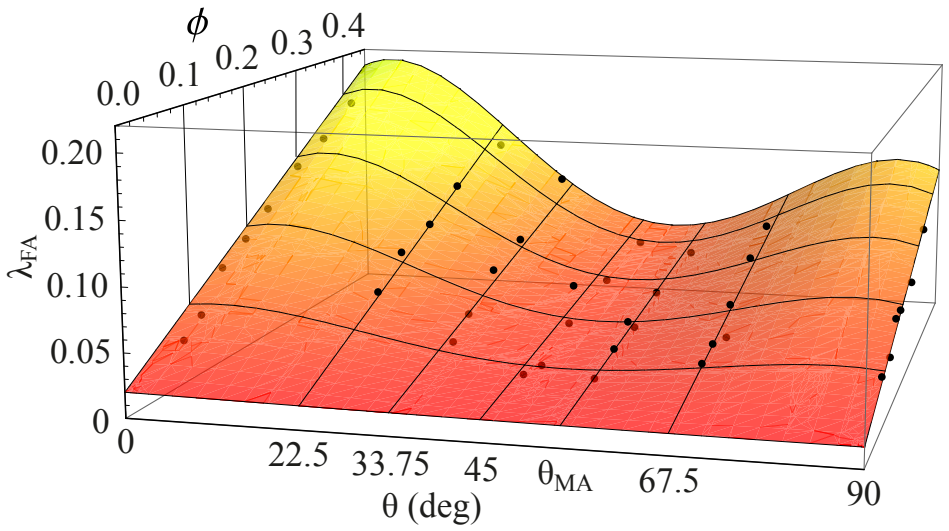

Figure 3.7: The fractional anisotropy, λ_{FA}, of the simulated DT, as a function of both fibre volume fraction, ϕ, and fibre orientation angle, θ. The surface is an expansion of the λ_{FA} by the real spherical harmonics up to $Re(Y_2^2)$. The weights of the data points in the expansion were calculated using the standard deviation of four separate simulation runs.

fibre networks, resulting in the equation:

$$\lambda_{FA(A)} = 0.43\phi + 0.001 \tag{3.5}$$

The non-zero intercept results from noise as discussed in section 3.1.5.

The simulated values of λ_{FA} and the corresponding least-squares fit surface values

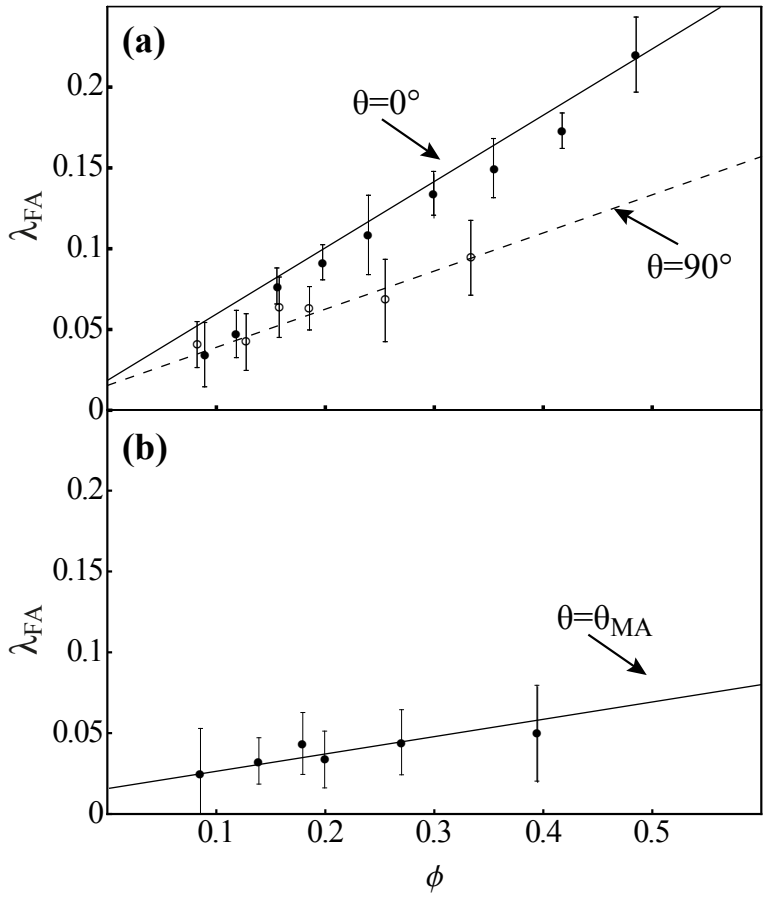

Figure 3.8: Fractional anisotropy, λ_{FA}, of the simulated diffusion tensor as a function of fibre volume fraction, ϕ: (a) The solid circles are the values of λ_{FA} for the identically aligned regularly spaced fibre networks; the open circles are the values of λ_{FA} for the networks with fibres oriented at 90° to the longitudinal axis. The lines represent the corresponding cross-sections of the 3D plot shown in Fig. 3.7. (b) Values of λ_{FA} for the networks with the fibres oriented at the magic angle and the line represents the corresponding cross-sections of the 3D plot shown in Fig. 3.7. The error bars are calculated as $\Delta\lambda_{FA} = 1/3((\sigma_{xx}/2\,\langle D_{xx}\rangle) + (\sigma_{yy}/2\,\langle D_{yy}\rangle) + (\sigma_{zz}/2\,\langle D_{zz}\rangle))$.

for networks with fibres aligned at the magic angle are shown in Fig. 3.8(b). In this plot, λ_{FA} approximately linearly increases with the increasing fibre volume fraction. This effect is due to a combination of statistical noise and fibre intersections, as discussed below in section 3.1.5.

Fig. 3.9 shows the cross-sections of the surface shown in Fig. 3.7, corresponding to fibre volume fractions of 0.1, 0.2, 0.3 and 0.4, as a function of fibre orientation angle θ.

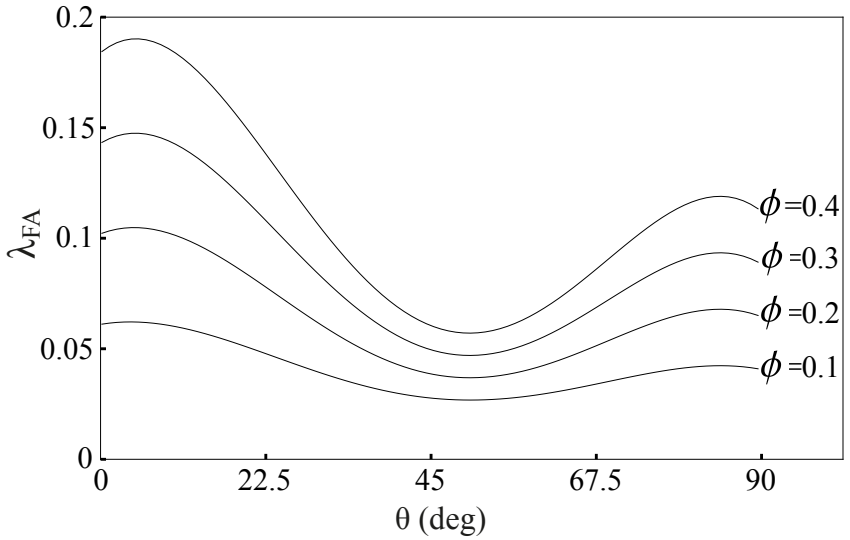

Figure 3.9: Cross-sections of the 3D plot shown in Fig. 3.7 showing the fractional anisotropy as a function of fibre orientation for fibre volume fractions 0.1, 0.2, 0.3 and 0.4. The values show a similar θ dependency as the square of the second Legendre polynomial (Eq. (3.7)).

3.1.5 Discussion

Diffusion of water in restricted environments

In bulk water, the distribution of displacements of water molecules undergoing diffusion is Gaussian and has a spherical symmetry [22]. In isotropic environments where diffusion is restricted (e.g. by macro-molecules with no particular ordering) the amount of restriction is dependent upon the volume fraction of the obstructing molecules.

In tissue such as brain white matter, muscle, eye lens tissue or articular cartilage, diffusion is restricted in some directions more than others due to anisotropic alignment of the cells or fibres. In such situations, molecular diffusion is characterised by an anisotropic diffusion tensor. In the case of brain white matter, the water molecules diffuse both within the myelin sheaths and in the surrounding tissue [139]. The corresponding diffusion tensor is a complex combination of the diffusion tensors related

to each of these compartments. AC fibre networks, on the other hand, are single-compartment, with the water diffusing only in the interstitial volume [132].

The diffusion tensor corresponding to any 3D volume contains information about the average diffusivity, the degree of diffusion anisotropy, and the principal directions of the diffusion ellipsoid within that volume. In the context of AC, the diffusion tensor is determined by the collagen volume fraction, the average alignment of the fibres, and the preferred direction of fibre alignment.

In the present study, the superficial zone of AC was modelled by aligning the fibres with the transverse plane as shown in Fig. 3.1. The middle, or transitional zone, was modelled using fibres rotated in groups of four about the $+x$, $+y$, $-x$ and $-y$ axis respectively in order to maintain axial symmetry as shown in Fig. 3.1 (also see section 3.1.3). The radial zone was modelled using identically aligned, regularly spaced fibres.

Proteoglycans

Proteoglycans provide the osmotic retention of water to enable the load bearing mechanical properties of articular cartilage [224][171]. They are comprised of many polyanionic polysaccharide chains covalently bonded to a protein core, and are distributed throughout the interstitial volume surrounding the collagen matrix. The concentration of proteoglycans varies throughout the structure of articular cartilage from $\sim 4\%$ near the articular surface to $\sim 7\%$ in the radial zone [155]. Various nuclear magnetic resonance studies indicate that the proteoglycan chains do not have any anisotropic order and consequently have no measurable effect on the fractional anisotropy of the diffusion tensor of water [74][76][225][134]. This is an important observation as it implies that any anisotropy of the diffusion tensor is exclusively due to structural anisotropy of the collagen fibre network.

However, proteoglycans restrict water diffusion, reducing the RMS displacement

of water molecules equally in all directions. For example, a DTI study of water diffusion in proteoglycan solutions by Comper and Williams found that as the concentration of proteoglycan aggregate (PGA) was increased, the effective diffusion coefficient was reduced [171]. In the present study, proteoglycans were not modelled explicitly. Instead, the bulk water diffusion coefficient was used as the basis for calculating the translational motion of the molecules. Although the proteoglycans do not affect diffusion anisotropy, knowledge of their concentration is important for quantitative interpretation of the DT in terms of both the collagen fibre volume fraction and fibre alignment. This is discussed further in Section 3.1.5.

Total diffusion time

In spatially resolved diffusion tensor imaging of AC, typical diffusion times (Δ) range between $5\,ms$ and $30\,ms$, resulting in RMS water molecule displacements of between $3\,\mu m$ and $12\,\mu m$ [74]. As this is much larger than the average separation between the collagen fibres, spatially resolved DTI measurements in AC can be said to sample the asymptotic long-Δ diffusion tensor [54]. For shorter values of Δ, water molecules only diffuse a short distance compared to the length-scale of the tissue structure. In this regime the DT can possess a lower degree of anisotropy than the long-Δ DT because the diffusing molecules have an insufficient time to fully sample the fibre network [76]. Another factor affecting the time dependence of the DT is the disorder correlation length with the onset of the long-Δ regime occurring at smaller diffusion times for more ordered structures [226].

To successfully model the local DT in cartilage, the duration of the diffusion simulation must therefore be large enough to allow the water molecules to sample a sufficient number of collagen fibres. In the present study, for networks with identically aligned fibres up to radius of $65\,nm$, and most partially aligned networks of fibre radius $50\,nm$, the diffusion time $\Delta = 0.1\,ms$ was chosen ($0.2\,ps$/step for 5×10^8 steps),

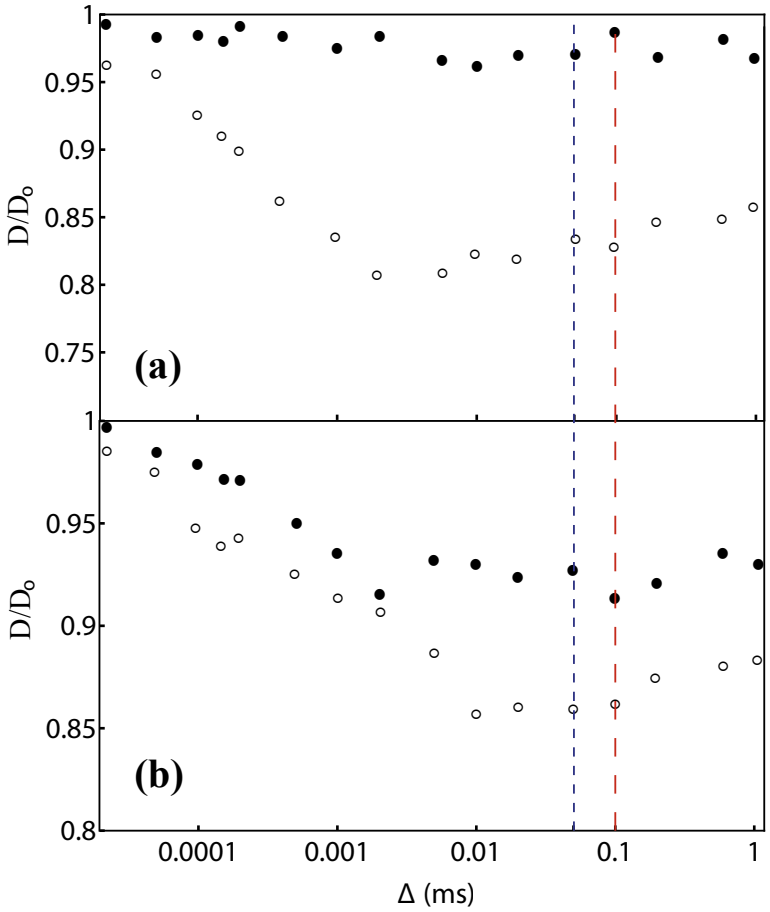

Figure 3.10: Time-dependent eigenvalues of the diffusion tensor of water in model articular cartilage. The solid and the hollow circles are the normalised longitudinal (D_l/D_o) and the transverse (D_t/D_o) diffusivities, respectively: (a) identically aligned fibre networks with a fibre volume fraction $\phi = 0.197$. The red (large-dashed) line indicates the diffusion time used to compute the diffusion tensors for the aligned networks as shown in Section 3.1.4. (b) Networks with fibres oriented at 45° with a fibre volume fraction $\phi = 0.214$. The blue (small-dashed) line indicates the diffusion time used in Fig. 3.5 for partially aligned fibre networks.

leading to an average RMS displacement of $(620 \pm 20)\, nm$. All other structures were simulated using a diffusion time of $\Delta = 0.05\, ms$ ($0.2ps$/step for 2.5×10^8 steps), resulting in an average RMS displacement of $(430 \pm 30)\, nm$.

Fig. 3.10 shows the time dependent longitudinal and transverse diffusivities for both the identically aligned fibre network of $\phi = 0.197$, and the 45° fibre network of $\phi = 0.214$. The number of tracer molecules for each simulation (N_p) was 10000, and the simulations were run for 5×10^9 steps with a time step of $0.2\, ps$ for a total diffusion

time of $1\,ms$. The plots in Fig. 3.10 demonstrate that the simulations of the present study (indicated by the vertical dashed lines) sample the asymptotic long-Δ diffusion tensor.

The statistical precision of the simulated DT eigenvalues is $\Delta D_i/D_o = \sqrt{3/N_p}$. For the ensemble size $N_p = 10000$, this was $\pm 1.7\%$. We note that the transverse eigenvalues, D_t/D_o, exhibit an apparent growing trend in the region $\Delta = 0.01\,ms$ to $1\,ms$ in both parts of Fig. 10. The variation of D_t/D_o in this range of Δ is within $\pm 1.7\%$, and the apparent trend is therefore of marginal statistical significance. It can be attributed to fluctuations of the fibre density within the simulation volume - an unavoidable artefact of the fibre network construction method described in Section 3.1.3.

Identically aligned fibre networks

Diffusion of water in identically aligned networks of cylinders has been the subject of theoretical [102], Monte-Carlo numerical [102][54], and experimental DTI studies [137]. In addition to partially aligned networks, diffusion in identically aligned networks was also simulated in the present study. This was to enable validation of the model design and simulation parameters, and also expand on the results of previous studies by modelling physically realistic water/fibre interactions.

Fig. 3.5(a) shows both the longitudinal diffusivity, D_l/D_o, and transverse diffusivity, D_t/D_o, for networks of regularly spaced and identically aligned fibres, with the collagen volume fraction of the networks ranging from 0.09 to 0.5. This plot shows that D_l/D_o remains approximately the same for all networks, whereas D_t/D_o approximately linearly decreases with increasing fibre volume fraction.

The values of D_l/D_o are close to 1 for all aligned networks as both the free

and bound water molecules do not experience obstructions in the longitudinal direction. This is because the calculation of the water/ fibre interaction forces in the LD simulations are directed normal to each fibre axis, and therefore even strongly bound water molecules are free to translate in the longitudinal direction unimpeded. This unobstructed longitudinal diffusivity in aligned fibre networks has been shown analytically [227], in other numerical studies [31][137] and experimentally in DTI measurements of diffusion in aligned cylindrical polyethylene fibres [137].

The decreasing transverse diffusivity shown in Fig. 3.5(a) is due to an increase in transverse obstruction which increases when the collagen fibres are thicker. A linear least squares fit to the simulated transverse diffusivity, D_t/D_o, resulted in the equation, $D_t/D_o = -0.6\phi + 0.963$.

This is similar to the result observed by Johannesson and Halle, [102], who performed random-flight particle simulations in a square array of cylinders. In the same paper, they demonstrated the applicability of the multipole method developed by Lord Rayleigh in 1892 [26], which gives for the normalised transverse diffusivity:

$$\frac{D_t}{D_o} = \frac{1}{1-\phi}\left(1 - \frac{2\phi}{1+\phi-0.3058\phi^4}\right) \tag{3.6}$$

The large-dashed line in Fig. 3.5(a) shows the values of Eq. (3.6) for $\phi < 0.5$ and is an excellent match to the results of transverse diffusivity in aligned fibre networks from the simulations of the present study.

The increase in transverse obstruction is also demonstrated as an increase in the fractional anisotropy of the DT shown in Fig. 3.8(a). A least-squares fit of a linear function to the simulation results gave $\lambda_{FA(A)} = 0.43\phi + 0.001$ (Eq. (3.5)). This is comparable to the result from Monte-Carlo simulations, which found $\lambda_{FA(A)} = 0.5066\phi + 0.0046$ [54]. Also, experimental DTI measurements of parallel cylindrical polyethylene fibres were performed by Fieremans et al, and a similar linear increase

in λ_{FA} for volume fractions up to $\phi = 0.55$ was observed of $\lambda_{FA(A)} = 0.46\phi + 0.01$ [137].

These identically aligned model fibre networks are useful for interpreting DTI measurements in the radial zone of AC, where the fibres are predominantly oriented approximately perpendicular to the articular surface (see Fig. 3.1). The approximation of perfect alignment is commonly used to interpret experimental DTI measurements of the radial zone in AC, and corresponds to the largest possible λ_{FA} for a given fibre volume fraction [54]. There is evidence however, that there exists some degree of fibre disorder in this zone [228][229]. In this case, and in the case of the other regions of AC, fibre disorder must be taken into account when interpreting the value of the λ_{FA}.

Partially aligned fibre networks

As alignment disorder is introduced into the fibre networks, two mechanisms combine to reduce diffusion anisotropy. First, obstructions to longitudinal diffusion are introduced by the tilted fibres, leading to a reduction in the longitudinal diffusivity. This reduction is evident from Fig. 3.4(a) and increases as the fibre tilt angle is increased. The second mechanism involves the interactions between the fibre surface and the diffusing water molecules. As discussed earlier, the force vector resulting from interactions between a given water molecule and a fibre surface, $\mathbf{F}_c$, is directed normal to the fibre axis. This means diffusing water molecules will experience a maximum obstructive effect along the direction of this vector. Maximum transverse obstruction will occur when this force vector is aligned with the transverse plane (as in the case of the identically aligned networks). Likewise, maximum longitudinal obstruction will occur when $\mathbf{F}_c$ is aligned with the longitudinal axis (as in the case of the networks with fibres oriented at $90°$). For the partially aligned networks, the transverse component of $\mathbf{F}_c$ scales as $\mathbf{F}_{xy} = \mathbf{F}_c \cos\theta$ where θ is the fibre orientation angle. This variation in the obstructive effect due to partially aligned fibres is demonstrated in the simulation

results for transverse diffusivity seen in Fig. 3.4(b).

In addition to being modulated by structural anisotropy, transverse and longitudinal diffusivity is also sensitive to fibre volume fraction. This is seen from Fig. 3.6 where the slopes of both the D_l and D_t plots are larger for larger fibre volume fractions. Also shown here are the corresponding average diffusivities (large dashed lines) which are smaller for larger fibre volume fractions but remain approximately constant for a given fibre volume fraction.

In the case of the identically aligned fibre networks, longitudinal diffusivity D_l is greater than the transverse diffusivity D_t for all fibre volume fractions as shown in Fig. 3.6. As the fibre disorder is increased ($0 < \theta < MA$), D_l and D_t begin to converge, and become equal when $\theta \approx MA$ (see Fig. 3.5b and 3.6). For fibre orientation angles $\theta > MA$, the order of D_l and D_t is the opposite of the identically aligned case (i.e. $D_t > D_l$). These three cases, which are shown in Fig. 3.5(a), (b) and (c) correspond to prolate, spherical and oblate diffusion ellipsoids, respectively.

As discussed earlier, the alignment of the fibres in the 90° networks is fundamentally different from the identically aligned case. In the 90° aligned case, there are no directions in which the water molecules can diffuse unimpeded (see Fig. 3.5(c)). The orientation of the fibres in this network is similar to the superficial zone in AC [230]. This is reflected in Fig. 3.5(c) where in addition to the decrease in D_t, D_l also decreases with increasing fibre volume fraction.

For networks with fibres oriented at the magic angle, D_l and D_t are approximately equal for all fibre volume fractions as seen in Fig. 3.5(b). This situation corresponds to the case of isotropic diffusion, and occurs when the fibres cause identical obstructions to diffusion in every direction [229][230]. Fig. 3.6, however, indicates that the exact angle where this occurs is not the same for all fibre volume fractions: the orientation of the fibres, θ, at which $D_l = D_t$, tends to be larger at smaller fibre volume fractions. This is demonstrated in Fig. 3.11, which shows the value of θ where $D_l = D_t$ for each

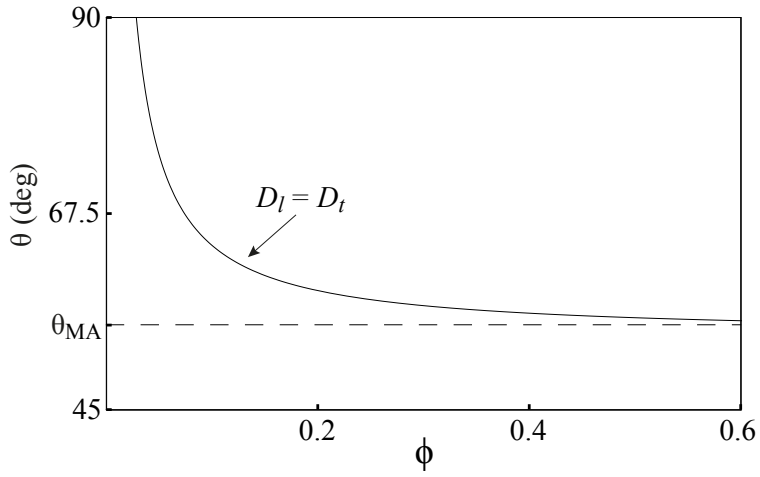

Figure 3.11: Value of θ where $D_l = D_t$ (solid line); the location of the apparently isotropic DT. The dashed line represents the magic angle.

fibre volume fraction. It can also be thought of as the line of intersection of the 3D plots shown in Fig. 3.4(a) and 3.4(b). Fig. 3.11 shows that as the fibre volume fraction is increased, the value of θ corresponding to the apparent isotropy of the DT approaches the magic angle. As this curve represents the intersections of the LSF surfaces of D_l and D_t (Fig. 3.4(a) and (b)), it is ultimately sensitive to the uncertainties in the DT. This means localising the region of maximum fibre disorder in DTI measurements of AC (corresponding to measurements of minimum diffusion anisotropy) is similarly sensitive to the local fibre volume fraction.

The value of fractional anisotropy is invariant to the value of D_o and therefore the proteoglycan content [74][76][225][134]. However, λ_{FA} alone is insufficient for determining the collagen fibre alignment unambiguously. This is seen in Fig. 3.7, where each value of λ_{FA} corresponds to a range of fibre volume fractions and fibre orientation combinations. Therefore, in order to narrow down the value of θ, specific knowledge of fibre volume fraction is required. Furthermore, even when the fibre volume fraction is known, many situations exist where a given value of λ_{FA} corresponds to two possible values of θ. This situation, however, can be removed by using the full DT which can identify if the fibres are oriented at angles less or greater than the magic angle.

The assumption of perfect fibre alignment is approximately applicable to the radial zone of AC. However, the use of this assumption in the interpretation of the DT can result in biased values of ϕ because some degree of disorder is present in the radial zone [130]. Fig. 3.12 shows the sensitivity of the apparent fibre volume fraction to fibre disorder for a given value of λ_{FA}. The dashed line indicates the maximum value of θ for a given λ_{FA}, before the fibre volume fraction, ϕ, varies by an amount greater than 0.025. This suggests that smaller values of λ_{FA} are insensitive to θ and only sensitive to ϕ. For example, an experimental DTI measurements of bovine patella cartilage gave a value of $\lambda_{FA} \approx 0.07$ in the radial zone (after the subtraction of $\lambda_{FA(noise)} \approx 0.05$) [130]. Using the perfect alignment approximation, and the results shown in Fig. 3.8(a), this value of λ_{FA} corresponds to a fibre volume fraction of 0.14 ± 0.02. Comparison of this with the results shown in Fig. 3.12 demonstrates that for this value of λ_{FA}, the assumption of perfect alignment is appropriate, even allowing for substantial fibre disorder ($\Delta\phi < 0.025$ for θ up to approximately 22.5° for $\lambda_{FA} \approx 0.07$).

Fig. 3.9 shows the cross-sections of the 3D plot shown in Fig. 3.7 for four different values of ϕ. This indicates that for any given ϕ within the range examined in the present study ($0 < \phi < 0.5$), λ_{FA} follows a θ dependence similar to the square of the second Legendre polynomial of $\cos(\theta)$:

$$\lambda_{FA} = A\left(\frac{3\cos^2\theta - 1}{2}\right)^2 + \lambda_{FA(noise)} \tag{3.7}$$

where A depends on ϕ, and $\lambda_{FA(noise)}$ is statistical noise as shown below in Eq. (3.8).

Fig. 3.9 shows that the value of the minimum λ_{FA} ($\lambda_{FA(min)}$) increases with increasing fibre volume fraction. This increase is also shown in Fig. 3.8(b). This dependency of $\lambda_{FA(min)}$ on ϕ is due to two distinct mechanisms: (1) $\lambda_{FA(noise)}$, which is a function of the average diffusivity, $\langle D \rangle$ (ϕ), and (2) the anisotropic distribution of

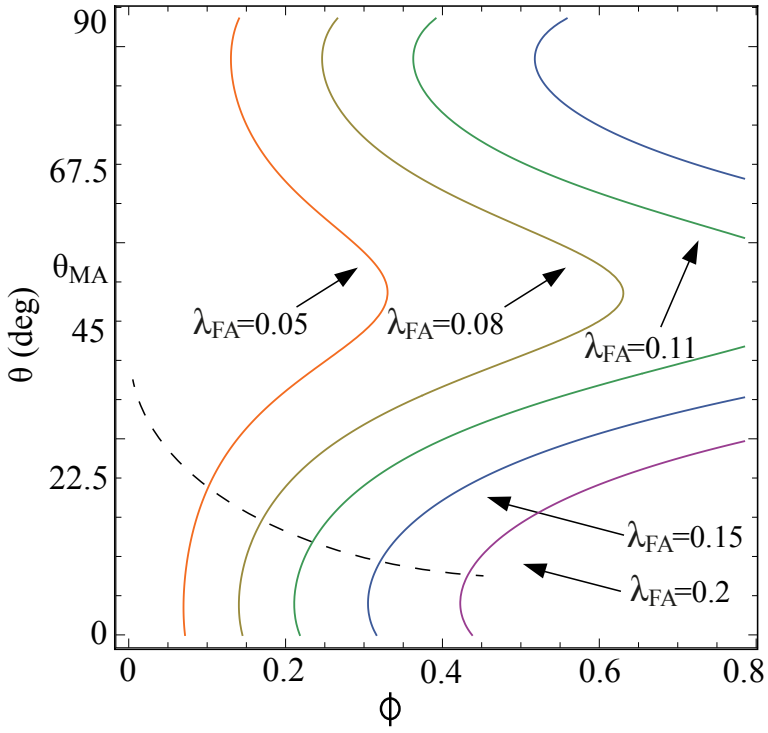

Figure 3.12: Contour plot of the least-squares fit surface shown in Fig. 3.7 for various values of λ_{FA} as a function of θ and ϕ. Under the assumption of perfect alignment, applied to the radial zone of AC, the value of ϕ for a given λ_{FA} is its respective value at $\theta = 0$. The dashed curve indicates the amount of network disorder allowed for a given λ_{FA}, before ϕ deviates from its $\theta = 0$ value by $\phi \pm 0.05$.

fibre intersections which are due to the method of fibre network construction used in the LD simulations (see section 3.1.3).

The noise component of λ_{FA} can be estimated as [221]:

$$\lambda_{FA(noise)} = \sqrt{\frac{3}{2}} \frac{\Delta D(N_p)}{\langle D \rangle (\phi)} \tag{3.8}$$

where $\Delta D(N_p)$ is the standard deviation of the diffusion tensor eigenvalues due to the finite number of water molecules (and measurement noise in the case of experimental DTI), and $\langle D \rangle (\phi)$ is the average diffusivity for a given value of ϕ. Fig. 3.6 shows that the value of $\langle D \rangle (\phi)$ decreases with increasing ϕ. $\Delta D(N_p)$ on the other hand, depends only on the number of tracer particles and is invariant to ϕ. This means that as the fibre volume fraction, ϕ, increases, so does the value of $\lambda_{FA(noise)}$. The magnitude

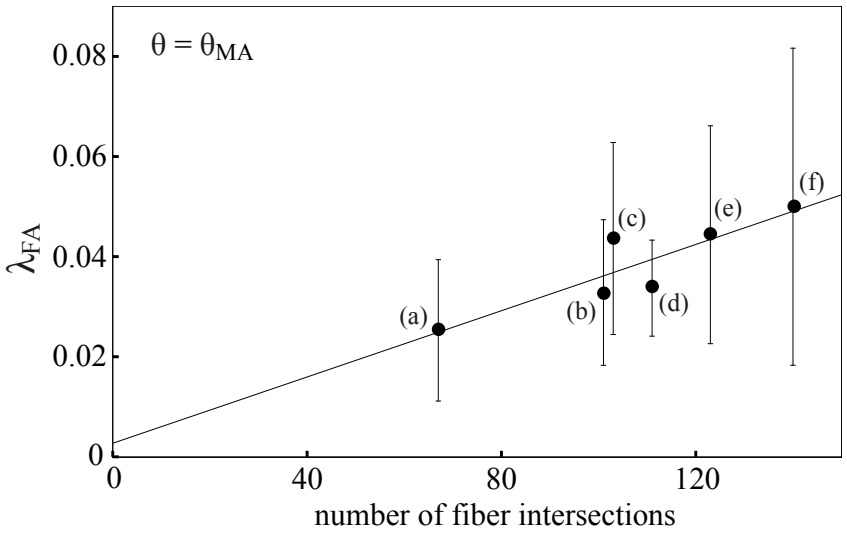

Figure 3.13: λ_{FA} at the magic angle plotted vs the number of intersections for AC networks with fibre radii of: (a) $40\,nm$, (b) $50\,nm$, (c) $55\,nm$, (d) $60\,nm$, (e) $70\,nm$ and (f) $80\,nm$.

of this increase, however, is insufficient to completely explain the magnitude of the dependence of $\lambda_{FA(min)}$ on ϕ seen in Fig. 3.8(b).

The largest contributor to the dependence of $\lambda_{FA(min)}$ on ϕ seen in Fig. 3.8(b), is additional anisotropy due to the presence of fibre intersections. The number of intersections is greater at the larger values of fibre volume fraction. In the case of isotropic fibre networks with non-intersecting fibres, obstruction is the same in all directions and the only non-zero anisotropy is due to noise as shown in Eq. (3.8). In the actual fibre networks used in the present study, fibre intersections were unavoidable and were randomly distributed throughout the simulation volume (see section 3.1.3). These intersections introduced additional diffusion anisotropy as illustrated in Fig. 3.13 which demonstrates the significance of the non-isotropic distribution of fibre intersections on λ_{FA}.

Simplified analytical model

As discussed in section 3.1.5, the multipole model (Eq. (3.6) and the long-dashed line in Fig. 3.5(a)) is a good predictor of D_t for a square lattice of identically aligned fibres for volume fractions up to 0.6 [102]. Combining this with the observation that in aligned fibre networks $D_l/D_o = 1$, the diffusion tensor for a square lattice of fibres aligned with the longitudinal axis, $D_A(\phi)$, can be analytically produced.

The corresponding diffusion tensor for fibres that are not aligned with the longitudinal axis can be produced by performing a unitary rotation of the longitudinally aligned fibre diffusion tensor $D_A(\phi)$ by the desired set of Euler angles (α, β, γ). The diffusion tensor for networks with fibres at many different orientations can then be approximately estimated by integrating over the relevant Euler angles:

$$D' \approx \int\int\int P(\alpha,\beta,\gamma) \cdot U^{\dagger}_{\alpha\beta\gamma} D_A(\phi) U_{\alpha\beta\gamma} d\alpha d\beta d\gamma \tag{3.9}$$

where $P(\alpha, \beta, \gamma)$ is the probability density of fibres having the orientation given by Euler angles α, β, γ; $U_{\alpha\beta\gamma}$ is the corresponding unitary rotation matrix, and $D_A(\phi)$ is the diffusion tensor corresponding to longitudinally aligned fibres of the desired fibre volume fraction, ϕ.

Equation (3.10) shows the result of applying Eq. (3.9) to an axially symmetric network of fibres with a given value of θ ($\alpha = 0..2\pi; \beta = \theta$ and $\gamma = 0$). In this expression, D_l is the longitudinal diffusivity of the aligned fibre network, and is invariant to ϕ ($D_l/D_o = 1$). $D_t(\phi)$ is the transverse diffusivity of the aligned fibre network as a function of ϕ and can be analytically produced using Eq. (3.6).

$$D(\phi,\theta) = \begin{bmatrix} \frac{1}{2}[D_t(\phi) + D_t(\phi)\cos^2\theta & 0 & 0 \\ \quad +D_l \sin^2\theta] & & \\ 0 & \frac{1}{2}[D_t(\phi) + D_t(\phi)\cos^2\theta & 0 \\ & \quad +D_l \sin^2\theta] & \\ 0 & 0 & D_t(\phi)\sin^2\theta \\ & & \quad +D_l \cos^2\theta \end{bmatrix} \tag{3.10}$$

Figure 3.14(a) shows the values of λ_{FA} corresponding to the eigenvalues of Eq. (3.10) for $0^\circ < \theta < 90^\circ$ and $\phi = 0.1$, 0.2, 0.3, and 0.4. In this plot, the value of $\lambda_{FA(min)} = 0$ for all ϕ, which corresponds to an idealised situation where $N_p \rightarrow \infty$. In actual ensemble-based simulations, where N_p is finite, $\lambda_{FA} > 0$ even in isotropic media due to the standard deviations of the DT eigenvalues behaving as $1/\sqrt{N_p}$ [54][221][95]. This results in the "isotropic" λ_{FA} also behaving as $1/\sqrt{N_p}$; we call this lower limit of the simulated value of fractional anisotropy $\lambda_{FA(noise)}$. This behaviour can be seen in Figs. 3.7, 3.8 and 3.9. Similar behaviour is observed in experimental DTI measurements as a consequence of the finite signal-to-noise ratio: Experimentally measured fractional anisotropy of the DT in isotropic saline is usually in the range $0.01 - 0.05$ [74]. $\lambda_{FA(real)}(\phi)$, therefore, represents the "real" fractional anisotropy corresponding to both the simulated and experimental diffusion tensors, and can be considered as a combination of both $\lambda_{FA(ideal)}$ and $\lambda_{FA(noise)}$:

$$\lambda_{FA(real)}(\phi,\theta)^2 = \lambda_{FA(ideal)}(\phi,\theta)^2 + \lambda_{FA(noise)}(\phi)^2 \tag{3.11}$$

By using Eq. (3.10) to estimate the values of $\lambda_{FA(ideal)}(\phi,\theta)$, and Eq. (3.8) to

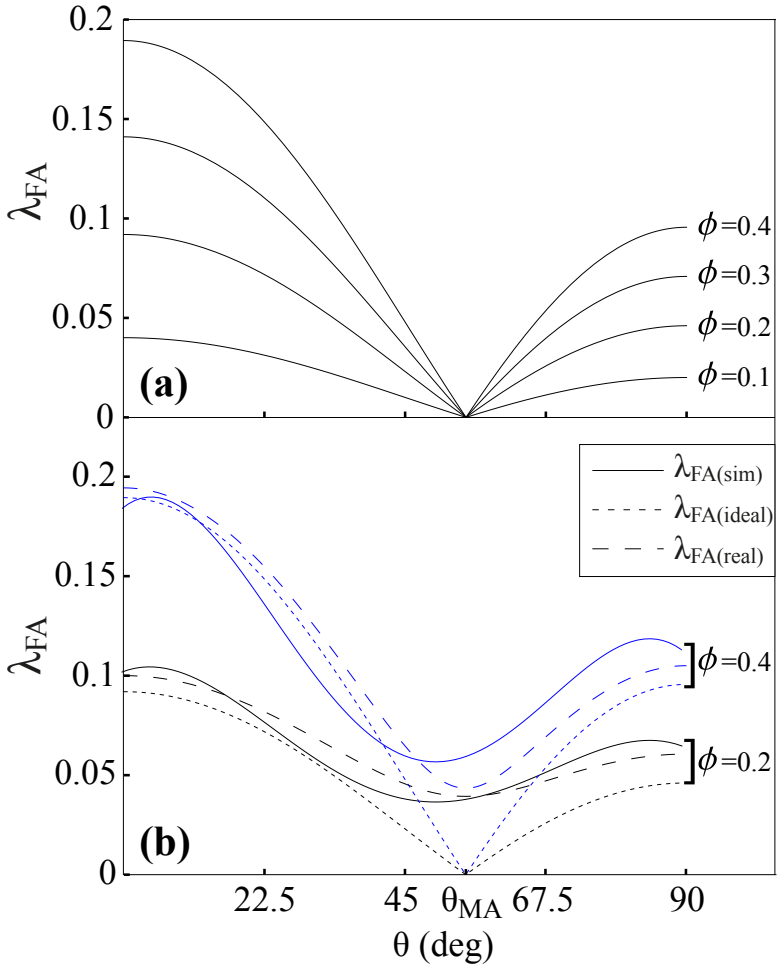

Figure 3.14: (a) λ_{FA} as a function of θ approximated using Eq. (3.10) for fibre volume fractions of 0.1, 0.2, 0.3, and 0.4. D_l and D_t used in Eq. (3.10) were computed using the Rayleigh multipole method (Eq. (3.6)). In all cases, $\lambda_{FA} = 0$ at the magic angle. (b) λ_{FA} of "noisy" diffusion tensors as a function of θ for fibre volume fractions of 0.2 and 0.4: the solid line represents λ_{FA} from the LD simulations of the present study; the small dashed line represents the values of $\lambda_{FA(ideal)}$ estimated from the eigenvalues of the DT estimated using Eq. (3.10); the large-dashed lines are the values of $\lambda_{FA(real)}$ estimated using Eq. (3.11), with the value of $\lambda_{FA(noise)}$ computed using the same ensemble size and fibre volume fractions as the corresponding LD simulations.

estimate the values of $\lambda_{FA(noise)}(\phi)$, an analytical estimate for $\lambda_{FA(real)}(\phi, \theta)$ can be calculated using Eq. (3.11). This is shown in Fig. 3.14(b) for $0^\circ < \theta < 90^\circ$ and $\phi = 0.2$ and $\phi = 0.4$ as the large dashed lines, along with the corresponding values of $\lambda_{FA(ideal)}(\phi, \theta)$. Also shown for comparison are the values of $\lambda_{FA(real)}(\phi, \theta)$ from the LD simulations performed in this study (solid lines).

Interpretation

Experimental DTI measurements of AC produce $\lambda_{FA(real)}$. As indicated in Eq. (3.11), this value is a combination of the anisotropy of the DT caused by the collagen fibres ($\lambda_{FA(ideal)}(\phi, \theta)$), and the anisotropy caused by noise ($\lambda_{FA(noise)}(\phi)$). In order to use theoretical models to interpret experimental measurements of fractional anisotropy in AC, the associated noise, $\lambda_{FA(noise)}(\phi)$, must be subtracted from the measured λ_{FA} value. In the case of experimental DTI measurements, $\lambda_{FA(noise)}(\phi)$ can be estimated as the λ_{FA} in a region of the tissue considered isotropic. For example, a recent study of diffusion in bovine articular cartilage measured $\lambda_{FA} \approx 0.07$ in the superficial zone, $\lambda_{FA(min)} \approx 0.05$ in the transitional zone and $\lambda_{FA} \approx 0.12$ in the radial zone [130]. As the transitional zone is considered as the region of maximum fibre disorder, the measured value $\lambda_{FA(min)} \approx 0.05$ can be considered to be due to noise. The corresponding values of $\lambda_{FA(ideal)}$ in the superficial and radial zones can therefore be estimated as 0.02 and 0.07, respectively. By comparing these values with $\lambda_{FA(ideal)}$ from the simplified analytical model shown in Fig. 3.14(a), the fibre volume fraction can be estimated as $\phi \approx 0.1$ in the superficial zone ($\theta = 90°$), and $\phi \approx 0.16$ in the radial zone ($\theta = 0°$).

This method of estimating fibre volume fraction, ϕ, is only applicable in the "classical" superficial and radial zones, where appropriate assumptions of fibre alignment can be made [230]. As discussed earlier, realistic assumptions of fibre alignment in some regions of AC cannot be made, particularly when considering the changes to fibre alignment in AC which occurs under mechanical load [228]. Given the combined effects of both ϕ and θ on the values of λ_{FA} as shown in Fig. 3.7, quantitative interpretation of experimental DT measurements in terms of tissue microstructure is limited. A possible method to remove this limitation is to use, in combination with the DTI measurements, another magnetic resonance imaging modality such as T_1. As T_1 has been shown to be sensitive to proteoglycan concentration [231][232], an

appropriate calibration model could be developed to relate measurements of T_1 to specific concentrations of proteoglycan throughout the AC. As both the proteoglycans and the collagen fibres restrict molecular diffusion, knowledge of the proteoglycan concentration can then be used to determine the collagen volume fraction in any region of the AC. Once the collagen fibre volume fraction is known, quantitative determination of fibre alignment can then be determined for any region of the AC using the models developed in this study.

The results of the present study are generalisable to other networks of packed impermeable cylinders [102][31][226], subject to the appropriate rescaling of the spatial and temporal variables and maintaining the long-Δ regime. The models developed could be extended to aid in investigations of muscle fibres, neural fibres, and other anisotropic tissue, with the appropriate modifications performed to take into account intracellular diffusion and chemical exchange between intra- and extra-cellular compartments.

3.1.6 Conclusion

In this study, we developed a Langevin dynamics model of diffusion in articular cartilage to investigate the effects of collagen volume fraction and fibre alignment distribution on the diffusion tensor of water. Langevin dynamics was used to compute molecular motion and enable physically realistic modelling of the interactions of the water molecules with collagen fibres and proteoglycans. Simulations of water diffusion in fibre networks of AC were performed for a range of fibre volume fractions and degrees of alignment disorder. We also developed an analytical approach for estimating the diffusion tensor of water corresponding to volumes containing partially aligned cylindrical obstructions. The interpretive models developed in this study relate measurements of diffusion anisotropy to microstructural characteristics such as fibre volume fraction and fibre orientation. The results demonstrate that fractional anisotropy

follows a dependancy on fibre alignment similar to the square of the second Legendre polynomial, with minimum ansitropy occurring at approximately the magic angle. Additionally, longitudinal diffusivity was shown to decrease as the fibres were oriented away from the longitudinal direction; at the same time, transverse diffusivity was shown to increase. It was also found that each measured λ_{FA} related to a range of valid collagen volume fraction/fibre orientation combinations. Specific determination of the tissue micro structure therefore requires knowledge, in addition to λ_{FA}, of either fibre orientation or relevant biopolymer concentrations within the tissue. This information could be accessed experimentally from T_1, T_2 or $T_{1\rho}$ maps, or a combination thereof.

3.1.7 Acknowledgments

This research was supported under Australian Research Council Discovery Projects funding scheme (project number DP0880346). Additional support also provided by the Institute of Health and Biomedical Innovation, Queensland University of Technology (QUT). Supercomputer resources and services used in this work were provided by the High-Performance Computing Centre and Research Support Group (HPC), QUT. We thank Dr Christina Theodoropoulos from the Analytical Electron Microscopy Facility, QUT, for assisting with the scanning electron microscopy imaging of bovine articular cartilage. We thank Mr Garth Brooks and Mrs Stacey Manson (Teys Bros Pty. Ltd., Beenleigh, Australia) for providing samples of bovine patellar cartilage. The authors also thank Nora Tischler, Dr Glen Oberman, and Dr Mark Wellard for many fruitful discussions.

The authors listed below have certified* that:

1. they meet the criteria for authorship in that they have participated in the conception, execution, or interpretation, of at least that part of the publication in their field of expertise;

2. they take public responsibility for their part of the publication, except for the responsible author who accepts overall responsibility for the publication;

3. there are no other authors of the publication according to these criteria;

4. potential conflicts of interest have been disclosed to (a) granting bodies, (b) the editor or publisher of journals or other publications, and (c) the head of the responsible academic unit, and

5. they agree to the use of the publication in the students thesis and its publication on the QUT ePrints database consistent with any limitations set by publisher requirements.

In the case of this chapter:

Computer modeling of diffusion in biological tissues

Sean K. Powell and Konstantin I. Momot, Procedia Information Technology and Computer Science, 3, (2013), 1227-1233

Contributor	**Statement of contribution***
Sean K. Powell QUT Verified Signature Signature 10-9-15 Date	Co-designed the research program, wrote the Langevin dynamics simulation software, generated the collagen fibre force field parameters, and ran all simulations, processed and analysed the data, wrote the paper and discussion.
Konstantin I. Momot*	Co-designed the research program, derived equations of motion, and supervised the research.

Principal Supervisor Confirmation

I have sighted email or other correspondence from all Co-authors confirming their certifying authorship.

Konstantin Momot	Konstantin Momot Digitally signed by Konstantin Momot Date: 2015.09.13 00:58:24 +10'00'	13 September 2015
Name	Signature	Date

3.2 Paper 2: Computer modelling of diffusion in biological tissues

Sean K. Powell and Konstantin I. Momot

School of Chemistry Physics and Mechanical Engineering, Queensland University of Technology, GPO Box 2434, Brisbane, Queensland 4001, Australia

Published in: Procedia Information Technology and Computer Science, 3, (2013), 1227-1233

3.2.1 Abstract

Molecular-level computer simulations of restricted water diffusion can be used to develop models for relating diffusion tensor imaging measurements of anisotropic tissue to microstructural tissue characteristics. The diffusion tensors resulting from these simulations can then be analysed in terms of their relationship to the structural anisotropy of the model used. As the translational motion of water molecules is essentially random, their dynamics can be effectively simulated using computers. In addition to modelling water dynamics and water-tissue interactions, the simulation software of the present study was developed to automatically generate collagen fibre networks from user-defined parameters. This flexibility provides the opportunity for further investigations of the relationship between the diffusion tensor of water and morphologically different models representing different anisotropic tissues.

3.2.2 Introduction

In this work, computer software was developed to simulate water diffusion in model biological tissues. This was to provide quantitative data for interpreting diffusion tensor magnetic resonance images of anisotropic tissue. Diffusion tensor imaging has direct applications in medical research such as brain research [139, 147], biomechanics and organisation of articular cartilage [74, 76], and clinical diagnosis of medical conditions such as stroke, diffuse axonal injury and brain tumours. By using magnetic field gradient pulses for spatial encoding and sensitisation of the signal to diffusion, diffusion tensor imaging can measure the diffusion tensor of water in tissues. The anisotropy of the diffusion tensor is indicative of the presence and degree of preferred alignment of cells, collagen or nerve fibres in the tissues imaged. Current knowledge about the relationship between the measured diffusion tensor and tissue morphology has been developed through the use of diffusion tensor imaging experiments on independently characterised tissues [31, 58, 74], theoretical analysis [218], and computer models [114]. For the present study, molecular water diffusion was simulated using Langevin dynamics in both ordered and partially disordered collagen fibre networks. The resulting diffusion tensors were analysed in terms of their relationship to the structural anisotropy of the model used. The effect of the integration step size on the accuracy of the water dynamics modelling was also investigated. A linear relationship was found between collagen volume fraction and Fractional Anisotropy in ordered cartilage models. It was also found that the introduction of positional and radial disorder into the networks did not appreciably change the diffusion tensor. The simulation software was written in c++ and optimised for processing on multi-CPU supercomputers. It was also designed to automatically generate fibre networks from user-defined parameters, providing the opportunity for the further studies of molecular water diffusion in a range of different anisotropic tissues.

3.2.3 Methods

Langevin dynamics equation

The governing equation for the water dynamics and water-fibre interactions used in the simulation software is given by the stochastic differential equation known as the Langevin equation,

$$m\frac{d^2\mathbf{r}}{dt^2} = \bigtriangledown U_C - \beta\frac{d\mathbf{r}}{dt} + \gamma(t) \tag{3.12}$$

Where m is the mass of the water molecule, and $\mathbf{r}$ is its location. In the context of the present study, this equation describes the net force acting on each water molecule as the sum of three different forces: (1) a quasi-randomly directed force arising from interactions with the surrounding water molecules, $\gamma(t)$ (2) a deterministic external force $\bigtriangledown U_C$, representing interactions with the model collagen fibre walls, and (3) a hydrodynamic friction force, $\beta\frac{d\mathbf{r}}{dt}$

Construction of the course-grained collagen fibre networks and simulation parameters

The molecular structure of the collagen found in articular cartilage consists of a triple helix of polypeptide chains or α chains [233]. This structure is assembled into long fibrils, which are further wound into larger fibre structures. These are cross linked into the matrix network of the cartilage with various degrees of disorder in different regions. To replicate the atomic structure of the larger fibres, the molecular structure of a segment of synthetic human type III collagen was obtained from the Protein Data Bank (Fig 3.15, left) [234]. This was assembled into the outer atoms of a partial cylinder for use in determining the surface interaction potential (Fig. 3.15, center). The forces between a probing water molecule and the surface atoms of the fibre model

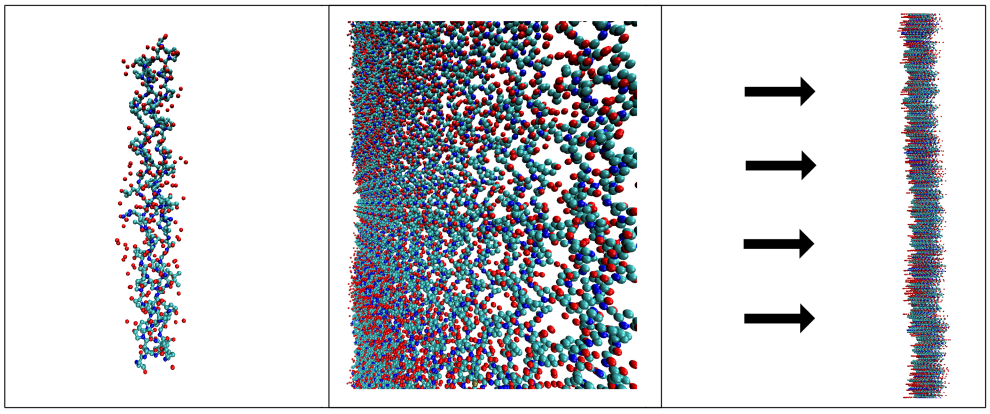

Figure 3.15: (left) a 3D molecular model of a synthetic collagen-like model peptide T3-785 containing a segment of human type III collagen. (mid) 3D image showing assembly of the model collagen fibre outer wall. (right) Profile image of the assembled collagen fibre showing the 'rough' surface at the atomic scale. The arrows indicate the direction of the paths used to compute the interactions between the probing water molecules and the fibre atoms.

were computed at discrete points along a series of paths normal to the surface, out to a distance of $5\,nm$ (Fig 3.15, right). A least squares fit of this data to a standard 6-12 Lennard-Jones potential was then performed.

The model collagen fibres in the Langevin dynamics simulations were represented as smooth walled cylinders. Simulations were run for fibre networks consisting of 8×8 identically aligned model collagen fibres with a regular lattice spacing of $180\,nm$ (Figs. 3.16(a) and 3.16(b)). The radii of the fibres were adjusted to achieve the desired volume fraction. Five simulations were run for each of 10 different fibre volume fractions, using a water molecule ensemble size of $50,000$. Further Langevin dynamics simulations were performed for 30 model AC structures containing 64 aligned $100\,nm$ thick fibres with their individual positions randomly varied. The water molecule ensemble size for these simulations was 5000 (Fig. 3.16(c)). The positional disorder parameter, SP, was computed for each structure as shown in Appendix C, Eq. (C.1). An additional set of Langevin dynamics simulations was performed for the same parameters, but with fibres regularly ordered and having randomly varied radii (Fig. 3.16(d)). The radial disorder parameter, SR, was computed as shown in the Appendix C, Eq. (C.2).

Data I/O and optimization of c++ code for SGI Altix supercomputer

The c++ Langevin dynamics simulation software was compiled and processed on a 1316 CPU core SGI Altix supercomputer. Periodically during the simulation, a molecule displacement file was also output so the latest simulation results were available in the event of unexpected simulation termination. Following completion of each simulation, the net molecule displacements, the molecule paths, and fibre models were output to data files for calculation of the diffusion tensors.

Simulations of water dynamics in cartilage structures

The Δt t for all simulations was $250\,fs$ and the number of simulation steps was $40,000,000$ for a total simulated duration of $10\,s$. Each simulation volume was $1.44\,m^3$ and periodic boundary conditions were implemented to optimise processing time and memory requirements. The longitudinal direction was defined as parallel to the axis of the model fibres. The net displacements of the water molecules were used to compute the diffusion tensor according to the established methodology [114]. Fractional Anisotropy was also computed using the methodology shown in Momot (2011) [114]. Multiple fibre networks were processed in parallel on the supercomputer with a total simulation processing time for each fibre network of approximately 20 hours.

3.2.4 Results and Discussion

The effect of integration step duration on computer simulation accuracy

The differential equations that govern molecular motion in Langevin dynamics simulations are integrated at discrete time steps, resulting in numerical errors. If the time step is too large, unrealistic modelling of the molecular dynamics occurs. However, to optimise processing efficiency it is desirable to make the step size as large as possible.

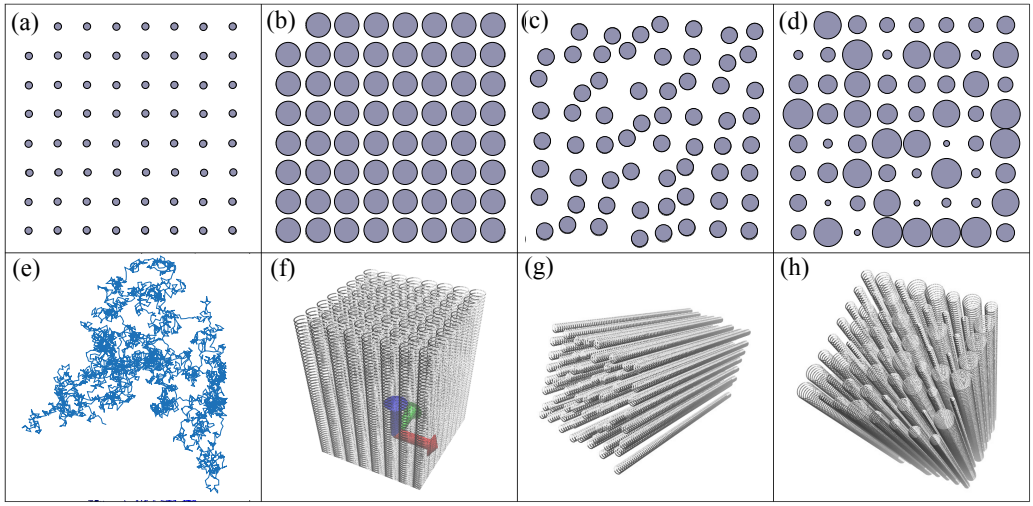

Figure 3.16: Top views of the simulation volume showing the arrangement of the model fibres for: (a) ordered networks with the smallest fibre volume fraction, (b) ordered networks with the largest fibre volume fraction, (c) fibre networks with positional disorder, (d) fibre networks with radial disorder. (e) 2D plot showing the trajectory of a water molecule interacting with a fibre wall (large-dashed line on right). Also shown are 3D perspective views of: (f) an ordered fibre network, (g) fibre network with positional disorder, and (h) fibre network with radial disorder.

One dimensional Langevin dynamics simulations were run for the case of a water molecule stepping toward, and interacting with, a model collagen fibre wall. Four simulations were run for Δt values of $0.75\,ps$, $0.5\,ps$, $0.25\,ps$ and $0.1\,ps$. Fig. 3.17 shows the position of the water molecule relative to the fibre wall for $\Delta t = 0.5\,ps$ and $\Delta t = 0.25\,ps$. These results indicate that unrealistic molecular displacements occur for $\Delta t > 0.5\,ps$ due to the water molecules stepping too far into the repulsive part of the Lennard-Jones potential in a single step. At $\Delta t < 0.5\,ps$, the water molecule will remain within the Lennard-Jones potential until it is translated away by a randomly directed force.

Langevin dynamics simulations of water diffusion in identically aligned fibre networks

Fig. 3.18(a) shows Fractional Anisotropy as a function of fibre volume fraction for the case of identically aligned and ordered fibre networks. The error bars are calculated

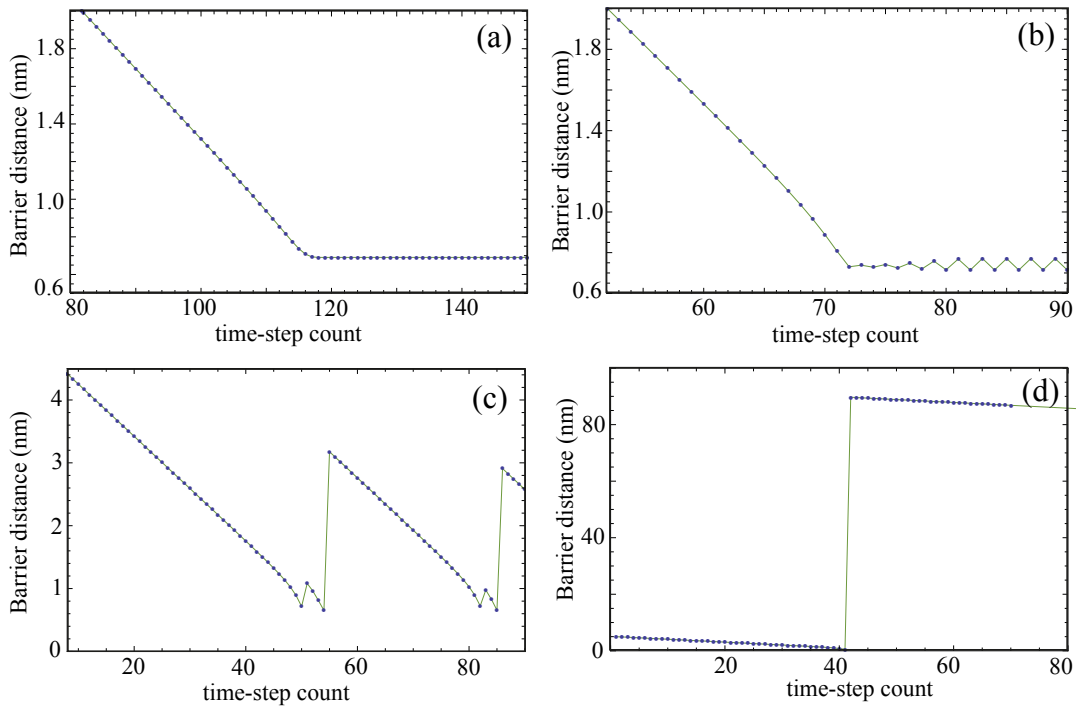

Figure 3.17: Plots showing the position of a 1D stepping molecule with respect to a fibre wall. In each step, the molecule is directed toward the fibre, and also interacts with the fibre potential: (a) integration step duration of $0.5\,ps$. It can be seen that the molecule experience a maximum repulsion at around 55 steps resulting in a displacement of approximately $3\,nm$ in a single step, beyond the effective extent of the water-fibre interaction potential (b) integration step duration of $0.25\,ps$. The maximum repulsion experienced by the molecule is insufficient to displace it outside the water-fibre interaction potential in a single step.

from the standard deviation of the computed Fractional Anisotropy (FA) for 5 sub-ensembles of 10,000 molecules each. A least-squares fit of the data to a linear model resulted in $FA = (0.47 \pm 0.02)\phi + (0.017 \pm 0.004)$. Fig. 3.18(b) shows longitudinal diffusivity remains approximately the same for all values of ϕ, whereas, transverse diffusivity reduces with increasing fibre volume fraction. This is comparable to the results from Monti-Carlo simulations by Momot (2011), which found a linear increase in Fractional Anisotropy of 0.5066ϕ for ordered and aligned model collagen fibres.

Fig. 3.18(c) shows that both longitudinal and transverse diffusivity are invariant to fibre positional disorder up to $SP \sim 0.4$. Fig. 3.18(d) shows that longitudinal diffusivity is invariant to radial disorder. Transverse diffusivity, however, appears to decrease

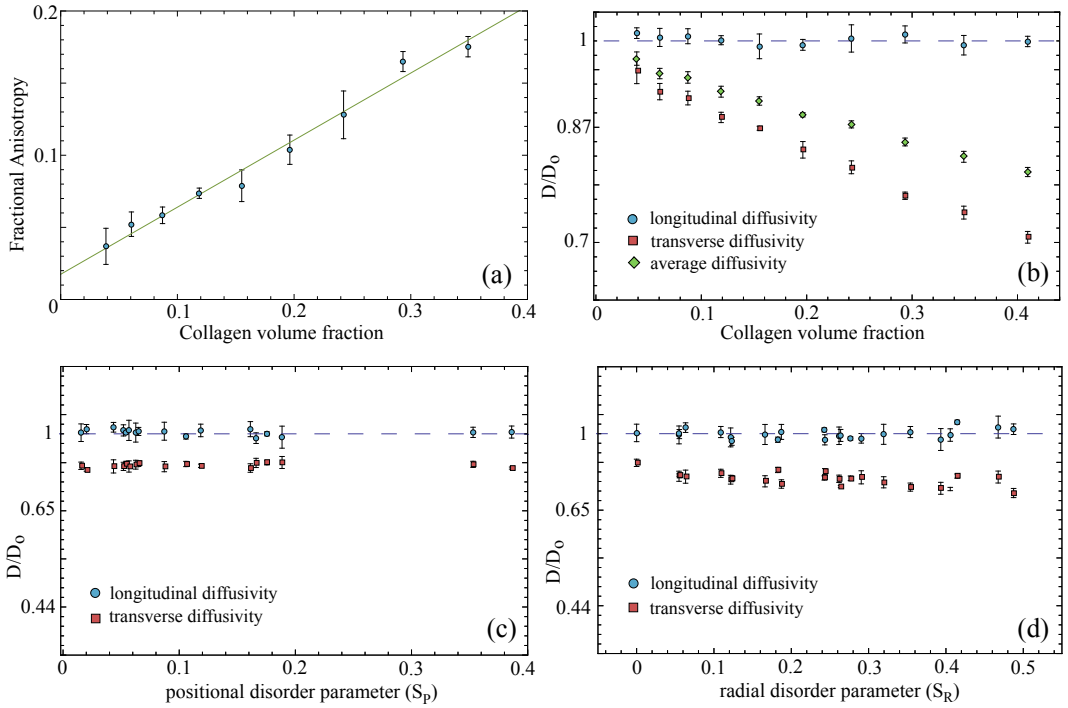

Figure 3.18: (a) Fractional Anisotropy of the diffusion tensor as a function of volume fraction for identically aligned ordered fibre networks. (b) Longitudinal and transverse diffusivity for aligned and ordered fibre networks. (b) Longitudinal and transverse diffusivity as a function of S_P for fibre networks with positional disorder (see Appendix C). The fibres were $100\,nm$ across in all networks. (d)) Longitudinal and transverse diffusivity as a function of S_R for fibre networks with radial disorder (see Appendix C).

with increasing radial disorder. To test if this decrease was due to variations in the fibre volume fraction, an F-test was performed to compare nested linear models. The full model included both volume fraction and radial disorder parameter as predictors, while volume fraction was the only predictor in the reduced model. The null-hypothesis of the test was that there was no improvement in using the full model over the reduced model. The P-value of 0.199 obtained from the test provides no evidence against the null-hypothesis. This means that radial disorder is not needed in addition to volume fraction to explain the variation in fractional anisotropy seen in the simulations of water diffusion in cartilage structures with radial disorder.

3.2.5 Conclusion

Computer simulations of molecular water dynamics provide the key for translating experimental diffusion tensor imaging data into the morphological characteristics of collagenous tissues. The results of this study can be applied in experimental diffusion tensor imaging to the study of microstructure and biomechanics of cartilage and related tissues. Additionally, the Langevin dynamics simulation software developed in this study can be used as a platform for further studies of molecular water diffusion in other anisotropic tissue such as neural fibres, tendons or muscle.

3.2.6 Acknowledgements

This research was supported under Australian Research Council Discovery Projects funding scheme (Project No. DP0880346) and the Institute of Health and Biomedical Innovation, QUT. Supercomputer resources and services were provided by the QUT High-Performance Computing Centre. The authors also thank Nora Tischler and Dr. Glen Oberman, and Dr. Mark Wellard.

Chapter 4

Computing restricted diffusion propagators.

Langevin dynamics and related stochastic modelling techniques are suited for simulating diffusion within periodic structures such as in articular cartilage, and where ensemble averaged and asymptotic long-Δ diffusion results are of interest. However, as these approaches only sample a very small subset of the total number of available diffusing particle trajectories they can only produce relatively 'noisy' diffusion propagators. Consequently, simulations are not ideal for detailed studies of complex or highly tortuous diffusion problems. These limitations motivated the development of the lattice path count algorithm (LPC). This algorithm can be considered as a numerical means for evaluating Wiener path-integrals of Brownian motion. In the path-integral approach, particle transit probabilities are calculated by integrating over all of the possible continuous trajectories, or paths. The LPC algorithm solves these path integrals by exactly counting all paths on a lattice and computing reflecting, absorbing, and semi-permeable barriers by accounting for their effect on path availability. Its physical meaning derives from the observation that the restricted diffusion propagator connecting two locations in time t is proportional to the exact count of length-t paths connecting the locations. Stochastic simulation techniques such as Langevin dynamics only sample a very small subset of the total number of available paths producing propagators with large statistical uncertainty. By exactly counting all particle trajectories on

a lattice using LPC, propagators can be produced that are free of noise. In this chapter, we compute LPC propagators for selected one and three-dimensional restricted diffusion problems. We also compute propagators for highly tortuous percolation systems using both LPC and a finite element scheme. Finally, we apply the LPC algorithm to the problem of aligned collagen fibres of articular cartilage from Chapter 3 and compare the results with corresponding Langevin dynamics propagators. In Appendix D, we further discuss the LPC and a related method, the Markov transfer matrix, to the problem of producing solutions for the quantitative interpretation of diffusion tensor imaging. This work is presented as a journal paper published in Microporous and Mesoporous Materials [12]. The research in the present chapter is presented as an expanded version of a journal article submitted to Physical Review E [11].

The authors listed below have certified* that:

1. they meet the criteria for authorship in that they have participated in the conception, execution, or interpretation, of at least that part of the publication in their field of expertise;

2. they take public responsibility for their part of the publication, except for the responsible author who accepts overall responsibility for the publication;

3. there are no other authors of the publication according to these criteria;

4. potential conflicts of interest have been disclosed to (a) granting bodies, (b) the editor or publisher of journals or other publications, and (c) the head of the responsible academic unit, and

5. they agree to the use of the publication in the students thesis and its publication on the QUT ePrints database consistent with any limitations set by publisher requirements.

In the case of this chapter:

Efficient calculation of restricted diffusion propagators using lattice path counts

Sean K. Powell, Glen J Oberman, and Konstantin I. Momot, Physical Review E, 2015 (in review)

Contributor	**Statement of contribution***
Sean K. Powell QUT Verified Signature Signature 10-9-15 Date	Co-designed the research program, co-developed the LPC method for counting paths, wrote the LPC software, ran all simulations, processed and analysed the data, wrote the paper and discussion. Also wrote the Monte Carlo software, helped solve analytic models and designed and solved the Comsol FEM percolation models
Glen J Oberman*	Proposed iterative method for computing lattice paths, helped solve some of the analytic models
Konstantin I. Momot*	Proposed the idea. Co-designed the research program, co-developed the LPC method, helped solve the analytic models, assisted with manuscript writing, supervised the research.

Principal Supervisor Confirmation

I have sighted email or other correspondence from all Co-authors confirming their certifying authorship.

Konstantin Momot	Konstantin Momot Digitally signed by Konstantin Momot Date: 2015.09.13 01:03:29 +10'00'	13 September 2015
Name	Signature	Date

4.1 Efficient calculation of restricted diffusion propagators using lattice path counts (expanded version).

Sean K. Powell[1] , Glen J. Oberman[2], and Konstantin I. Momot[1]

[1]School of Chemistry Physics and Mechanical Engineering, Queensland University of Technology, GPO Box 2434, Brisbane, Queensland 4001, Australia

[2]School of Mathematical Sciences, Queensland University of Technology, GPO Box 2434, Brisbane, Queensland 4001, Australia

Submitted to: Physical Review E 2015

4.1.1 Abstract

We introduce an efficient and highly accurate algorithm for computing time-dependent propagators of restricted diffusion. Our approach, the Lattice-Path Count (LPC) method, enumerates all available particle trajectories on a discrete lattice while accounting for absorbing, reflecting and semi-permeable barriers. We demonstrate an excellent agreement between LPC propagators and respective analytic solutions for selected one and three-dimensional systems. We also compare LPC with existing diffusion modelling techniques such as Monte Carlo and Finite Element Methods. LPC is also suitable for computing diffusion problems involving concentration gradients and multiple particles with starting points distributed throughout a given pore space. As LPC exactly counts random walks on a lattice, it has potential applications to problems involving path counting beyond modelling restricted diffusion.

4.1.2 Introduction

Restricted diffusion occurs when a diffusing particle encounters obstructions. This process can be characterised by the restricted diffusion propagator, $P(\mathbf{r_o}, \mathbf{r}, t)$, which gives the probability density of finding a particle originally at $\mathbf{r_o}$ at position $\mathbf{r}$ after time t. The shape of the propagator depends on the geometry and topology of the obstructions, as well as the relationship between the correlation length of the pore space, the diffusion coefficient and the diffusion time t [51, 56]. The inverse problem is to infer geometrical information from the diffusion propagator [36, 235]. Approximate solutions to the inverse problem are of considerable interest for characterisation of porous media [29, 236, 237] and tissue microstructure using diffusion-sensitive magnetic resonance [2, 130, 238].

For a small number of simple pore-space geometries, the propagator of restricted diffusion can be computed analytically. More commonly, numerical techniques are used, often taking one of two approaches: solving the diffusion equation through finite-differencing or finite element schemes [239] or simulating individual particle trajectories via Monte-Carlo methods [9, 35, 90]. Numerical solutions can be computationally demanding, however, with accuracy usually entailing long processing times.

Here we present applications of the Lattice-Path Count (LPC) algorithm [12] for the efficient and highly accurate calculation of restricted diffusion propagators. Physically, the LPC approach can be viewed as a discretised means of evaluating the Wiener path integrals for Brownian motion. In the path-integral approach to random walk problems, molecular transit probabilities are calculated by integrating over all possible continuous molecular trajectories, or paths [240]. To illustrate the link between path counts and the diffusion propagator, we first consider an unrestricted, unbiased, one-dimensional (1D) discrete random walk. A diffusing particle starts at $x_o = 0$ and in each time step undergoes a displacement $\Delta x = \pm 1$. During a walk of n steps,

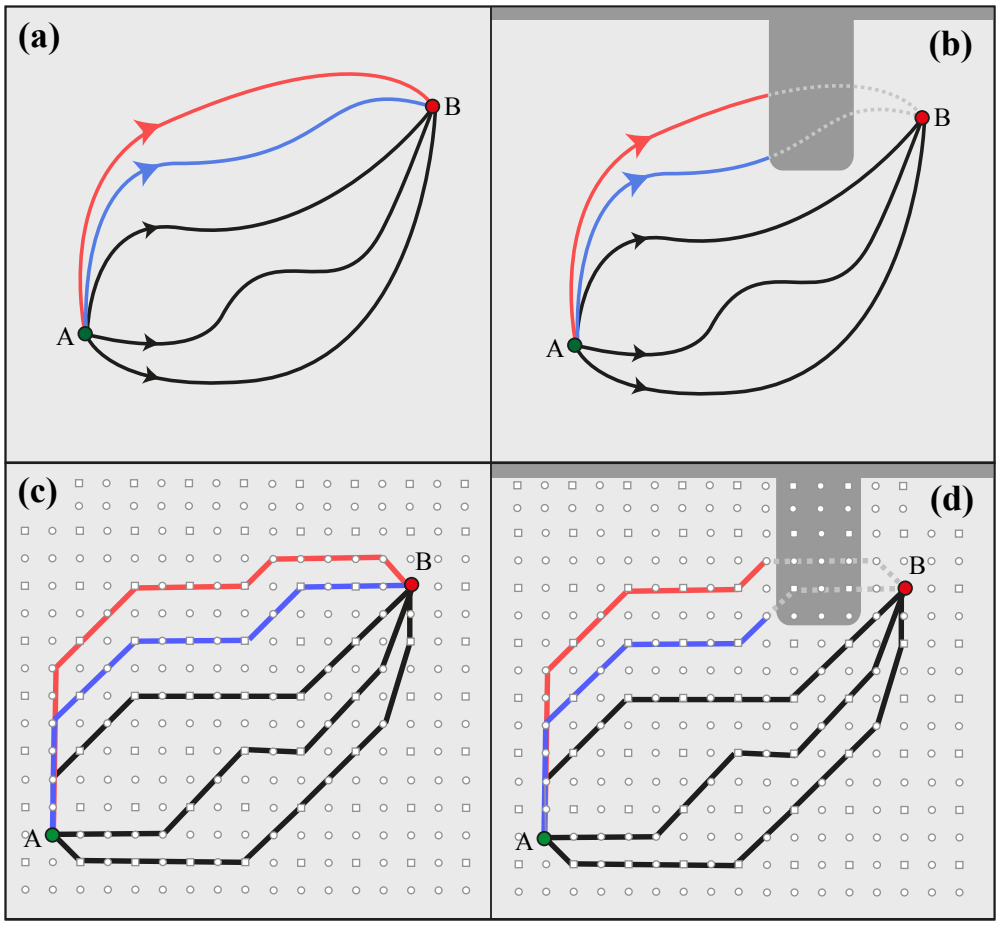

Figure 4.1: Illustration of particle trajectories between locations A and B. (a) the continuous unrestricted case. (b) Some of the trajectories are removed by the presence of an absorbing barrier, (c) a sample of lattice paths of a given length between A and B. Unlike the continuous case, the paths are now countable. (d) The barrier has removed the paths leading to B thereby reducing the number of paths at B.

the particle must take one of 2^n paths, where a *path* is defined as a length-n ordered sequence of positive and negative displacements. At the end of the n-step walk, the final position of the particle can be any of: $-n, -n+2, ..., n-2, n$. For a particle to arrive at a final position x in n steps, it must take a path consisting of $n_+ = (n+x)/2$ steps to the right and $n_- = (n-x)/2$ steps to the left, in any order. The number of paths connecting 0 and x in n steps is therefore $n!/(n_+! \times n_-!)$. Assuming that all 2^n paths are equally probable, the probability for the particle to the have the final position x is,

$$P(0,x,n) = \frac{1}{2^n} \cdot \frac{n!}{\left(\frac{n+x}{2}\right)!\left(\frac{n-x}{2}\right)!} \tag{4.1}$$

It is easily seen that in the limit of large n this equation is equivalent to the well-known unrestricted diffusion propagator in one-dimension:

$$P(0,x,t) = \frac{1}{\sqrt{4\pi Dt}} \exp\left(-\frac{x^2}{4Dt}\right) \tag{4.2}$$

where $t = n$ and $D = 1/2$.

In the following, we extend this approach to the general problem of computing the restricted diffusion propagator within a two-dimensional (2D) and three-dimensional (3D) pore space. We account for obstructions by evaluating their effect on the number of discrete paths available to the diffusing particles and compute an exact path count for a given discrete lattice. A key to the computational efficiency of the LPC approach is that the paths themselves need not be remembered; in fact, having to do so would render the problem infeasible beyond a very modest value of n ($\sim 10 - 20$ for 3D walks). Rather, an iterative approach is employed whereby the diffusion propagator at step n is computed from the propagator at step $n - 1$, after which the previous propagator and the previous path history are erased. Further efficiency is gained by computing and storing the exact path counts using long integers, removing the need for the computationally expensive floating-point arithmetic used in other methods [239, 241]. The use of unlimited-length integers also means that the LPC algorithm doesn't suffer rounding error accumulation as with other methods. These significant optimisations allow solutions for large 2D and 3D lattices containing tens of millions of nodes, making it suitable for the studies of porous media with complex pore geometry. Further, the LPC approach extends naturally to modelling diffusive transport processes, such as the evolution of concentration gradients and diffusion from constant-concentration sources. In its most general form, the LPC method is a means for exactly

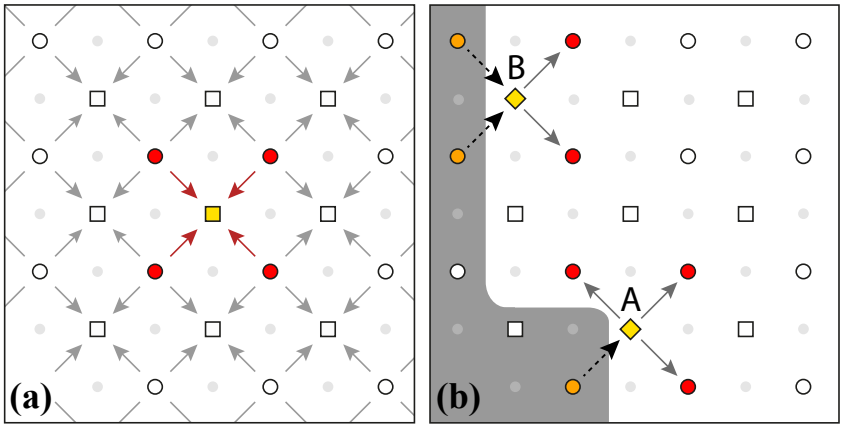

Figure 4.2: The 2D lattice geometry used to describe the LPC approach. (a) The arrows indicate diagonal steps and the operation of Eq. (4.3). The squares represent odd time-steps, hollow circles even time-steps, and small grey circles are unavailable nodes. (b) Reflecting barriers redirect path branches to available liquid nodes as described in Eq. (4.4).

computing lattice random walks. As such, it has direct application beyond diffusion: percolation modelling [5], finance and economics [6], biology [7], astrophysics [8].

4.1.3 LPC method - unrestricted diffusion

We represent the positions available to diffusing particles as a lattice of discrete nodes. In the following we use a 2D square lattice to introduce the LPC methodology, however, the approach is easily extended to other dimensions and lattice geometries.

Unrestricted diffusion in two orthogonal directions is mutually independent. Therefore, in a given time-step a diffusing particle can make a single step to the left or right and, independently, a single step up or down. This results in a jump to any of four diagonal-neighbor nodes, as shown in Fig. 4.2(a). After n time-steps, the path of the particle can be described as a sequence of n diagonal jumps. In each time step, each path branches into four; therefore, the total number of n-step paths originating from a given node of the 2D lattice is 4^n. The number of paths terminating at the node (i, j) in time-step n, $N_{i,j}(n)$, can be calculated as the sum of the numbers of paths terminating at each of the immediate diagonal-neighbor nodes $(i \pm 1, j \pm 1)$ in the

previous time-step, $n-1$:

$$N_{i,j}^{n+1} = \sum_{k,l=\pm 1} N_{i+k,j+l}^{n} \tag{4.3}$$

As a consequence of the diagonal jumps, the values of both i and j are even for each even time-step, and odd for for each odd time-step as illustrated in Fig. 4.2(a). Iterative application of Eq. (4.3) computes the propagation of all paths throughout the lattice. This approach produces the number series known as Pascal's pyramid. Similarly, its 1D application produces the binomial coefficients, or Pascal's triangle. After n time-steps, the normalised 2D unrestricted diffusion propagator is $P_{i,j}(n) = N_{i,j}(n)/4^n$. This propagator can also be obtained analytically using a multidimensional generalisation of Eq. (4.1).

4.1.4 LPC method - restricted diffusion

The LPC method computes propagators of restricted diffusion by introducing obstructions into the lattice. We divide the nodes of the lattice into liquid $N_{i,j}^{L}$ which are available for diffusion, and walls $N_{i,j}^{W}$ which are not. We further identify the subset of the liquid nodes at the interface between the liquid and walls $N_{i,j}^{I}$. The interface nodes can be subject to reflecting or partially reflecting boundary conditions as described below. Through absorption or reflection of the diffusing particles, the walls act to modify the number of available paths. The value of the restricted diffusion propagator is subsequently taken as the normalised number of n-step paths joining two locations after the paths blocked by the walls are eliminated.

Consider, for example, a path arriving at an interface node in time-step n (e.g. node *A* in Fig. 4.2(b)). In time-step $n+1$, the branches of this path continuing through the liquid neighbour nodes are unrestricted, and therefore handled as described above for unrestricted diffusion.

Paths branching into absorbing wall nodes are terminated. We implement this by setting the number of paths arriving at these nodes ($N^W_{i,j}(n)$) to zero in all time steps. Due to the loss of these branches of the path-tree, the total number of n-step paths from a given origin will tend to be smaller than 4^n; the reduction factor being dependent on the relative location of the absorbing wall.

Paths branching into reflecting wall nodes are not terminated but are redirected through all available neighbouring liquid nodes (see Fig. 4.2(b)). We compute this by modifying the number of paths branching into the interface nodes. For an interface node with P neighbouring liquid nodes and Q neighbouring wall nodes, the number of paths branching into each of the interface nodes in time-step n is

$$N^{I,n+1}_{i,j} = \left(1 + \frac{Q}{P}\right) \sum_{k,l=\pm 1} N^{L,n}_{i+k,j+l} \tag{4.4}$$

and $N^W_{i,j}(n) = 0$. Partially-reflecting walls can also be modelled using this approach by adjusting the ratio Q/P. In a similar way, semi-permeable barriers can also be modelled

Iterative application of these equations over the entire lattice for n time-steps yields the LPC restricted diffusion propagator,

$$P^t_{i,j} = \frac{N^{L,n}_{i,j}}{\sum N^{L,n}_{i,j}} \tag{4.5}$$

where the diffusion time t corresponds to the number of discrete time-steps, n.

The LPC approach can also model diffusive transport problems and the evolution of concentration profiles with no additional computational overhead. This is achieved by configuring the initial values $N_{i,j}(0)$ to reflect the desired initial concentrations. The presence of multiple path origins does not increase the computational size of the problem because the number of paths branching from every lattice node must be

counted in every time step, irrespective of where the paths originated. Sources of constant concentration can be modelled by setting the number of paths branching from a given node in time-step n to 4^n (see Fig. 4.6).

4.1.5 Computational considerations

To evaluate the exact path counts and avoid round-off errors, we used integers of unlimited length. Because the path counts scale as p^n, where p is the number of neighbours per node, the computer memory requirements become significant. For example, the number of paths of length $n = 9000$ in the 3D model of Fig. 4.5 is $\sim 6.5 \times 10^{8127}$. We coded all lattice models in c++ and used the GMP multi-precision arithmetic library [242] for arithmetic operations. The models were run on a combination of standard desktop computers and individual SGI Altix XE supercomputer nodes.

4.1.6 Model validation

In order to validate the LPC method, we used selected 1D and 3D restricted diffusion problems with known analytic solutions as test-cases. In each test-case, the restricted diffusion propagators were calculated using the LPC method and compared to the respective analytic solutions.

The first test-case was 1D diffusion between reflecting walls (Fig. 4.3). We placed the walls at $x = 0$ and $x = 4500$, and set the initial concentration profile as a delta-function at $x_o = 2700$. The diffusing particles were allowed to step $\Delta x = \pm 1$, corresponding to the diffusion coefficient $D_o = 1/2$ units^2/step. The diffusion time was $n = 1,500,000$ steps. Figure 4.3 illustrates the resulting propagator, with the inset showing the difference between the LPC model and the analytic propagator (the "residuals plot").

The second test-case was 1D diffusion that was unrestricted in one direction and

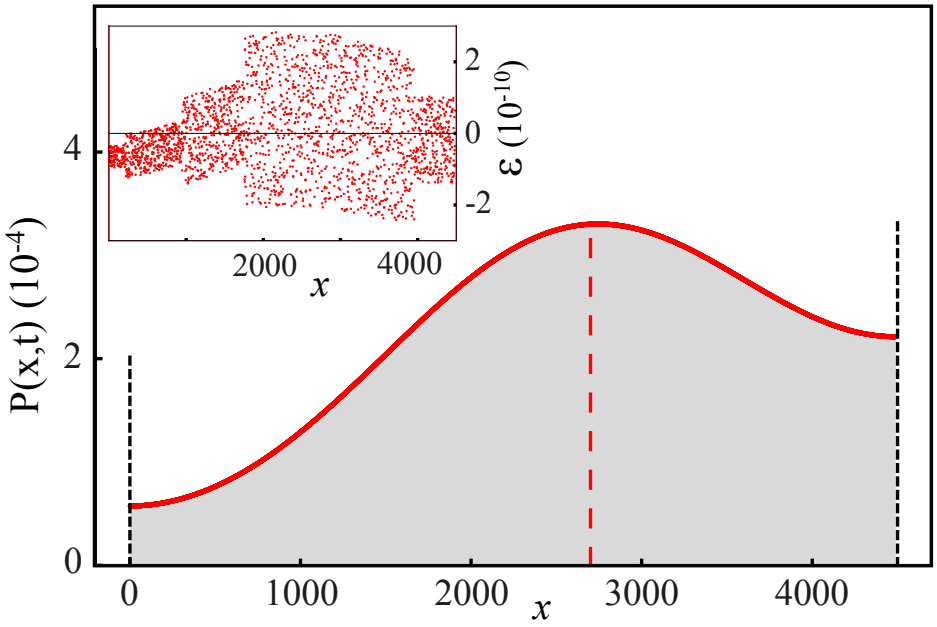

Figure 4.3: Propagators for 1D confined diffusion between barriers at $x = 0$ and $x = 4500$, particle source $x = 2700$ and, diffusion time $n = 1,500,000$ steps. The red line and grey area shows the analytic and LPC propagators, respectively. The inset shows the corresponding residuals plot.

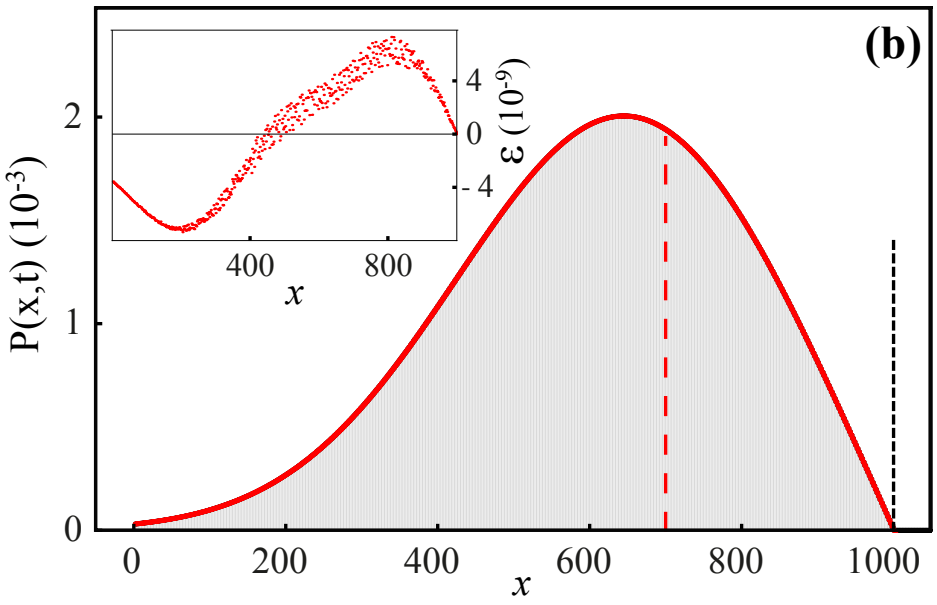

Figure 4.4: Propagators for 1D diffusion with a single absorbing barrier at $x = 1000$, particle source $x = 700$ and, diffusion time $n = 50,000$ steps. The red line and grey area shows the analytic and LPC propagators, respectively. The Inset shows the corresponding residuals plot.

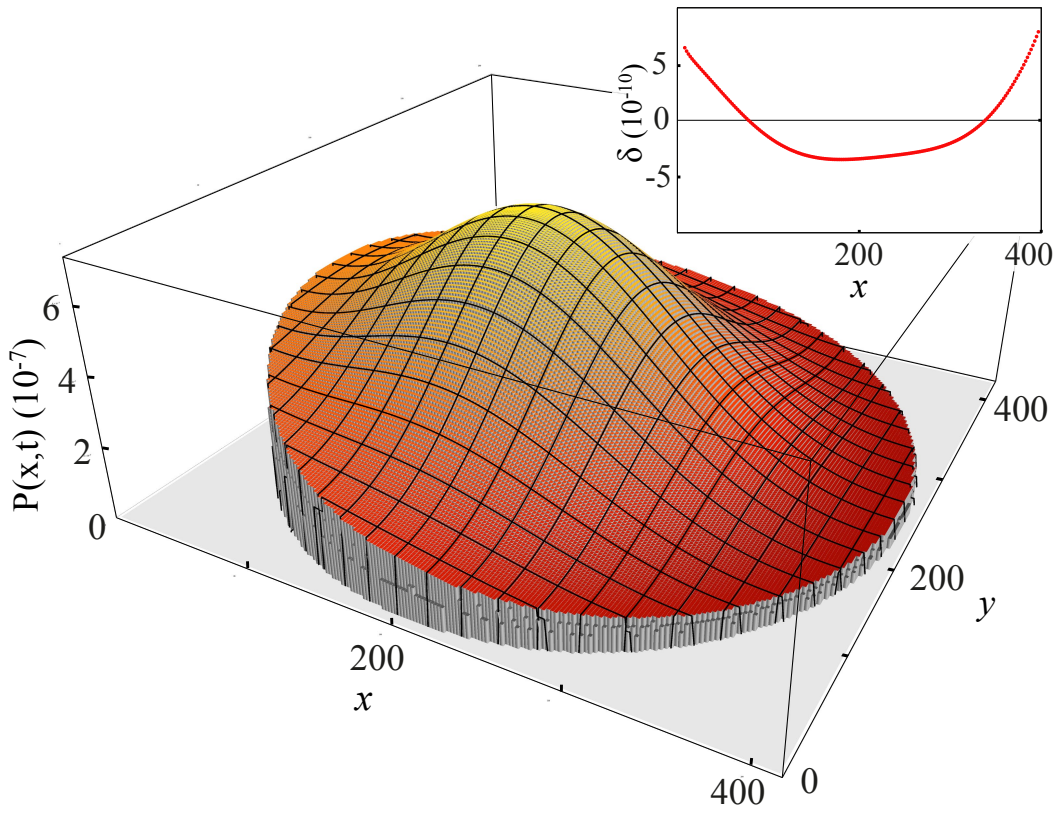

Figure 4.5: Cross section of the propagator at the i, j plane ($k = 0$) for restricted diffusion within a sphere. The initial concentration was offset from the centre by 20%, and the diffusion time was $t = 9000$. The solid lines and vertical bars are the analytic and LPC results, respectively. The inset shows the residuals for the line $0 < i < 400, j = 200, k = 200$.

with an absorbing wall at $x = 1000$ (Fig. 4.4). The initial concentration profile was a delta-function at $x_o = 700$. As with the first test-case, the diffusing particles were allowed to step $\Delta x = \pm 1$, corresponding to the diffusion coefficient $D_o = 1/2$ units^2/step. The diffusion time was $n = 50,000$ steps. Figure 4.4 illustrates the propagator, with inset showing the residuals plot.

The next test case was 3D diffusion within a sphere. We placed the sphere within a cubic lattice of 400^3 nodes and partitioned the nodes between liquid (those within 200 nodes of the centre) and walls (the remaining nodes). The initial concentration profile was a delta-function at $(i, j, k) = (180, 200, 200)$. The step-size $\Delta(i, j, k) = \pm 1$ corresponded to $D_o = 1/2$ units^2/step and the diffusion time was $n = 9000$ steps. We evaluated the analytic solution [243] at the corresponding location of the LPC

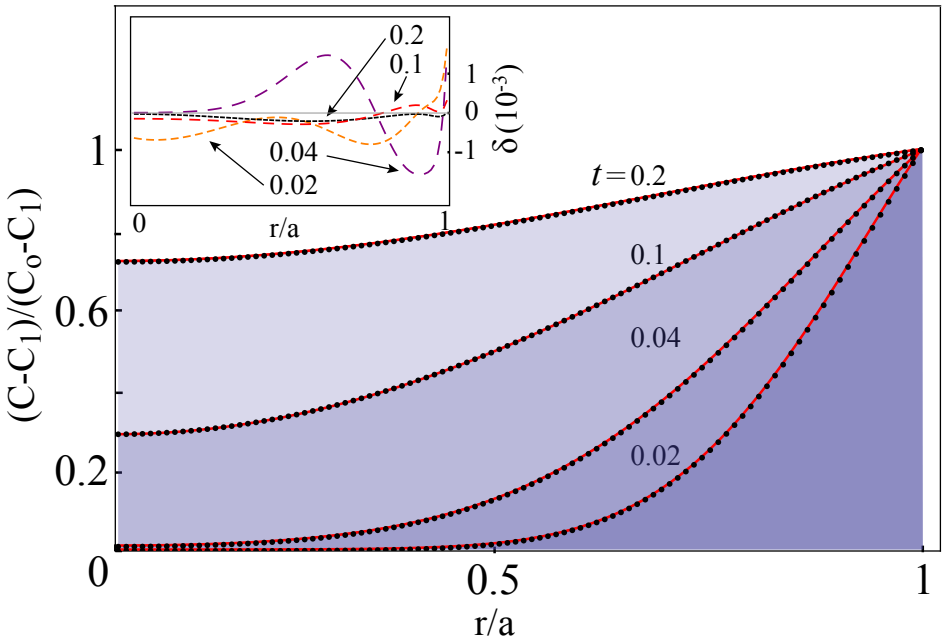

Figure 4.6: Diffusional ingress into an initially hollow sphere with constant surface concentration. The solid lines (red) and black circles are the radial concentration profiles for the analytic and LPC models, respectively. The diffusion times are in units of $t = Dn/a^2$. The inset shows the centred residuals.

nodes. Figure 4.5 shows a cross-section of the resulting propagators in the i, j plane ($k = 0$); the solid lines show the analytic solution, and the coloured vertical bars are the LPC results. The inset shows the corresponding residuals plot for the line $0 < i < 400, j = 200, k = 200$.

The final test-case was diffusional ingress into a sphere from a constant-concentration bath. The initial concentration profile was a spherical void of radius $a = 200$ within a pool of constant concentration. This system was modelled using the same lattice as the second test-case, but with the path counts at the walls scaled in time as $N_{i,j,k}(n) = 8^n$. This was to maintain a constant concentration at the surface of the sphere for all n. We evaluated the analytic solution [22] at the corresponding locations of the LPC nodes. The resulting concentration profiles are shown in Fig. 4.6 for the diffusion times, $n = 1600; 3200; 8000; 16000$. The solid (red) lines and the dots are the analytic and LPC results, respectively. The inset shows the corresponding plot of residuals.

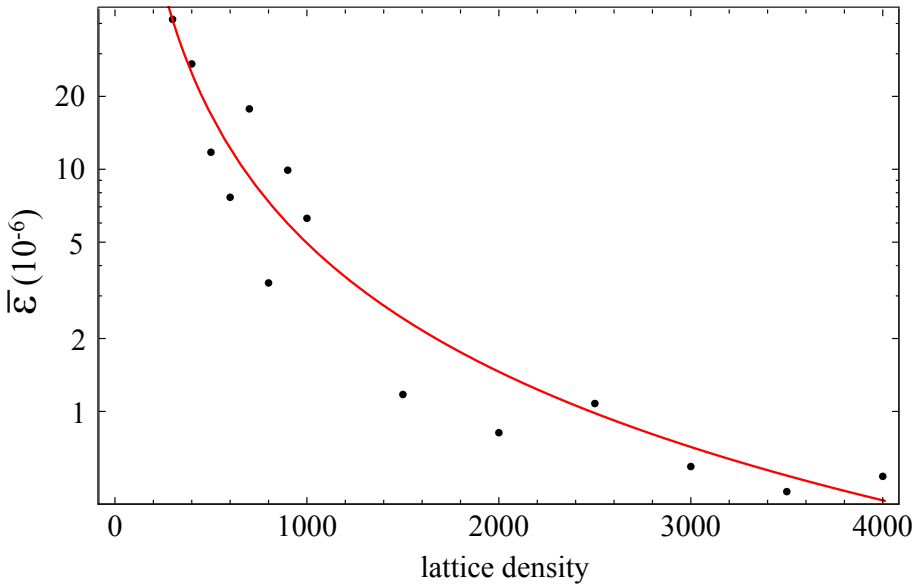

Figure 4.7: The relative residuals (defined as the RMS of residual divided by the mean value of the propagator, σ) as a function of the number of lattice nodes N for the model of Fig 4.3. The solid (red) line is a regression model $\sigma = 0.97N^{-1.764}$.

4.1.7 Discussion

A comparative examination of the results presented in Figs. 4.3, 4.4, 4.5 and 4.6 demonstrates the excellent numerical accuracy of the LPC method. The corresponding residual plots in each of these test-cases indicate that the residuals δ contain both systematic and random contributions. We attribute the systematic errors to the discretisation of space and time of the LPC method, as well as truncation of the infinite sums in the analytic solutions. The random errors, which are approximately proportional to the magnitude of the residuals, are attributed to floating-point rounding. This is particularly apparent in the residuals plot of Fig. 4.3.

The relative magnitude of the discretisation error as a function of lattice density is illustrated in Fig. 4.7 for the case of 1D confined diffusion. As the number of nodes is increased (the lattice spacing is decreased), the relative residuals decrease and the LPC propagators approach the analytic solution. The solid line is a regression model; the empirical fit has the form $\sigma = 0.97N^{-1.764}$. As demonstrated in the residual plot

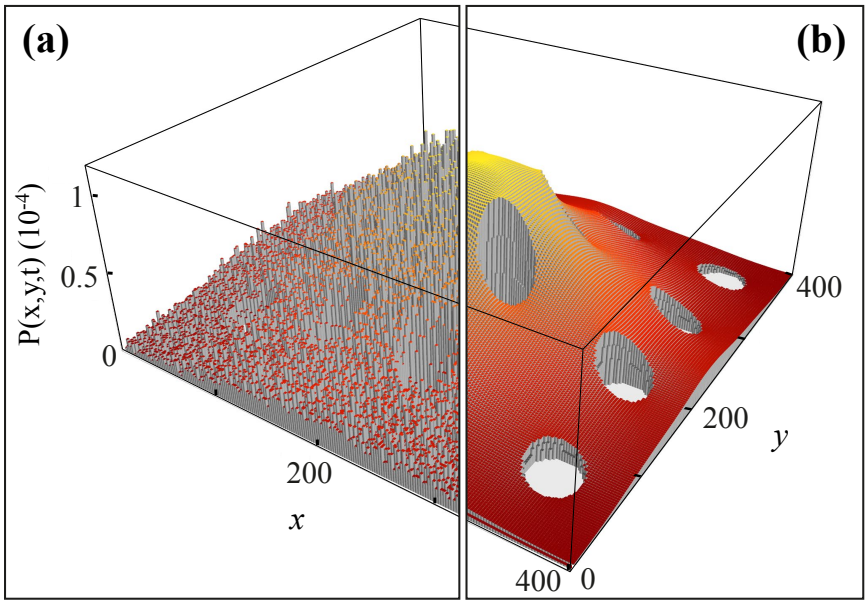

Figure 4.8: Propagators for diffusion within the interstitial volume of a cube containing an array of 16 cylinders; diffusion time $t = 9000$. (a) Monte-Carlo simulation results for 1×10^8 particles. (b) LPC results.

Fig. 4.3 inset (a), the systematic errors become swamped by random numerical errors at a certain lattice density, and further increases in n do not improve model accuracy. However, the random errors are so small that LPC produces propagators free of noise.

This numerical accuracy of LPC compares favourably to stochastic methods such as Monte-Carlo simulations (MC). For comparison we computed propagators for diffusion within the interstitial volume of a cube containing 16 impermeable cylinders using both the LPC and MC methods. No analytic solution is available for this system [90]. For both models, the diffusion time was $n = 9000$ steps. The particle count for the MC was $N_p = 100,000,000$, and the LPC method used a cubic lattice with sides of 400 nodes. The uncertainty in the MC results can be shown to be proportional to the square root of the number of tracer particles and the value of the propagator itself:

$$\Delta P(\mathbf{r},t) \propto \sqrt{N_p} \cdot \sqrt{P(\mathbf{r},t)} \tag{4.6}$$

where N_p is the number of particles in the simulation and $P(\mathbf{r},t)$ is value of the

propagator at location $\mathbf{r}$ after t time-steps. Unlike the MC approach, which computes the particle trajectories individually, the LPC method essentially computes the trajectories of very many particles simultaneously. Consequently, the computation times of both propagators in Fig. 4.8 were similar, despite the marked differences in accuracy: 86 hours for Monte Carlo and 72 hours for the LPC method.

It is often of interest to compute a diffusion propagator for diffusing particles with starting locations distributed throughout a given pore space. This allows sample-averaging of the resulting diffusion metrics to produce net-displacements, in a manner analogous to diffusion sensitive magnetic resonance measurements. Monte Carlo simulation techniques are suited to these scenarios as they simulate the trajectories of tracer particles with randomly starting positions [9, 35]. Deterministic methods such as LPC can also compute sample-averaged diffusion metrics with spatially distributed particle starting locations (see Fig. 4.6). The percolation networks of Figs 4.9(b), (c) and (d) illustrate a scenario where the paths for 300 particles are computed with the starting locations placed along a horizontal line in the centre. The resulting propagators represent the convoluted paths of the 300 particles after $10,000$ steps. Although it is not possible to deconvolve the path counts to produce independent particle propagators, sample-averaged RMS displacements can be computed along the direction perpendicular to the starting line, $\alpha\perp$ via,

$$MSD_{\alpha\perp} = \frac{\sum_{\beta} L_{\alpha\pm\beta} \cdot \beta^2}{\sum_{ij} N_{ij}} \tag{4.7}$$

where α indicates the row of nodes of the starting line, β is an index to the nodes in the direction normal to the starting line, and $L_{\alpha\pm\beta}$ is the sum of the nodes of a given row parallel to the starting line that are exactly $\pm\beta$ orthogonal nodes away.

Using the displacements of particles along several non-collinear directions, the elements of a non diagonal diffusion tensor can be calculated; the minimum number of

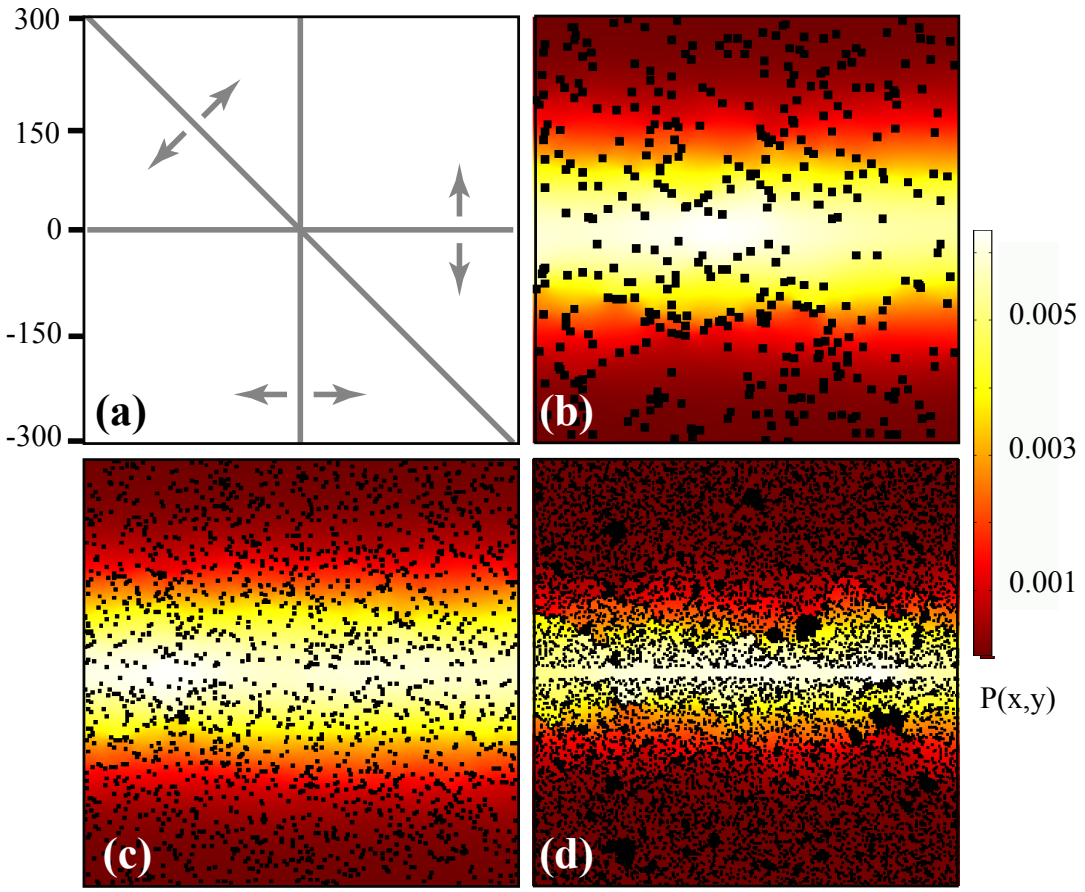

Figure 4.9: LPC propagators for three 2D percolation clusters of increasing complexity. All particles originated along a horizontal line in the centre of each cluster. The black squares indicate reflecting walls. (a) Indicates the starting positions (lines), and the directions (arrows) that need to be computed using LPC to produce a 2D diffusion tensor. (b, c, and d) show the propagators for three 600×600 lattice node percolation clusters of increasing complexity solved using LPC for $10,000$ steps.

directions depending on the spatial dimension. For example, to produce a 2D diffusion tensor for the systems of Fig. 4.9, the RMS displacements along three non-collinear directions are required. LPC can produce this by calculating three propagators with the starting location of the particles set along a horizontal, diagonal and vertical line, respectively, as indicated in Fig. 4.9(a).

Methods such as Finite Element (FEM) and Finite Difference (FDM) are part of a family of algorithms that solve the diffusion equation numerically on a mesh. The algorithms can produce comparable propagators to LPC in that they contain no statistical uncertainty. Their capabilities have significantly evolved over recent decades

and they are capable of producing numerical solutions for pore spaces of arbitrary geometry [239, 244–246]. However, unlike LPC which explicitly models individual particle trajectories, FEM and related methods calculate the time evolution of concentration gradients by solving the diffusion equation on a mesh. Modelling particle concentrations means that FEM methods are affected by floating-point numerical errors inevitably arising in the calculation of the derivatives [239]. Furthermore, FEM schemes are subject to numerical stability requirements in the case of explicit methods placing an upper limit on the size of the time step and potentially further increasing computation time [95]. Implicit FEM are numerically stable and converge, but can be computationally intensive through the need to solve a system of equations in each time-step.

To further explore the performance and stability characteristics of LPC and FEM in highly tortuous geometries, we produced three random percolation systems of increasing complexity. These systems are shown in Figs. 4.9(b), (c) and (d) and are identified as networks A, B and C, respectively. We constructed these networks using custom Mathematica code as 300×300 node lattices with randomly placed reflecting square barriers. Network A contained 200 barriers of 5×5 nodes, network B contained 1000 3×3 nodes, and network C contained 6000 barriers of 2×2 nodes each. After generation, the networks were imported into LPC software and represented as a square 600×600 node lattice. We then propagated all $10,000$ node long paths for each of 300 particles originating along a horizontal line in the centre of each network. The FEM solutions were computed using commercial software (Comsol Multiphysics, Sweden). Each percolation network was imported into Comsol and scaled to 600×600 meters. The element meshing was set to automatically compute at the highest resolution setting of the software. The initial particle concentration was a horizontal line in the centre of the mesh. The diffusion coefficient was $1/2$ meters/second and the solutions obtained for $10,000$ seconds. We used 4th order Runge-Kutta for the explicit method and

Backward Differentiation Formula for the implicit method. For both the LPC and FEM solutions, the vertical RMS displacements were computed via Eq. (4.7).

The LPC algorithm was numerically stable for all three percolation networks yielding RMS displacements of 43.65, 42.09 and 25.57 for network A, B and C, respectively. The explicit FEM approach produced a solution for network A with an RMS displacement of 44.65 using a time-step of $0.01s$. However, the explicit method did not converge with the more complex networks of B and C even with the use of a very small time-step of $0.001s$. The implicit solver was numerically stable for all three networks producing RMS displacements of 44.66, 43.49, and 30.18 for networks A, B and C, respectively. These results highlight the fundamental differences between the FEM and LPC approaches; LPC systematically computing all possible particle trajectories and FEM solving the diffusion equation.

4.1.8 Conclusion

In this work, we detailed an efficient and highly accurate method for computing time-dependent propagators of restricted diffusion in pore spaces containing reflecting and absorbing obstructions. In the context of particle diffusion, our approach can be considered as a numerical means for solving the Wiener path integrals describing restricted Brownian motion. The resulting propagators are shown to be an excellent match to the exact analytic solutions for select 1D and 3D restricted diffusion problems. In its most general form, the LPC approach is a highly efficient means for the exact enumeration of lattice random walks; capable of modelling very large lattices ($> 10^9$ nodes). It accurately accounts for nodes that act to modify path availability, and can model lattices of any dimension and geometry. The results are free from statistical noise and therefore LPC is ideal as a benchmark solution where no analytic solution is available. As lattice random walks are used for modelling a large range of phenomenon, we expect that the LPC method have broad applicability beyond

restricted diffusion modelling.

4.1.9 Acknowledgments

S.K.P. acknowledges financial support from the Institute of Health and Biomedical Innovation, Queensland University of Technology (QUT). Supercomputer resources and services used in this work were provided by the High-Performance Computing Centre and Research Support Group (HPC), QUT. The authors would like to thank Monique Tourell for helpful discussions.

Chapter 5

Diffusion tensor imaging of fibre networks.

The LD and LPC algorithms are each optimised to model restricted diffusion at different spatial and temporal scales. This enables the application of this thesis to encompass a large range of restricted diffusion problems, from intermediate-Δ diffusion in highly tortuous percolation clusters to asymptotic long-Δ diffusion problems in large periodic structures. The physical insights of the theoretical studies also provide valuable knowledge about restricted diffusion in biological tissue. This chapter presents experimental diffusion tensor imaging studies of highly ordered fibre networks. An aim of these experiments is to extend the results of existing DTI studies of anisotropic tissue through the investigation of diffusion within direct-write melt-electrospun fibre networks. We produce networks with spacings in the order of 150 μm to allow investigations of the diffusion tensor within the intermediate-Δ diffusion regime. These results provide valuable experimental data that demonstrates the effect of cross-hatch fibre network architecture on the time-dependent experimental diffusion tensor. In addition to the general aims of this thesis, the paper introduces diffusion tensor imaging as a means for mapping the evolution of the micro-structure and molecular transport pathways in tissue engineering scaffolds during tissue growth. This study is presented as an expanded version of a published journal article.

The authors listed below have certified* that:

1. they meet the criteria for authorship in that they have participated in the conception, execution, or interpretation, of at least that part of the publication in their field of expertise;

2. they take public responsibility for their part of the publication, except for the responsible author who accepts overall responsibility for the publication;

3. there are no other authors of the publication according to these criteria;

4. potential conflicts of interest have been disclosed to (a) granting bodies, (b) the editor or publisher of journals or other publications, and (c) the head of the responsible academic unit, and

5. they agree to the use of the publication in the students thesis and its publication on the QUT ePrints database consistent with any limitations set by publisher requirements.

In the case of this chapter:

Characterization of the Microarchitecture of Direct Writing Melt Electrospun Tissue Engineering Scaffolds Using Diffusion Tensor and Computed Tomography Microimaging

Sean K. Powell, Nikola Ristovski, Sam Liao, Keith A. Blackwood, Maria A. Woodruff and Konstantin I. Momot, 3D Printing and Additive Manufacturing, 1(2), (2014), DOI: 10.1089/3dp.2013.0011

Contributor	**Statement of contribution***
Sean K. Powell QUT Verified Signature Signature 10-9-15 Date	Co-designed the research program, wrote the paper, performed the DTI experiments and analysis, co-produced the electrospun fibre networks
Nikola Ristovski*	Performed the μCT measurements and analysis, co-wrote the μCT discussion, co-produced the electrospun fibre networks, co-developed the electrospin platform
Sam Liao*	co-produced the electrospun fibre networks
Keith A. Blackwood*	co-developed the electrospin platform and fabrication methodology
Maria A. Woodruff*	supervised the production of the electrospun scaffolds, supervised the analysis.
Konstantin I. Momot*	Co-designed the research program and supervised the research.

Principal Supervisor Confirmation

I have sighted email or other correspondence from all Co-authors confirming their certifying authorship.

Konstantin Momot	Konstantin Momot Digitally signed by Konstantin Momot Date: 2015.09.13 01:05:03 +10'00'	13 September 2015
Name	Signature	Date

5.1 Characterization of the microarchitecture of direct writing melt electrospun tissue engineering scaffolds using diffusion tensor and computed tomography microimaging.

Sean K. Powell[1,2] , Nikola Ristovski[1,2], Sam Liao[1], Keith A. Blackwood[1,2], Maria A. Woodruff [1,2] and Konstantin I. Momot[1,2]

[1]School of Chemistry Physics and Mechanical Engineering, Queensland University of Technology, Brisbane, Queensland, Australia

[2]Institute of Health and Biomedical Innovation, Kelvin Grove, Queensland, Australia

Published in: 3D Printing and Additive Manufacturing, 1(2), (2014), DOI: 10.1089/3dp.2013.0011

Special Section on Bioprinting

5.2 Abstract

This paper describes the first steps towards comprehensive characterisation of molecular transport within scaffolds for tissue engineering. The scaffolds were fabricated using a novel melt electro-spinning technique capable of constructing 3D lattices of layered polymer fibres with well-defined internal micro-architectures. The general morphology and structure order was then determined using T_2 weighted magnetic resonance imaging and X-Ray micro-computed tomography (μCT). Diffusion tensor micro-imaging (μDTI) was used to measure the time-dependent diffusivity and diffusion anisotropy within the scaffolds. The measured diffusion tensors were anisotropic and consistent with the cross-hatched geometry of the scaffolds: diffusion was least restricted in the direction perpendicular to the fibre layers. The results demonstrate that the cross-hatched scaffold structure preferentially promotes molecular transport

vertically through the layers (z-axis), with more restricted diffusion in the directions of the fibre layers (x-y plane). Diffusivity in the x-y plane was observed to be invariant to the fibre thickness. The characteristic pore size of the fibre scaffolds can be probed by sampling the diffusion tensor at multiple diffusion times. Prospective application of diffusion tensor imaging for the real-time monitoring of tissue maturation and nutrient transport pathways within tissue-engineering scaffolds is discussed.

5.3 Introduction

Tissue engineering holds great promise for the customised fabrication of 3D tissues and organs. It is a multidisciplinary field which links advanced materials and fabrication technologies with biological agents such as cells and growth factors to produce bio-physical substitutes for the replacement or restoration of lost tissue or organ function [247]. Research strategies can be broadly grouped into three approaches; exogenous scaffold-based fabrication [201], direct cell-based methods [248] and hybrid methods which integrate cells and metabolites with polymer scaffolds during fabrication [182]. Cell-based methods directly fabricate tissue using only living cells, proteins and other biomaterials, often supported within hydrogels [180]. Such techniques include solid free forming, inkjet printing, stereo-lithography, cell sheet lamination and bio laser printing [249–252]. Although the resulting structures have well defined anatomical geometries and specific cellular arrangements [253], their utility can be compromised by a relatively limited mechanical resistance and stiffness [254]. Scaffold and hybrid techniques are capable of producing mechanically stiff engineered tissue constructs suitable for implantation. Their success, however, depends on a very well defined internal micro-architecture that is conducive to the attachment, infiltration, growth and function of the required cells, as well as the facile transport of nutrients and metabolites through the scaffold [255, 256]. Advances in fabrication capabilities are overcoming

these limitations, enabling the fabrication of 3D scaffolds with a highly controlled internal micro-architecture. A thorough understanding of molecular transport dynamics within these scaffolds is one of the key requirements of successful scaffold design.

Electrospinning is a well established method for the fabrication of fibrous scaffolds with random fibre distributions [257]. By combining melt electrospinning with a controllable x-y stage, direct writing of fibres [201] is achieved using fundamentals of additive manufacturing [199]. The use of direct writing processes with melt electrospinning has been successful in producing controlled fibre deposition enabling the fabrication of scaffolds with well-defined 3D architectures. Melt electrospinning is more suitable for biological purposes than conventional fused deposition modelling (FDM) techniques as it can fabricate scaffolds with significantly smaller fibre sizes and therefore higher surface area to volume ratios [258].

Although studies of the penetration rates of cells into electrospun scaffolds exist [257–260], there remains limited research on the quantitative relationship between scaffold micro-architecture and molecular transport. Filling this gap is the overall aim of this research. The objective of this work was to explore the use of magnetic resonance imaging for characterisation of molecular transport within the microstructure of fibre scaffolds. Diffusion-tensor microimaging (μDTI) was used to observe the time-dependent diffusivities and diffusion anisotropy of H2O within 2 melt electrospun scaffolds fabricated with 90 degree cross-hatch architecture. This architecture was chosen as it represents a fundamental building block in advanced electrospun scaffolds comprising complex fibre microstructures. Beyond initial scaffold characterisation, the study aims to identify the required imaging parameters and measurement limitations of diffusion tensor micro-imaging for this purpose. Structural and diffusion anisotropy was characterised through complementary analysis of diffusion tensor and computed tomography microimaging. The long-term aim of this research is to evaluate the suitability of diffusion tensor microimaging for non-invasive, real-time characterisation of

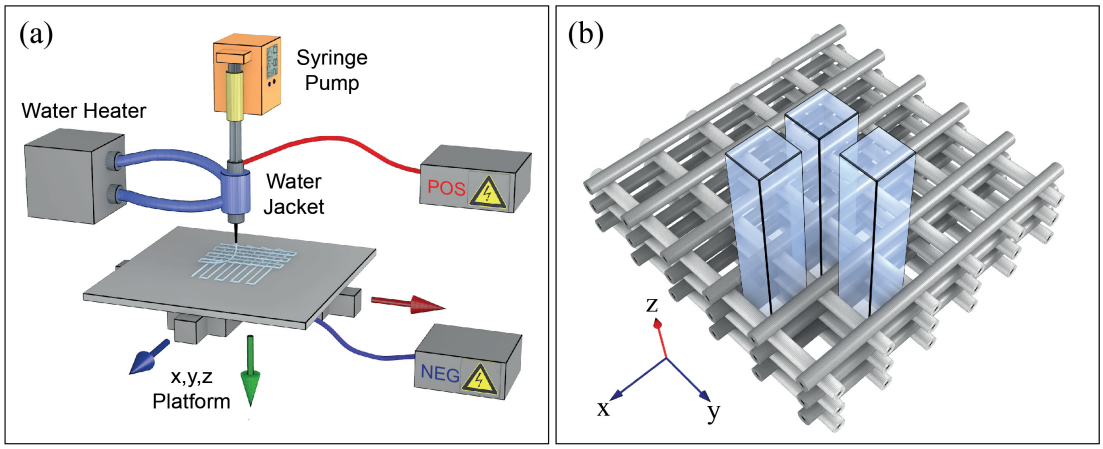

Figure 5.1: (a) Schematic of the melt electrospinning device used to fabricate the test scaffolds. (b) Illustration of the scaffold geometry. The blue rectangular prisms indicate idealised volumes of relatively facile diffusion.

cell growth and the evolution of molecular transport pathways in tissue regeneration applications.

5.4 Materials and methods

5.4.1 PCL scaffolds.

Three-dimensional polycaprolactone (PCL) scaffolds were produced using proprietary melt electrospinning direct writing techniques according to previous methodology [201, 261], with the following changes; PCL (Capa 6400, Perstorp UK Limited) was melted in a syringe at $63^o\,C$. The polymer was pumped at $40\,\mu L/h$ using a syringe pump (World Precision Instruments, AL-1000). Dual powerpacks provided a voltage of $3.5\,kV$ to the tip of the needle and $-7\,kV$ to a metal stage for a total potential difference of $10.5\,kV$. The distance between the tip and stage was kept constant at $10\,mm$. The stage was then moved using computer numerically controlled (CNC) stepper motors controlled via Mach3 (ArtSoft, USA) (see Fig. 5.1(a)).

Two PCL fibre scaffolds, scaffold A and scaffold B, were fabricated using regular fibre spacing of $150\,\mu m$ and fibre diameters of $10\,\mu m$ and $50\,\mu m$, respectively, as illustrated in Fig. 5.1(b). These parameters give projected fibre volume fractions of 0.05 for Scaffold A and 0.26 for Scaffold B.

The scaffolds were produced with horizontal dimensions of $25 \times 25\,mm$ and a vertical dimension of approximately $2\,mm$.

5.4.2 X-Ray micro-tomography (μCT)

PCL scaffolds were dried in a vacuum oven at $50^o\,C$ and $-60\,kPa$ for 6 hours to remove any water pockets. The scaffolds were scanned in air using the μCT 40 microcomputer tomography scanner (Scanco Medical, Brttisellen, Switzerland) at an energy of $45\,kVp$ and intensity of $177\,\mu A$ with $300\,ms$ integration time. Scans were constructed into 3D models using isotropic voxels with a resolution of $(6\,\mu m)^3$ per voxel. The scans were analysed using the distance transformation method to determine pore size and fibre diameter.

5.4.3 Magnetic resonance microimaging

Magnetic Resonance Imaging was performed using a 300 MHz Bruker Avance MR spectrometer with a vertical bore 7 T magnet. A Micro2.5 micro-imaging probe was used with a $15\,mm$ birdcage ^{1}H resonator as the radiofrequency coil (Bruker, Germany) and the system was equipped with a $1.1\,T/m$ triple-axis gradient set. Each PCL scaffold was cut to approximately $1\,cm$ across. Scaffold A was placed in a solution of 5 molar NaOH for 24 hours to enable wetting of the polymer fibre surface. This solution was subsequently flushed and the scaffold was placed in reverse-osmosis water for a further hour. In order to remove air pockets, the scaffold was placed in a vacuum chamber for 1 hour followed by an ultrasonic bath for 30 min. Scaffold B was placed

in the NaOH solution for 48 hours and soaked in reverse osmosis water for 72 hours, followed by vacuum exposure and sonication, with the longer treatment time chosen due to the smaller pore size of this scaffold. The success of the scaffold pre-treatments was confirmed using T_2 weighted imaging as described below. The scaffolds and water were then placed inside a $15\,mm$ Wilmad NMR tube. Teflon plugs were placed above and below the sample to support the scaffolds during imaging as well as restrict the surrounding H_2O in order to maximise the signal to noise ratio. The samples were oriented in the spectrometer so that the scaffold layers (x-y plane) were perpendicular to the magnetic field, B_o. All MRI measurements were made at room temperature.

The scaffold dimensions were measured using MR images; (1) scaffold A: transverse dimensions, $9.5\,mm \times 11\,mm$; vertical dimension (height), $1.7\,mm$. Using the design parameters, this equates to 66 parallel fibres in each layer with ~ 150 layers. (2) scaffold B: transverse dimensions, $11.5\,mm \times 10.5\,mm$; vertical dimension (height), $2.3\,mm$. Using the design parameters, this equates to 73 parallel fibres in each layer with ~ 50 layers.

T_2 weighted axial MR images were acquired for each scaffold using multiple-slice multiple-echo (MSME) imaging pulse sequences (x-y imaging plane, slice thickness of $0.5\,mm$ centred on each sample, in-plane resolution $56 \times 56\,\mu m$, 12 image averages). These images were used to ensure successful hydration prior to the diffusion measurements as well as confirm the successful removal of air pockets by the sample pre-treatment process. (Fig. 5.2(c,d)).

Diffusion tensor images were obtained using a single-echo diffusion-weighted spin-echo sequence. Five evenly spaced vertical slices were imaged with a slice thickness $300\,\mu m$ and in-plane spatial resolution $300 \times 300\,\mu m)$ (image matrix size 100×100; field of view $30 \times 30\,mm$). The repetition time for all measurements was $4000\,ms$. The diffusion tensor was sampled along 20 evenly distributed gradient directions. Three diffusion experiments were performed on each scaffold: (1) diffusion time (Δ) $50\,ms$;

gradient pulse duration (δ) $3.5\,ms$; echo time (TE) $60\,ms$; 6 image averages; imaging time $\sim 14\,hrs$; (2) $\Delta = 200\,ms$; $\delta = 3.5\,ms$; $TE = 210\,ms$; 14 image averages; imaging time $\sim 34\,hrs$, (3) $\Delta = 250\,ms$; $\delta = 3.5\,ms$; $TE = 260\,ms$; 16 image averages; imaging time $\sim 39\,hrs$.

Following imaging, the voxel-specific diffusion tensor was determined using a linearised least-squares fit of the diffusion-attenuation equation [58] to the measured signal amplitudes. This was done using in-house Mathematica (Wolfram Research, Illinois) code based on previously published work [130]. In each imaging slice, two regions-of-interest (ROIs) were selected: a ROI containing only voxels with isotropic saline (used for calibration of the gradient amplitudes) and an ROI with voxels fully contained within the scaffold sample. The eigenvalues (diffusivities) and the corresponding eigenvectors of the diffusion tensor within the scaffold ROI voxels were computed. Histograms of the voxel-specific diffusivities were produced, and the corresponding average diffusivities and standard deviations were computed.

5.5 Results

5.5.1 MicroCT

The 3D images of the μCT scans shown in figure 5.2(a) and 5.2(b) for scaffolds A and B, respectively, shows the 90 degree cross-hatch architecture and relative fibre dimension and spacing. Table 5.1 shows the pore size, eigenvalues of the mean intercept length tensor (MIL), and the theoretical and measured porosity for both scaffolds. Scaffold B, with the thicker fibres, was observed to have a slightly larger pore size. All three MIL tensor eigenvalues were observed to be smaller in scaffold B than scaffold A. The porosities were larger in scaffold A, with a measured value of 83.6% for scaffold

	Pore size (μm)	$\mathbf{H_x}$ (μm)	$\mathbf{H_y}$ (μm)	$\mathbf{H_z}$ (μm)	Theoretical porosity (%)	Measured porosity (%)
Scaffold A	121.9	167.1	161.2	127.6	94.8	83.6
Scaffold B	125.2	147.1	144.6	114.9	73.8	78.5

Table 5.1: Comparative table showing the mean pore size and porosity for each scaffold and the corresponding mean intercept length for each principal axis. H_x, H_y, and H_z are the eigenvalues of the mean intercept length tensor.

A and 78.5% for scaffold B.

5.5.2 T^2-weighted MRI

The cross-hatch pattern of the fibres is clearly visible in the T_2 weighted images of both scaffolds in Fig. 5.2(c,d). On close inspection, the image of scaffold A shows more visible fibres than scaffold B: scaffold A, ~ 50 fibres; scaffold B, ~ 10 fibres. The imaging resolution of $\sim 56\,\mu m$ is similar to the fibre thickness of scaffold B and the transverse fibre separation of $150\,\mu m$ equates is approximately 3 imaging pixels.

5.5.3 Diffusion tensor imaging

Testing of the imaging parameters and data processing software was performed by measuring the DT of bulk water. The resulting averaged eigenvalues were of $(2.3 \pm 0.1) \times 10^{-3}\,mm^2s^{-1}$, $(2.3 \pm 0.2) \times 10^{-3}\,mm^2s^{-1}$, and $(2.29 \pm 0.4) \times 10^{-3}\,mm^2s^{-1}$ for the z, x and y axes, respectively. These values correspond to the accepted bulk water diffusion coefficient of approximately $2.3 \times 10^{-3}\,mm^2s^{-1}$ Figure 5.3 shows the distribution of diffusivities along each principal direction for each scaffold (x, y and z) and for each diffusion time ($\Delta = 50\,ms, 200\,ms$,and $250\,ms$). These probability density plots are based on a smooth kernel histogram estimate of the respective DT eigenvalues.

The average diffusivities for the x-axis and y-axis are approximately the same at

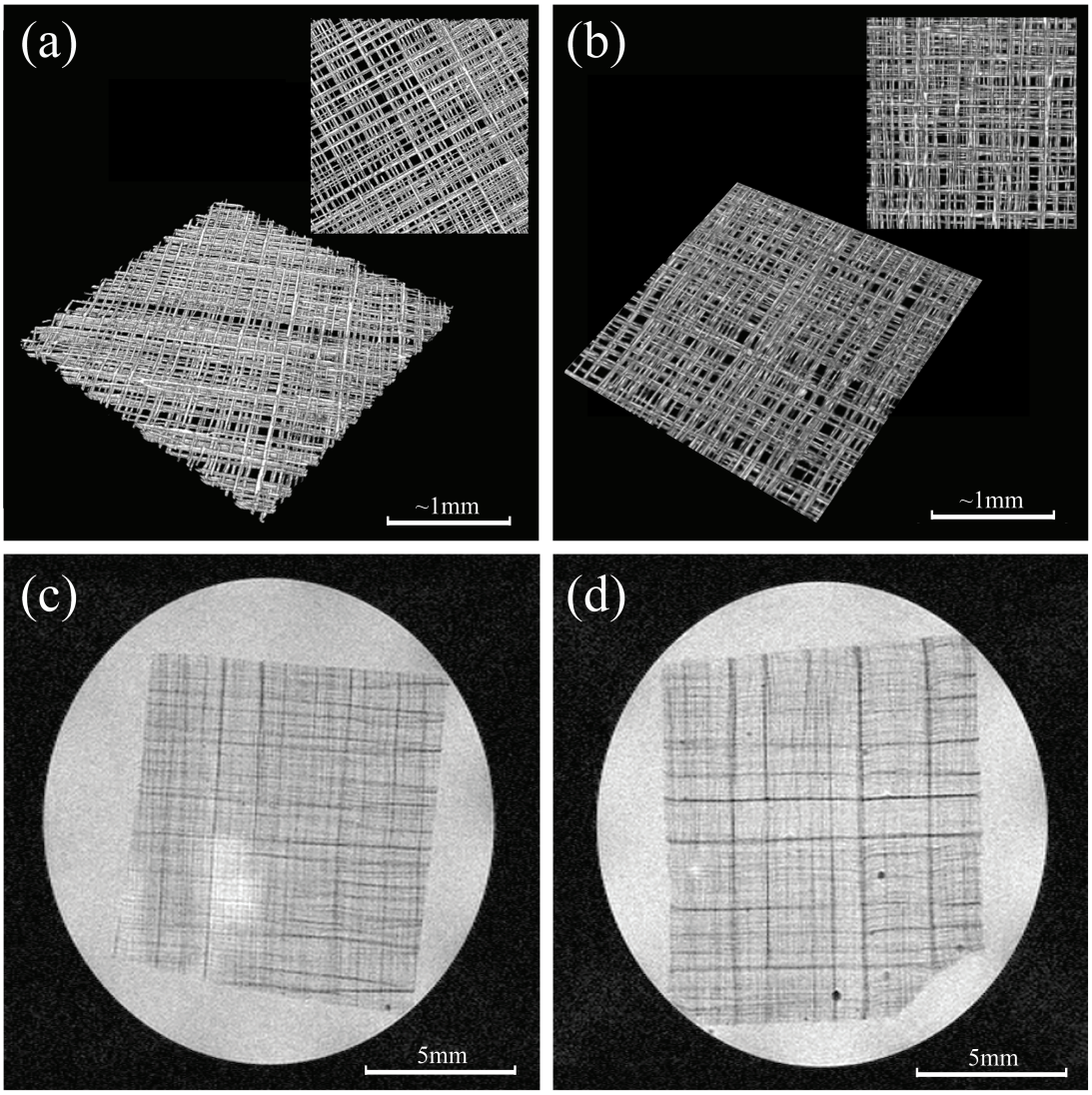

Figure 5.2: 3D images of cropped μCT data: (a) scaffold A; fibre spacing $\sim 150\,\mu m$, fibre thickness $\sim 10\,\mu m$. (b) scaffold B; fibre spacing $\sim 150\,\mu m$, fibre thickness $\sim 50\,\mu m$. Insets show plan views μCT images of scaffold sections. T_2-weighted magnetic resonance images of fibre scaffolds using an axial slices $500\,\mu m$ thick; (c) Scaffold A, (d) Scaffold B.

each Δ. A relative broadening of the distribution of transverse diffusivities is also apparent compared to the vertical diffusivities. Generally, a broadening of the distributions is observed for increasing Δ. This larger variation results from the greater number of interactions between the diffusing water molecules and the scaffold microstructure at longer diffusion times.

The time-dependent diffusivities for both scaffolds are shown in Fig. 5.4. The solid

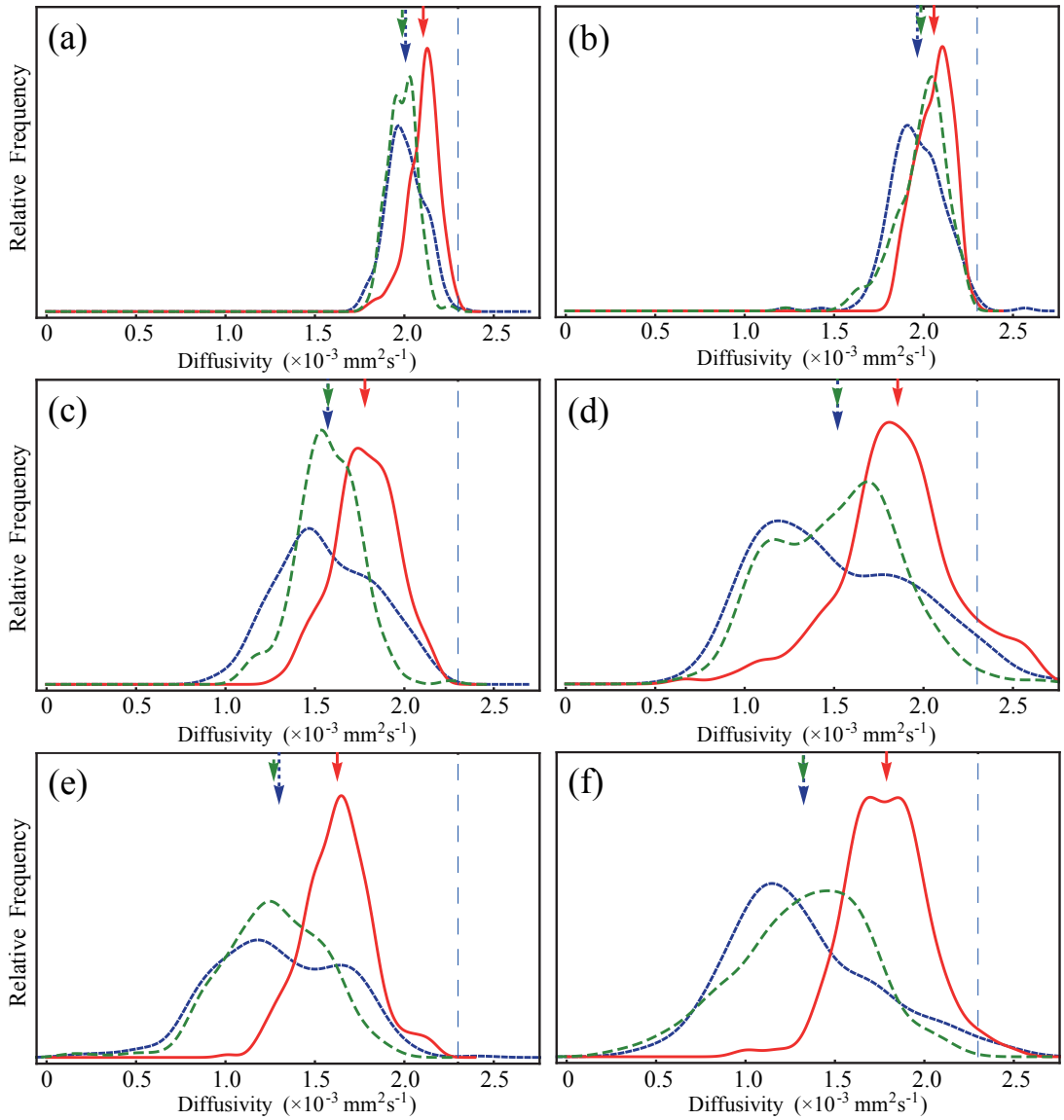

Figure 5.3: Smooth kernel density histograms of the diffusivities along the x, y and z axes shown as small dashed blue lines, large-dashed green lines, and solid red lines, respectively. The arrows indicate the average diffusivity for each axis. The large-dashed grey vertical line indicates the free diffusion co-efficient of water at $2.3 \times 10^{-3}\, mm^2 s^{-1}$. (a), (c) and (e) show the diffusivities for scaffold A at $\Delta = 50\, ms$, $200\, ms$, and $250\, ms$, respectively. (b), (d) and (f) show the corresponding diffusivities for scaffold B.

dots show the average diffusivity along the vertical direction and correspond to the red arrows in Fig. 5.3. The hollow dots indicate the average diffusivity in the transverse plane. The solid and dashed lines are a least squares fit of the diffusivities to a 2nd order polynomial, and are included for illustration purposes.

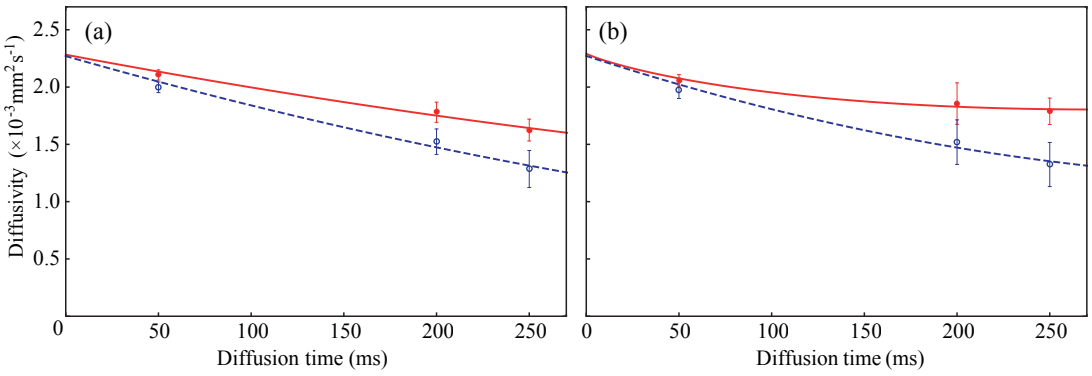

Figure 5.4: The time-dependent diffusivities of the scaffolds. The solid red dots are the diffusivity along the z axis, the hollow blue dots are the average of the diffusivities for the x and y axes. The error bars are computed from the standard deviations. The solid red and dashed blue lines are polynomial least-squares fits to the data for illustration purposes with the 0 ms value chosen to be the unrestricted diffusion coefficient of water ($2.3 \times 10^{-3}\, mm^2 s^{-1}$). (a) results for scaffold A; (b) results for scaffold B.

5.6 Discussion

5.6.1 Electrospun scaffold production

Electrospinning was used in this work to fabricate scaffolds with highly controlled fibre spacing on a scale optimised for diffusion measurements. Melt-electrospinning in direct writing mode builds upon the advantages of other additive manufacturing techniques but, through the use of controlled electric fields, allows the fabrication of structures using fibres with diameters in the tens of micron scale. In the context of tissue engineering, the resulting structures have porosities and surface to volume ratios ideal for cell migration, adhesion and growth [262, 263]. The results shown in Table 1 indicate that scaffolds A and B have pore sizes of approximately $120\,\mu m$, which is in the ideal range for bone cell growth within scaffolds. In addition, the scaffolds have high measured porosities of $\approx 80\%$, which is also desirable for tissue engineering purposes [263].

As the electrospun fibres are guided by electric fields during fabrication, the stability of the fields is an important factor. As the number of fibre layers increase, however, the fields are distorted by charge build up in the fabricated structure. This limits the ability to precisely control the structure order and achieve the desired fibre spacing for thicker scaffolds; ultimately limiting the scale of the scaffolds. For example, scaffolds produced using conventional electrospinning techniques in direct writing mode can produce regular structures at micron scales as demonstrated by Brown et al. [201], however this fibre order is only maintained over relatively few layers, with significant loss of order above $\sim 0.5\,mm$. The scaffolds of the present study were fabricated using an advanced electrospinning platform which enables precise control of the electric potential between the extruder and collector plate. This mitigates the effect of charge accumulation in the extruded layers enabling the production of scaffolds with improved regularity and thickness.

Both scaffolds were fabricated with identical 90 degree cross-hatch architectures and target fibre spacing of $150\,\mu m$, with a fibre thicknesses of $10\,\mu m$ and $50\,\mu m$ for scaffolds A and B, respectively. The cross-hatch pattern was chosen because it represents a fundamental microstructure that can form a building block for more complex scaffolds, as well as its common use in studies of melt-electrospun scaffolds [201, 255, 262, 264]. The fibre separation and different fibre thicknesses were chosen to produce scaffolds with different pore-sizes and internconnectivity. This was to allow investigations into the sensitivity requirements of DTI to observe the effect of pore size on diffusivity and diffusion anisotropy at this scale.

5.6.2 μCT scaffold characterisation

Micro-computed tomography (μCT) imaging is a powerful method for assessing 3-dimensional structures such as scaffolds for tissue engineering purposes. It is a non-destructive method for determining geometric properties such as fibre size, pore size

and porosity. Electrospun scaffolds were assessed using μCT analysis to confirm their geometric properties for evaluation of the results created via MRI scans.

Fibre diameter and pore size were controlled throughout the production of the scaffolds by using the fundamentals of 3D printing. μCT analysis was used to assess this 3D printing technique and its ability to produce highly controlled architecture in the micro-scale range. Data collected was processed using a trabecular bone method; which output fibre diameter, pore size and porosity of the scaffolds. μCT data was also used to assess anisotropy of the scaffold. Anisotropy was assessed via the measurement of the mean intercept length (MIL) tensor.

The results correlate with μDTI results and show that there is no statistically significant geometric difference between transverse axis (H_x, H_y) while there is a significant difference in the vertical axis (H_z). This result is to be expected as the 90 degree cross-hatch architecture should produce identical x and y morphologies. The MIL is measured by randomly orienting vectors of set length through the scaffold. Analysis of the μCT in Figs. 5.2(a,b) suggest that fibres are not perfectly stacked on top of each other, creating a smaller MIL tensor in the axial direction. In addition, the MIL is sensitive to the distance separating the fibre layes. However, it should be noted that although the MIL may describe scaffold morphology, it does not characterise diffusion anisotropy.

Scaffold porosity is an important fundamental factor in tissue engineering, with demonstrated correlations between structure porousity and cell-seeding efficiency [187]. Other important characteristics are the surface to volume ratio and permeability of the scaffold [259]. Melt electrospinning as a direct writing technique shows great promise as a successful tissue engineering technique due to its ability to use electric fields to control fibre deposition, resulting in scaffolds with high porosity and controllable pore size. For fibre layers close to the collector plate, the ordering is very high, with less ordering as the number of layers increases due to charge buildup in the

existing structure. Figure 5.2(a,b) shows small sections of scaffold A and B taken approximately $1\,mm$ from the layer closest to the collector plate. These images show that the electrospinning technique provides a controllable average interfibre distance. μCT analysis of the scaffolds that were produced showed porosities of 83.6% and 78.5% respectively (as shown in Table 5.1). In addition, the average measured pore size for scaffolds A and B was $121.9\,\mu m$ and $125.2\,\mu m$, respectively. Studies indicate that scaffolds with high porosities and high surface-area to volume ratios are desirable for improved cell colonisation and tissue infiltration [187, 262, 265]. For example, one study found that porosities in the order of 90% are ideal for successful tissue-polymer interactions and to allow adequate diffusion during tissue culture in musculoskeletal tissue engineering scaffolds [263]. The ability for μCT to determine porosity without the use of mercury porosimetry or other invasive methods makes it an ideal method for studying samples which are scarce in supply, may be damaged by such chemicals or have poor pore interconnectivity [264].

As μCT can directly measure the geometry of the scaffold, it is also possible to determine a number of other physical properties which are necessary for assessing properties that relate to biological activity. Important physical characteristics that relate to biological activity include: porosity, surface area to volume ratio, interconnectivity, pore size, fibre thickness, anisotropy, apparent surface area and permeability [264]. Micro-CT characterisation is capable of providing these parameters in a non-destructive manner, and a number of studies have categorized the use of μCT analysis against other standard methods of measurement [264, 266]. With the incorporation of μDTI, it is possible to directly measure the geometric properties and the molecular transport within the scaffold, both of which are essential for successful tissue engineered scaffold designs [267].

5.6.3 Diffusion

Diffusion within tissue engineering scaffolds is a fundamental process that enables the transport of oxygen, nutrients and metabolites to and from growing tissue. Quantitative experimental data concerning diffusion within scaffolds is desirable in order to enable the development of predictive models describing the relationship between molecular diffusion and scaffold micro-architecture. It can also enable the modelling of changes in molecular transport pathways due to tissue infiltration into the scaffolds during the growth phase. Theoretical models of restricted diffusion within partially aligned fibre networks have been developed and are a first-step investigation into this problem [29, 51]. The theoretical and experimental models can form the basis for the development of next-generation scaffold designs in order to ensure optimised molecular transport within the regenerating tissue.

Diffusion is a transport phenomenon resulting from the thermally driven random motion of molecules. In the absence of barriers, diffusing molecules displace isotropically with a root-mean-squared displacement given by,

$$\Delta r = \sqrt{6D\Delta} \tag{5.1}$$

where D is the diffusion coefficient of the molecule, and Δ is the time-interval of the diffusion measurement ("diffusion time").

In heterogeneous environments, such as electrospun scaffolds, diffusion is usually restricted. This is particularly the case in the layered electrospun scaffold of the present study; diffusion within a layer of fibres (the x-y plane) tends to be obstructed more than in the z direction. To account for this, diffusion is characterised by an anisotropic diffusion tensor rather than the diffusion coefficient D. The diffusion tensor can be measured in a spatially resolved manner using diffusion tensor imaging (DTI).

This involves acquiring a set of diffusion-weighted images corresponding to different directions of the diffusion gradient. These images are subsequently processed to create maps of diffusion tensors. The eigenvalues and eigenvectors of these tensors describe the magnitude and principal directions of diffusivity, respectively.

Because the diffusion tensor interrogates the geometry and internal organisation of the scaffold, DTI is extremely useful for characterising scaffold internal micro-architecture. Diffusion tensor maps can provide 3D information about fibre spacing, uniformity, and predominant fibre orientation throughout the entire scaffold. Target fibre spacing can be checked by comparing variations in the diffusion tensor between voxels. Diffusion tensor maps are also useful in tractography analysis for mapping fluid channels [9]. For structures with regular internal micro-architectures, such as the scaffolds of the present study, diffusion tensor maps can be replaced with average diffusivity and diffusion anisotropy, as variations in the microstructure are not expected.

Both the μCT MIL tensors and μDTI diffusion tensors for both scaffolds indicate anisotropy, with their principal vectors closely aligned with the z-axis. However, the ellipsoids described by these tensors are very different, with the MIL tensor describing an oblate ellipsoid (Table 5.1) and the DT ellipsoid being prolate (Fig. 5.4). These observations can be explained by considering the different features of the scaffold probed by each technique. DTI measures diffusion and therefore provides direct information about molecular transport within scaffolds. This is in contrast to μCT, which directly images the scaffold structure [265].

The diffusion tensor in restricted environments depends on the diffusion measurement time (Δ). At short diffusion times, only a small fraction of the diffusing molecules will encounter obstructions. Consequently, the diffusion tensor in this short-Δ regime is close to the isotropic bulk-water diffusion tensor and fails to interrogate the geometry of the obstructions effectively. The anisotropy of the DT in this regime increases with increasing Δ at a rate proportional to the surface-to-volume ratio of

the scaffold [35]. Time-dependent measurements of the diffusion tensor within this intermediate regime can therefore provide useful information about scaffold microarchitecture [268]. The opposite extreme is very long diffusion time. In this regime (the long-Δ regime) a large fraction of the diffusing molecules will encounter the obstructions, often many times. The DT in the long-Δ regime eventually reaches an asymptotic value, such that further increase in Δ no longer results in changes in the measured diffusivities. It is in this regime that the DT probes the scaffold microstructure in the most efficient way. The characteristic time at which the transition from one regime to the other occurs depends on the bulk diffusion coefficient and the characteristic length-scales of the pores [35]. As such, it is of interest to take measurements of the DT in the intermediate-Δ regime and observe the rate at which the long-Δ limit is approached. This provides valuable information about the pore geometry, such as the characteristic fibre spacing [268].

The time-dependent diffusivities of the electrospun scaffolds are shown in Fig. 5.4. These indicate that the DTI measurements remain in intermediate-Δ regime. To sample the DT in the long-Δ regime, the RMS displacements of the diffusing molecules would need to be larger than the characteristic pore length. In the present study, the largest Δ achieved was $250\,ms$ which corresponds to an RMS displacement of $59\,\mu m$; below the transverse fibre spacing of $\sim 100\,\mu m$ for scaffold B. Molecular simulations in similar geometries suggest that in order to sample the long-Δ diffusivity, the RMS displacements need to be at least 1.5 times the pore-length [29, 51]. To achieve comparable RMS displacements within the scaffolds of the present study, Δ values of between 1 and 2 seconds are required. These relatively long diffusion times are difficult to achieve due to the decay of the magnetic resonance (MR) signal. One method for overcoming this is to place the scaffolds in a H_2O/D_2O solution to improve the MR signal to noise ratio at longer measurement times. While this approach may be possible for initial scaffold characterisation, it may be unsuitable for scaffold

characterisation during the tissue growth phase due to the effect of the D_2O on the cells. Another option is to measure the long-Δ DT for a given scaffold architecture for use as a benchmark value. This would subsequently allow the intermediate-Δ DT to be used to estimate the long-Δ DT in scaffolds with similar architectures. The advantage of this approach is that the benchmark long-Δ DT can be obtained for a given scaffold architecture in vitro, and long-Δ DT values predicted from the intermediate-Δ DT measurements for similar scaffolds in vivo.

Advanced tissue scaffolds contain multi-scale interconnected pores for both the efficient flow of metabolites and the retention of synthesising cells. These scaffolds are immersed in bioreactors which optimise fluid flow for tissue growth [269, 270]. In areas of high flow-rate, advection dominates and diffusion plays a lesser role in matter transport. However, with the onset of tissue infiltration, the fluid flow through highly tortuous and confined pore spaces becomes restricted and diffusion becomes the dominant transport mechanism. Additionally, diffusion measurements can also be a proxy for the laminar flow within tissue engineering scaffolds. Characterisation of diffusion is particularly relevant within electro-spun scaffolds which, by virtue of their micro-fibres, have very small pore sizes (see Fig. 5.2). In the context of the delivery and removal of metabolites within scaffolds, measurements of diffusion anisotropy can provide information about the relative rates of transport along different directions within a volume element. As the PCL material used in the fabrication of the scaffolds does not interact chemically with the water molecules, it is only the geometry which contributes to diffusion anisotropy. With respect to the present study, the diffusion anisotropy apparent in Figs. 5.3 and 5.4 indicate that preferential molecular transport occurs vertically through the scaffolds, albeit with some residual transverse component. Furthermore, this anisotropy increases with longer diffusion times for both scaffolds.

Numerical simulations of restricted diffusion in partially aligned fibre networks

by Powell and Momot, 2012 [9] included computed a simulated diffusion tensor for similar cross-hatched fibre networks as in present study. The corresponding tensors, however, indicate that diffusion is least restricted in the transverse direction (x,y) (see Fig. 3.5(c) of Chapter 3), which is the opposite of the findings shown in Fig. 5.4. This can be explained by their different transverse architectures, with the fibre layers of the electrospun scaffold directly in contact, and the fibre layers of the LD study separated by a distance many times that of the fibre diameter. The increased obstructions in the directly contacting layers resulted in smaller transverse diffusivity than longitudinal diffusivity. This can be further understood by comparing the diffusivities of the theoretical and experimental studies via the concept of a 2D projection of the fibre architecture onto the transverse and longitudinal planes. This involves calculating the total area of a unit cell within the pattern then subtracting the projected area occupied by the fibres to give the unobstructed area within the unit cell. This is then divided by the total unit cell area to give the fraction of unobstructed surface per unit cell within the fibre networks for both the transverse and longitudinal direction to compare with the respective diffusivities. The projected 2D unobstructed surface for the electrospun fibre networks in the longitudinal and transverse directions was $\sim 87\%$ and $\sim 47\%$, respectively. This is comparable with the DTI observations which indicate diffusivity is least restricted in the longitudinal direction. The projected 2D unobstructed surface for the LD simulated structure, however, was $\sim 87\%$ and $\sim 99\%$ for the longitudinal and transverse directions, respectively. This compares with the simulated DTI results which indicated that for all fibre volume fractions studied, the transverse diffusivity was greater than the longitudinal diffusivity (see Fig. 3.5(c) of Chapter 3). The results of the LD simulations in Chapter 3 also indicate that an increase in fibre volume fraction corresponds to an increase in the anisotropy of the diffusion tensor. The experimental results in Fig. 5.4 indicate an increase in the anisotropy with the increasing diffusion time for both scaffolds. However, the experimental uncertainties resulted in the inability to discriminate between the

diffusivities of the two scaffolds.

In order for DTI to be a useful method for the evaluation of tissue engineering scaffolds with micron-scale architectural differences, such as those of the present study, the measurement uncertainties need to be significantly reduced from that stated above. A common approach to achieving this is to perform multiple repeated measurements and average the signal over these in order to improve the signal-to-noise ratio. A disadvantage of this approach, however, is the increase in the overall measurement time due to these additional measurements. For example, the total imaging time required to sample the diffusion tensor along 20 different gradient directions with a repetition time of $4000\,ms$ was approximately 39 hours for 16 image averages. Increasing the number of image averages would improve the signal to noise ratio but also increase the total experiment duration. One potential approach to mitigate this is to reduce the total number of gradient directions. Given that the geometry of the ordered cross-hatched scaffolds of the present study is known *a priori*, the number of gradient directions along which diffusion is sampled could potentially be reduced to the laboratory frame x, y and z axes. This would enable significantly more image averages to be acquired within a given total experiment time, thereby increasing the signal-to-noise ratio. This improvement, however, would come at the cost of discarding knowledge of the diffusion tensor. To investigate the suitability of this approach for cross-hatched tissue engineering scaffolds, we performed a voxel by voxel comparison between the undiagonalised diffusion tensor values along the three principal laboratory axes, and the corresponding eigenvalues of the diffusion tensor sampled along 20 different gradient directions for Scaffold A of the present study. The histograms of Fig. 5.5 show the distributions of the relative differences between the corresponding tensors. These plots indicate that there are notable relative differences between these two approaches that, in some voxels along the z axis, exceed 0.35. Another notable result is that the longitudinal eigenvalue always appears larger than the

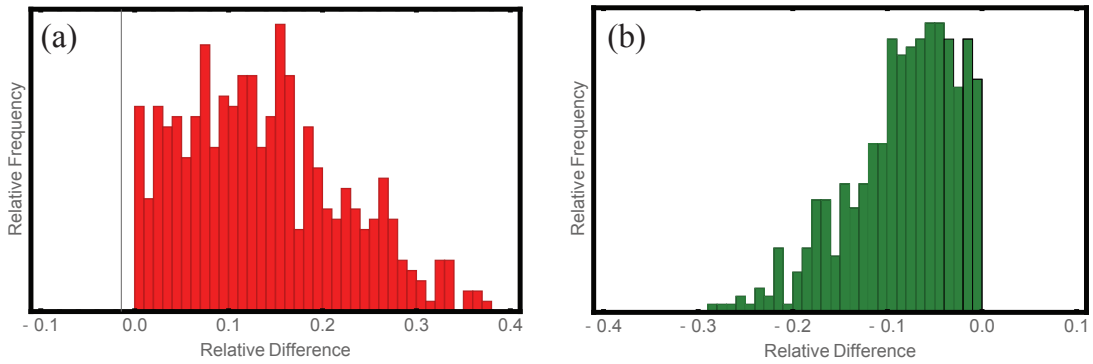

Figure 5.5: Histograms showing the relative difference between the diffusion tensor eigenvalues and PGSE diffusivity along the x, y and z axes for all voxels of scaffold A at Δ=250ms. (a) Longitudinal diffusion tensor eigenvalues minus the z axis diffusivity (b) Average transverse diffusion tensor eigenvalues minus the average of the x and y axes.

z axis diffusivity, whereas the degenerate transverse eigenvalues are smaller than the corresponding diffusivities in the x, y plane. The can be explained by partial voluming effects caused by the comparable scale of the scaffold fibres and the imaging voxels. For example, consider a voxel containing only part of a fibre that is aligned with the y axis as depicted in Fig. 5.6. In this case, the diffusivity along the z-axis, D_{zz}, will be restricted by the fibre. The diagonalised principal eigenvector, D_1, however, will be rotated into the y-axis with a diffusivity larger than D_{zz}. The transverse eigenvectors will be also rotated in this case, yielding an average of the transverse eigenvalues that is smaller than the corresponding average of the x, y diffusivities.

DTI appears to be a highly promising technique for the real-time monitoring of tissue regeneration in scaffolds. This is especially relevant for advanced scaffold designs which possess regions of varying fibre density and pathways for molecular transport. By observing variations in the diffusion tensor throughout the scaffold, changes in scaffold morphology due to tissue infiltration can be determined. This is particularly important as tissue infiltration reduces diffusivity within the scaffold, thereby potentially restricting oxygen transport and leading to unintentional hypoxia followed by cell death. Conversely, features that restrict molecular transport can be incorporated into scaffold design, thereby inducing intentional hypoxia to stimulate

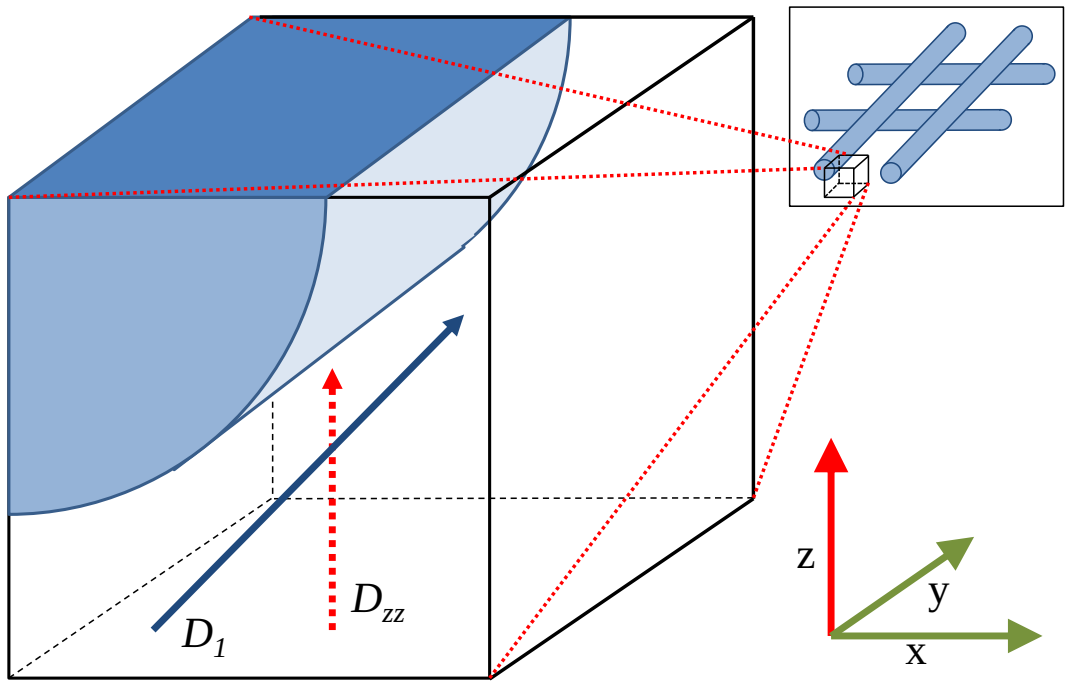

Figure 5.6: Simplified example of the effect of partial voluming on diffusivity. A fibre is aligned along the y axis and partially intrudes within the voxel. The z axis diffusivity is restricted by the fibre to a greater extent than the principal eigenvalue of the diffusion tensor. The average x-y diffusivity is larger than the average degenerate eigenvalues.

and increase angiogenesis, thereby improving cell development [271]. As DTI is non-invasive, non-ionising and provides directional information about diffusion and diffusion anisotropy, it is potentially more suitable for biological investigations than other methods such as confocal microscopy and μCT. In addition, DTI measurements can be combined with other magnetic resonance modalities which can provide complimentary tissue and scaffold microstructure information during tissue growth [138]. A novel bioreactor design can also be incorporated to enable the repeated transfer of developing scaffolds between the bioreactor and an MRI instrument under sterile conditions.

The results in Fig. 5.4 indicate that the variation in measured diffusivities throughout the scaffold becomes greater when the diffusion time is increased. This is potentially due to two factors; (1) The DTI voxel sizes are comparable to the scaffold

fibre diameters. As such, a given voxel can encompass a volume containing either no fibres, a part of a fibre or fibres, or multiple fibres. Variations in diffusivities, therefore, reflect variations in the possible geometries within each voxel. Comparisons of the degree of variation in the diffusion tensors throughout multiple periodic structures could consequently be useful as an indicator of the relative sizes of features within these structures. (2) The magnetic resonance signal used in measuring diffusion decays with time. This leads to increased noise and subsequent variations in diffusivity measurements. In contrast to the model scaffolds of the present study, scaffolds for engineering complex tissue and organs are designed with multi-scale pore sizes and complex pore interconnectivity. In these cases, DT image maps could be a useful indicator of metabolite migration pathways within the scaffolds. Furthermore, changes in these transport pathways during the tissue regeneration can also be mapped, leading to the development of theoretical models for guiding the design of scaffold micro-architectures optimised to facilitate the transport of nutrients and metabolites between the repair site and the surrounding tissue.

5.7 Conclusion

The results presented in this study form the basis for a quantitative experimental evaluation of molecular transport within scaffolds for tissue engineering. This is important because molecular transport is fundamental to the exchange of nutrients and metabolites in tissue engineered scaffolds. Model scaffolds were produced using a novel electro-spinning technique and characterised using μCT and μDTI. As μCT directly observes microstructure and μDTI directly observes molecular transport, these techniques provide complementary information for superior characterisation of the

scaffolds. Diffusion ansitropy was observed and found to be consistent with the scaffold geometry, with the larger anisotropy apparent at longer diffusion times. This work demonstrates that experimental diffusion tensor measurements of tissue engineering scaffolds can be useful for evaluating molecular transport within tissue engineering scaffolds. It also suggests that DTI is a promising experimental tool for the real-time monitoring of tissue regeneration processes that could have use in both in tissue cultures and in vivo.

5.8 Acknowledgements

K.A.B. and M.A.W. acknowledge the support from the Australian Research Council Linkage Grant LP110200082. M.A.W. also acknowledges the support from the Australian Research Council Linkage Grant LP100200084. S.K.P. acknowledges the financial support by the Institute of Health and Biomedical Innovation (IHBI). S.K.P. and K.I.M. thank Dr Mark Wellard for technical assistance with DTI measurements.

Chapter 6

Conclusions and recommendations

6.1 Summary of the research

In this thesis we carried out theoretical and experimental studies of restricted diffusion with the aim of developing efficient methods for producing quantitative models for interpreting diffusion tensor images of biological tissue and tissue engineering scaffolds. Using these methods, we produced interpretive models to improve the utility of diffusion tensor imaging for the study of the composition and organisation of anisotropic biological tissue. We also combined diffusion tensor imaging and interpretive models to enable the study of the micro-structure and molecular transport within tissue engineering scaffolds.

To achieve our aims, we created two different theoretical methods for calculating restricted diffusion propagators; a computer simulation approach based on Langevin dynamics, and a means for calculating diffusion propagators by enumerating random walks on a lattice. Each was optimised to model diffusion at a given spatial and temporal scale to enable the work of this thesis to encompass a wide range of restricted diffusion problems.

Computer software based on Langevin dynamics was developed to simulate diffusion in the interstitial volume surrounding collagen fibres of articular cartilage. The resulting simulated diffusion tensors, detailed in Chapter 3, were then used to produce a quantitative model to interpret DTI measurements of articular cartilage in terms of the compositional and organisational structure of its collagen fibres. Using this software, we also found that the diffusion tensor was invariant to any positional and radial fibre disorder. The details and results of this work are presented as two published peer-reviewed papers which comprise Chapter 3 of this thesis.

We also found that simulation based approaches, such as Langevin dynamics, produce 'noisy' propagators as they only simulate a very small number of the total possible particle trajectories. Subsequently, they are not ideally suited for producing detailed time-dependent propagators for restricted diffusion in complex or highly tortuous environments. This limitation led to the development of the Lattice Path Count algorithm. The LPC approach enumerates all paths available to a diffusing particle on a lattice while accounting for absorbing, reflecting, and semi-permeable barriers. Another valuable feature of the LPC approach is that it offers an important insight into the physical meaning of the diffusion propagator as the number of paths of a given length connecting two locations. The algorithm is highly computationally efficient, requiring only simple arithmetic calculations and avoiding the need for complex floating point computations through the use of unlimited-length integer processing. We used LPC to produce propagators for various 1D, 2D and 3D restricted diffusion problems to enable direct comparison with analytic and finite element solutions to the diffusion equation, and the Langevin dynamics simulations. In the context of the overall aims of this thesis, LPC is optimised for producing highly accurate propagators for complex pore spaces in the intermediate-Δ diffusion regime. The LPC approach also extends naturally to modelling diffusive transport processes such as diffusion from sources with a constant particle concentration and changes in the spatial distribution of the

relative concentrations of substances within fluids. As LPC is essentially a method for exactly computing lattice random walks, it has direct application beyond diffusion in fields such as percolation modelling, finance and economics, astrophysics, biology. It also provides an intuitive physical picture of diffusion, where the probability of a particle diffusing between two locations in a given time is proportional to the number of connecting paths of a given length, and restricted diffusion occurs when some of the paths become unavailable. The details and results of the lattice path count approach is presented as two papers, one detailed in chapter 4, and the other in Appendix D.

The experimental component of this thesis involved a series of diffusion tensor imaging and x-ray computed tomography measurements of electrospun tissue engineering scaffolds. Electrospinning is an additive manufacturing technique capable of producing micron-scale fibre networks with customisable micro-architectures. This capability makes it an excellent candidate technology for the construction of phantoms for experimental validation of theoretically produced interpretive models of DTI. The results showed that for stacked 90 degree fibre networks, diffusivity was least restricted in the direction vertically through the fibre layers, and that the anisotropy of the DT increased with increasing diffusion time. In the context of tissue engineering scaffolds, we found that DTI is a valuable technique for evaluating molecular transport. This technique also has potential for longitudinal studies of the evolution of molecular transport pathways in tissue engineering scaffolds during tissue growth. The application of the theoretical techniques of this thesis to the problem of evaluating the performance of scaffold microarchitecture can lead to improved scaffold design. This work is presented as a published peer-reviewed journal paper which comprises Chapter 5 of this thesis.

In summary, the general aim of this thesis was to provide an improved understanding of restricted diffusion in quasi-periodic fibre networks and complex porous media. The specific aim was to develop methods to produce quantitative models for

interpreting diffusion magnetic resonance images, particularly of biological tissue and tissue engineering scaffolds. These aims were achieved through the development of analytic and numerical algorithms and associated software, with the results applicable to the quantitative interpretation of diffusion tensor images of anisotropic tissue fibre networks and tissue engineering scaffolds. In addition, we explored the accuracy and limitations of these techniques within the general context of modelling restricted diffusion processes, and demonstrated their application to providing important physical insight into fundamental transport processes. The theoretical studies were supported by experimental magnetic resonance measurements of the fibre networks in tissue engineering scaffolds. The specific findings of each component of this overall work were detailed in each respective chapter and associated peer-reviewed publications.

6.2 Recommendations

The Langevin dynamics simulation software of this thesis was used to produce quantitative models for interpreting diffusion tensor images of articular cartilage in terms of its collagen volume fraction and relative fibre orientations. However, we found that each measured fractional anisotropy related to a range of possible combinations of collagen volume fraction and fibre orientations. In order to use this model to discriminate between these effects, independent knowledge of either the fibre orientation or the collagen/proteoglycan content is required. We therefore suggest that other magnetic resonance imaging modalities such as T_1, T_2, or $T_{1\rho}$ be developed as techniques to determine specific collagen volume fraction in AC and thus allow diffusion measurements to be used to infer the fibre orientations. The Langevin dynamics method could also be adapted to model permeable barriers to extend its application to studies of other biological systems such as neural fibres. This would involve modifying the code that computes the barrier interaction to incorporate a transit probability for an incident particle across the barrier and into the bounded volume.

We also suggest the further development of the lattice path count algorithm to improve its computational performance and increase the number of computable lattice nodes. This could be achieved by pre-computing parts of the barrier calculations, and through the reuse of the path counts of selected node pairs thereby significantly reducing the number of elementary calculations. Further optimisation could be achieved through the use of different lattice geometries and adaptive lattice spacing, i.e. reducing lattice density in large unrestricted volumes and increasing lattice density near barriers. In the context of improving the quantitative interpretation of diffusion tensor images, further LPC studies of the effects of network disorder and highly confined geometries on the diffusion propagators could be undertaken.

In addition to reflecting and absorbing barriers, LPC could also be modified to model diffusion across semi-permeable barriers. This has important applications for modelling diffusion in many biological systems from neural networks to the permeable membranes surrounding cells. This permeable boundary condition differs from the purely reflecting case in that there is a non-zero transition probability for a particle across a barrier. Current modelling approaches include Monte-Carlo simulations [62] and new methods such as the Markov Transfer Matrix methods detailed in Appendix D. In principle, LPC could compute such scenarios by altering the ratio Q/P in Eq. (4.4), where Q and P correspond to the fraction of reflecting and transmitting paths, respectively, for the semi-permeable barriers. The requirement of integer computation for the path counts can be handled through the use of an integer division function which in some cases will result in a small number of remainder paths carried over from the computation. Due to the extremely small number of these remainder paths, it would not be expected that this approach would introduce any significant error.

The experimental component of this thesis demonstrated the use of direct-write melt-electrospinning (DWME) as a technique for producing custom made tissue phantoms for experimental validation of theoretical diffusion models. The scale of the

produced structures, however, limited the diffusion measurements to the intermediate-Δ regime. In order to serve as test structures for diffusion measurements in the long-Δ diffusion regime, much smaller structures are required. To achieve this, advanced fabrication techniques are required such as selective laser sintering, stereolithography, or near-field solution electrospinning. The use of diffusion tensor imaging to infer the micron-scale structural characteristics of tissue engineering scaffolds is limited by the uncertainty in the acquired data. This uncertainty could be reduced by increasing the number of image averages acquired for each gradient direction, however, this also increases the total experiment duration. As the general orientation of the fibre networks within the scaffolds is already known from the fabrication process, it should be possible to perform PGSE measurements along the x, y and z axis to reconstruct similar information as obtained from the measurements of Chapter 5 and significantly reduce the number of gradient directions required. This experiment is the subject of a current research project.

References

[1] E. L. Hahn, "Spin Echoes," *Physical Review Online Archive*, vol. 56(1), pp. 580–594, 1950.

[2] H. Y. Carr and E. M. Purcell, "Effects of diffusion on free precession in nuclear magnetic resonance experiments," *Physical Review*, vol. 94, pp. 630–638, May 1954.

[3] E. O. Stejskal and J. E. Tanner, "Spin diffusion measurements: Spin echoes in the presence of a time-dependent field gradient," *The Journal of Chemical Physics*, vol. 42, no. 1, p. 288, 1965.

[4] P. J. Basser, J. Mattiello, and D. LeBihan, "MR diffusion tensor spectroscopy and imaging," *Biophysical Journal*, vol. 66, no. 1, pp. 259–267, 1994.

[5] I. Majid, D. B. Avraham, S. Havlin, and H. E. Stanley, "Exact-enumeration approach to random walks on percolation clusters in two dimensions," *Physical Review B*, vol. 30, pp. 1626–1628, Aug. 1984.

[6] E. Scalas, "The application of continuous-time random walks in finance and economics," *Physica A: Statistical Mechanics and its Applications*, vol. 362, pp. 225–239, Apr. 2006.

[7] E. A. Codling, M. J. Plank, and S. Benhamou, "Random walk models in biology," *Journal of the Royal Society, Interface*, vol. 5, pp. 813–834, Aug. 2008.

[8] M. Ferraro and L. Zaninetti, "Statistics of visits to sites in random walks," *Physica A: Statistical Mechanics and its Applications*, vol. 338, pp. 307–318, July 2004.

[9] S. K. Powell and K. I. Momot, "Langevin dynamics modeling of the water diffusion tensor in partially aligned collagen networks," *Physical Review E*, vol. 86, p. 031917, Sept. 2012.

[10] S. K. Powell and K. I. Momot, "Computer modeling of diffusion in biological tissues," *Procedia Information Technology and Computer Science*, vol. 3, no. 1, pp. 1227–1233, 2013.

[11] S. K. Powell, G. J. Oberman, and K. I. Momot, "Efficient calculation of restricted diffusion propagators using lattice path counts," *Physical Review E*, vol. Submitted, 2015.

[12] K. I. Momot, S. K. Powell, and M. C. Tourell, "Further development of discrete computational techniques for calculation of restricted diffusion propagators in porous media," *Microporous and Mesoporous Materials*, vol. 205, pp. 24–30, Mar. 2015.

[13] S. K. Powell, N. Ristovski, S. Liao, K. A. Blackwood, M. A. Woodruff, and K. I. Momot, "Characterization of the microarchitecture of direct writing melt electrospun tissue engineering scaffolds using diffusion tensor and computed tomography microimaging," *3D Printing and Additive Manufacturing*, vol. 1, no. 2, pp. 95–103, 2014.

[14] A. Einstein, "On the theory of the Brownian movement," *Annalen der Physik*, vol. 4, no. 19, pp. 371–381, 1906.

[15] H. C. Berg, *Random walks in biology*. Princeton paperbacks, Princeton University Press, illustrate ed., 1993.

[16] E. L. Cussler, *Diffusion: mass transfer in fluid systems*. Cambridge Series in Chemical Engineering, Cambridge University Press, 2009.

[17] H. Johansen-Berg and T. E. Behrens, *Diffusion MRI : From quantitative measurement to in-vivo neuroanatomy*. Academic Press, 2, revised ed., 2013.

[18] H. J. V. Tyrrell and K. R. Harris, *Diffusion in liquids: A theoretical and experimental study*. Butterworth-Heinemann, 2013.

[19] C. Berthollet, "XXI. Researches respecting the laws of affinity," *The Philosophical Magazine: Comprehending the Various Branches of Science, the Liberal and Fine Arts, Agriculture, Manufactures, and Commerce*, vol. 10, no. 38, pp. 129–142, 1801.

[20] J. B. J. baron Fourier, *The analytical theory of heat*. The University Press, 1878.

[21] A. Fick, "On liquid diffusion," *The London, Edinburgh, and Dublin Philosophical Magazine and Journal of Science*, vol. 10, no. 63, pp. 30–39, 1855.

[22] J. Crank, *The mathematics of diffusion*. Clarendon Press, illustrate ed., 1979.

[23] K. E. Shuler and U. Mohanty, "Random walk properties from lattice bond enumeration: Anisotropic diffusion in lattices with periodic and randomly distributed scatterers," *Proceedings of the National Academy of Sciences of the United States of Am*, vol. 78, no. 11, pp. 6576–6578, 1981.

[24] A. V. Luikov, *Analytical heat diffusion theory*. Elsevier, 2012.

[25] T. L. Bergman, F. P. Incropera, and A. S. Lavine, *Fundamentals of heat and mass transfer*. John Wiley & Sons, 2011.

[26] L. Rayleigh, "On the influence of obstacles arranged in rectangular order upon

the properties of a medium," *Philosophical Magazine Series 5*, vol. 34, no. 211, pp. 481–502, 1892.

[27] J. VandeVondele, F. Mohamed, M. Krack, J. Hutter, M. Sprik, and M. Parrinello, "The influence of temperature and density functional models in ab initio molecular dynamics simulation of liquid water.," *The Journal of chemical physics*, vol. 122, p. 14515, Jan. 2005.

[28] C. G. Gray, K. E. Gubbins, and C. G. Joslin, *Theory of molecular fluids*. Oxford University Press, 2011.

[29] P. P. Mitra, P. N. Sen, L. M. Schwartz, and P. L. Doussal, "Diffusion propagator as a probe of the structure of porous media," *Physical Review Letters*, vol. 68, no. 24, pp. 3555–3558, 1992.

[30] L. L. Latour, K. Svoboda, P. P. Mitra, and C. H. Sotak, "Time-dependent diffusion of water in a biological model system," *Proceeding of the National Acedemy of Sciences of the USA*, vol. 91, no. 4, pp. 1229–1233, 1994.

[31] L. Avram, E. Özarslan, Y. Assaf, A. Bar-Shir, Y. Cohen, and P. J. Basser, "Three-dimensional water diffusion in impermeable cylindrical tubes: theory versus experiments," *NMR in Biomedicine*, vol. 21, no. 8, pp. 888–898, 2008.

[32] Y. Assaf, R. Z. Freidlin, G. K. Rohde, and P. J. Basser, "New modeling and experimental framework to characterize hindered and restricted water diffusion in brain white matter," *Magnetic Resonance in Medicine*, vol. 52, no. 5, pp. 965–978, 2004.

[33] E. Özarslan, P. J. Basser, T. M. Shepherd, P. E. Thelwall, B. C. Vemuri, and S. J. Backband, "Observation of anomalous diffusion in excised tissue by characterizing the diffusion-time dependence of the MR signal," *Journal of Magnetic Resonance*, vol. 183, no. 2, pp. 315–323, 2006.

[34] R. Brown, "A brief account of microscopical observations made in the months of June, July and August 1827, on the particles contained in the pollen of plants; and on the general existence of active molecules in organic and inorganic bodies," *Philosophical Magazine Series 2*, vol. 4, no. 21, pp. 161–173, 1828.

[35] M. C. Tourell, S. K. Powell, and K. I. Momot, "Diffusion tensor of water in partially aligned collagen networks," *Journal of Physics D: Applied Physics*, vol. 46, no. 45, p. 455401, 2013.

[36] M. Kac, "Can one hear the shape of a drum?," *The American Mathematical Monthly*, vol. 73, no. 4, pp. 1–23, 1966.

[37] S. M. Kirkup and M. Wadsworth, "Solution of inverse diffusion problems by operator-splitting methods," *Applied Mathematical Modelling*, vol. 26, no. 10, pp. 1003–1018, 2002.

[38] J. V. Beck, B. Blackwell, and C. R. St. Clair, *Inverse heat conduction: Ill-posed problems*. Wiley, 1985.

[39] J. L. Lebowitz and H. Spohn, "Microscopic basis for Fick's law for self-diffusion," *Journal of Statistical Physics*, vol. 28, pp. 539–556, July 1982.

[40] J. Mehra and H. Rechenberg, *The historical development of quantum theory*. Erwin Schr{ö}dinger and the Rise of Wave Mechanics, Springer Science & Business Media, 2000.

[41] R. Newburgh, J. Peidle, and W. Rueckner, "Einstein, Perrin, and the reality of atoms: 1905 revisited," *American Journal of Physics*, vol. 74, no. 6, p. 478, 2006.

[42] P. Olver, *Introduction to partial differential equations*. Undergraduate Texts in Mathematics, Springer Science & Business Media, 2013.

[43] S. Kocherlakota and K. Kocherlakota, *Bivariate discrete distributions volume 132 of statistics: A series of textbooks and monographs*. Statistics: A Series of Textbooks and Monographs, CRC Press, 1992.

[44] D. A. McQuarrie, *Statistical Thermodynamics*. University Science Books, 1973.

[45] M. Chaichain and A. Demichev, *Path integrals in physics*. CRC Press, 2001.

[46] R. Graham, "Path integral formulation of general diffusion processes," *Zeitschrift f{ü}r Physik B Condensed Matter*, vol. 26, no. 3, pp. 281–290, 1977.

[47] H. S. Wio, *Path integrals for stochastic processes: An introduction*. Universidad de Cantabria, Spain, 2013.

[48] C. Liu, R. Bammer, B. Acar, and M. E. Moseley, "Characterizing non-Gaussian diffusion by using generalized diffusion tensors," *Magnetic Resonance in Medicine*, vol. 51, no. 5, pp. 924–937, 2004.

[49] J. H. Jensen, J. a. Helpern, A. Ramani, H. Lu, and K. Kaczynski, "Diffusional kurtosis imaging: The quantification of non-Gaussian water diffusion by means of magnetic resonance imaging," *Magnetic Resonance in Medicine*, vol. 53, no. 6, pp. 1432–1440, 2005.

[50] H. Lu, J. H. Jensen, A. Ramani, and J. a. Helpern, "Three-dimensional characterization of non-gaussian water diffusion in humans using diffusion kurtosis imaging," *NMR in Biomedicine*, vol. 19, no. 2, pp. 236–247, 2006.

[51] P. N. Sen, "Time-dependent diffusion coefficient as a probe of geometry," *Concepts in Magnetic Resonance Part A*, vol. 23A, pp. 1–21, Sept. 2004.

[52] B. A. Landman, J. A. D. Farrell, S. A. Smith, D. S. Reich, P. A. Calabresi, and P. C. M. van Zijl, "Complex geometric models of diffusion and relaxation in healthy and damaged white matter," *NMR Biomedicine*, vol. 23, no. 2, pp. 152–162, 2010.

[53] J. Hrabe, S. Hrabetová, and K. Segeth, "A model of effective diffusion and tortuosity in the extracellular space of the brain.," *Biophysical Journal*, vol. 87, pp. 1606–1617, Sept. 2004.

[54] K. I. Momot, "Diffusion tensor of water in model articular cartilage," *European Biophysics Journal*, vol. 40, no. 1, pp. 81–91, 2011.

[55] C. Lenglet, J. S. W. Campbell, M. Descoteaux, G. Haro, P. Savadjiev, D. Wassermann, A. Anwander, R. Deriche, G. B. Pike, G. Sapiro, K. Siddiqi, and P. M. Thompson, "Mathematical methods for diffusion MRI processing," *NeuroImage*, vol. 45, pp. S111–S122, Mar. 2009.

[56] P. P. Mitra, P. N. Sen, and L. M. Schwartz, "Short-time behavior of the diffusion coefficient as a geometrical probe of porous media," *Physical Review B*, vol. 47, no. 14, pp. 8565–8574, 1993.

[57] P. N. Sen, L. M. Schwartz, P. P. Mitra, and B. Halperin, "Surface relaxation and the long-time diffusion coefficient in porous media: periodic geometries," *Physical Review B*, vol. 49, no. 1, pp. 215–225, 1994.

[58] P. J. Basser, J. Mattiello, and D. Lebihan, "Estimation of the effective self-diffusion tensor from the NMR spin echo," *Journal of Magnetic Resonance*, vol. 103, no. 3, pp. 247–254, 1994.

[59] P. J. Basser and C. Pierpaoli, "A simplified method to measure the diffusion tensor from seven MR images," *Magnetic Resonance in Medicine*, vol. 39, no. 66, pp. 928–934, 1998.

[60] J.-D. Tournier, F. Calamante, D. G. Gadian, and A. Connelly, "Direct estimation of the fiber orientation density function from diffusion-weighted MRI data using spherical deconvolution," *NeuroImage*, vol. 23, no. 3, pp. 1176–1185, 2004.

[61] M. Descoteaux, R. Deriche, D. L. Bihan, J.-F. Mangin, and C. Poupon, "Diffusion propagator imaging: using Laplace's equation and multiple shell acquisitions to reconstruct the diffusion propagator," *Information Processing in Medical Imaging*, vol. 5636, no. 1, pp. 1–13, 2009.

[62] D. G. Regan and P. W. Kuchel, "Mean residence time of molecules diffusing in a cell bounded by a semi-permeable membrane: Monte carlo simulations and an expression relating membrane transition probability to permeability," *European Biophysics Journal*, vol. 29, no. 3, pp. 221–227, 2000.

[63] P. W. Kuchel and C. J. Durrant, "Permeability coefficients from nmr q-space data: models with unevenly spaced semi-permeable parallel membranes," *Journal of Magnetic Resonance*, vol. 139, no. 2, pp. 258–272, 1999.

[64] O. K. Dudko, A. M. Berezhkovskii, and G. H. Weiss, "Time-dependent diffusion coefficients in periodic porous materials.," *The Journal of Physical Chemistry B*, vol. 109, pp. 21296–21299, Nov. 2005.

[65] J. Mitchell, T. Chandrasekera, and L. Gladden, "Obtaining true transverse relaxation time distributions in high-field nmr measurements of saturated porous media: removing the influence of internal gradients," *The Journal of Chemical Physics*, vol. 132, no. 24, p. 244705, 2010.

[66] S. Godefroy, J. Korb, M. Fleury, and R. Bryant, "Surface nuclear magnetic relaxation and dynamics of water and oil in macroporous media," *Physical Review E*, vol. 64, no. 2, p. 021605, 2001.

[67] L. L. Latour, P. P. Mitra, R. L. Kleinberg, and C. H. Sotak, "Time-dependent diffusion coefficient of fluids in porous media as a probe of surface-to-volume ratio," *Journal of Magnetic Resonance*, vol. 101, no. 3, pp. 342–346, 1993.

[68] K. Keating, "A laboratory study to determine the effect of surface area and bead

diameter on nmr relaxation rates of glass bead packs," *Near Surface Geophysics*, vol. 12, no. 2, pp. 243–254, 2014.

[69] B. P. Boudreau, "The diffusive tortuosity of fine-grained unlithified sediments," *Geochimica et Cosmochimica Acta*, vol. 60, no. 16, pp. 3139–3142, 1996.

[70] A. M. Heemskerk and G. J. Strijkers, "Determination of mouse skeletal muscle architecture using three-dimensional diffusion tensor imaging," *Magnetic Resonance in Medicine*, vol. 53, no. 6, pp. 1333–1340, 2005.

[71] S. Givli and K. Bhattacharya, "A coarse-grained model of the myofibril: Overall dynamics and the evolution of sarcomere non-uniformities," *Journal of the Mechanics and Physics of Solids*, vol. 57, no. 2, pp. 221–243, 2009.

[72] D. F. Scollan, A. Holmes, R. Winslow, and J. Forder, "Histological validation of myocardial microstructure obtained from diffusion tensor magnetic resonance imaging," *American Journal of Physiology-Heart and Circulatory Physiology*, vol. 275, no. 6, pp. H2308—-H2318, 1998.

[73] B. M. Damon, Z. Ding, A. W. Anderson, A. S. Freyer, and J. C. Gore, "Validation of diffusion tensor MRI-based muscle fiber tracking," *Magnetic Resonance in Medicine*, vol. 48, no. 1, pp. 97–104, 2002.

[74] R. Meder, S. K. de Visser, J. C. Bowden, T. Bostrom, and J. M. Pope, "Diffusion tensor imaging of articular cartilage as a measure of tissue microstructure," *Osteoarthritis and Cartilage*, vol. 14, pp. 875–881, Sept. 2006.

[75] S. K. de Visser, R. W. Crawford, and J. M. Pope, "Structural adaptations in compressed articular cartilage measured by diffusion tensor imaging," *Osteoarthritis and Cartilage*, vol. 16, no. 1, pp. 83–89, 2008.

[76] R. Knauss, J. Schiller, G. Fleischer, J. Karger, and K. Arnold, "Self diffusion

of water in carilage and cartilage components as studied bypulsed field gradient NMR," *Magnetic Resonance in Medicine*, vol. 41, no. 2, pp. 285–292, 1999.

[77] K. I. Momot, J. M. Pope, and R. M. Wellard, "Anisotropy of spin relaxation of water protons in cartilage and tendon," *NMR in Biomedicine*, vol. 23, pp. 313–324, Apr. 2010.

[78] P. N. Sen and P. J. Basser, "Modeling diffusion in white matter in the brain: a composite porous medium.," *Magnetic Resonance Imaging*, vol. 23, pp. 215–220, Feb. 2005.

[79] D. S. Tuch, T. G. Reese, M. R. Wiegell, and V. J. Wedeen, "Diffusion MRI of complex neural architecture," *Neuron*, vol. 40, no. 5, pp. 885–895, 2003.

[80] K. Rojkova, E. Volle, M. Urbanski, F. Humbert, F. DellAcqua, and M. Thiebaut de Schotten, "Atlasing the frontal lobe connections and their variability due to age and education: a spherical deconvolution tractography study," *Brain Structure and Function*, pp. 1–16, Feb. 2015.

[81] C. P. Hess, P. Mukherjee, E. T. Han, D. Xu, and D. B. Vigneron, "Q-ball reconstruction of multimodal fiber orientations using the spherical harmonic basis," *Magnetic Resonance in Medicine*, vol. 56, pp. 104–117, July 2006.

[82] X. Liu, *Magnetic resonance diffusion tensor imaging: distortion correction methods and their applications in high-resolution in vivo monkey brain scans*. ProQuest, 2009.

[83] J. Philibert, "One and a half century of diffusion: Fick, Einstein before and beyond," *Diffusion Fundamentals*, vol. 2, pp. 1–10, 2005.

[84] M. F. Wehner and W. G. Wolfer, "Numerical evaluation of path-integral solutions to Fokker-Planck equations," *Physical Review A*, vol. 27, pp. 2663–2670, May 1983.

[85] A. N. Drozdov, "High-accuracy discrete path integral solutions for stochastic processes with noninvertible diffusion matrices," *Physical Review E*, vol. 55, pp. 2496–2508, Mar. 1997.

[86] G. F. Lawler and V. Limic, *Random walk: A modern introduction*. Cambridge: Cambridge University Press, 2010.

[87] X.-Z. Wang, J.-H. Zhai, and S.-F. Zhang, "A model of finite-step random walk with absorbent boundaries," *International Journal of Computer Mathematics*, vol. 85, pp. 1685–1696, Nov. 2008.

[88] W. Cen, D. Liu, and B. Mao, "Molecular trajectory algorithm for random walks on percolation systems at criticality in two and three dimensions," *Physica A: Statistical Mechanics and its Applications*, vol. 391, pp. 925–929, Feb. 2012.

[89] Q. Dong, R. C. Welsh, T. L. Chenevert, R. C. Carlos, P. Maly-Sundgren, D. M. Gomez-Hassan, and S. K. Mukherji, "Clinical applications of diffusion tensor imaging," *Journal of Magnetic Resonance Imaging*, vol. 19, pp. 6–18, Jan. 2004.

[90] K. I. Momot, "Diffusion tensor of water in model articular cartilage.," *European Biophysics Journal*, vol. 40, pp. 81–91, Jan. 2011.

[91] D. T. Gillespie and E. Seitaridou, *Simple brownian diffusion: An introduction to the standard theoretical models*. OUP Oxford, 2012.

[92] G. D. Smith, *Numerical solution of partial differential equations: Finite difference methods*. Oxford applied mathematics and computing science series, Clarendon Press, 1985.

[93] N. Ozisik, *Finite difference methods in heat transfer*. Heat Transfer, Taylor & Francis, 1994.

[94] J. Douglas, Jr., "On the relation between stability and convergence in the numerical solution of linear parabolic and hyperbolic differential equations,"

Journal of the Society for Industrial and Applied Mathematics, vol. 4, pp. 20–37, Mar. 1956.

[95] W. H. Press, S. A. Teukolsky, W. T. Vetterling, and B. Flannery, *Numerical recipes in FORTRAN: The art of scientific computing*. Cambridge: Cambridge University Press, 1992.

[96] D. C. Rapaport, *The art of molecular dynamics simulation*. Cambridge University Press, 2004.

[97] W. L. Jorgensen, J. Chandrasekhar, J. D. Madura, R. W. Impey, and M. L. Klien, "Comparison of simple potential functions for simulating liquid water," *Journal of Chemical Physics*, vol. 79, no. 2, pp. 926–935, 1983.

[98] W. L. Jorgensen and J. Tirado-Rives, "Potential energy functions for atomic-level simulations of water and organic and biomolecular systems," *Proceedings of the National Academy of Sciences*, vol. 102, pp. 6665–6670, May 2005.

[99] J. M. Haile, *Molecular dynamics simulation: Elementary methods*. New York: Wiley Interscience, 1997.

[100] P. J. Basser and C. Pierpaoli, "Microstructural and physiological features of tissues elucidated by quantitative-diffusion-tensor MRI," *Journal of Magnetic Resonance*, vol. 213, pp. 560–570, Dec. 2011.

[101] H.-G. Lipinski, "Monte Carlo simulation of extracellular diffusion in brain tissues," *Physics in Medicine and Biology*, vol. 35, pp. 441–447, Mar. 1990.

[102] H. Johannesson and B. Halle, "Solvent diffusion in ordered macrofluids: A stochastic simulation study of the obstruction effect," *The Journal of Chemical Physics*, vol. 104, no. 17, p. 6807, 1996.

[103] M. Saxton, "Anomalous diffusion due to obstacles: a Monte Carlo study," *Biophysical Journal*, vol. 66, pp. 394–401, Feb. 1994.

[104] P. Liu, E. Harder, and B. J. Berne, "On the calculation of diffusion coefficients in confined fluids and interfaces with an application to the liquidvapor interface of water," *The Journal of Physical Chemistry B*, vol. 108, pp. 6595–6602, May 2004.

[105] R. W. Pastor, "Techniques and applications of Langevin dynamics simulations," in *The Molecular Dynamics of Liquid Crystals*, pp. 85–138, Springer, 1994.

[106] W. L. Dunn and J. K. Shultis, *Exploring Monte Carlo methods*. Elsevier, 2011.

[107] M. Kalos and P. Whitlock, *Monte Carlo methods*. John Wiley & Sons, 2008.

[108] A. Kalampokis, P. Argyrakis, and P. Macheras, "No Title," *Pharmaceutical Research*, vol. 16, no. 1, pp. 87–91, 1999.

[109] A. Luiten, F. Knoet, M. T. Vlaardingerbroek, and J. A. Boer, *Magnetic resonance imaging: theory and practice*. Springer Berlin Heidelberg, 2013.

[110] S. C. Bushong and G. Clarke, *Magnetic resonance imaging: physical and biological principles*. Elsevier Health Sciences, 2013.

[111] S. W. Atlas, *Magnetic resonance imaging of the brain and spine*. LWW medical book collection, Lippincott Williams & Wilkins, 2009.

[112] K. Thayalan, *The physics of radiology and imaging*. JP Medical Ltd, 2014.

[113] H. Johansen-Berg and T. E. Behrens, *Diffusion MRI: From quantitative measurement to in vivo neuroanatomy*. Academic Press, 2013.

[114] K. I. Momot, J. M. Pope, and R. M. Wellard, *Medical image processing*. Biological and Medical Physics, Biomedical Engineering, New York, NY: Springer New York, 2011.

[115] A. M. Leferink, R. M. Fratila, M. a. Koenrades, C. a. van Blitterswijk, A. Velders, and L. Moroni, "An open source image processing method

to quantitatively assess tissue growth after non-invasive magnetic resonance imaging in human bone marrow stromal cell seeded 3D polymeric scaffolds," *PLoS ONE*, vol. 9, p. e115000, Dec. 2014.

[116] M. Sarntinoranont, X. Chen, J. Zhao, and T. H. Mareci, "Computational model of interstitial transport in the spinal cord using diffusion tensor imaging," *Annals of Biomedical Engineering*, vol. 34, pp. 1304–1321, Aug. 2006.

[117] D. Sinnaeve, "The Stejskal–Tanner equation generalized for any gradient shapean overview of most pulse sequences measuring free diffusion," *Concepts in Magnetic Resonance Part A*, vol. 40, no. 2, pp. 39–65, 2012.

[118] Y. van de Looij, N. Kunz, P. Hüppi, R. Gruetter, and S. Sizonenko, "Diffusion tensor echo planar imaging using surface coil transceiver with a semiadiabatic RF pulse sequence at 14.1T," *Magnetic Resonance in Medicine*, vol. 65, pp. 732–737, Mar. 2011.

[119] E. Staroswiecki, K. L. Granlund, M. T. Alley, G. E. Gold, and B. A. Hargreaves, "Simultaneous estimation of T2 and apparent diffusion coefficient in human articular cartilage in vivo with a modified three-dimensional double echo steady state (DESS) sequence at 3 T," *Magnetic Resonance in Medicine*, vol. 67, no. 4, pp. 1086–1096, 2012.

[120] D. A. Feinberg and K. Setsompop, "Ultra-fast MRI of the human brain with simultaneous multi-slice imaging," *Journal of Magnetic Resonance*, vol. 229, pp. 90–100, Apr. 2013.

[121] K. Setsompop, R. Kimmlingen, E. Eberlein, T. Witzel, J. Cohen-Adad, J. McNab, B. Keil, M. Tisdall, P. Hoecht, P. Dietz, S. Cauley, V. Tountcheva, V. Matschl, V. Lenz, K. Heberlein, A. Potthast, H. Thein, J. Van Horn, A. Toga, F. Schmitt, D. Lehne, B. Rosen, V. Wedeen, and L. Wald, "Pushing the limits

of in vivo diffusion MRI for the Human Connectome Project," *NeuroImage*, vol. 80, pp. 220–233, Oct. 2013.

[122] R. H. Hashemi, W. G. Bradley, and C. J. Lisanti, *MRI: the basics*. Lippincott Williams & Wilkins, 2012.

[123] H. Luong, B. Goossens, J. Aelterman, L. Platisa, and W. Philips, "Optimizing image quality in MRI: On the evaluation of k-space trajectories for under-sampled MR acquisition," in *2012 Fourth International Workshop on Quality of Multimedia Experience*, pp. 25–26, IEEE, IEEE, July 2012.

[124] A. Lutti, D. L. Thomas, C. Hutton, and N. Weiskopf, "High-resolution functional MRI at 3 T: 3D/2D echo-planar imaging with optimized physiological noise correction," *Magnetic Resonance in Medicine*, vol. 69, no. 6, pp. 1657–1664, 2013.

[125] D. K. Jones, "The effect of gradient sampling schemes on measures derived from diffusion tensor MRI: A Monte Carlo study," *Magnetic Resonance in Medicine*, vol. 51, pp. 807–815, Apr. 2004.

[126] C. Lebel, T. Benner, and C. Beaulieu, "Six is enough? Comparison of diffusion parameters measured using six or more diffusion-encoding gradient directions with deterministic tractography," *Magnetic Resonance in Medicine*, vol. 68, no. 2, pp. 474–483, 2012.

[127] S. B. Vos, D. K. Jones, B. Jeurissen, M. a. Viergever, and A. Leemans, "The influence of complex white matter architecture on the mean diffusivity in diffusion tensor MRI of the human brain," *NeuroImage*, vol. 59, pp. 2208–2216, Feb. 2012.

[128] H. Duffau, *Brain mapping: from neural basis of cognition to surgical applications*. Springer Vienna, 2011.

[129] Y. Yonekawa, T. Tsukahara, A. Valavanis, and N. Khan, *Changing Aspects in Stroke Surgery: Aneurysms, Dissection, Moyamoya angiopathy and EC-IC Bypass*. Acta Neurochirurgica Supplement, Springer Vienna, 2008.

[130] S. de Visser, J. Bowden, E. Wentrup-Byrne, L. Rintoul, T. Bostrom, J. Pope, and K. Momot, "Anisotropy of collagen fibre alignment in bovine cartilage: comparison of polarised light microscopy and spatially resolved diffusion-tensor measurements," *Osteoarthritis and Cartilage*, vol. 16, pp. 689–697, June 2008.

[131] J. G. Raya, A. P. Arnoldi, D. L. Weber, L. Filidoro, O. Dietrich, S. Adam-Neumair, E. Mützel, G. Melkus, R. Putz, M. F. Reiser, P. M. Jakob, and C. Glaser, "Ultra-high field diffusion tensor imaging of articular cartilage correlated with histology and scanning electron microscopy," *Magnetic Resonance Materials in Physics, Biology and Medicine*, vol. 24, pp. 247–258, Aug. 2011.

[132] L. Filidoro, O. Dietrich, J. Weber, E. Rauch, T. Oerther, M. Wick, M. Reiser, and C. Glaser, "High-resolution diffusion tensor imaging of human patellar cartilage: Feasibility and preliminary findings," *Magnetic Resonance in Medicine*, vol. 53, pp. 993–998, May 2005.

[133] R. Knauss, J. Schiller, G. Fleischer, J. Krger, and K. Arnold, "Self-diffusion of water in cartilage and cartilage components as studied by pulsed field gradient NMR," *Magnetic Resonance in Medicine*, vol. 41, pp. 285–292, Feb. 1999.

[134] X. Deng, M. Farley, M. T. Nieminen, M. Gray, and D. Burstein, "Diffusion tensor imaging of native and degenerated human articular cartilage," *Magnetic Resonance Imaging*, vol. 25, pp. 168–171, Feb. 2007.

[135] J. L. Finney, "The water molecule and its interactions: the interaction between

theory, modelling, and experiment," *Journal of Molecular Liquids*, vol. 90, pp. 303–312, Feb. 2001.

[136] D. Le Bihan, J.-F. Mangin, C. Poupon, C. A. Clark, S. Pappata, N. Molko, and H. Chabriat, "Diffusion tensor imaging: Concepts and applications," *Journal of Magnetic Resonance Imaging*, vol. 13, pp. 534–546, Apr. 2001.

[137] E. Fieremans, Y. De Deene, S. Delputte, M. S. Özdemir, Y. DAsseler, J. Vlassenbroeck, K. Deblaere, E. Achten, and I. Lemahieu, "Simulation and experimental verification of the diffusion in an anisotropic fiber phantom," *Journal of Magnetic Resonance*, vol. 190, pp. 189–199, Feb. 2008.

[138] H. Xu, S. F. Othman, and R. L. Magin, "Monitoring tissue engineering using magnetic resonance imaging," *Journal of Bioscience and Bioengineering*, vol. 106, pp. 515–527, Dec. 2008.

[139] C. Beaulieu, "The basis of anisotropic water diffusion in the nervous system - a technical review," *NMR in Biomedicine*, vol. 15, pp. 435–455, Nov. 2002.

[140] B. Taouli, V. Vilgrain, E. Dumont, J.-L. Daire, B. Fan, and Y. Menu, "Evaluation of liver diffusion isotropy and characterization of focal hepatic lesions with two single-shot echo-planar MR imaging sequences: Prospective study in 66 patients," *Radiology*, vol. 226, pp. 71–78, Jan. 2003.

[141] A. M. Heemskerk, T. K. Sinha, K. J. Wilson, and B. M. Damon, "Change in water diffusion properties with altered muscle architecture," *Proceedings of the International Society of Magnetic Resonance in Medicine*, vol. 16, p. 1787, 2008.

[142] J. M. Clark, "The organisation of collagen fibrils in the superficial zones of articular cartilage.," *Journal of Anatomy*, vol. 171, pp. 117–130, 1990.

[143] H. G. Potter, B. R. Black, and L. R. Chong, "New techniques in articular cartilage imaging," *Clinics in Sports Medicine*, vol. 28, pp. 77–94, Jan. 2009.

[144] P. W. Kuchel, A. Coy, and P. Stilbs, "Nmr diffusion-diffraction of water revealing alignment of erythrocytes in a magnetic field and their dimensions and membrane transport characteristics," *Magnetic Resonance in Medicine*, vol. 37, no. 5, pp. 637–643, 1997.

[145] B. Noehren, A. Andersen, T. Feiweier, B. Damon, and P. Hardy, "Comparison of twice refocused spin echo versus stimulated echo diffusion tensor imaging for tracking muscle fibers," *Journal of Magnetic Resonance Imaging*, vol. 41, pp. 624–632, Mar. 2015.

[146] R. Davies and B. Morris, *Molecular biology of the neuron*. Oxford University Press, 2006.

[147] S. Mori and J. Zhang, "Principles of diffusion tensor imaging and its applications to basic neuroscience research," *Neuron*, vol. 51, pp. 527–539, Sept. 2006.

[148] T. Dhollander, L. Emsell, W. Van Hecke, F. Maes, S. Sunaert, and P. Suetens, "Track Orientation Density Imaging (TODI) and Track Orientation Distribution (TOD) based tractography," *NeuroImage*, vol. 94, pp. 312–336, July 2014.

[149] M. Perrin, C. Poupon, B. Rieul, P. Leroux, A. Constantinesco, J.-F. Mangin, and D. LeBihan, "Validation of q-ball imaging with a diffusion fibre-crossing phantom on a clinical scanner," *Philosophical Transactions of the Royal Society B: Biological Sciences*, vol. 360, pp. 881–891, May 2005.

[150] S. De Santis, D. Barazany, D. K. Jones, and Y. Assaf, "Resolving relaxometry and diffusion properties within the same voxel in the presence of crossing

fibres by combining inversion recovery and diffusion-weighted acquisitions," *Magnetic Resonance in Medicine*, vol. 00, pp. n/a–n/a, Mar. 2015.

[151] R. Neto Henriques, M. M. Correia, R. G. Nunes, and H. A. Ferreira, "Exploring the 3D geometry of the diffusion kurtosis tensorImpact on the development of robust tractography procedures and novel biomarkers," *NeuroImage*, vol. 111, pp. 85–99, May 2015.

[152] P. L. Hubbard, F.-L. Zhou, S. J. Eichhorn, and G. J. Parker, "Biomimetic phantom for the validation of diffusion magnetic resonance imaging," *Magnetic Resonance in Medicine*, vol. 73, pp. 299–305, Jan. 2015.

[153] J. S. Temenoff and A. G. Mikos, "Review: tissue engineering for regeneration of articular cartilage," *Biomaterials*, vol. 21, pp. 431–440, Mar. 2000.

[154] K. A. Athanasiou, E. M. Darling, J. C. Hu, G. D. DuRaine, and A. H. Reddi, *Articular cartilage*. Taylor & Francis, 2013.

[155] Y. XIA, "Magic-angle effect in magnetic resonance imaging of articular cartilage," *Investigative Radiology*, vol. 35, pp. 602–621, Oct. 2000.

[156] J. G. Raya, A. Horng, O. Dietrich, S. Krasnokutsky, L. S. Beltran, P. Storey, M. F. Reiser, M. P. Recht, D. K. Sodickson, and C. Glaser, "Articular cartilage: In vivo diffusion-tensor imaging," *Radiology*, vol. 262, pp. 550–559, Feb. 2012.

[157] T. Hayami, M. Pickarski, Y. Zhuo, G. a. Wesolowski, G. a. Rodan, and L. T. Duong, "Characterization of articular cartilage and subchondral bone changes in the rat anterior cruciate ligament transection and meniscectomized models of osteoarthritis," *Bone*, vol. 38, pp. 234–243, Feb. 2006.

[158] Y. Xia, J. Moody, N. Burton-Wurster, and G. Lust, "Quantitative in situ correlation between microscopic MRI and polarized light microscopy studies

of articular cartilage," *Osteoarthritis and Cartilage*, vol. 9, pp. 393–406, July 2001.

[159] J. Mollenhauer, M. Aurich, Z. Zhong, C. Muehleman, A. Cole, M. Hasnah, O. Oltulu, K. Kuettner, A. Margulis, and L. Chapman, "Diffraction-enhanced X-ray imaging of articular cartilage," *Osteoarthritis and Cartilage*, vol. 10, pp. 163–171, Mar. 2002.

[160] M. T. Nieminen, J. Rieppo, J. Toyras, J. M. Hakumaki, J. Silvennoinen, M. M. Hyttinen, H. J. Helminen, and J. S. Jurvelin, "T2 relaxation reveals spatial collagen architecture in articular cartilage: A comparative quantitative MRI and polarized light microscopic study," *Magnetic Resonance in Medicine*, vol. 46, pp. 487–493, Sept. 2001.

[161] N. M. Menezes, M. L. Gray, J. R. Hartke, and D. Burstein, "T2 andT1p MRI in articular cartilage systems," *Magnetic Resonance in Medicine*, vol. 51, pp. 503–509, Mar. 2004.

[162] C. F. Maier, S. G. Tan, H. Hariharan, and H. G. Potter, "T2 quantitation of articular cartilage at 1.5 T," *Journal of Magnetic Resonance Imaging*, vol. 17, pp. 358–364, Mar. 2003.

[163] T. J. Mosher, H. Smith, B. J. Dardzinski, V. J. Schmithorst, and M. B. Smith, "MR imaging and T2 mapping of femoral cartilage," *American Journal of Roentgenology*, vol. 177, pp. 665–669, Sept. 2001.

[164] Y. Xia, J. B. Moody, and H. Alhadlaq, "Orientational dependence ofT2 relaxation in articular cartilage: A microscopic MRI (uMRI) study," *Magnetic Resonance in Medicine*, vol. 48, pp. 460–469, Sept. 2002.

[165] M. J. Kääb, I. a. Gwynn, and H. P. Nötzli, "Collagen fibre arrangement in the

tibial plateau articular cartilage of man and other mammalian species.," *Journal of Anatomy*, vol. 193, pp. 23–34, July 1998.

[166] F. A. Wentorf, *Non-invasive quantification of collagen fiber orientation in articular cartilage*. PhD thesis, University of Minnesota, 2010.

[167] A. K. Jeffery, G. W. Blunn, C. W. Archer, and G. Bentley, "Three-dimensional collagen architecture in bovine articular cartilage.," *The Journal of Bone and Joint Surgery. British Volume*, vol. 73, no. 5, pp. 795–801, 1991.

[168] N. D. Broom and H. Silyn-Roberts, "Collagen-collagen versus collagen-proteoglycan interactions in the determination of cartilage strength," *Arthritis & Rheumatism*, vol. 33, pp. 1512–1517, Oct. 1990.

[169] J. M. Clark, "Variation of collagen fiber alignment in a joint surface: A scanning electron microscope study of the tibial plateau in dog, rabbit, and man," *Journal of Orthopaedic Research*, vol. 9, pp. 246–257, Mar. 1991.

[170] L. Kjellen and U. Lindahl, "Proteoglycans: structures and interactions," *Annual Review of Biochemistry*, vol. 60, pp. 443–475, June 1991.

[171] W. D. Comper and R. P. Williams, "Hydrodynamics of concentrated proteoglycan solutions.," *Journal of Biological Chemistry*, vol. 262, pp. 13464–13471, Oct. 1987.

[172] S. Federico and W. Herzog, "On the anisotropy and inhomogeneity of permeability in articular cartilage," *Biomechanics and Modeling in Mechanobiology*, vol. 7, pp. 367–378, Oct. 2008.

[173] O. M. Abdullah, S. F. Othman, X. J. Zhou, and R. L. Magin, "Diffusion tensor imaging as an early marker for osteoarthritis," in *Proceedings of the International Society of Magnetic Resonance in Medicine*, vol. 15, p. 814, 2007.

[174] D. M. Pierce, W. Trobin, J. G. Raya, S. Trattnig, H. Bischof, C. Glaser, and G. A. Holzapfel, "DT-MRI based computation of collagen fiber deformation in human articular cartilage: a feasibility study," *Annals of Biomedical Engineering*, vol. 38, no. 7, pp. 2447–2463, 2010.

[175] D. A. Binks, R. J. Hodgson, M. E. Ries, R. J. Foster, S. W. Smye, D. McGonagle, and A. Radjenovic, "Quantitative parametric MRI of articular cartilage: a review of progress and open challenges," *The British Journal of Radiology*, vol. 86, p. 20120163, Mar. 2013.

[176] K. I. Momot, "Microstructural magnetic resonance imaging of articular cartilage," *Biomedical Spectroscopy and Imaging*, vol. 1, no. 1, pp. 27–37, 2012.

[177] T. Ukai, M. Sato, T. Yamashita, Y. Imai, G. Mitani, T. Takagaki, K. Serigano, and J. Mochida, "Diffusion tensor imaging can detect the early stages of cartilage damage: a comparison study," *BMC Musculoskeletal Disorders*, vol. 16, no. 1, p. 35, 2015.

[178] S. Yang, K.-F. Leong, Z. Du, and C.-K. Chua, "The design of scaffolds for use in tissue engineering. Part I. Traditional factors," *Tissue Engineering*, vol. 7, pp. 679–689, Dec. 2001.

[179] N. Zhu and X. Chen, *Advances in biomaterials science and biomedical applications*. InTech, Mar. 2013.

[180] M. Nakamura, S. Iwanaga, C. Henmi, K. Arai, and Y. Nishiyama, "Biomatrices and biomaterials for future developments of bioprinting and biofabrication," *Biofabrication*, vol. 2, p. 014110, Mar. 2010.

[181] N. Ristovski, N. Bock, S. Liao, S. K. Powell, J. Ren, G. T. S. Kirby, K. A. Blackwood, and M. A. Woodruff, "Improved fabrication of melt electrospun

tissue engineering scaffolds using direct writing and advanced electric field control," *Biointerphases*, Mar. 2015.

[182] D. Seliktar, D. Dikovsky, and E. Napadensky, "Bioprinting and tissue engineering: Recent advances and future perspectives," *Israel Journal of Chemistry*, vol. 53, no. 9-10, pp. 795–804, 2013.

[183] J.-H. Shim, J. Y. Kim, M. Park, J. Park, and D.-W. Cho, "Development of a hybrid scaffold with synthetic biomaterials and hydrogel using solid freeform fabrication technology," *Biofabrication*, vol. 3, p. 034102, Sept. 2011.

[184] F. Pati, J. Jang, D.-H. Ha, S. Won Kim, J.-W. Rhie, J.-H. Shim, D.-H. Kim, and D.-W. Cho, "Printing three-dimensional tissue analogues with decellularized extracellular matrix bioink," *Nature Communications*, vol. 5, pp. 1–11, June 2014.

[185] S. N. Jayasinghe, S. Irvine, and J. R. McEwan, "Cell electrospinning highly concentrated cellular suspensions containing primary living organisms into cell-bearing threads and scaffolds," *Nanomedicine*, vol. 2, pp. 555–567, Aug. 2007.

[186] C. Agrawal and R. B. Ray, "Biodegradable polymeric scaffolds for musculoskeletal tissue engineering," *Journal of Biomedical Materials Research*, vol. 55, no. 2, pp. 141–150, 2001.

[187] D. W. Hutmacher, "Scaffolds in tissue engineering bone and cartilage.," *Biomaterials*, vol. 21, pp. 2529–2543, Dec. 2000.

[188] S. Konopnicki, B. Sharaf, C. Resnick, A. Patenaude, T. Pogal-Sussman, K.-G. Hwang, H. Abukawa, and M. J. Troulis, "Tissue-engineered bone with 3-dimensionally printed β-Tricalcium Phosphate and Polycaprolactone scaffolds and early implantation: An in vivo pilot study in a porcine mandible msodel,"

Journal of Oral and Maxillofacial Surgery, vol. 73, pp. 1016.e1–1016.e11, May 2015.

[189] C. J. Rivet, K. Zhou, R. J. Gilbert, D. I. Finkelstein, and J. S. Forsythe, "Cell infiltration into a 3D electrospun fiber and hydrogel hybrid scaffold implanted in the brain.," *Biomatter*, vol. 5, no. 1, p. e1005527, 2015.

[190] M. Lee, B. M. Wu, and J. C. Y. Dunn, "Effect of scaffold architecture and pore size on smooth muscle cell growth," *Journal of Biomedical Materials Research Part A*, vol. 87A, pp. 1010–1016, Dec. 2008.

[191] D. W. Hutmacher, M. Sittinger, and M. V. Risbud, "Scaffold-based tissue engineering: rationale for computer-aided design and solid free-form fabrication systems," *Trends in Biotechnology*, vol. 22, pp. 354–362, July 2004.

[192] G. Feng, X. Jin, J. Hu, H. Ma, M. J. Gupte, H. Liu, and P. X. Ma, "Effects of hypoxias and scaffold architecture on rabbit mesenchymal stem cell differentiation towards a nucleus pulposus-like phenotype," *Biomaterials*, vol. 32, pp. 8182–8189, Nov. 2011.

[193] S. J. Hollister, "Porous scaffold design for tissue engineering.," *Nature Materials*, vol. 4, no. 7, pp. 518–524, 2005.

[194] A. C. Bean and R. S. Tuan, "Fiber diameter and seeding density influence chondrogenic differentiation of mesenchymal stem cells seeded on electrospun poly(ϵ -caprolactone) scaffolds," *Biomedical Materials*, vol. 10, p. 015018, Jan. 2015.

[195] W.-Y. Yeong, C.-K. Chua, K.-F. Leong, and M. Chandrasekaran, "Rapid prototyping in tissue engineering: challenges and potential," *Trends in Biotechnology*, vol. 22, pp. 643–652, Dec. 2004.

[196] R. H. Harrison, J.-P. St-Pierre, and M. M. Stevens, "Tissue engineering and regenerative medicine: A year in review," *Tissue Engineering Part B: Reviews*, vol. 20, pp. 1–16, Feb. 2014.

[197] A. D. Lantada and P. L. Morgado, "Rapid Prototyping for Biomedical Engineering: Current Capabilities and Challenges," *Annual Review of Biomedical Engineering*, vol. 14, no. 1, pp. 73–96, 2012.

[198] J. M. Sobral, S. G. Caridade, R. a. Sousa, J. a. F. Mano, and R. L. Reis, "Three-dimensional plotted scaffolds with controlled pore size gradients: Effect of scaffold geometry on mechanical performance and cell seeding efficiency," *Acta Biomaterialia*, vol. 7, pp. 1009–1018, Mar. 2011.

[199] P. D. Dalton, C. Vaquette, B. L. Farrugia, T. R. Dargaville, T. D. Brown, and D. W. Hutmacher, "Electrospinning and additive manufacturing: converging technologies," *Biomaterials Science*, vol. 1, no. 2, pp. 171–185, 2013.

[200] S. V. Murphy and A. Atala, "3D bioprinting of tissues and organs," *Nature Biotechnology*, vol. 32, pp. 773–785, Aug. 2014.

[201] T. D. Brown, P. D. Dalton, and D. W. Hutmacher, "Direct writing by way of melt electrospinning," *Advanced Materials*, vol. 23, pp. 5651–5657, Dec. 2011.

[202] L. D. Loozen, F. Wegman, F. C. Öner, W. J. A. Dhert, and J. Alblas, "Porous bioprinted constructs in BMP-2 non-viral gene therapy for bone tissue engineering," *Journal of Materials Chemistry B*, vol. 1, no. 48, p. 6619, 2013.

[203] H. A. Almeida and P. J. Bártolo, "Structural and vascular analysis of tissue engineering scaffolds, part 1: numerical fluid analysis," in *Computer-Aided Tissue Engineering*, pp. 183–207, Springer, 2012.

[204] R. McCoy, C. Jungreuthmayer, and F. O'Brien, "Influence of flow rate and scaffold pore size on cell behavior during mechanical stimulation in a flow

perfusion bioreactor," *Biotechnology and Bioengineering*, vol. 109, pp. 1583–1594, June 2012.

[205] L. D. Garza-García, E. García-López, S. Camacho-León, M. Del Refugio Rocha-Pizaña, F. López-Pacheco, J. López-Meza, D. Araiz-Hernández, E. J. Tapia-Mejía, G. Trujillo-de Santiago, C. A. Rodríguez-González, and M. M. Alvarez, "Continuous flow micro-bioreactors for the production of biopharmaceuticals: the effect of geometry, surface texture, and flow rate.," *Lab on a Chip*, vol. 14, no. 7, pp. 1320–9, 2014.

[206] M. S. Hossain, X. B. Chen, and D. J. Bergstrom, "Investigation of the in vitro culture process for skeletal-tissue-engineered constructs using computational fluid dynamics and experimental methods.," *Journal of Biomechanical Engineering*, vol. 134, no. 12, p. 121003, 2012.

[207] J. Rnjak-Kovacina and A. S. Weiss, "Increasing the pore size of electrospun scaffolds," *Tissue Engineering Part B: Reviews*, vol. 17, pp. 365–372, Oct. 2011.

[208] L. Ma, J. Barker, C. Zhou, W. Li, J. Zhang, B. Lin, G. Foltz, J. Küblbeck, and P. Honkakoski, "Towards personalized medicine with a three-dimensional micro-scale perfusion-based two-chamber tissue model system," *Biomaterials*, vol. 33, pp. 4353–4361, June 2012.

[209] P. Karuppuswamy, J. R. Venugopal, B. Navaneethan, A. L. Laiva, S. Sridhar, and S. Ramakrishna, "Functionalized hybrid nanofibers to mimic native ECM for tissue engineering applications," *Applied Surface Science*, vol. 322, pp. 162–168, Dec. 2014.

[210] A. Weigand, A. M. Boos, J. P. Beier, and R. E. Horch, "Comments on: In vivo bone regeneration usingtubular perfusion system bioreactor cultured nanofibrous scaffolds vascularizationOne challenge of tissue engineering," *Tissue Engineering Part A*, vol. 20, pp. 1778–1779, June 2014.

[211] F. Pennella, G. Cerino, D. Massai, D. Gallo, G. Falvo DUrso Labate, A. Schiavi, M. a. Deriu, A. Audenino, and U. Morbiducci, "A survey of methods for the evaluation of tissue engineering scaffold permeability," *Annals of Biomedical Engineering*, vol. 41, pp. 2027–2041, Oct. 2013.

[212] S. F. Othman, K. Wartella, V. Khalilzad Sharghi, and H. Xu, "The e-incubator: A magnetic resonance imaging-compatible mini incubator," *Tissue Engineering Part C: Methods*, vol. 21, pp. 347–355, Apr. 2015.

[213] P. Langevin, "On the theory of Brownian motion," *C. R. Academy of Science (Paris)*, vol. 146, pp. 530–533, 1908.

[214] T. E. J. Behrens, H. J. Berg, S. Jbabdi, M. F. S. Rushworth, and M. W. Woolrich, "Probabilistic diffusion tractography with multiple fibre orientations: What can we gain?," *NeuroImage*, vol. 34, no. 1, pp. 144–155, 2007.

[215] A. M. Bhosale and J. B. Richardson, "Articular cartilage: Structure, injuries and review of management," *British Medical Bulletin*, vol. 87, no. 1, pp. 77–95, 2008.

[216] B. Brodsky and J. Baum, "Structural biology: Modelling collagen diseases.," *Nature*, vol. 453, no. 7198, pp. 998–999, 2008.

[217] K.-D. Merboldt, W. Hanicke, and J. Frahm, "Self-diffusion NMR imaging using stimulated echoes," *Journal of Magnetic Resonance (1969)*, vol. 64, pp. 479–486, Oct. 1985.

[218] K. M. Hasan and P. A. Narayana, "Retrospective measurement of the diffusion tensor eigenvalues from diffusion anisotropy and mean diffusivity in DTI," *Magnetic Resonance in Medicine*, vol. 56, no. 1, pp. 130–137, 2006.

[219] Lihui Wang, Yuemin Zhu, Hongying Li, Wanyu Liu, and I. E. Magnin, "Multiscale modeling and simulation of the cardiac fiber architecture for

DMRI," *IEEE Transactions on Biomedical Engineering*, vol. 59, pp. 16–19, Jan. 2012.

[220] E. Fieremans, D. S. Novikov, J. H. Jensen, and J. A. Helpern, "Monte Carlo study of a two-compartment exchange model of diffusion," *NMR in Biomedicine*, vol. 23, pp. 711–724, Sept. 2010.

[221] K. I. Momot, J. M. Pope, and M. R. Wellard, *In medical image processing: techniques and applications, edited by Geoff Dougherty*. Springer, New York, 2011.

[222] C. Pierpaoli and P. J. Basser, "Toward a quantitative assessment of diffusion anisotropy," *Magnetic Resonance in Medicine*, vol. 36, pp. 893–906, Dec. 1996.

[223] S. N. Jespersen, C. R. Bjarkam, J. R. Nyengaard, M. M. Chakravarty, B. Hansen, T. Vosegaard, L. Ø stergaard, D. Yablonskiy, N. C. Nielsen, and P. Vestergaard-Poulsen, "Neurite density from magnetic resonance diffusion measurements at ultrahigh field: Comparison with light microscopy and electron microscopy," *NeuroImage*, vol. 49, no. 1, pp. 205–216, 2010.

[224] X. Lux Lu, C. Miller, F. H. Chen, X. Edward Guo, and V. C. Mow, "The generalized triphasic correspondence principle for simultaneous determination of the mechanical properties and proteoglycan content of articular cartilage by indentation," *Journal of Biomechanics*, vol. 40, no. 11, pp. 2434–2441, 2007.

[225] J. G. Raya, G. Melkus, S. Adam-Neumair, O. Dietrich, E. Mützel, B. Kahr, M. F. Reiser, P. M. Jakob, R. Putz, and C. Glaser, "Change of diffusion tensor imaging parameters in articular cartilage with progressive proteoglycan extraction.," *Investigative Radiology*, vol. 46, no. 6, pp. 401–409, 2011.

[226] D. S. Novikov and V. G. Kiselev, "Effective medium theory of a diffusion-weighted signal," *NMR in Biomedicine*, vol. 23, pp. 682–697, Sept. 2010.

[227] A. Szafer, J. Zhong, and J. C. Gore, "Theoretical model for water diffusion in tissues," *Magnetic Resonance in Medicine*, vol. 33, pp. 697–712, May 1995.

[228] M. J. Kääb, K. Ito, B. Rahn, J. M. Clark, and H. P. Nötzli, "Effect of mechanical load on articular cartilage collagen structure: a scanning electron-microscopic study.," *Cells, Tissues, Organs*, vol. 167, no. 2-3, pp. 106–120, 2000.

[229] R. Minns and F. Steven, "The collagen fibril organisation in human articular cartilage," *Journal of Anatomy*, vol. 123, no. 2, pp. 437–457, 1976.

[230] J. Rieppo, J. Hallikainen, J. S. Jurvelin, I. Kiviranta, H. J. Helminen, and M. M. Hyttinen, "Practical considerations in the use of polarized light microscopy in the analysis of the collagen network in articular cartilage," *Microscopy Research and Technique*, vol. 71, pp. 279–287, Apr. 2008.

[231] U. Duvvuri, R. Reddy, S. D. Patel, J. H. Kaufman, J. B. Kneeland, and J. S. Leigh, "T1ρ-relaxation in articular cartilage: Effects of enzymatic degradation," *Magnetic Resonance in Medicine*, vol. 38, pp. 863–867, Dec. 1997.

[232] V. Mlynárik, S. Trattnig, M. Huber, A. Zembsch, and H. Imhof, "The role of relaxation times in monitoring proteoglycan depletion in articular cartilage," *Journal of Magnetic Resonance Imaging*, vol. 10, no. 4, pp. 497–502, 1999.

[233] G. Karp, *Cell and molecular biology: concepts and experiments*. John Wiley and Sons, 2009.

[234] R. Z. Kramer, J. Bella, P. Mayville, B. Brodsky, and H. M. Berman, "Sequence dependent conformational variations of collagen triple-helical structure," 1999.

[235] J. B. Keller, "Inverse problems," *The American Mathematical Monthly*, vol. 83, p. 107, Feb. 1976.

[236] N. Shemesh, C.-F. Westin, and Y. Cohen, "Magnetic resonance imaging by synergistic diffusion-diffraction patterns," *Physical Review Letters*, vol. 108, p. 058103, Jan. 2012.

[237] J. H. Strange, M. Rahman, and E. G. Smith, "Characterization of porous solids by NMR," *Physical Review Letters*, vol. 71, pp. 3589–3591, Nov. 1993.

[238] D. Le Bihan, "Molecular diffusion, tissue microdynamics and microstructure.," *NMR in Biomedicine*, vol. 8, no. 7-8, pp. 375–386, 1996.

[239] S. N. Hwang, C.-L. Chin, F. W. Wehrli, and D. B. Hackney, "An image-based finite difference model for simulating restricted diffusion," *Magnetic Resonance in Medicine*, vol. 50, pp. 373–382, Aug. 2003.

[240] N. Wiener, "The average of an analytic functional and the Brownian movement," *Proceedings of the National Academy of Sciences USA*, vol. 7, no. 10, pp. 294–298, 1921.

[241] C. Vamo, N. Suciu, and H. Vereecken, "Generalized random walk algorithm for the numerical modeling of complex diffusion processes," *Journal of Computational Physics*, vol. 186, pp. 527–544, Apr. 2003.

[242] L. Fousse, G. Hanrot, V. Lefèvre, P. Pélissier, and P. Zimmermann, "MPFR," *ACM Transactions on Mathematical Software*, vol. 33, pp. 13–es, June 2007.

[243] T. Bickel, "A note on confined diffusion," *Physica A: Statistical Mechanics and its Applications*, vol. 377, pp. 24–32, Apr. 2007.

[244] D. Van Nguyen, J.-R. Li, D. Grebenkov, and D. Le Bihan, "A finite elements method to solve the Bloch–Torrey equation applied to diffusion magnetic resonance imaging," *Journal of Computational Physics*, vol. 263, pp. 283–302, 2014.

[245] J. Xu, M. D. Does, and J. C. Gore, "Numerical study of water diffusion in biological tissues using an improved finite difference method," *Physics in Medicine and Biology*, vol. 52, no. 7, p. N111, 2007.

[246] S. Fichele, M. N. J. Paley, N. Woodhouse, P. D. Griffiths, E. J. R. van Beek, and J. M. Wild, "Investigating 3He diffusion NMR in the lungs using finite difference simulations and in vivo PGSE experiments," *Journal of Magnetic Resonance*, vol. 167, no. 1, pp. 1–11, 2004.

[247] R. Langer and J. P. Vacanti, "Tissue engineering," *Science*, vol. 260, no. 5110, pp. 920–6, 1993.

[248] C. Norotte, F. S. Marga, L. E. Niklason, and G. Forgacs, "Scaffold-free vascular tissue engineering using bioprinting," *Biomaterials*, vol. 30, pp. 5910–5917, Oct. 2009.

[249] T. Shimizu, "Fabrication of pulsatile cardiac tissue grafts using a novel 3-dimensional cell sheet manipulation technique and temperature-responsive cell culture surfaces," *Circulation Research*, vol. 90, pp. 40e–48, Feb. 2002.

[250] B. Dhariwala, E. Hunt, and T. Boland, "Rapid prototyping of tissue-engineering constructs, using photopolymerizable hydrogels and stereolithography.," *Tissue Engineering*, vol. 10, no. 9-10, pp. 1316–1322, 2004.

[251] D. R. Albrecht, G. H. Underhill, T. B. Wassermann, R. L. Sah, and S. N. Bhatia, "Probing the role of multicellular organization in three-dimensional microenvironments," *Nature Methods*, vol. 3, pp. 369–375, May 2006.

[252] T. Boland, T. Xu, B. Damon, and X. Cui, "Application of inkjet printing to tissue engineering," *Biotechnology Journal*, vol. 1, pp. 910–917, Sept. 2006.

[253] D. L. Cohen, E. Malone, H. Lipson, and L. J. Bonassar, "Direct freeform

fabrication of seeded hydrogels in arbitrary geometries," *Tissue Engineering*, vol. 12, pp. 1325–1335, May 2006.

[254] W. Schuurman, V. Khristov, M. W. Pot, P. R. van Weeren, W. J. a. Dhert, and J. Malda, "Bioprinting of hybrid tissue constructs with tailorable mechanical properties," *Biofabrication*, vol. 3, p. 021001, June 2011.

[255] S. Giannitelli, D. Accoto, M. Trombetta, and A. Rainer, "Current trends in the design of scaffolds for computer-aided tissue engineering," *Acta Biomaterialia*, vol. 10, pp. 580–594, Feb. 2014.

[256] B. A. Blakeney, A. Tambralli, J. M. Anderson, A. Andukuri, D. J. Lim, D. R. Dean, and H. W. Jun, "Cell infiltration and growth in a low density, uncompressed three-dimensional electrospun nanofibrous scaffold," *Biomaterials*, vol. 32, no. 6, pp. 1583–1590, 2011.

[257] R. Murugan and S. Ramakrishna, "Design strategies of tissue engineering scaffolds with controlled fiber orientation," *Tissue Engineering*, vol. 13, pp. 1845–1866, Aug. 2007.

[258] B. L. Farrugia, T. D. Brown, Z. Upton, D. W. Hutmacher, P. D. Dalton, and T. R. Dargaville, "Dermal fibroblast infiltration of poly(ϵ-caprolactone) scaffolds fabricated by melt electrospinning in a direct writing mode," *Biofabrication*, vol. 5, p. 025001, June 2013.

[259] I. Shabani, V. Haddadi-Asl, E. Seyedjafari, and M. Soleimani, "Cellular infiltration on nanofibrous scaffolds using a modified electrospinning technique," *Biochemical and Biophysical Research Communications*, vol. 423, pp. 50–54, June 2012.

[260] J. L. Lowery, N. Datta, and G. C. Rutledge, "Effect of fiber diameter, pore size and seeding method on growth of human dermal fibroblasts in electrospun

poly(-caprolactone) fibrous mats," *Biomaterials*, vol. 31, pp. 491–504, Jan. 2010.

[261] N. Detta, T. D. Brown, F. K. Edin, K. Albrecht, F. Chiellini, E. Chiellini, P. D. Dalton, and D. W. Hutmacher, "Melt electrospinning of polycaprolactone and its blends with poly(ethylene glycol)," *Polymer International*, vol. 59, pp. 1558–1562, Nov. 2010.

[262] S. T. Ho and D. W. Hutmacher, "A comparison of micro CT with other techniques used in the characterization of scaffolds," *Biomaterials*, vol. 27, pp. 1362–1376, Mar. 2006.

[263] A. Salerno, D. Guarnieri, M. Iannone, S. Zeppetelli, and P. a. Netti, "Effect of micro- and macroporosity of bone tissue three-dimensional-poly(-caprolactone) scaffold on human mesenchymal stem cells invasion, proliferation, and differentiation in vitro," *Tissue Engineering Part A*, vol. 16, pp. 2661–2673, Aug. 2010.

[264] H. Yoshimoto, Y. Shin, H. Terai, and J. Vacanti, "A biodegradable nanofiber scaffold by electrospinning and its potential for bone tissue engineering," *Biomaterials*, vol. 24, pp. 2077–2082, May 2003.

[265] T. S. Karande, J. L. Ong, and C. M. Agrawal, "Diffusion in musculoskeletal tissue engineering scaffolds: design issues related to porosity, permeability, architecture, and nutrient mixing.," *Annals of Biomedical Engineering*, vol. 32, pp. 1728–1743, Dec. 2004.

[266] J. R. Jones, R. C. Atwood, G. Poologasundarampillai, S. Yue, and P. D. Lee, "Quantifying the 3D macrostructure of tissue scaffolds," *Journal of Materials Science: Materials in Medicine*, vol. 20, pp. 463–471, Feb. 2009.

[267] S. Even-Ram and K. M. Yamada, "Cell migration in 3D matrix," *Current Opinion in Cell Biology*, vol. 17, pp. 524–532, Oct. 2005.

[268] D. E. Sosnovik, R. Wang, G. Dai, T. G. Reese, and V. J. Wedeen, "Diffusion MR tractography of the heart," *Journal of Cardiovascular Magnetic Resonance*, vol. 11, no. 1, p. 47, 2009.

[269] I. Martin, D. Wendt, and M. Heberer, "The role of bioreactors in tissue engineering," *Trends in Biotechnology*, vol. 22, pp. 80–86, Feb. 2004.

[270] B. J. Lawrence, M. Devarapalli, and S. V. Madihally, "Flow dynamics in bioreactors containing tissue engineering scaffolds," *Biotechnology and Bioengineering*, vol. 102, pp. 935–947, Feb. 2009.

[271] J. Malda, T. J. Klein, and Z. Upton, "The roles of hypoxia in the in vitro engineering of tissues," *Tissue Engineering*, vol. 13, pp. 2153–2162, Sept. 2007.

[272] A. Einstein, "Über die von der molekularkinetischen Theorie der Wärme geforderte Bewegung von in ruhenden Flüssigkeiten suspendierten Teilchen," *Annalen der Physik*, vol. 322, no. 8, pp. 549–560, 1905.

[273] K. Toukan and A. Rahman, "Molecular-dynamics study of atomic motions in water," *Physical Review B*, vol. 31, pp. 2643–2648, Mar. 1985.

[274] A. Bondi, "van der Waals volumes and radii," *The Journal of Physical Chemistry*, vol. 68, pp. 441–451, Mar. 1964.

[275] F. Franks, *Water: a matrix of life*. Royal Society of Chemistry, Cambridge, 2000.

[276] Y. Wu, H. L. Tepper, and G. A. Voth, "Flexible simple point-charge water model with improved liquid-state properties," *The Journal of Chemical Physics*, vol. 124, no. 2, p. 024503, 2006.

[277] D. K. Jones, *Diffusion MRI: Theory, methods, and applications*. New York: Oxford University Press, 2011.

[278] F. Reif, *Fundamentals of statistical and thermal physics:*. New York: McGraw-Hill, 1965.

[279] C. S. Johnson, "Encyclopedia of Nuclear Magnetic Resonance," in *Encyclopedia of Nuclear Magnetic Resonance*, pp. 1626–1644, New York: Wiley, 1966.

[280] M. Descoteaux, R. Deriche, D. Le Bihan, J.-F. Mangin, and C. Poupon, "Multiple q-shell diffusion propagator imaging," *Medical Image Analysis*, vol. 15, no. 4, pp. 603–621, 2011.

[281] A. P. Hosseinbor, M. K. Chung, Y.-C. Wu, and A. L. Alexander, "Bessel Fourier Orientation Reconstruction (BFOR): An analytical diffusion propagator reconstruction for hybrid diffusion imaging and computation of q-space indices," *NeuroImage*, vol. 64, no. 0, pp. 650–670, 2013.

[282] D. Grebenkov, "NMR survey of reflected Brownian motion," *Reviews of Modern Physics*, vol. 79, pp. 1077–1137, Aug. 2007.

[283] D. S. Grebenkov, "Pulsed-gradient spin-echo monitoring of restricted diffusion in multilayered structures," *Journal of Magnetic Resonance*, vol. 205, no. 2, pp. 181–195, 2010.

[284] W. Wyss, "The fractional diffusion equation," *Journal of Mathematical Physics*, vol. 27, no. 11, pp. 2782–2785, 1986.

[285] R. Metzler and J. Klafter, "The random walk's guide to anomalous diffusion: a fractional dynamics approach," *Physics Reports*, vol. 339, no. 1, pp. 1–77, 2000.

[286] H. Jiang, F. Liu, I. Turner, and K. Burrage, "Analytical solutions for the multi-term timespace CaputoRiesz fractional advectiondiffusion equations on a finite

domain," *Journal of Mathematical Analysis and Applications*, vol. 389, no. 2, pp. 1117–1127, 2012.

[287] J. E. Tanner, "Transient diffusion in a system partitioned by permeable barriers. Application to NMR measurements with a pulsed field gradient," *The Journal of Chemical Physics*, vol. 69, no. 4, pp. 1748–1754, 1978.

[288] A. L. Sukstanskii, D. A. Yablonskiy, and J. J. H. Ackerman, "Effects of permeable boundaries on the diffusion-attenuated {MR} signal: insights from a one-dimensional model," *Journal of Magnetic Resonance*, vol. 170, no. 1, pp. 56–66, 2004.

[289] M. Nordin, M. Nilsson-Jacobi, and M. Nydén, "A mixed basis approach in the SGP-limit," *Journal of Magnetic Resonance*, vol. 212, no. 2, pp. 274–279, 2011.

[290] G. Mohanty, *Lattice path counting and applications*. Probability and mathematical statistics, Academic Press, 2014.

[291] E. W. Montroll and G. H. Weiss, "Random walks on lattices. II," *Journal of Mathematical Physics*, vol. 6, no. 2, pp. 167–181, 1965.

[292] J. R. Norris, *Markov Chains*. Cambridge Series in Statistical and Probabilistic Mathematics, Cambridge: Cambridge University Press, 1997.

[293] G. F. Lawler, *Introduction to stochastic processes, second edition*. Chapman & Hall/CRC Probability Series, Taylor & Francis, 2006.

[294] N. G. Van Kampen, *Stochastic processes in physics and chemistry*. Amsterdam: North-Holland, 1981.

[295] H. Risken, *The Fokker-Planck equation: Methods of solution and applications*. Springer Berlin Heidelberg, 1996.

[296] E. M. LaBolle, J. Quastel, and G. E. Fogg, "Diffusion theory for transport in porous media: Transition-probability densities of diffusion processes corresponding to advection-dispersion equations," *Water Resources Research*, vol. 34, no. 7, pp. 1685–1693, 1998.

[297] A. V. Barzykin and S. Hashimoto, "Reaction kinetics in zeolites as a random walk problem: Theory versus experiment," *The Journal of Chemical Physics*, vol. 113, no. 7, pp. 2841–2845, 2000.

[298] F. Cadini and E. Zio, "Simulation of reactive diffusion in clays by a continuous-time Markovian particle-tracking scheme," *The Journal of Physical Chemistry C*, vol. 117, no. 36, pp. 18510–18519, 2013.

Appendix A

Derivation of Langevin dynamics equations of motion

Water diffusion is the stochastic translational motion of water molecules driven by their thermal energy (Brownian motion) [272]. This seemingly random motion arises from instabilities in the evolving many-body system, and is commonly simulated using stochastic dynamics methods such as Monte-Carlo or Langevin dynamics. In this study, molecular motion was modelled using the Langevin equation:

$$m\frac{d^2\mathbf{r}}{dt^2} = -\nabla U_c - \beta\frac{d\mathbf{r}}{dt} + \boldsymbol{\gamma}(t) \tag{A.1}$$

This stochastic differential equation describes the net force acting on each water molecule as the sum of three different forces: (1) a quasi-randomly directed force arising from interactions with the surrounding water molecules, $\boldsymbol{\gamma}(t)$, (2) a deterministic external force, $-\nabla U_c$, and (3) a hydrodynamic friction force, $-\beta\ d\mathbf{r}/dt$. Numerical integration of this equation was used in the simulations to compute molecular displacements.

The integration time step, Δt, was chosen to be greater than the velocity autocorrelation time of water (VACT $\approx 150\,fs$ [273]). As a result, the quasi-random force, $\boldsymbol{\gamma}(t)$, can be considered uncorrelated with its value in previous times steps and with the current direction of the conservative force, $\mathbf{F}_c$:

$$\langle \boldsymbol{\gamma}(t-\Delta t)\cdot\boldsymbol{\gamma}(t)\rangle = 0 : \Delta t \neq 0 \tag{A.2}$$

$$\langle \boldsymbol{\gamma}(t)\cdot\mathbf{F}_c(t)\rangle = 0 \tag{A.3}$$

In the absence of the quasi-random force, $\boldsymbol{\gamma}(t)$, the only forces experienced by a water molecule in a potential are due to the potential itself, and the associated hydrodynamic friction force. As $\Delta t >>$ VACT, the molecule will almost immediately reach its terminal velocity within each time step. Consequently, for most of the time step, Δt, the conservative force can be considered to balance the friction force:

$$\mathbf{F}_c = 6\pi\eta R\frac{d\mathbf{r}}{dt} \tag{A.4}$$

where η is the viscosity of the surrounding medium, R is the Stokes radius of the water molecule, and $d\mathbf{r}/dt$ is its velocity. We note that the condition $\Delta t >>$ VACT is not an approximation and therefore does not serve as a source of systematic error in the LD simulations presented. The physical diffusion process is not divided into time steps; rather, the time-dependent quantities $\gamma(t), \mathbf{F}_c(t)$ and $\mathbf{r}(t)$ are subject to continuous stochastic change. The condition $\Delta t >>$ VACT reflects the physical reality of this process in that the hydrodynamic friction force balances the conservative force at any given time t, not just at the end of fictitious time steps. Integration of Eq. (A.4) results in an expression for the displacement due to conservative and friction forces:

$$\Delta \mathbf{r}_c = \mathbf{F}_c \frac{\Delta t}{6\pi\eta R} \tag{A.5}$$

In the presence of the quasi-random force, the water molecule undergoes a randomly directed step of fixed length. The magnitude of the step is a function of the integration time, Δt, and the empirical diffusion coefficient of water molecules in bulk water, D_o, defined via the Einstein relation:

$$\Delta \mathbf{r}_r = \xi \sqrt{6 D_o \Delta t} \tag{A.6}$$

where ξ is a unit vector with an uncorrelated random direction chosen for each time step. As a consequence, the displacement of water molecules due to the randomly directed force and its associated friction, $\Delta \mathbf{r}_r(t)$, and the displacement due to the conservative force and its associated friction, $\Delta \mathbf{r}_c(t)$ can be independently calculated. These two displacements can then be combined to produce the net displacement during the time interval Δt:

$$\Delta \mathbf{r} = \Delta \mathbf{r}_r(\Delta t) + \Delta \mathbf{r}_c(\Delta t) \tag{A.7}$$

The typical magnitude of Δr corresponding to $\Delta t = 0.2\,ps$ was 0.5 Å to 1 Å, depending on the proximity of the tracer molecule to a fibre This step size was several orders of magnitude smaller than fibre diameter but comparable to the length scale of the van der Waals potential from a given fibre (see Appendix B).

Appendix B

Coarse-grained water/fibre interaction potential

The model collagen fibres used in this study were based on a molecular model of a synthetic collagen-like model peptide T3-785 containing a segment of human type III collagen (PDB Id:1BKV [234]). The sequence used contained the atom types and locations for an 8nm long triple helical structure. This collagen segment was then assembled into the outer layer of a partial cylinder for use in determining the force field parameters for the course-grained fibre model. The assembly process involved vertically stacking these segments to form long fibrils which were then placed next to each other to form the cylindrical surface of the required radius.

The potential energy of a H_2O molecule near a fibre was modelled as a pair-wise sum of Lennard-Jones-like potentials describing the interaction between the water molecule and each atom on the surface of the fibre:

$$V_i(F) = \sum_{j=1}^{N} \left(4\varepsilon \left[\left(\frac{\sigma_{ij}}{r_{ij}} \right)^{12} - \left(\frac{\sigma_{ij}}{r_{ij}} \right)^{6} \right] \right) \tag{B.1}$$

where V_i is the potential energy of molecule i, ε is the LJ parameter for energy

between water molecule i and fibre atom j, σ_{ij} is the LJ distance parameter, and r_{ij} is the separation between the water molecule i and the fibre atom j.

The values of σ_{ij} for each of the pair-wise interactions were calculated using their respective van der Walls radii (vdW) [274]:

$$\sigma_{ij} = \frac{(r_{vdW_{H_2O}} + r_{vdW_j})}{2^{1/6}} \tag{B.2}$$

where $r_{vdW_{H_2O}} = 1.41 \times 10^{-10}\, m$ is the effective vdW radius of water [275]. The value for ε was taken as the energy representing the $O \cdots O$ interactions from the SPC water model ($0.1554\, kcal/mol$ [276]).

The value of $V_i(F)$ was calculated for a series of paths directed toward the fibre axis. Each path extended approximately $5\, nm$ from the fibre wall and had different z locations. These results were then averaged and a least squares fit of this data was performed to a Lennard-Jones function for use in the course-grained fibre model ($\varepsilon = 4.017\, kJmol^{-1}$ and $\sigma = 6.892$ Å).

It is advantageous to carry out an error analysis of the LD simulations presented. The random error of the simulated DT eigenvalues behaves in a way identical to Monte Carlo DT simulations [54]. It is controlled by the ensemble size (N_P): the relative uncertainty of diffusivities is $\Delta D_s/D_o = \sqrt{3/N_p}$. The principal source of systematic error is the assumption that the conservative force remains constant throughout the time step (see Eq. A.4). In the first order of approximation, this leads to the following systematic error of the simulated diffusivities:

$$\Delta D_s = \frac{\sqrt{2D_o}}{2(6\pi\eta R)^2}\frac{\Delta t^{5/2}}{N_T\Delta t}\left\langle \sum_{i=1}^{N_T}\sum_{j=1}^{N_T}\xi_{is}(\partial_s F_{js})F_{js}\right\rangle + \frac{2}{2(6\pi\eta R)^3}\frac{\Delta t^3}{N_T\Delta t}\left\langle \sum_{i=1}^{N_T}\sum_{j=1}^{N_T}F_{is}(\partial_s F_{js})F_{js}\right\rangle + \frac{1}{4(6\pi\eta R)^2}\frac{\Delta t^4}{N_T\Delta t}\left\langle \sum_{i=1}^{N_T}\sum_{j=1}^{N_T}(\partial_s F_{is})F_{is}(\partial_s F_{js})F_{js}\right\rangle$$

where N_T is the number of time steps in the simulation; $s = x$, y or z; ξ_i is the unit vector corresponding to the direction of the random force in time step i; $\mathbf{F}_i$ is the conservative force in time step i; $\partial_s F_{is}$ is the derivative of the s-th component of $\mathbf{F}_i$ with respect to the coordinate s; and the averaging $< ... >$ is performed over the ensemble. For a fixed total diffusion time $t = N_T\Delta t$, the three terms in Eq. (B.3) grow with the time step size as $O(\Delta t)$, $O(\Delta t)$, and $O(\Delta t^2)$, respectively. Under the simulation conditions used, only the first term was significant; therefore for a fixed total t the systematic error can be expected to be proportional to Δt. For the simulation parameters described in Chapter 3, the typical systematic error $\Delta D_s/D_o$ was $\sim 0.1\%$, well below the statistical error of 1.7%.

Appendix C

Positional and radial disorder parameters

The position disorder parameter, S_P, was calculated as,

$$S_P = \frac{1}{N^2} \sum_{i=1}^{N} \sum_{j=1}^{N} (\mathbf{P}_i - \mathbf{P}_{oi}) \cdot (\mathbf{P}_j - \mathbf{P}_{oj}) \tag{C.1}$$

where N is the number of fibres $\mathbf{P}_{oi}$ is the location of the unperturbed fibre i, and $\mathbf{P_i}$ is the randomly chosen location of the perturbed fibre i.

The radial disorder parameter, S_R, was calculated as,

$$S_R = \frac{1}{N^2} \sum_{i=1}^{N} \sum_{j=1}^{N} (R_i - R_{oi}) \cdot (R_j - R_{oj}) \tag{C.2}$$

where R_{oi} is the initial radius of fibre i, and R_i is the perturbed radius of fibre i.

Appendix D

Further development of discrete computational techniques for calculation of restricted diffusion propagators in porous media.

The authors listed below have certified* that:

1. they meet the criteria for authorship in that they have participated in the conception, execution, or interpretation, of at least that part of the publication in their field of expertise;

2. they take public responsibility for their part of the publication, except for the responsible author who accepts overall responsibility for the publication;

3. there are no other authors of the publication according to these criteria;

4. potential conflicts of interest have been disclosed to (a) granting bodies, (b) the editor or publisher of journals or other publications, and (c) the head of the responsible academic unit, and

5. they agree to the use of the publication in the students thesis and its publication on the QUT ePrints database consistent with any limitations set by publisher requirements.

In the case of this appendix:

Further development of discrete computational techniques for calculation of restricted diffusion propagators in porous media

Konstantin I. Momot, Sean K. Powell and Monique C Tourell, *Microporous and Mesoporous Materials*, 205(1), 24-30, (2014)

Contributor	**Statement of contribution***
Sean K. Powell QUT Verified Signature Signature 18-01-2016 Date	Co-developed the lattice path count (LPC) method, wrote the LPC software, developed the simulation volume and performed the LPC simulations for the paper. Also adapted the Langevin dynamics simulation software of Chapter 3 to produce the Monte-Carlo simulations of Fig. D.6. Generated the MC and LPC data, analysis and plots for Fig. D.6
Konstantin I. Momot*	Proposed the idea for both the LPC and Markov transition matrix (MTM) methods. Co-developed the LPC method and developed the MTM method. Performed all MTM simulations and analysis. Wrote the manuscript and supervised the research.
Monique C. Tourell	Wrote the Monte-Carlo software and performed the simulations and data analysis for Fig. D.3. Produced figure D.3.

Principal Supervisor Confirmation

I have sighted email or other correspondence from all Co-authors confirming their certifying authorship.

QUT Verified Signature

Konstantin Momot 18/01/2016

Name Signature Date

D.1 Further development of discrete computational techniques for calculation of restricted diffusion propagators in porous media.

Konstantin I. Momot, **Sean K. Powell**, and Monique C. Tourell

School of Chemistry Physics and Mechanical Engineering, Queensland University of Technology, GPO Box 2434, Brisbane, Queensland 4001, Australia

Published in: Microporous and Mesoporous Materials, In Press, 2015

doi:10.1016/j.micromeso.2014.08.037

D.1.1 Abstract

Magnetic resonance is a well-established tool for structural characterisation of porous media. Features of pore-space morphology can be inferred from NMR diffusion-diffraction plots or the time-dependence of the apparent diffusion coefficient. Diffusion NMR signal attenuation can be computed from the restricted diffusion propagator, which describes the distribution of diffusing particles for a given starting position and diffusion time.

We present two techniques for efficient evaluation of restricted diffusion propagators for use in NMR porous-media characterisation. The first is the Lattice Path Count (LPC). Its physical essence is that the restricted diffusion propagator connecting points A and B in time t is proportional to the number of distinct length-t paths from A to B. By using a discrete lattice, the number of such paths can be counted exactly. The second technique is the Markov transition matrix (MTM). The matrix represents the probabilities of jumps between every pair of lattice nodes within a single timestep. The propagator for an arbitrary diffusion time can be calculated as the appropriate matrix power. For periodic geometries, the transition matrix needs to be defined only for a

single unit cell. This makes MTM ideally suited for periodic systems.

Both LPC and MTM are closely related to existing computational techniques: LPC, to combinatorial techniques; and MTM, to the FokkerPlanck master equation. The relationship between LPC, MTM and other computational techniques is briefly discussed in the paper. Both LPC and MTM perform favourably compared to Monte Carlo sampling, yielding highly accurate and almost noiseless restricted diffusion propagators. Initial tests indicate that their computational performance is comparable to that of finite element methods. Both LPC and MTM can be applied to complicated pore-space geometries with no analytic solution. We discuss the new methods in the context of diffusion propagator calculation in porous materials and model biological tissues.

D.1.2 Introduction and background

Diffusion magnetic resonance

Molecular diffusion is a physical phenomenon that arises from random thermal motion of molecules [277]. The molecules in a liquid undergo continuous translational motion due to their possessing a non-zero kinetic energy (thermal energy) [278]. The molecules continuously interact and collide with each other, resulting in a chaotic, quasi-random motion pattern. The trajectory of a diffusing molecule is therefore represented by a random walk. A well-known property of diffusion is that the mean-squared displacement of the diffusing molecules, $\langle \Delta x^2 \rangle$, is proportional to time:

$$\left\langle \Delta x^2 \right\rangle = 2Dt \tag{D.1}$$

where t is the time elapsed and D is known as the diffusion coefficient. In an isotropic liquid, there is no preferred diffusion direction, and Eq. (D.1) describes the displacement of molecules in any given direction. On a more detailed level, the distribution of molecular displacements is described by the probability density function known as the diffusion propagator:

$$P(0|x,t) = \frac{1}{\sqrt{4\pi Dt}} e^{-\frac{x^2}{4Dr}} \tag{D.2}$$

Analysis of Eq. (D.2) shows that the characteristic width of the molecules distribution grows as $\sqrt{2Dt}$ in other words, the molecules spread away from their original positions. This behaviour is exploited in diffusion-sensitive nuclear magnetic resonance (NMR) spectroscopy. The basic setup of a diffusion NMR measurement can be illustrated using the experiment known as pulsed field gradient spin echo (PGSE) [3], which is illustrated in Fig. D.1. The first radiofrequency (RF) pulse in this sequence

(the 90° RF pulse) converts the equilibrium longitudinal nuclear magnetisation into a uniform comb of transverse magnetisation, while the first gradient pulse winds this comb into a helix of the pitch $2\pi/\gamma g\delta$, where γ , g and δ are the magnetogyric ratio of the nucleus, the amplitude and the duration of the field gradient pulse, respectively. It is convenient to introduce the diffusion wavevector q, whose amplitude describes the tightness of the magnetisation helix:

$$q = \gamma g \delta \tag{D.3}$$

The interval Δ shown in Fig. D.1 is known as the diffusion interval. Due to random molecular diffusion during the interval Δ, the magnetisation components of different phases become mixed up, causing attenuation of the amplitude of the helix. Assuming that δ is short, the magnetisation helix at the end of the diffusion interval Δ can be described as a convolution of the original helix and the propagator given by Eq. (D.2). The magnetisation is then refocused into a detectable (but attenuated) comb using the 180° RF pulse and the second gradient pulse. The diffusive attenuation of the refocused magnetisation and the relative amplitude of the measured signal are given by [279]:

$$\frac{S(g)}{S_0} = e^{-Dtq^2} \tag{D.4}$$

where t is the effective diffusion time (for the PGSE experiment, $t = \Delta\delta/3$).

The diffusion coefficient can be extracted by repeating the spin-echo experiment multiple times with different values of q and plotting the logarithm of the signal, $\ln(S)$, vs the quantity $tq^2 = \gamma^2 g^2 \delta^2 (\Delta\delta/3)$. This plot is known as the StejskalTanner plot. In solution (or, more generally, in the case of unrestricted diffusion), this plot is a straight line whose slope is the negative of the diffusion coefficient.

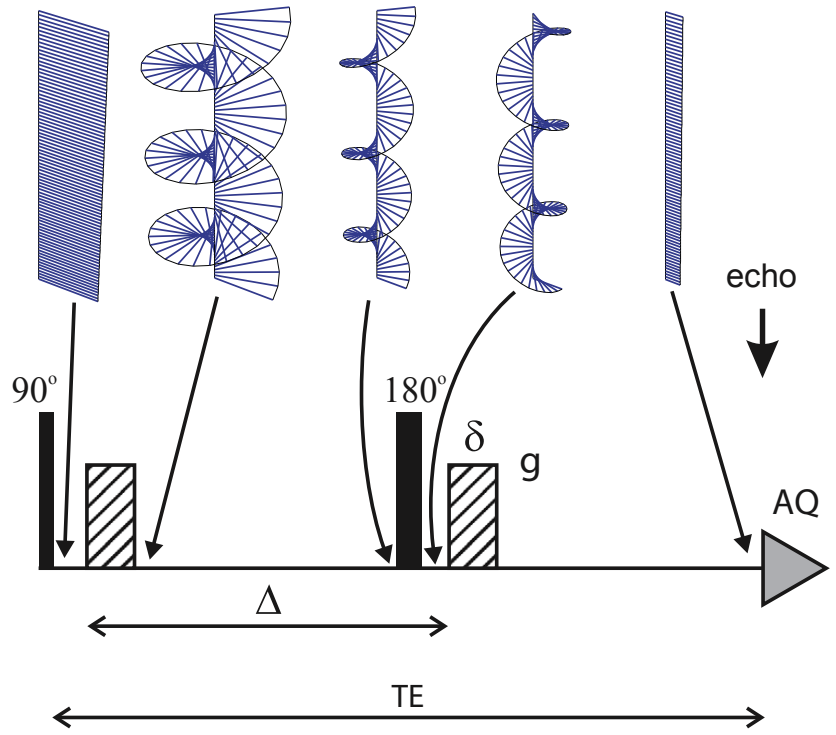

Figure D.1: The PGSE diffusion experiment: the NMR pulse sequence and the state of transverse magnetisation within the sample. The solid rectangles in the pulse sequence are RF pulses; the hatched rectangles are gradient pulses. The $90°$ RF pulse converts the equilibrium longitudinal magnetisation into a uniform comb of transverse magnetisation. The first gradient pulse winds the comb into a helix of the pitch $2\pi/\gamma g\delta$, sensitising the magnetisation to diffusion. Diffusion during the interval Δ mixes the magnetisation of different phases, causing the helix to attenuate. The $180°$ RF pulse and the second gradient pulse refocus the helix into a uniform (but attenuated) comb; its amplitude is the amplitude of the measured signal. The interval TE is the echo time. The diffusive attenuation of the signal is given by Eq. (D.4).

Diffusion NMR for porous media characterisation

Diffusion in solution is non-directional, meaning that the 3D generalisation of the diffusion propagator given by Eq. (D.2) is spherically symmetric and Gaussian. However, this is not generally the case for diffusion within porous media. The diffusional motion of molecules within porous media is obstructed by the walls forming the pore space; this is known as restricted diffusion. The walls can be either solid walls (e.g., in sedimentary rocks) or, in biological tissues, cell membranes or components of the extracellular matrix. In general, these structures have a twofold effect on the motion of diffusing molecules: first, some locations are no longer available for the molecules to diffuse into; and second, the presence of obstructions cuts out some of the paths that would otherwise be present for a molecule diffusing from an available location r to another available location r. As a result, the mathematical function describing the restricted diffusion propagator $P(r|r,t)$ is in general no longer Gaussian. This function can become very complicated and, in most cases, cannot be expressed in a compact analytic form. Nevertheless, the diffusion propagator and the detected PGSE signal are still related in the short-δ limit via the convolution operation:

$$s(g,\triangle) = \int\int \rho(\mathbf{r})P(\mathbf{r}|\mathbf{r}',\triangle)e^{i\mathbf{q}\cdot(\mathbf{r}'-\mathbf{r})}d^3\mathbf{r}d^3\mathbf{r}' \tag{D.5}$$

Here, the function $\rho(r)$ describes the spin density within the pore space; it is zero within solid walls but non-zero within the pores themselves. As seen from Eq. (D.5), the restricted diffusion propagator $P(r|r,\Delta)$ provides the link between the pore space geometry and the diffusive signal attenuation measured in NMR experiments [29] and [51]. Analysis of the diffusion propagator can therefore enable an improved understanding of the relationship between the NMR signal and features of the pore space morphology. The restricted diffusion propagator is therefore a crucial construct for the interpretation of NMR diffusion measurements. Besides providing a link between the

pore space geometry and the MR signal, the diffusion propagator is significant in its own right. In diffusion propagator imaging and related techniques [280] and [281], the ensemble average propagator is used to characterise tissue microstructure.

Techniques for calculation of the diffusion propagator

The techniques presented in this paper draw on the wide field of existing approaches to diffusion propagator calculation in porous media and biological tissues. Representative approaches include:

(1) Analytic solution This entails solving the diffusion equation subject to the boundary conditions, which are determined by the nature of the pore space. The boundary conditions typically encountered in physical or biological systems are reflecting walls ($\frac{\partial P}{\partial x} = 0$ at the boundary), absorbing walls ($P = 0$ at the boundary), and partially reflecting walls ($\frac{\partial P}{\partial x}$ across the boundary is related to the concentration difference and the permeability of the boundary). The solution of the diffusion equation describes the distribution of the diffusing molecules as a function of time and position for a given starting position and the given pore space. For simple pore geometries, the solution may be able to be expressed analytically, often as an infinite series. Analytic solution of the diffusion equation often benefits from the use of special techniques, e.g. the Laplace transform [282] and [283] or fractional calculus [284], [285] and [286]. Nevertheless, the set of pore space geometries for which a compact analytic solution is feasible remains limited and includes only relatively simple geometries. Approximate analytic methods are available for more complicated pore-space geometries [226].

(2) Eigenfunction expansion This approach is closely related to the analytic approach and entails representation of the propagator as a combination of eigenfunctions of the diffusion operator subject to the given boundary conditions. The boundary

conditions determine the eigenvalues of the diffusion operator, and these in turn determine the valid set of eigenfunctions. The propagator then has the form of a linear combination of the eigenfunctions that exponentially decay in time at a rate determined by the respective eigenvalue. This approach can also be prone to complications. For example, in the classic problem considered by Tanner [287], an equidistant stack of semipermeable bilayers separates N compartments of water (see Fig. D.2). The eigenvalues in this problem occur in tightly spaced groups of $(N2)$. Within each group the characteristic function oscillates extremely rapidly, making accurate determination of the eigenvalues very challenging for an N greater than ~ 8. In this particular system the complication has been overcome through the use of Laplace transform [288]. Approximate eigenfunction-based approaches are also available [289].

(3) Finite element (FE) and finite difference (FD) methods This is a broad family of numerical methods where the diffusion equation is solved numerically on a mesh. This approach is very powerful and computationally efficient. It has significantly evolved over recent decades and is capable of producing numerical solutions for pore spaces of arbitrary geometry [244], [245], [246] and [239]. The applicability of this approach can be limited by its convergence properties, especially in complicated, multiscale pore spaces or when a sharp initial distribution of particles is involved.

(4) Monte Carlo and Langevin dynamics simulations These are two closely related methods where diffusion is sampled statistically using an ensemble of tracer molecules and a series of time steps. In every time step, the simulation is based directly on the molecular-level interaction of the tracer with the environment. The simulation is therefore straightforward, makes a minimal number of physical assumptions and can be applied to complicated pore space geometries. Fig. D.3 illustrates results previously published by our group [35] and [9], where Monte Carlo or Langevin dynamics simulations were used to sample the fractional anisotropy of the water diffusion tensor

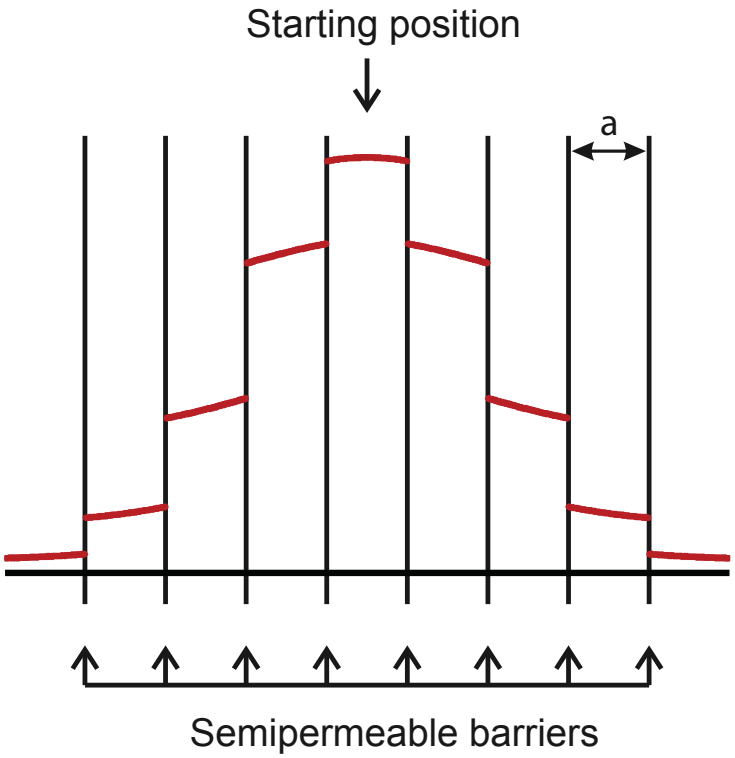

Figure D.2: The stacked bilayer problem considered by Tanner [287]: an equidistant stack of parallel semipermeable bilayers separated by distance a. The compartments between the bilayers are filled with water. Water molecules are able to cross a bilayer from one compartment into the next; however, this crossing is not effortless and a certain fraction of molecules are reflected by the bilayer. As a result, the concentration profile of the diffusing molecules exhibits discontinuities at the bilayers. The internal boundary conditions are given by two sets of equations: the first postulates the continuity of the concentration gradient (and therefore the flux) at each semipermeable boundary [Eq. (6) in Ref. [287]]; the second set relates the flux across each boundary to the bilayer permeability [Eq. (6) in Ref. [287]]. Furthermore, either end of the simulation volume is treated as an absorbing boundary.

in partially aligned networks of fibres. The networks serve as models of the collagen network in articular cartilage. Fig. D.3 also reveals a drawback of the Monte Carlo approach: its inherent noise, which is proportional to $1\sqrt{N_P}$, the inverse square root of the number of tracer particles. The results shown in Fig. D.3 were obtained with $N_P = 150,000$; even with such a large number of tracer particles, the amount of noise is significant. Each data point in Fig. D.3 represents a simulation that took between 1 CPU-hour and 10 CPU-hours on a supercomputer. This example illustrates the high computational cost of accurate and precise Monte Carlo sampling of restricted

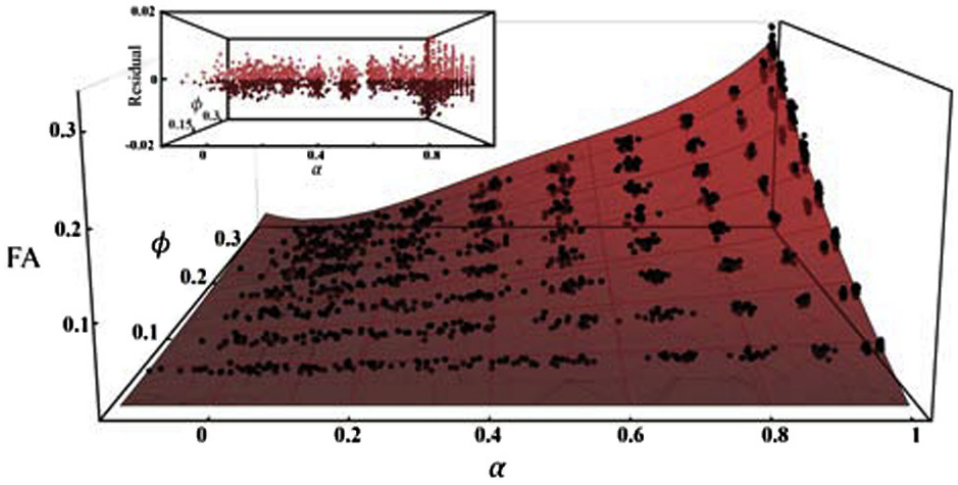

Figure D.3: The fractional anisotropy (FA) of the simulated water diffusion tensor in networks of partially aligned collagen fibres. The independent variables are collagen volume fraction (ϕ) and the fibre order parameter (α). The surface is an expansion of the simulated FA using polynomial functions of ϕ and real spherical-harmonic functions of α. The insert shows the fit residuals, illustrating the noise inherent in Monte Carlo sampling. Based on the results previously published by Tourell et al. [35]

.

diffusion. On the other hand, Monte Carlos advantage is that it is naturally able to sample the average diffusion propagator, taking into account the distribution of the starting positions of diffusing particles.

In the following we present two new computational techniques that complement the existing methods for the calculation of restricted diffusion propagators. The first technique is called the Lattice Path Count (LPC). Its name is due to the fact that it evaluates the diffusion propagator by literally counting the number of distinct length-t paths on a discrete lattice. The propagator connecting points A and B in time t is proportional to the number of such paths from A to B. Lattice Path Counting in general is a well-established branch of combinatorics [290] and [291]; however, to our knowledge, the present work is the first explicit application of Lattice Path Counting to restricted diffusion.

The second technique presented is the Markov transition matrix (MTM). The name of this technique is due to the fact that diffusion is simulated using a Markovian matrix

containing the probabilities of jumps between every pair of lattice nodes within a single timestep. The matrix description of Markovian processes is well-established in the literature [292] and [293]. MTM is also closely related to the operator description of diffusion processes, most notably the FokkerPlanck master equation [294] and [295]. Nevertheless, MTM is sufficiently distinct from the existing techniques to be viewed as a new method. To our knowledge, this work describes its first explicit application to restricted diffusion.

In the following, we present a brief introduction to both methods with a view to publishing a more comprehensive technical description in subsequent manuscripts. We briefly discuss the relationship between LPC, MTM and the existing techniques, as well as the elements of novelty of the two new methods in the context of restricted diffusion in porous media. For the purposes of this introduction, we illustrate applications of the two methods using relatively simple systems: LPC using a simplified model of articular cartilage [35], [9] and [114] and MTM using a system of parallel stacked bilayers [287]. Nevertheless, both methods are generally applicable to complex, irregular pore-space geometries with no analytic solutions. We discuss the applications of both methods to porous media and their respective advantages and limitations.

D.1.3 Methods

Lattice Path Count (LPC)

The LPC method considers the diffusion of a particle on a regular discrete lattice. The idea underpinning this method is that, for a particle undergoing a random walk consisting of N time steps, every distinct length-N path is equally probable. This assumption is valid when the translational diffusion is completely random and there is no bias in the particles translational displacement within a given time step. It then follows that the probability for the particle known to start at an initial location A to

diffuse to a final location B over N time steps is simply the relative number of distinct length-N paths connecting A and B. This idea is easily illustrated for unobstructed diffusion, where the number of such paths can be obtained analytically. For an N-step random walk in one dimension, there are 2^N distinct paths that connect the starting location (say $x_0 = 0$) with some final location. For the particle to arrive at the final location x, it must take, in any order, $N^+ = (N + x)/2$ steps to the right and $N^- = (N - x)/2$ steps to the left. Simple combinatorial analysis shows that the absolute conditional probability for the particle starting at $x_0 = 0$ to end up at x after N time steps is

$$P(0, x, n) = \frac{1}{2^n} \cdot \frac{n!}{\left(\frac{n+x}{2}\right)! \left(\frac{n-x}{2}\right)!} \tag{D.6}$$

Eq. (D.6) is the discretised diffusion propagator describing the distribution of translational displacements of the diffusing particles. It is easily seen that the expression in Eq. (D.6) is normalised: the sum of the probabilities over all possible values of $x = -N, -N + 2\ , \ldots\ , N - 2, N$ is 1 for any value of N. Plotting Eq. (D.6) vs x for various values of N reveals that at large N the discrete propagator asymptotically approaches the Gaussian propagator given by Eq. (D.2), where $t = N$ and $D = 1/2$. Therefore, by applying the appropriate scale of spatial discretisation relative to the RMS diffusional displacement of the particles, Eq. (D.6) can be used to calculate the unrestricted diffusion propagator with any desired degree of accuracy. The presence of absorbing or reflecting walls (obstructions) has the effect of making some of the paths unavailable to the diffusing particles. The reduction of the number of available paths is dependent in a complicated way upon the geometry of the obstructions, the initial and the final positions of the diffusing particle, and the nature of the boundary conditions (e.g. absorbing, reflecting or semipermeable). In general, it is not possible to obtain a compact analytic expression similar to Eq. (D.6) for restricted-diffusion situations. However, the number of the available paths can still be counted numerically for an

arbitrary pore-space geometry. It is worth emphasising that the paths themselves need not be memorised only their number needs to be evaluated. This is accomplished in a computationally efficient way by using a Pascal triangle-like counting algorithm generalised to the two- or three-dimensional case and taking into account the reflection or absorption at the boundaries. The number of paths available is astronomically large even for modest-size random walks, and their counting is still a challenging computational problem. However, the paths can be counted exactly through the use of unlimited-length integers. As was the case for unrestricted diffusion, the normalised number of paths is the discretised restricted-diffusion propagator describing the distribution of translational displacements of the diffusing particles.

Markov transition matrix (MTM)

The MTM method can also be illustrated using one-dimensional unrestricted diffusion as an example. Consider a discretised random walk on an equidistantly spaced grid. Such a random walk can be viewed as a Markovian process whereby the system performs transitions between available discrete states. Following well-established methodology [292] and [293], the evolution of the distribution of occupied states can be described by the Markov transition matrix $\mathbf{M}$. The elements of $\mathbf{M}$ are the probabilities of transition from an initial location x_i to a final location x_f within time step Δt:

$$M_{fi} = \frac{C_i}{\sqrt{4\pi D\Delta t}} e^{-\frac{(x_f - x_i)^2}{4D\Delta t}} \tag{D.7}$$

Eq. (D.7), which is illustrated in Fig. D.4(a), is a discretised version of the unrestricted diffusion propagator given by Eq. (D.2). The coefficients C_i arise out of the discretisation and ensure that the probabilities given by Eq. (D.7) are normalised. These coefficients can be calculated numerically as the sum of the matrix elements

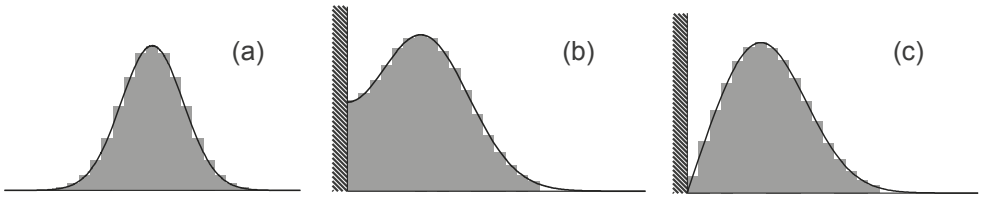

Figure D.4: Discretisation of the diffusion propagator in the MTM method: (a) for unrestricted isotropic diffusion, the Gaussian propagator given by Eq. (D.2) is discretised, resulting in the transition matrix given by Eq. (D.7). (b) For diffusion near a single reflecting wall, a similar discretisation procedure is performed, but for the analytic propagator that takes into account the presence of the reflecting boundary condition, $\partial P(0)/\partial x = 0$. The corresponding solution is given by Eq. (D.8) with the + sign. (c) Diffusion near a single absorbing wall: the boundary condition is $P(0) = 0$. The analytic propagator being discretised is given by Eq. (D.8) with the sign.

$M_f i$ over all values of f; in the limit of extremely fine discretisation C_i tends to 1.

The distribution of the diffusing particles in the MTM formalism is represented as a column vector whose elements correspond to the probability for a particle to be at a given position. For particles starting from the same initial position, the initial vector $\mathbf{v_0}$ is a vector of all zeroes and a single 1. The distribution of the diffusing particles at the end of the time step Δt is then the matrix product $\mathbf{M} \cdot \mathbf{v_0}$, as illustrated in Fig. D.5. The distributions at a longer time $t = N\Delta t$ can be computed as $\mathbf{M^N} \cdot \mathbf{v_0}$, where N is the integer number of time steps and the matrix $\mathbf{M^N}$ is computed numerically as the N-th matrix power of $\mathbf{M}$.

The presence of obstructions can be easily incorporated into the MTM method by employing small time steps. If the RMS displacement during time step Δt is significantly smaller than the characteristic distance between obstructions, then it is extremely improbable for the diffusing particle to encounter more than one obstruction during a single time step. Under these circumstances, all obstructions can be considered single-sided and the diffusion propagator near an obstruction can be calculated analytically. For example, for diffusion near a single reflecting or absorbing wall the propagator to be discretised is given by

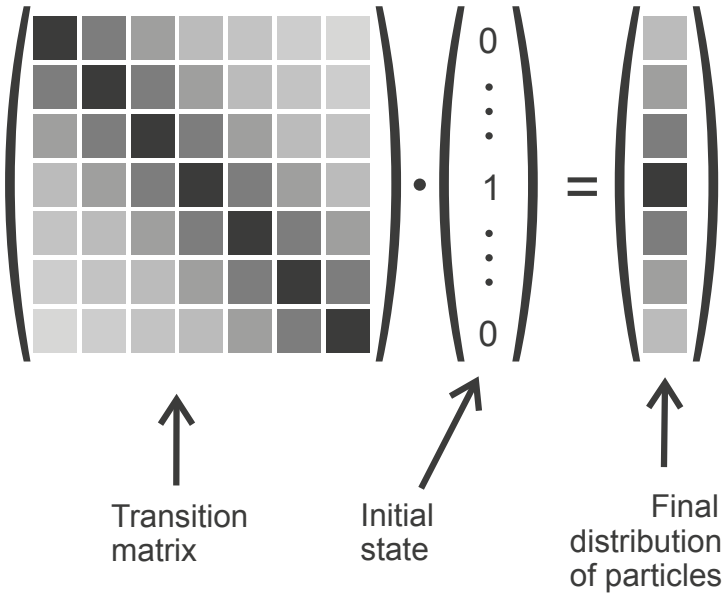

Figure D.5: Calculation of the distribution of positions of the diffusing particles in the MTM method. The column vector on the left-hand side represents the initial distribution of the particles. The matrix is the Markov transition matrix corresponding to time t, calculated as the N-th power of the infinitesimal transition matrix if $t = N\Delta t$ (see text). The greyscale qualitatively corresponds to the relative amplitude of the matrix elements. The final distribution of the diffusing particles, represented by the column vector on the right-hand side, is the matrix product of the transition matrix and the initial-distribution vector.

$$P(x_0|t,x) = \frac{1}{\sqrt{4\pi Dt}}\left(e^{-\frac{(x-x_0)^2}{4Dt}} \pm e^{-\frac{(x-x_0)^2}{4Dt}}\right) \tag{D.8}$$

where the "+" and the "-" signs apply in the reflecting and the absorbing case, respectively, and x_0 is the initial position of the diffusing particles. The elements of the matrix $\mathbf{M}$ corresponding to the initial positions near obstructions can then be calculated by discretising the respective analytic propagator in the manner similar to Eq. (D.7). Discretisation near reflecting and absorbing walls is illustrated in Fig. D.4(b) and (c), respectively. Semipermeable barriers can also be treated and are considered as an example in the following section. For a long diffusion time t, it is computationally efficient to select a time step Δt such that t is a power-of-2 multiple of $\Delta t : t = 2K\Delta t$. The N-step Markov matrix can then be computed in $k = log_2 N$ rather than N steps:

$$\begin{aligned}
\mathbf{M}(2\Delta t) &= \mathbf{M}^2(\Delta t) \\
\mathbf{M}(4\Delta t) &= \mathbf{M}^2(2\Delta t) \\
&\cdots \\
\mathbf{M}(2^k\Delta t) &= \mathbf{M}^2(2^{k-1}\Delta t)
\end{aligned} \tag{D.9}$$

Although the MTM method exhibits a superficial similarity to Finite Difference and Finite Element methods, it is in fact distinct from these two families of methods. The differences between MTM and FD/FE are outlined in the following section.

D.1.4 Results and discussion

Lattice Path Count

A significant advantage of the LPC method is its ability to enumerate the exact number of distinct lattice paths available to the diffusing particles through the use of unlimited-length integers. While the numerical answer for the computed propagator must inevitably be rounded off, the rounding can occur at the last stage of the computation process, significantly reducing the potential for error accumulation.

The application of LPC is illustrated in Fig. D.6 for a regular network of perfectly aligned fibres. The fibre network serves as an idealised model of the extracellular matrix of articular cartilage [35] and [54]. The diffusing particles start at the centre of the simulation volume and perform a random walk of $N_T = 9000$ time steps. Fig. D.6 presents a comparison of the diffusion propagator computed using Monte Carlo sampling [Fig. D.6(a)] and Lattice Path Count [Fig. D.6(b)]. The LPC simulation was carried out on a three-dimensional grid of $400 \times 400 \times 400$ nodes; the 3D (rather than the much faster 2D) implementation was done for the purpose of comparison

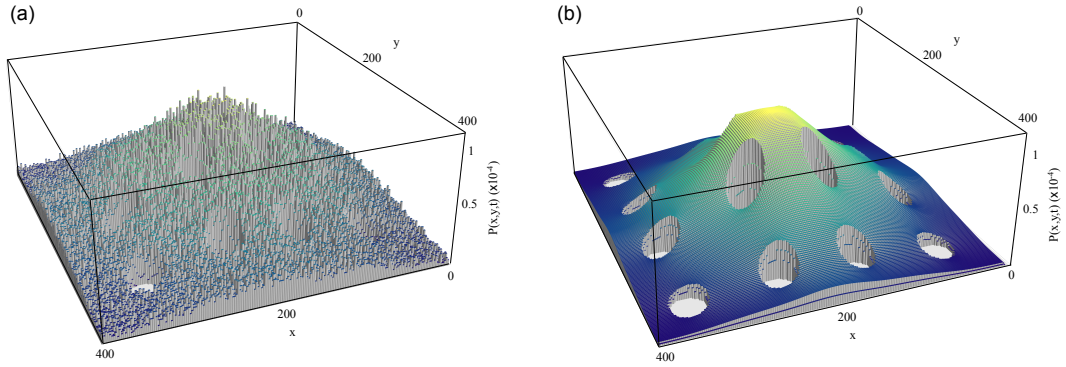

Figure D.6: Comparison of the diffusion propagator within a regular network of identically aligned collagen fibres computed using: (a) Monte Carlo sampling with $N_P = 10^8$ tracer molecules and (b) LPC on a $400 \times 400 \times 400$ discrete grid. The LPC propagator is practically noiseless, while the Monte Carlo propagator exhibits a considerable amount of sampling noise. The simulation volume was subject to reflecting boundary conditions. The execution times were $\sim 86\,h$ for Monte Carlo and $\sim 72\,h$ for LPC.

with the past MC simulations for the same system [35]. As can be expected from an examination of Fig. D.3, the Monte Carlo propagator exhibits a significant level of noise. The LPC propagator exhibits a negligible level of noise compared to Monte Carlo. The two diffusion propagators exhibit no significant systematic differences. Intuitively, the significant difference in the precision of the two propagators can be attributed to the fact that the LPC method performs an exact count of all the available diffusion paths ($89000 \approx 6 \times 10^{8127}$ paths), while Monte Carlo samples only a very limited subset of $N_P = 10^8$ paths.

The other important difference between the Monte Carlo and LPC propagators is the spatial distribution of the sampling errors. Because Monte Carlo sampling is statistical, its accuracy is non-uniform: the uncertainty of the computed propagator is proportional not only to the square root of the number of tracer particles, but also to the square root of the value of the propagator itself:

$$\Delta P(\mathbf{r},t) \propto \sqrt{N_p} \cdot \sqrt{P(\mathbf{r},t)} \tag{D.10}$$

The LPC method does not suffer from this artifact and provides a spatially uniform sampling accuracy.

We have not comprehensively examined the computational efficiency of LPC; however, it appears to be in the same ballpark as FE methods. For example, in Nguyen et al. [244] a FE solution of the BlochTorrey equation on a 3D lattice of $\sim 400,000$ nodes took ~ 40 minutes. Allowing a 4-fold shorter time for the computationally less demanding diffusion equation and rescaling the computation time for a lattice of $(400)^3$ nodes, the estimated time of the FE calculation would have been $(10\,min) \times 64,000,000/400,000 = 1600\,min = 27\,h$, which is comparable to the $72\,h$ LPC computation time. No claim is being made by us as to whether LPC has the capacity, with the appropriate algorithmic and code optimisations, to exceed the computational efficiency of FE. Nevertheless, computational efficiency was not the principal motivation in the development of this technique. In our view, the insight into the physical meaning of the diffusion propagator as the relative number of paths of a certain length connecting a pair of points is in itself a valuable feature of LPC. Furthermore, LPC appears attractive for calculation of path-based metrics of the pore space, e.g. tortuosity.

The key disadvantage of LPC is its inherent requirement of a finite simulation volume bounded by absorbing, reflecting or periodic boundaries. This limits the applicability of LPC to very long diffusion times. Nevertheless, LPC is an excellent technique when an extremely precise restricted-diffusion propagator at short to intermediate diffusion times (the number of steps of a few hundred to a few thousand) is required.

D.1.5 Markov transition matrix

The use of Markov chains has been explored previously for the modelling of transport processes in heterogeneous systems [296], [297] and [298]. A significant advantage of the MTM method is the computational complexity that scales with the number of time

steps as $log_2 N$. This feature makes MTM ideally suited for very long diffusion times. To illustrate the application of MTM, we use Tannerss stacked-bilayer system shown in Fig. D.2 [287]. The system simulated here had the dimensionless permeability, $\kappa = ap/D_0$, of 0.18 (where a is the bilayer spacing, p is the permeability in m/s, and D_0 is the bulk diffusion coefficient of water). The range of the dimensionless diffusion times probed, $T = D_0\Delta/a^2$, was from $T = 0.002$ to $T = 262$ (where Δ is the diffusion time in seconds). Fig. D.7 shows the simulated dependence of the apparent diffusion coefficient on the diffusion time. The time axis in this figure is logarithmic: every next point corresponds to double the diffusion time of the previous point. The plot clearly demonstrates the three diffusion regimes characteristic of porous media. The short-Δ regime, where the diffusion coefficient is nearly identical to that of bulk water (D_0), is represented by points 14. The long-Δ regime, where the apparent diffusion coefficient is limited by the bilayer permeability and approaches the asymptotic value $D_\infty = \kappa D_0/(\kappa + 1)$, is represented by points 1118. Points 510 represent the intermediate-Δ regime, where the apparent diffusion coefficient exhibits a strong dependence upon the diffusion time Δ. The width of the long-Δ range sampled in this example is at least a 100-multiple of the time corresponding to the onset of the long-Δ regime. The simulations were performed overnight on an average desktop PC using Mathematica. This is an outstanding computational performance in terms of sampling very long diffusion times, especially considering the lack of pre-compiled code or any computational optimisation of the MTM simulations. This example illustrates the excellent suitability of MTM for sampling the asymptotic long-Δ regime of restricted diffusion in porous media.

From the computational point of view, the matrix $\mathbf{M}$ describing the transition probabilities within a single time step Δt has a near-diagonal form, which corresponds to the fact that the displacement of the diffusing particles during a short Δt can be only a few lattice nodes at the most. As t increases, the N-step transition matrix $\mathbf{M}_N$

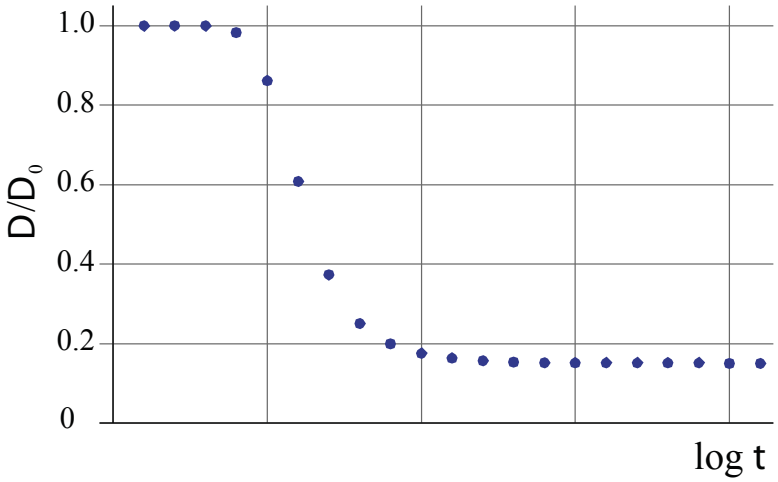

Figure D.7: The apparent diffusion coefficient of water in Tanners stacked bilayer system [287] computed for a range of diffusion times using the MTM method. The system simulated consisted of $N = 33$ water compartments with 55 grid points per compartment; the resulting size of the Markov matrix M was 1817×1817. The end bilayers on either side were treated as absorbing; the remaining bilayers were treated as semipermeable with the dimensionless permeability $\kappa = ap/D_0 = 0.18$. The dimensionless diffusion times sampled, $T = D_0\Delta/a^2$, were $0.001{\cdot}2^K$, where K ranged from 1 to 18. The time axis of the plot is logarithmic, with each point corresponding to double the diffusion time of the previous point.

becomes more diffuse, with the relative size of off-diagonal terms growing. At large values of t it eventually becomes necessary to increase the size of M, corresponding to the need to include a greater number of nodes for long diffusion times compared to intermediate times. This requirement is not unique to MTM and applies equally to FD/FE simulations.

MTM exhibits a similarity with Finite Difference methods in that both methods make use of a regular grid of lattice points and propagate small time-step increments in order to obtain a solution at longer times. Nevertheless, this similarity is superficial, and the following important differences between MTM and FD exist. The first, procedural, difference is that FD involves the solution of the discretised diffusion equation, while MTM directly models a dispersive stochastic process (the spreading out of the distribution of particles). While the MTM and FD solutions are identical in the limiting case, they are arrived at in very different ways. The second difference is computational

and relates to the treatment of boundary conditions. FD calculation requires that absorbing or reflecting boundary conditions be handled on a step-by-step basis. On the other hand, in MTM boundary conditions are implicitly built into the Markov transition matrix M as shown in Eq. (D.8) and Fig. D.4(b) and (c). This obviates the need for handling the boundary conditions at every time step Δt, providing a computational advantage at long diffusion times. The third important distinction is summarised by Eq. (D.9), which demonstrates that the computational complexity of MTM scales with the diffusion time as $O(log_2 t)$ rather than $O(t)$. This further enhances MTMs attractiveness for the analysis of asymptotic long-Δ diffusion regime, as discussed above.

In analysing the computational efficiency of MTM, it should be kept in mind that the method is not limited to the simple system used to illustrate it in the present work. A facile analytic solution exists for Tanners stacked-bilayer system [288]; and any numerical method, including MTM, is unlikely to be computationally faster than that solution. However, MTM is a general method that can be applied to complex pore-space geometries for which no analytic solution exists.

The other important advantage of MTM is its efficiency in handling restricted diffusion in periodic systems. Periodic boundary conditions are commonly used in order to limit the size of the simulation volume required to be considered [99]. However, special precautions are needed in order for periodic-BC simulations to be suitable for the calculation of the apparent translational diffusion coefficient. This requirement arises from the distortion of the diffusing particles positions by boundary crossings. In Monte Carlo simulations, an unbiased diffusion coefficient can be reconstructed by keeping track of the number of boundary crossings for each particle and reconstructing the particles true positions [35]. The same objective can be achieved in MTM as follows. In the presence of periodic boundary conditions the transition matrix shown in Fig. D.5 has the structure comprising three clusters: the near-diagonal cluster

representing the particles remaining in the same periodic unit cell during the time step Δt, as well as upper-right and lower-left corner clusters that represent boundary crossings to the right and to the left, respectively. By selecting a sufficiently small time step Δt, the three clusters can be kept well separated. In calculating evolution of the particles distribution according to the scheme shown in Eq. (D.9), it is also possible to keep different crossover orders separate and thus enable the reconstruction of the particles true positions, yielding an unbiased diffusion propagator and apparent diffusion coefficient. As a result, MTM enables computational handling of restricted diffusion in unbounded periodic systems without requiring the introduction of an unbounded spatial grid. This further adds to MTMs capacity to significantly simplify restricted-diffusion simulations at very long diffusion times.

D.1.6 Conclusions

The Lattice Path Count (LPC) method enables calculation of extremely accurate restricted diffusion propagators at short to intermediate diffusion times. Importantly, it also provides insight into the physical meaning of the diffusion propagator as the relative number of paths of a certain length connecting a pair of points. This makes LPC attractive for calculation of path-based metrics of the pore space, such as tortuosity.

The Markov transition matrix (MTM) method is suitable for periodic or quasi-periodic pore space geometries. It is also compares very favourably to Monte Carlo with respect to simulating restricted diffusion at very long times and sampling the asymptotic tail of the apparent diffusion coefficient. MTM is also amenable to the inclusion of spin relaxation or surface interactions, which can both be built into the transition matrix. Finally, as a matrix-based formalism, MTM appears attractive in terms of solving the inverse problem, using the diffusion propagator in order to characterise the morphology of the pore space and thus expanding the applications of diffusion NMR to morphological characterisation of porous materials.

D.1.7 Acknowledgements

The authors acknowledge Dr Glen J. Oberman (QUT School of Mathematical Sciences) for proposing the efficient path-counting algorithm for use in LPC. Supercomputer resources and services used in this work were provided by the High-Performance Computing Centre and Research Support Group (HPC), Queensland University of Technology. SKP and MCT acknowledge the finical support by QUTs Institute of Health and Biomedical Innovation (IHBI). The authors are indebted to the reviewers for their critical analysis of the work.